Universität Münster

JÜLICH Forschungszentrum | HELMHOLTZ-INSTITUT MÜNSTER

Interphase Modification and Investigation by Advanced Operando Raman Spectroscopy in High-Voltage Lithium-Ion Batteries

Inauguraldissertation

zur Erlangung des Doktorgrades

der Naturwissenschaften im Fachbereich Chemie und Pharmazie

der Mathematisch-Naturwissenschaftlichen Fakultät

der Universität Münster

Vorgelegt von

Felix Amandus Pfeiffer

aus Münster

-2025-

Institut für Physikalische Chemie

Forschungszentrum Jülich GmbH

IMD – 4 Helmholtz Institut Münster

wissen.leben

Dekan: Prof. Dr. Dagmar Klostermeier

Erster Gutachter: Prof. Dr. Martin Winter

Zweiter Gutachter: PD Dr. Gunther Brunklaus

Tag der mündlichen Prüfung: ___.___.___

Tag der Promotion: ___.___.___

Für meine Eltern

Abstract

The interphases formed on anode and cathode in lithium-ion batteries (LIBs) play a vital role in enhancing galvanostatic cycling performance and lifetime. Moreover, stable and effective interphases are crucial to implement next generation electrode materials to enhance LIB energy density. The introduction of film-forming electrolyte additives is a promising approach to facilitate interphase formation. However, state-of-the-art electrolyte additives often struggle to cope with the challenges arising from novel electrode materials or increased operational voltage. Underlying interphase formation mechanisms have to be comprehensively understood to ensure a straightforward development of promising new additive candidates. In an ideal case, these information are obtained under real LIB cell working conditions. Nevertheless, performing interphase characterization under these demanding conditions is challenging and suitable methods are scarce. *Advanced* vibrational spectroscopy techniques, like near-field Raman spectroscopy, are powerful candidates to realize the *operando* investigation of interphases in LIBs. Therefore, the focus of this presented work is the characterization of evolving (additive-derived) interphases in high-voltage LIBs using shell-isolated nanoparticle enhanced Raman spectroscopy (SHINERS). Moreover, promising film-forming electrolyte additives will be presented and investigated, regarding their influence on the galvanostatic cycling performance in high-voltage LIBs, and their interphase-forming ability.

As SHINERS is a new characterization technique in the battery context, presented studies are scarce and not systematic. Therefore, the first part of this thesis is focused on the optimization and implementation of SHINERS into high-voltage LIBs and the validation of the introduced system. In NMC111||graphite LIBs *operando* SHINERS was employed to capture the formation of a thiophene-based interphase on the cathode's surface. Besides identifying polythiophene as main interphase component, *operando* SHINERS investigation also provided insights into the oxidative electro-polymerization of thiophene. Based on the obtained results, a reaction mechanism was proposed, supported by quantum chemistry (QC) calculations.

In the second part of this thesis the validated SHINERS technique is employed to characterize the optimized cathode-electrolyte interphase (CEI) in high-voltage NMC811||graphite pouch cells. A variety of thiophene-based electrolyte additives was investigated, revealing 3-thiophene boronic (3-THP-BOH) acid as most promising candidate. With an optimized concentration of 3-THP-BOH, galvanostatic cycle life of the employed LIBs was quadrupled and capacity fading decreased. Supported by SEM and EDX investigation, *operando* SHINERS measurements showed the formation of a CEI in the presence of 3-THP-BOH, demonstrating the polymerization of the additive. The SHINERS investigations not only captured CEI formation, but also showed a direct influence of the boronic acid group on the polymerization mechanism, compared to thiophene.

In the third part of the thesis, focus is shifted towards the investigation of the cross-talk behavior of film-forming electrolyte additives in LIBs. Here, different ethylene carbonated-derived electrolyte additives were employed in high-voltage NMC622||graphite pouch cells. Galvanostatic cycling experiments demonstrated notably enhanced performance in the presence of vinyl ethylene carbonate (VEC), reaching a cycle number 350% higher compared to the other considered electrolyte formulations. Gas chromatography mass spectrometry measurements suggested the formation of an ineffective solid-electrolyte interphase (SEI) in the presence of VEC. Instead, additional *operando* SHINERS experiments captured the formation of a VEC-derived CEI, accounting for the enhanced electrochemical performance. Based on the results of the Raman spectroscopy experiments performed on the surface of cathode and anode, a cross-talk mechanism was postulated. Starting on the anode side, VEC is reductively degraded, followed by transport on subsequent oxidative electro-polymerization on the cathode side.

Kurzfassung

Die an den Anoden und Kathoden von Lithium-Ionen-Batterien (LIBs) gebildeten Interphasen spielen eine entscheidende Rolle bei der Verbesserung der galvanostatischen Zyklusleistung und der Lebensdauer. Darüber hinaus sind stabile und effektive Interphasen essenziell, um die Verwendung von Elektrodenmaterialien der nächsten Generation zu ermöglichen und die Energiedichte von LIBs zu erhöhen. Die Einführung von filmbildenden Elektrolytadditiven ist ein vielversprechender Ansatz um die Ausbildung von effektiven Interphasen zu gewährleisten. Allerdings stoßen die derzeitigen Elektrolytadditive häufig an ihre Grenzen, wenn es um neuartige Elektrodenmaterialien oder erhöhte Betriebsspannungen geht.

Die zugrundeliegenden Mechanismen der Interphasenbildung müssen umfassend verstanden werden, um eine zielgerichtete Entwicklung neuer, vielversprechender Elektrolytadditive zu ermöglichen. Idealerweise sollten diese Informationen unter den realen Arbeitsbedingungen einer LIB ermittelt werden. Dennoch ist die Charakterisierung von Interphasen unter diesen anspruchsvollen Bedingungen herausfordernd, und geeignete Methoden sind selten. Fortschrittliche Vibrations-Spektroskopietechniken, wie die Nahfeld-Raman-Spektroskopie, sind vielversprechende Kandidaten für die *operando*-Untersuchung von Interphasen in LIBs. Der Schwerpunkt dieser Arbeit liegt daher auf der Charakterisierung von sich bildenden (additivbasierten) Interphasen in Hochspannungs-LIBs unter Verwendung von Schalen-isolierter nanopartikelverstärkter Raman Spektroskopie (SHINERS). Darüber hinaus werden vielversprechende filmbildende Elektrolytadditive hinsichtlich ihres Einflusses auf die galvanostatische Zyklusleistung in Hochspannungs-LIBs sowie ihrer Interphasenbildung untersucht.

Da SHINERS eine relativ neue Charakterisierungstechnik in der Batterieforschung ist, sind bisherige Studien selten und nicht systematisch. Der erste Teil dieser Arbeit konzentriert sich daher auf die Optimierung und Einführung von SHINERS in Hochspannungs-LIBs sowie auf die Validierung des eingeführten Systems. In NMC111||Graphit-LIBs wurde *operando* SHINERS eingesetzt, um die Bildung einer thiophenbasierten Interphase auf der Kathodenoberfläche zu beobachten. Neben der Identifizierung von Polythiophen als Hauptbestandteil der Interphase lieferte die *operando* SHINERS-Untersuchung auch Einblicke in die oxidative Elektropolymerisation von Thiophen. Basierend auf den gewonnenen Ergebnissen wurde ein Reaktionsmechanismus vorgeschlagen, der durch quantenchemische (QC) Berechnungen gestützt wurde.

Im zweiten Teil dieser Arbeit wird die nun validierte SHINERS-Technik verwendet, um die optimierte Kathoden-Elektrolyt-Interphase (CEI) in Hochspannungs-NMC811||Graphit-Pouch-Zellen zu charakterisieren. Verschiedene thiophenbasierte Elektrolyt-Additive wurden untersucht, wobei 3-Thiophen-Borsäure (3-THP-BOH) als vielversprechendster Kandidat

identifiziert wurde. Mit einer optimierten Konzentration von 3-THP-BOH wurde die galvanostatische Lebensdauer der eingesetzten LIBs vervierfacht und der Kapazitätsverlust verringert. Unterstützt durch SEM- und EDX-Untersuchungen zeigten *operando* SHINERS-Messungen die Bildung einer CEI in Anwesenheit von 3-THP-BOH, wobei die Polymerisation des Additivs nachgewiesen werden konnte. Die SHINERS-Untersuchungen erfassten allerdings nicht nur die CEI-Bildung, sondern zeigten im Vergleich zu Thiophen auch einen direkten Einfluss der Borsäuregruppe auf den Polymerisationsmechanismus.

Im dritten Teil der Arbeit liegt der Fokus auf der Untersuchung des Cross-Talk-Verhaltens von filmbildenden Elektrolytadditiven in LIBs. Hierbei wurden verschiedene ethylencarbonatbasierte Elektrolytadditive in Hochspannungs-NMC622||Graphit-Pouch-Zellen eingesetzt. Galvanostatische Zyklisierungsexperimente zeigten eine deutlich verbesserte Leistung in Anwesenheit von Vinylethylencarbonat (VEC), wobei eine um 350% höhere Zyklenzahl im Vergleich zu den anderen betrachteten Elektrolyten erreicht wurde. Messungen mittels Gaschromatographie-Massenspektrometrie deuteten auf die Bildung einer ineffektiven Festelektrolyt-Interphase (SEI) in Anwesenheit von VEC hin. Stattdessen erfassten zusätzliche *operando* SHINERS-Experimente die Bildung einer VEC-basierten CEI, die für die verbesserte elektrochemische Leistung verantwortlich ist. Basierend auf den Ergebnissen der Raman-Spektroskopie-Experimente, die an der Oberfläche von Kathode und Anode durchgeführt wurden, wurde ein Cross-Talk-Mechanismus postuliert. Beginnend auf der Anodenseite wird VEC reduktiv abgebaut, gefolgt von einem Transport und einer anschließenden oxidativen Elektropolymerisation auf der Kathodenseite.

.

Table of Contents

Abstract I
Kurzfassung III
Table of Contents V
1. General Introduction 1
2. Scientific Background 3
2.1. Lithium-Ion Batteries 3
2.2. Interphase Design Strategies 6
2.3. Interphase Characterization Techniques 10
2.4. Raman Spectroscopy for LIB Characterization 14
2.4.1. Conventional Raman Spectroscopy 14
2.4.2. Near-field Raman Spectroscopy 17
3. Motivation 23
4. Materials and Experimental Methods 26
4.1. Materials 26
4.2. Experimental Methods 28
4.2.1. Electrolyte Preparation 28
4.2.2. Cell Preparation 28
4.2.3. Electrochemical Characterization 29
4.2.3.1. Galvanostatic Charge/Discharge Cycling 29
4.2.3.2. Potentiostatic Investigation 30
4.2.3.3. Electrochemical Impedance Spectroscopy 30
4.2.4. Raman Investigation 31
4.2.5. Raman Sample Preparation 31
4.2.5.1. Nanoparticle Synthesis 32
4.2.5.2. Au Nanoparticles 32
4.2.5.2.1. 55 nm Au Nanoparticle Synthesis 32
4.2.5.2.2. 120 nm Au Nanoparticle Synthesis 32
4.2.5.2.3. 20 nm Au Nanoparticle Synthesis 33
4.2.5.3. Ag Nanoparticles 33
4.2.5.3.1. 12 nm Au Seed Synthesis 33
4.2.5.3.2. 100 nm Ag Nanoparticle Synthesis 33
4.2.5.3.3. Synthesis of Ag Nanoparticles with different sizes 34
4.2.6. Nanoparticle Characterization 34
4.2.7. SERS and SHINERS Sample Preparation 36
4.2.8. Cell and Electrode Configurations 37
4.3. Challenges of SHINERS 38
4.4. Additional Characterization Techniques 39

4.4.1. Scanning Electron Microscopy 39
4.4.2. Electron-Dispersive X-Ray Spectroscopy 39
4.4.3. Focused Ion Beam – Secondary Ion Mass Spectrometry 39
4.4.4. Gas Chromatography 40
4.4.5. Gas Chromatography with High Resolution-Accurate Mass 40
4.4.6. Nuclear Magnetron Resonance Spectroscopy 41
4.4.7. Quantum Chemistry and DFT Calculations 41
4.5. Synthesis 42
4.5.1. Synthesis of the VEC Reduction Product 42
5. Implementation of SHINERS for Interphase Investigation in High-Voltage LIBs – a Proof-of-Concept 43
5.1. Introduction 43
5.2. Electrochemical Investigation of THP-Containing LIBs 44
5.3. Surface Investigations by SEM and EDX 49
5.4. Interphase Characterization *via Operando* SHINERS 50
5.5. Mechanistic Investigation of CEI Formation *via Operando* SHINERS and Quantum Chemistry Calculations 52
5.6. Conclusion 55
6. Optimization of the NMC811-Electroyte Interphase by Thiophene-derived Additives 56
6.1. Introduction 56
6.2. Optimizing the NMC811-Electrolyte Interphase 57
6.2.1. Identification of Promising Electrolyte Additive Candidates 57
6.2.2. Electrochemical Characterization of the Optimized NMC811-Electrolyte Interphase 60
6.3. Surface Characterization *via* SEM and EDX 66
6.4. Characterization of the 3-THP-BOH-Based Interphase *via Operando* SHINERS 67
6.5. Unraveling the Interphase Formation Mechanism *via* Quantum Chemistry Calculations 72
6.6. Conclusion 75
7. Unraveling the Cross-Talk Mechanism of Ethylene Carbonate-based Electrolyte Additives 76
7.1. Introduction 76
7.2. Electrochemical Characterization of the Electrochemical Performance of EC-derived Electrolyte Additives 77
7.3. GC-MS Investigation of the Aged Electrolyte 83
7.4. SEI Characterization *via Operando* SHINERS 85
7.5. Revealing the Formation of a VEC-derived CEI 88
7.6. Characterization of the VEC-derived CEI by Raman Spectroscopy 93
7.7. Unraveling the Cross-Talk Mechanism of VEC 95
7.8. Conclusion 98

8. General Conclusion and Future Perspectives 100
9. Appendix 105
9.1. Appendix for Chapter 4 105
9.2. Appendix for Chapter 5 115
9.2.1. Electrochemical Investigation 115
9.2.2. Surface Characterization by SEM, EDX and Raman Spectroscopy 119
9.2.3. QC Calculations 120
9.3. Appendix for Chapter 6 122
9.3.1. Electrochemical Investigation 122
9.3.2. Surface Characterization via SEM, EDX and Raman Spectroscopy 129
9.3.3. QC Calculations 136
9.4. Appendix for Chapter 7 137
9.4.1. Electrochemical Investigation 137
9.4.2. GC-MS Investigation of the Aged Electrolyte 139
9.4.3. SHINERS SEI Investigation 141
9.4.4. Electrochemical Cathode Characterization 154
9.4.5. Surface Characterization *via* ToF FIB-SIMS 157
9.4.6. CEI Characterization by Raman Spectroscopy 159
9.4.7. Raman Reference Spectra 169
10. Glossary 170
10.1. List of Figures 170
10.2. List of Appendix Figures 176
10.3. List of Tables 183
10.4. List of Appendix Tables 183
10.5. List of Abbreviations 185
10.6. Licenses 187
11. References 188
12. Acknowledgements 202
13. Curriculum Vitae 204
14. Contributions to Scientific Journals 205

1. General Introduction

Since the beginning of the industrial revolution in the late 18th century, the steadily increasing consumption of fossil fuels led to ever higher concentrations of atmospheric greenhouse gases, driving global warming. In the last few years, the effects of the anthropogenic climate change on our everyday lives and the global economy became undeniable. For example, the magnitude and frequency of extreme weather events caused by global warming has notably increased in the last years, accompanied by growing economic damage and loss of life.[1] Addressing this challenge requires a dramatic shift towards renewable energy sources to stem further greenhouse emissions. However, many clean energy sources, like wind- or solar-power, are governed by weather dependent inconsistencies, hindering a reliable supply of energy. The development of efficient and capable (electrochemical) energy storage systems to enhance grid stability is the key to ensure a successful implementation of renewable energy sources. Lithium-ion batteries (LIBs) are one of these electrochemical energy storage technologies holding great promise. Besides their ever-increasing role in the storage of renewably produced electricity in the last few years, LIBs are also the solution to electrify the (individual) transport sector, which is accountable for about a fifth of the global CO_2 emissions,[2] helping to reduce our society's dependency on fossil fuels dramatically.[3–9] However, to meet high marked demands and the challenging criteria necessary for the application in electric vehicles, LIBs still have to be improved in crucial aspects, *e.g.* cost, safety, sustainability, and, especially, energy density.[5,8,10–12] While implementing high capacity electrode materials into the next generation LIBs is a straightforward approach to improve these criteria, it is also the origin of new challenges. For example, Si-based anodes greatly benefit from the high specific capacity of silicon, which is almost ten times higher compared to graphite anodes, commonly used as anode material in state-of-the-art (SOTA) LIBs. However, Si-based electrodes undergo dramatic volume changes of up to 400%, resulting in severe material degradation and ongoing electrolyte decomposition, greatly limiting the lifetime of these electrodes.[3,13–15] Nickel-rich $LiNi_xCo_yMn_zO_2$ (NMC, $x > 0.6$) cathodes promise a higher specific capacity of about 180 mAh g^{-1} to 190 mAh g^{-1}, compared to the specific capacity of NMC111 and $LiFePO_4$ cathodes (≈ 160 mAh g^{-1}) employed in SOTA LIBs. Moreover, these next generation cathodes also offer higher operational voltage windows, increasing the energy density of the respective cell.[10,16–18] Nevertheless, these materials are unstable at higher operational voltages. This results in irreversible phase transition and the dissolution of transition metal ions into the electrolyte, facilitating the growth of lithium dendrites, leading to micro-short-circuits, and the rapid loss of capacity (roll-over failure).[19–21] Moreover, the increased operational voltage often exceeds the anodic stability of the electrolyte solvents, resulting in additional electrolyte decomposition.[8,10,22,23] The formation of effective

interphases on the anode (solid-electrolyte interphase, SEI) and the cathode (cathode-electrolyte interphase, CEI) is a potent tool to overcome the challenges caused by the implementation of novel electrode materials.[3,6,13] "Native" interphases formed in SOTA carbonate-based electrolytes, comprising of electrolyte degradation products, often fail to mitigate the degrading effects of next generation LIB electrode materials, due to poor chemical and mechanical properties. The use of specialized film-forming additives is a straightforward strategy to facilitate interphase formation, and molecules like fluoroethylene carbonate (FEC) or vinylene carbonate (VC) are already commonly used in commercial LIBs.[6,13,24,25] Typically, film-forming additives decompose prior to the bulk electrolyte solvents, forming a refined interphase based on their respective decomposition products. Therefore, the use of selected film-forming additives allows the control of key interphase characteristics by tailoring the functionality of the employed molecules. To ensure that the design of new functional electrolyte additives does not lapse into trial and error approaches, a deep understanding of the mechanisms leading to the interphase formation is necessary, ideally obtained under real working conditions.[5,6,26]

While many commonly used interphase characterization techniques, such as X-ray photoelectron spectroscopy (XPS), are very challenging to operate under these demanding conditions, vibrational spectroscopy techniques, such as Raman spectroscopy, are promising alternatives.[27–30] Raman spectroscopy is an ideal candidate for investigations under *operando* conditions as it features a simple experimental setup and fast data acquisition. In addition, it offers a high spectral resolution and detailed information, *e.g.* on the sample's composition, molecular structure, orientation, and chemical environment, while the combination with electrochemistry is straightforward. For these reasons, Raman spectroscopy is already a well-established technique in the battery research community.[30–32] While *conventional* Raman spectroscopy is commonly employed for the investigation of electrolytes and electrode materials, advanced near-field Raman spectroscopy techniques, like shell-isolated nanoparticle enhanced Raman spectroscopy (SHINERS) are particularly suitable for the characterization of nanometric interphases on a variety of electrode materials under real working conditions.[30,33–35] As SHINERS is a fairly new technique in battery research, studies on the characterization of interphases in LIBs are scarce and not systematic. Therefore, one of the main objectives of this thesis is the optimization of SHINERS for the successful implementation in LIBs, allowing the systematic characterization of additive-derived interphases to gain a deep understanding of the underlying formation mechanisms. In this context, the first part of this thesis will focus on the optimization of the SHINERS technique and its implementation into an established battery system as part of a proof-of-concept study. In the second and third part of this thesis, the now-established SHINERS technique will then be transferred to next generation LIB

and electrolyte systems. Here SHINERS will be employed, to analyze the interphases formed by different classes of film-forming additives, and to unravel the mechanisms leading to interphase formation, explaining the observed phenomena and galvanostatic cycling behavior.

2. Scientific Background

In this chapter, different concepts and general methods, which were employed in this work, will be discussed in detail. This includes a brief overview of the working principle of LIBs and corresponding interphases, and different approaches to facilitate the formation of effective interphase, focusing on film-forming electrolyte additives. In addition, challenges arising with the implementation of next generation LIBs and how effective interphases can help to mitigate these drawbacks will be addressed. Most importantly, this chapter will present a discussion of different interphase characterization techniques and a detailed introduction to the fundamentals of *conventional* and *near-field* Raman spectroscopy.

2.1. Lithium-Ion Batteries

To fully understand the limitations and strategies to improve LIBs, the general working principle of this system has to be discussed. Moreover, this will enable the reader to follow the conceptualization and motivation of this work. Due to higher energy densities, lower weight, and a lower rate of self-discharge, LIBs oust other battery technologies. Subsequently, LIBs became the most common energy storage system, leading to their widespread application not only in portable electronics, but also in electric vehicles. The working principle of a SOTA LIB is based on the redox reaction of the active materials of the negative electrode (anode) and the positive electrode (cathode), as depicted in **Figure *1***. These redox reactions are initiated by the migration of Li-ions between the two electrodes, also known as the “rocking chair” mechanism, caused by the application of external current.[36,37] Upon charge, Li-ions are extracted from the cathode active material and intercalate in between the graphene layers of the (graphite-)anode, forming LiC_6 at a state of full lithiation. This process is inverted during discharge. Li-ions deintercalate from the anode and re-insert into the vacancies in the cathode active material. In SOTA LIBs, the negative electrode usually consists of graphite, while lithium transition metal oxides ($LiCoO_2$, NMC) or phosphates ($LiFePO_4$) are utilized on the cathode.[7,16,38] To avoid short circuits, both electrodes are physically separated by a ceramic, glassy or polymeric separator.[16,39]

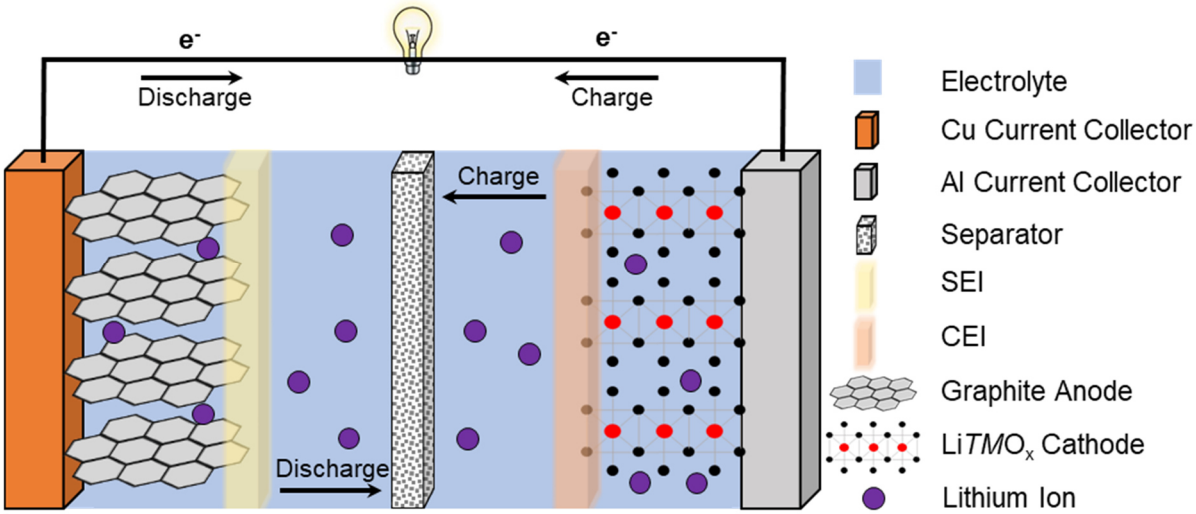

Figure 1: Schematic illustration of a LIB, consisting of a graphite anode and a layered lithium transition metal oxide (Li*TM*O$_x$) cathode. The electrodes are separated using a separator, soaked with a Li ion-containing electrolyte. Upon charging, electrons and Li-ions migrate to the anode. During discharge, this process is reverted. Li-ions deintercalate from the anode active material and migrate to the cathode side, re-inserting into the vacancies of the Li*TM*O$_x$ host cathode. During charge and discharge interphases form on the surfaces of the anode and cathode, the so called SEI and CEI, respectively.

The ionic exchange between the electrodes is facilitated by an electrolyte, typically comprised of a mixture of cyclic and linear carbonates, like ethylene carbonate (EC), ethyl methyl carbonate (EMC), dimethyl carbonate (DMC), or diethyl carbonate (DEC), as well as a conducting salt, most commonly $LiPF_6$.[16,19,22,24,37] In addition, polymer-based electrolytes have attracted more and more attention in the last years, promising higher safety, mechanical and chemical stability, and energy density compared to liquid electrolytes.[40–42] During operation of the LIB, the electrochemical potential of the respective electrodes changes, depending on their degree of lithiation. As an example: fully lithiated graphite electrodes show a potential similar to the one of metallic lithium (LiC_6; 0.10 V *vs.* Li|Li$^+$).[43,44] The very low potential of the negative electrode often exceeds the cathodic electrochemical stability of common electrolyte solvents, resulting in the reductive decomposition of the electrolyte. On the cathode side, the high electrochemical potential of delithiated cathode active materials may cause oxidative electrolyte decomposition. Comprising from these electrolyte decomposition products, passivating films containing organic (polycarbonates, polyolefins, and various semi-carbonates) and inorganic (LiF, Li_2O, Li_2CO_3) species are forming on the surface of the electrodes; the so-called solid-electrolyte interphase and cathode-electrolyte interphase on the anode and cathode, respectively.[3–6,13,19,25,26,45] However, because of these parasitic degradation reactions active lithium is consumed, reducing the overall capacity of the LIB.

Already many SEI models have been established in the research community, suggesting a heterogenous, mosaic-like structure with an inner layer dominated by inorganic species, while the outer layers typically consist more of organic compounds (**Figure 2**).[5,45–47] In

contrast, models for the CEI are scarce and many key properties and functionalities are still under debate.[19,23,26,27]

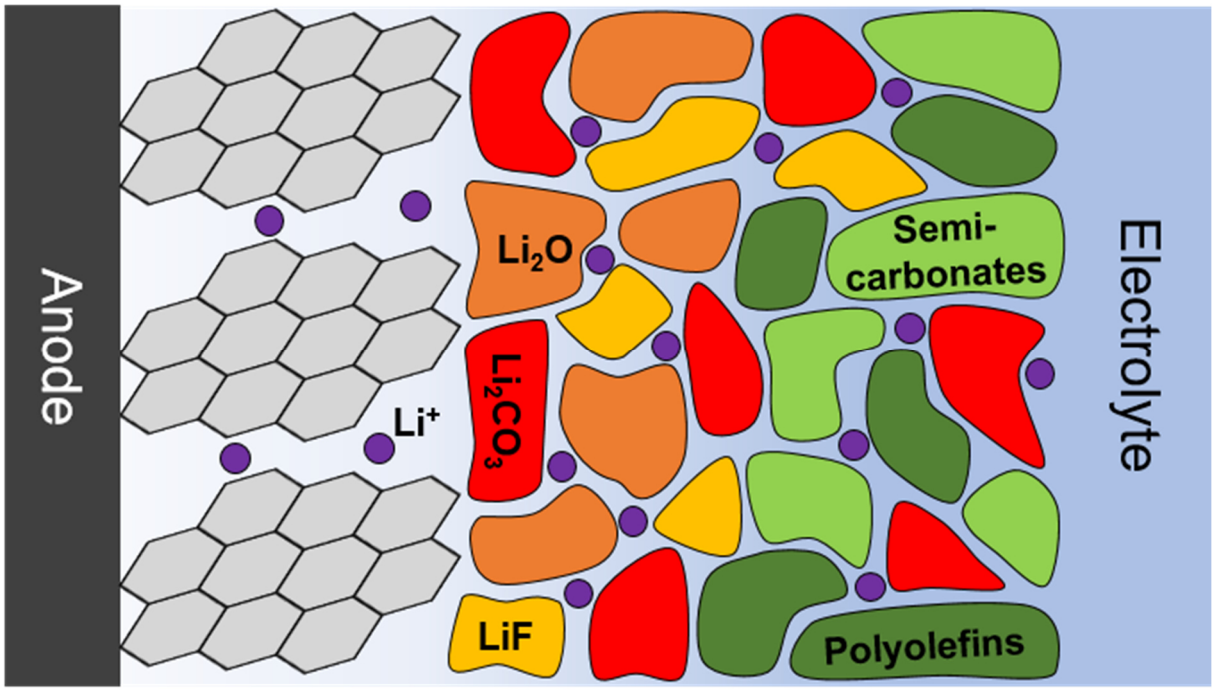

Figure 2: Schematic representation of the SEI on the surface of a graphite anode consisting of an inner layer dominated by inorganic species like LiF, Li_2O, and Li_2CO_3, and an outer layer comprising mostly organic semi-carbonates and polyolefins. Li-ions can still migrate through the interphase, facilitating functionality of the LIB.

Nevertheless, both SEI and CEI play a critical role in LIBs. On the one hand, these interphases suppress continuous electrolyte decomposition due to their electronic insulating properties, protecting electrolyte and electrode. On the other hand, they can impede the Li-ion transport, increasing the internal cell resistance. Therefore, the formation and maintenance of an effective interphase is one of the most important tasks in maintaining a high-performance LIB.[3,4,17,19,25–27,45]

While LIB electrodes and electrolytes notably improved since LIB introduction in the 1980s, key characteristics still have to be enhanced to meet high market demands, including cost, safety, and sustainability. However, especially the increased energy density is the focus of modern battery research. The implementation of novel electrode materials is a promising approach to reach these ambitious goals. On the anode side, the use of Li-metal or silicon-based electrodes offers drastically increased capacities but also imposes severe challenges when implemented in SOTA LIB systems.[14,41,46] The use of Li-metal anodes is severely hindered by the extreme reactivity of the material, leading to increased electrolyte decomposition.[41,46,48] Moreover, the formation of Li-dendrites during cycling poses a serious safety hazard, as dendrites can easily grow towards the cathode, causing short circuits and thermal runaways.[3,5,40,46] Silicon-based electrodes suffer notably from the enormous volume changes the material undergoes during lithiation and delithiation, which

can be up to 400%.[49] These volume changes lead to continuous SEI breakage and reformation, reducing the amount of active lithium in the cell, consuming the available electrolyte. In addition, material degradation and pulverization result in the loss of electrode active material, further limiting the capacity of the cell.[3,13–15,45] Novel cathode active materials, including $LiNi_xMn_yO_z$ (LNMO) or Ni-rich NMC materials, promise improved capacities compared to SOTA electrode materials. Most importantly, they enable higher operational voltages (> 4.20 V), essential for the crucial increase in energy density. However, the implementation of these novel materials is accompanied by new challenges as well.[16–18] Despite enabling high-voltage applications, the LNMO and NMC materials exhibit severe degradation reactions at these extreme conditions. Irreversible phase transitions and particle cracking result in reduced capacity, while the release of oxygen, during phase transitions triggers oxidative electrolyte decomposition.[17,19,50] Electrolyte oxidation is further accelerated by the widened operational voltage window, often exceeding the anodic stability of electrolyte solvents.[8,10,22,23,51] Similar to the anode side, aggravated electrolyte decomposition reduces the amount of active lithium, while simultaneously increasing the resistance of the electrode. Another severe challenge is the dissolution of transition metal ions from the cathode material into the electrolyte, caused by HF-etching reactions, phase transitions and material degradation.[17,18,50–52] Upon further cycling these transition metal ions deposit on the surface of the anode, poisoning the surface and the SEI and triggering the growth of lithium dendrites. Especially the dendrite growth leads to micro short circuits and a rapid loss of capacity, a phenomenon known in the literature as “roll-over failure”.[20,21,53]

As most of the above-mentioned challenges occur on the boundary between the electrolyte and the electrode material, formation of effective interphases can be the solution to the successful implementation of novel electrode materials.[6,8,13,15,54] Therefore, different strategies regarding facilitated interphase formation will be discussed in the following chapter.

2.2. Interphase Design Strategies

As already introduced in the previous section, interphases play a vital role in LIBs, greatly influencing their performance and cycle life. Ideal interphases create a stable barrier between the electrolyte and the electrode, blocking the transfer of electrons and suppressing further (reductive or oxidative) decomposition of the electrolyte. Moreover, interphases limit the co-intercalation of electrolyte solvent molecules into a layered electrode material, preventing mechanical degradation. Simultaneously, effective interphases still allow the transport of Li-ions with minimal limitations, facilitating the functionality of the LIB. However, as the interphases derive from the decomposition

products of the electrolyte, interphase formation often equals the loss of active lithium. In addition, the electrical insulating properties of the interphase correspond directly to their respective thickness, meaning that thicker interphases are more effective in preventing electrolyte decomposition. Nevertheless, the formation of thicker interphases is accompanied by the additional consumption of active lithium and a higher impact on the Li-ion transport, increasing the interfacial resistance. Despite this double-edged characteristic, establishing specialized interphases is the crucial step toward the implementation of novel electrode materials, and necessary to further improve LIBs, as key characteristics can be controlled directly by the composition of the interphase. For these reasons, facilitating the formation of effective interphases is of great interest to the battery research community.[3,4,46] In general, strategies to facilitate interphase formation can be divided into two groups: *in vitro* and *in vivo* interphase formation (**Figure 3)**.

In vitro interphase formation approaches focus on the buildup of an artificial interphase prior to cell assembly. This provides the access to a wide variety of reagents or techniques, which could not be employed in *in vivo* interphase formation strategies, limited by properties of the electrode material or the electrolyte composition. Due to this flexibility, the formation of "artificial" interphases enables the design of an interphase, tailored to address the challenges of the chosen battery chemistry. In an ideal case, the artificial interphase features all beneficial effects of "natural" interphases formed during charge/discharge cycling. This includes high Li-ion conductivity and the blocking of electron tunneling, while ruling out their respective disadvantages, such as insufficient mechanical strength or flexibility to cope with the drastic volume changes of conversion-type anodes.[3,46,52] Moreover, as the interphase formation is already completed prior to the first cycle, the loss of active lithium through the interphase formation and the risk of undesired parasitic side reactions on the electrode surface are drastically reduced.[24] The fabrication techniques available for *in vitro* interphase formation are typically separated into top-down and bottom-up strategies. Top-down strategies are focused on the build-up of macro-structures from bulk substrates, rendering them simple, cost-effective, and easily scalable. Commonly used techniques for top-down interphase formation are magnetron sputtering[14,15,50,52] or coating *via* dripping, dropping, or blade distribution.[3,46,48,55–57] On the contrary, bottom-up techniques, including vapor deposition, electrodeposition,[24,58–61] and (electro-)chemical grafting, enable the build-up of interphases from a molecular or even atomic level, promising highly resolved material manipulation. However, this precision is accompanied by the loss of scalability and cost-effectiveness.[3] Common artificial interphases include a coating of the active material with inorganic layers, comprising of $Li_xPO_yN_z$,[14,15,24,50,52] Li_3PO_4,[48,62–64] and Al_2O_3.[24,26,61,65,66] In addition, polymeric organic artificial interphases of modified

polyethylene oxide,[57] polytetrafluorethylene,[55,67] and polyacrylic acid[68,69] derivatives were presented in the literature.[24,46]

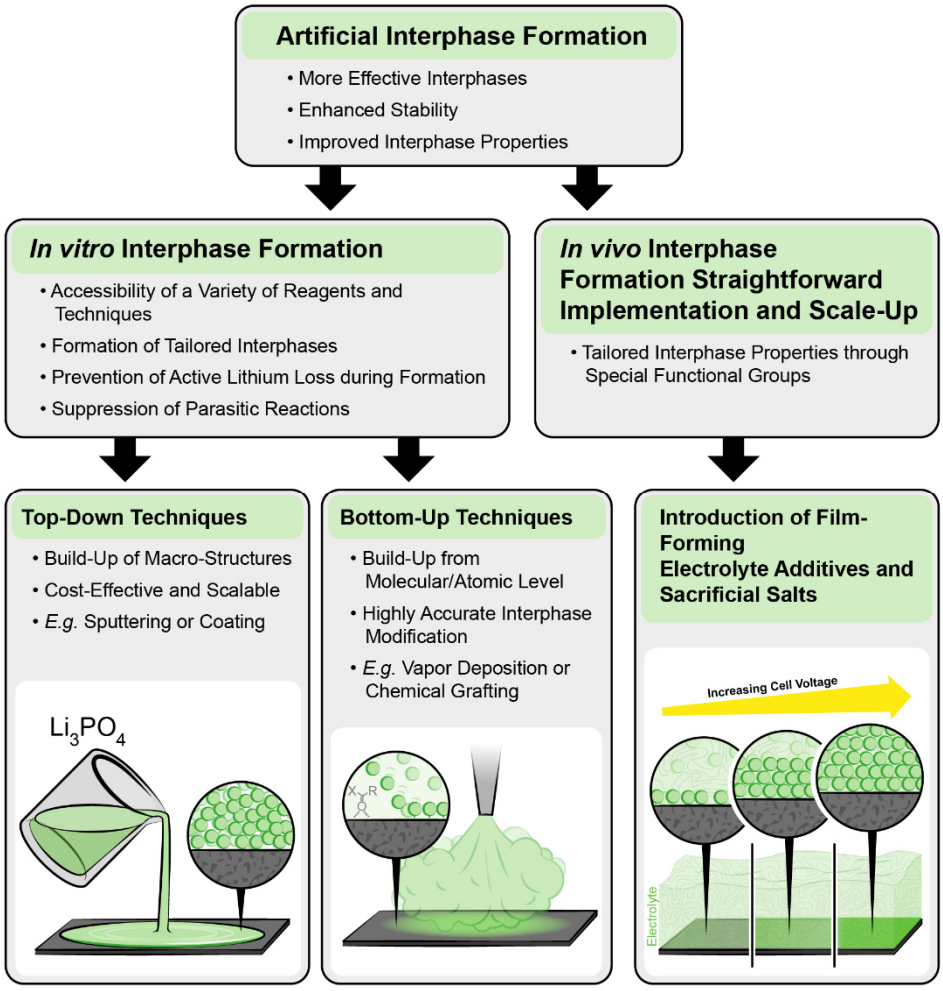

Figure 3: Schematic overview of the different strategies of artificial interphase formation strategies, divided into *in vitro* and *in vivo* techniques. Note that the *in vitro* techniques are further divided into top-down and bottom-up techniques. For every subgroup specific advantages are noted and exemplary techniques visualized. Note that in the depicted images the artificially formed interphase is represented by the green layer on the electrode (dark grey).

While holding great promise, the *in vitro* formation of artificial interphases is not yet applicable for industrial LIB manufacturing, as many techniques still show a need for drastic improvement. Moreover, the implementation of an additional fabrication step is expensive, and many of the utilized strategies, while being feasible for lab-size batches, are not scalable to industrial needs. It has to be noted however, that coating of electrode materials already is a common practice in the industry.

In contrast, *in vivo* approaches like the implementation of film-forming additives into industrial processes is straightforward, as no additional fabrication steps or techniques have to be included in the manufacturing process. The idea behind this strategy is the implementation of “sacrificial” functional molecules into the electrolyte formulation, which decompose prior to the main electrolyte components. In an ideal case, the interphase

formed by the degradation products of the additive is stable enough to effectively prevent decomposition reactions of the main electrolyte at lower or higher electrode potentials, respectively. Moreover, through specialized design of additive molecules, *e.g.* by the introduction of functional groups, key parameters of the additive-derived interphase can be controlled to tailor the interphase properties. Due to its simplicity, the use of film-forming additives for facilitated interphase formation has already been extensively investigated in the past, especially on the anode side. Electrolyte additives as FEC and VC are already well-known to the research community for the formation of effective and uniform SEIs and are commercially used in SOTA LIBs.[6,13,24,25,70] In addition, great effort has been spent to analyze the composition of the respective VC- and FEC-derived SEIs. Interestingly, for both additives reductive decomposition routes are known leading to the formation of polycarbonates (poly(VC) and poly(FEC)).[13,24,25,71–74] Nevertheless, an alternative mechanism for FEC was proposed by Nakai *et al.*, claiming the formation of polyene-species on the surface of silicon electrodes.[75] In addition, the presence of FEC also increases the content of LiF in the SEI. Due to the combination of organic and inorganic species, FEC-derived interphases exhibit a high mechanical strength, as well as excellent Li-ion transport properties, making FEC a promising candidate for the stabilization of Si-based electrodes and other conversion-type anodes.[13,25,70,76] While a number of film-forming additives for the anode side are already well established, dedicated CEI-forming additives are still rare, as the CEI only recently moved into the focus of battery research.[24,26] As the electrochemical stability window of most electrolyte formulations exceeds the upper operational voltage of SOTA LIB chemistries, resulting in little to no oxidative electrolyte decomposition and interphase formation, the need for an optimized CEI was not given so far. However, with the introduction of high-voltage cathodes this changed. The increased operational voltage and the instability of the cathode materials result in oxidative electrolyte decomposition, oxygen release and the dissolution of transition metals. An example of a possible class of CEI-forming candidates are thiophene and its derivatives.[28,29,77,78] Due to the higher energy levels of the highest occupied molecular orbital of aromatic molecules, they exhibit notably lower oxidation potentials compared to carbonate-based solvents, facilitating their decomposition and the following CEI formation prior to the oxidation of the carbonate-based electrolyte.[24] For thiophene and thiophene derivatives, multiple studies already suggested the formation of a polythiophene-based CEI on different high-voltage cathodes *via* oxidative electro-polymerization.[24,28,29,79–82] In addition to the aromatic additives, sacrificial salts like lithium bis(oxalato)borate, lithium difluoro(oxalate)borate, and lithium difluorophosphate (LiDFP) are known to stabilize the cathode in high-voltage applications.[8,18,23,26,51,83,84] Especially LiDFP was proven to mitigate the roll-over failure

mechanism by complexing transition metal ions in the electrolyte, preventing their deposition on the anode.[20,21]

Nevertheless, there still is a great need for the development of new film-forming additives, especially on the cathode, but also on the anode side, as the established candidates struggle to cope with the challenges arising from the implementation of the next generation electrode materials. However, a deep understanding of the additive's degradation reactions and interphase formation mechanisms is crucial, to ensure a target-driven development of promising candidates. To gain these vital information, suitable characterization techniques are necessary.[5,23,27,45,85] In the following chapter, techniques commonly used for the characterization of interphases will be discussed, and advantages and disadvantages will be addressed.

2.3. Interphase Characterization Techniques

In this chapter, techniques commonly used for the characterization of interphases will be discussed. Due to the focus of this thesis on interphases formed in liquid carbonate-based electrolytes, only techniques applied to comparable systems will be mentioned to limit the scope of this section.

In general, the different available interphase characterization techniques can be divided into groups based on sample preparation or experimental set-up. This is an important factor to consider, as the sample preparation or experimental set-up can have a major influence on the sample composition, the risk of contamination, the available information, as well as the context for the gained information. In general, there are three categories: *post mortem* or *ex situ*, *in situ,* and *operando*. For *post mortem* and *ex situ*, the sample, *e.g.* an electrochemically aged electrode, is extracted from the cell after reaching its end of life (*post mortem*) or after a defined amount of time (*ex situ*). While simple to implement, these techniques bear the risk of sample of mechanical damage, the contamination during preparation, altering of the sample composition due to exposure to certain environments, *e.g.* high vacuum or ambient air, sparking artificial degradation of highly reactive species. Most importantly, this way of sample preparation does not allow dynamic data acquisition, as the state of the sample is fixed. This is especially troublesome for the investigation of the formation mechanisms of interphases, as these techniques only capture the end result and no steps in between.[24,27,85,86] Nevertheless, many of the *post mortem* / *ex situ* techniques are well-established in battery research and have provided valuable information in various studies.

Probably the most commonly used *post mortem* / *ex situ* technique is XPS. The calculated binding energies of detected photoelectrons emitted from the radiated atoms provide

specific information on the composition of the sample, making XPS a powerful method to characterize the top layers of various materials. It is worth noting that *in situ* XPS interphase investigations were realized by Benayad *et al.* in the presence of a C_1C_6ImTFSI ionic liquid electrolyte on a Li-metal anode, identifying LiF and polyoxysulfurs as main SEI components.[85] Despite great effort put into the development of advanced experimental set-ups, *in situ* XPS characterization of interphases formed by carbonate-based electrolytes is still severely limited by the ultra-high vacuum conditions necessary during the measurements.[87] In addition, XPS is further hindered by challenging sample preparation, low spatial resolution, high cost of the instrument, and its susceptibility to technical defects. Moreover, sample destruction is an additional challenge regarding the employment of XPS. Nevertheless, it has to be noted that great effort has been spent to develop advanced XPS set-ups, allowing sample investigation under low or even ambient pressure.[88–90] Despite the complexity of the technique, XPS is capable of providing crucial information on interphase composition on an atomic level and information on the chemical environment of the sample. Moreover, depth profiles can be obtained by XPS *via* sputtering, giving insights into the structure of the probed interphase.[91–96] In an exemplary study by Heidrich *et al.*, XPS was utilized to characterize the SEI formed by a carbonate-based electrolyte on graphite anodes and NMC622 cathodes. Using XPS, it was possible to identify organic and inorganic carbonates, alkoxides, phosphates, LiF and $LiPO_xF_y$ as SEI and CEI components, as well as to determine the thickness of the organic and inorganic SEI.[97] Similar results were presented by Lee *et al.* who employed XPS to study the SEIs formed on graphite electrodes in the presence of carbonate-based electrolyte containing VC and VEC. The authors identified the presence of lithium-oxygen species, as well as organic carbonate-derived species and inorganic $LiPO_xF_y$ compounds, deriving from electrolyte decomposition.[98] The results reported by Shobukawa *et al.* generated from the surface of Si-based anodes, are in good agreement with the previous studies, identifying electrolyte degradation products in the SEI.[99]

Another powerful technique available for the investigation of interphases in LIBs is nuclear magnetron resonance (NMR) spectroscopy. In NMR spectroscopy, the interaction of atomic nuclei in a strong magnetic field with electromagnetic radiation provides detailed information on the molecular structure and environment of the probed sample. In addition, the selection of specific nuclei for each measurement makes analysis of the obtained spectra straightforward. However, the challenging experimental set-up of NMR and difficult sample preparation greatly hinder its application in *in situ* interphase characterization studies. Still, advances in dynamic nuclear polarization NMR and the development of new sample holders hold great promise for future studies. In battery research NMR is often employed to track the deposition of Li or the formation of dendritic or “dead” Li.[100–103] Nevertheless, NMR can

also provide valuable insights into the composition of interphases.[104–107] In a study presented by Michan *et al.,* solid-state NMR spectroscopy was employed to investigate the SEI formed on silicon-based electrodes. Based on the obtained spectra, specific interphase products deriving from either the decomposition of EC or DMC were identified. For EC decomposition, known organic (semi-)carbonates like lithium ethylcarbonate (LEC), dilithium ethylene dicarbonate (LEDC) and dilithium butylene dicarbonate (LBDC), polyethylene oxide (PEO)-type species, Li_2CO_3 and ethene were proposed. In contrast, the decomposition of DMC results in the formation of lithium methylcarbonate (LMC), as well as Li_2CO_3 and ethene. In addition, LiF was detected as only fluorine-containing species, besides $LiPF_6$.[108]

In contrast to the techniques discussed prior, scanning electron microscopy (SEM) can only be used for the topographic investigation of the interphases and does not give information on the composition of the respective sample. Nevertheless, SEM provides valuable insights into the interphase uniformity, thickness, and homogeneity, which are crucial for its evaluation and characterization.[93–95,109,110] In SEM investigations, the surface of the sample is scanned by a focused electron beam. The analysis of the interaction of the electrons with the sample's surface allows the construction of highly magnified and resolved images. Despite its many benefits, due to the high vacuum necessary in the sample chamber, *in situ* investigations of interphases formed by liquid electrolytes have not been achieved yet. In a recent study by Tripathi *et al.* SEM was employed to characterize the morphological changes of SEIs derived from a carbonate-based electrolyte with and without FEC on silicon electrodes. With SEM, the authors of the study were able to highlight not only the formation of a more uniform interphase in the presence of FEC, but also a higher stability of the FEC-SEI, leading to reduced cracking of the interphase and the active material.[111]

Electron dispersive X-ray spectroscopy (EDX) is another powerful tool for the characterization of surfaces. For EDX, energies of characteristic X-rays are detected from excited atoms, quickly giving detailed qualitative and quantitative information on the elemental composition of the probed sample. In addition, an easy coupling of EDX with SEM allows the direct combination of imaging with the elemental analysis, providing additional insights. In comparison to XPS, EDX fails to provide information on the chemical environment of the detected atoms, allowing only analysis on an elemental level. Moreover, the detection of light elements like lithium is not possible with EDX, which is a great setback for the utilization of EDX in the characterization in LIBs. Also, the penetration depth of EDX is higher, compared to XPS, leaving this technique less sensitive for interphase investigation. Similar to SEM, employing EDX in *in situ* studies is hindered by the necessity of the high vacuum in the sample chamber, preventing the use of volatile liquid electrolytes. Nevertheless, many studies have been presented in which EDX has been employed for the

investigation of interphases in LIBs.[93,95,109,112,113] One exemplary study, which highlights the powerful combination of SEM and EDX was presented by Weiling *et al*. In this study, a sulfur-based electrolyte additive was introduced to stabilize the SEI on SiO_x/Graphite electrodes. The authors were able to show the accumulation of sulfur on the surface of SiO_x particles, while a lower concentration of sulfur was found on the surrounding graphite particles, indicating an enhanced and localized additive degradation on the SiO_x-particles.[114]

In contrast to the first group of characterization techniques, *in situ* techniques provide insights into ongoing processes and reactions, allowing a dynamic investigation of interphases. For *in situ* experiments, often model systems are chosen, which mimic the original system, enabling the transfer of results between different experiments. However, the requirements of the characterization techniques have to meet to be suitable for *in situ* investigations are high. The selected techniques must be non-destructive and have to allow fast acquisition of data. In addition, they have to be compatible with the experimental set-up and ensure no altering of the chemical environment of the sample (*e.g.* electrolyte decomposition). Due to these challenging requirements, available techniques are scarce and their implementation is difficult.[54,85,86,115]

A fairly simple method for the *in situ* characterization of interphases is the use of electrochemical impedance spectroscopy (EIS). In EIS, an alternating current with a variable frequency is applied onto an electrochemical system. Based upon the voltage response and especially the voltage to current ratio (impedance) at different applied frequencies, information can be gathered on charge transfer, diffusion, and the resistance of electrodes, electrolytes, and interphases. As EIS can be easily implemented into galvanostatic cycling routines, it can be used to dynamically measure the resistance of evolving interphases and to gain insights on interphase properties and growth.[116–119] In a study by Kitz *et al.*, *in situ* EIS was employed to characterize the interphases derived from FEC and VC on graphite anodes. The results showed a distinct influence of both additives on the transport properties of the respective interphases dependent on the operating potential of the anode.[120]

Another promising technique for the characterization of interphases on LIBs is transmission electron microscopy (TEM). Similar to SEM, TEM can only obtain visual information of the samples. Due to its notably higher resolution and magnification, TEM images can capture processes on the atomic level, which are crucial to understand interphase formation processes and structural changes in the interphases and electrode materials. For TEM imaging, an electron beam is passed through the respective sample. During penetration of the sample, the electrons interact with the sample, resulting in a generation of information about the sample properties based on the distinct scattering of electrons after interaction

with specific atoms. In addition to the investigation of electrode materials, TEM can also be used for imaging of interphases in LIBs. Similar to SEM, the investigation of carbonate-based electrolyte systems is hindered by high vacuum conditions in the sample chamber. Though, recent developments in sealed liquid cells finally allowed the *in situ* investigation of interphases in liquid electrolyte systems by TEM.[121–123] Employing *in situ* TEM, Dachraoui *et al.* were able to visualize the growth of the SEI on a glassy carbon electrode in a carbonate-based electrolyte. In addition, the authors of the study were able to monitor the mosaic structure of the formed interphase, as well as the growth of the interphase during repeated cyclic voltammetry scans.[112]

Compared to the complex experimental set-ups required for *in situ* experiments, the implementation of *operando* investigations is even more challenging. *Operando* experiments mimic the reality as closely as possible. In the case of interphase investigations, real electrode materials, realistic cell configurations and operating conditions have to be employed, further limiting the scope of available techniques. Nevertheless, the results and information gathered by these experiments can directly be put into context with the results of other experiments, *e.g.* galvanostatic cycling, and therefore, are extremely valuable for the understanding of interphase formation mechanisms.[85,86,115,124] Due to their robustness and the straightforward experimental set-up, vibrational spectroscopy techniques are promising candidates for *operando* interphase characterization.[124] In the next chapter, Raman spectroscopy, as well as the optimization of Raman spectroscopy for the successful characterization of interphases in LIBs will be discussed in detail.

2.4. Raman Spectroscopy for LIB Characterization

Vibrational spectroscopy techniques, like Raman spectroscopy, are already widely established in the battery research community. Due to their robustness, simple experimental set-up, dynamic data acquisition, sensitivity, and straight-forward combination with electrochemical experiments, these methods are also very promising for the *operando* investigation of components and processes in LIBs. In this chapter, the basic working principle and common challenges of *conventional* Raman spectroscopy will be introduced. In addition, the working principle of near-field Raman spectroscopy, different variants and applications will be addressed in detail.

2.4.1. Conventional Raman Spectroscopy

All vibrational spectroscopy techniques, including Raman spectroscopy, are based on the interaction between light and matter. Depending on the properties of the irradiated molecule and the frequency of the emitted photon, photons either are scattered on the surface of the sample or are absorbed, dividing vibrational spectroscopy techniques into absorption and

scattering spectroscopy. Generally, these techniques rely on the excitation of molecules from a vibrational ground state (g_0) to a state of higher energy to obtain information about the sample (**Figure 4**). In absorption spectroscopy, a light source emitting a broad range of wavelengths is used. If the frequency of one of the emitted photons matches the energy of a specific state transition of the sample molecule, that photon is absorbed. Consequently, by comparison of the wavelengths of the emitted light before and after interaction with the sample, an absorption spectrum can be generated. One prominent example for absorption spectroscopy techniques is infrared (IR) spectroscopy.

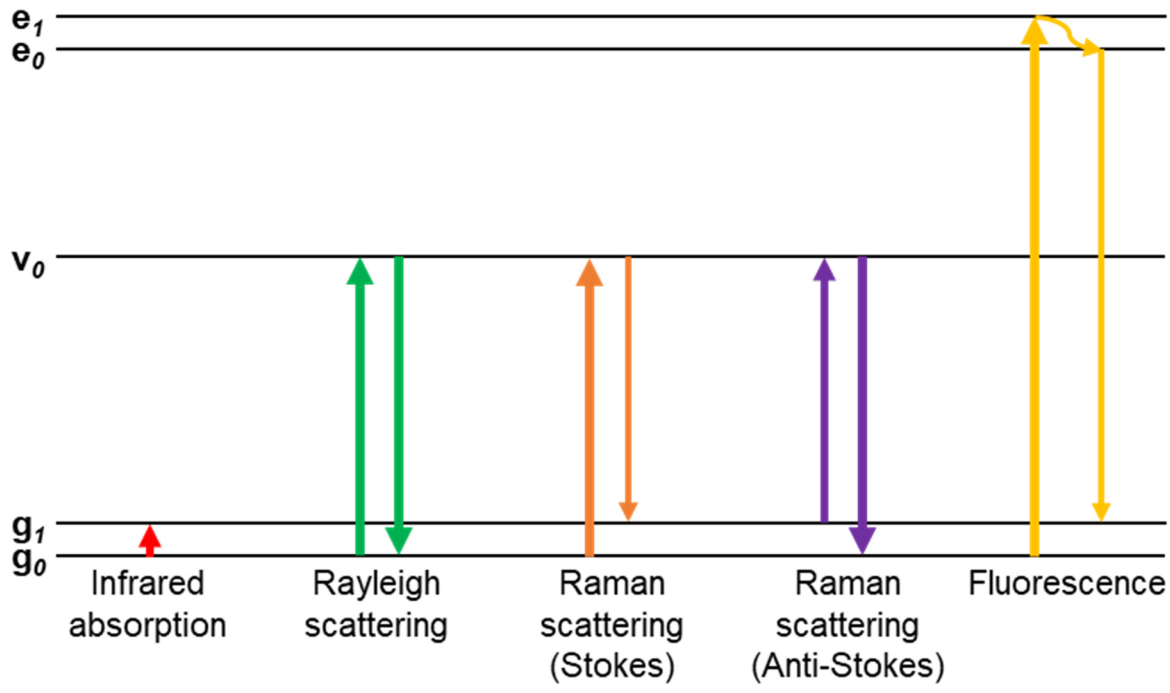

Figure 4: Schematic representation of the working principle of IR and Raman spectroscopy. The figure includes the process of IR absorption, Raman scattering, and fluorescence. Arrows symbolize the excitation of molecules from the vibrational ground state (g_x) to a state of higher energy, including virtual states (v_o) or excited states (e_x). The thickness of the arrows corresponds to the energy of the irradiated or emitted / scattered photon, while curved arrows depict relaxation of the molecule.

In contrast, Raman spectroscopy represents the scattering spectroscopy techniques. Here, instead of absorbing specific wavelengths of a broad spectrum, a light source emitting a single wavelength is employed. The spectrum is generated based on the frequencies of the scattered photons. For the process of Raman scattering, the emitted photons irradiate the sample molecule, interacting and polarizing the electron clouds surrounding the nuclei. Based on this polarization, the molecule is temporarily transferred to a state of higher energy, the virtual state (v_0). Since the virtual state is instable, shortly after excitation (femtoseconds), the molecule relaxes back into its original vibrational ground state (g_0), re-emitting or scattering the irradiating photon. In most cases, irradiation of the sample molecule will only result in distortion of the electron cloud. In these cases, the scattered

photon has the same frequency as the irradiating photon. This process is called elastic or Rayleigh scattering. Only in 1 out of 10^6 – 10^8 cases, irradiation of the sample molecule creates a distortion (vibration) of the molecule itself, notably changing its polarizability. In these cases, the excited molecule will fall from the virtual state into a vibrational state of higher energy (g_1) instead of relaxing to the vibrational ground state. Thereby, energy is transferred from the irradiating photon onto the sample molecule. This energy transfer is also reflected in the frequency of the re-emitted photon, exhibiting a lower frequency compared to the irradiating photon. This process is called inelastic Stokes scattering.

Alternatively, depending on the occupation of the molecular excitation states, excitation into the virtual state can occur starting from an energetically higher vibrational ground state (g_1). Here, relaxation to a vibrational ground state with a lower energy (g_0) is possible, resulting in the transfer of energy from the molecule to the scattered photon, increasing its frequency. This process is called Anti-Stokes scattering. In Raman spectroscopy, these absolute differences in the energy or frequency of the scattered photons, compared to the frequency of the irradiating photon are depicted in the spectra as the Raman shift. As the energy differences are characteristic for the vibration of different bonds, groups or molecules, the Raman spectra provide detailed information on the composition and structure of various samples.

Understanding the basic working principles of the Raman scattering process allows easy estimations of the Raman activity of certain molecules or functional groups. For example, ionic species are often Raman-inactive, as vibration of these species does not result in sufficient changes in the molecules polarizability. In contrast, vibrations which notably alter the polarizability of the sample molecule are considered highly Raman active, *e.g.* symmetric vibrations. Moreover, estimation of Raman or IR activity can be made upon the following rule of thumb: In molecules with a center of symmetry, no vibration can be simultaneously Raman- and IR-active. In general, if the center of symmetry is retained upon vibration, it is considered to be Raman-active, while vibrations breaking the center of symmetry are considered IR-active. For molecules without a center of symmetry, vibrations can be both Raman- and IR-active.[125–128]

A more detailed understanding of Raman-activity can be obtained from group theory and group charts, with excellent reviews published regarding the topic.[125–128]

Based on the working principle of the Raman scattering process, intrinsic limitations of this technique can be easily understood and thus overcome. One of the biggest challenges in Raman spectroscopy is the interference with fluorescence. For fluorescence, similar to the process of Raman scattering, molecules are excited from a ground state (g_0) to an excited state (e_1) upon photon irradiation. However, instead of direct relaxation to a ground state, the molecule undergoes a series of relaxations, *e.g.* internal conversion, putting the

molecule in an excited state with a lower energy (e_0). From this state, the molecule can finally relax back to the ground state, re-emitting a photon with a lower frequency compared to the absorbed photon. It is also worth to note that, due to the additional relaxation, fluorescence is notably slower (nanoseconds) than Raman scattering.

In Raman scattering, the energy transitions are well defined and thus the “number” of photon frequencies is limited, resulting in relatively sharp, defined bands in the obtained spectrum. In contrast, for fluorescence a lot of energy transitions are possible, resulting in a plethora of photon frequencies. The result is a very broad fluorescent background in the obtained spectrum. In addition, fluorescence is notably stronger than the inherently weak Raman scattering. Therefore, if a sample exhibits fluorescence, this can dramatically hinder the analysis of Raman spectra, as Raman bands are easily covered by the fluorescent background and the signal to noise ratio decreases drastically.[129–131]

A relatively simple strategy to overcome this challenge is the use of laser sources with a preferably higher wavelength to avoid fluorescence excitation. Another strategy is the use of time- or Kerr-gated Raman spectroscopy, separating the fast Raman signal from the slower fluorescence.[129–132] Also, the use of near-field Raman spectroscopy techniques is very promising. Using near-field Raman spectroscopy allows to drastically increase the intensity of Raman signals, overruling the effect of fluorescence on the Raman spectrum. Moreover, near-field Raman spectroscopy solves another intrinsic limitation of *conventional* Raman spectroscopy. As only 1 out of 10^6 to 10^8 photons is scattered inelastically, Raman signals are inherently weak. Increasing the power of the incident laser provides a sufficient number of photons to create defined spectra of bulk material samples like electrodes or electrolytes. In contrast, the investigation of samples with a low concentration or samples, which only provide a limited amount of material, *e.g.* interphases, are challenging to capture by *conventional* Raman spectroscopy. Instead, employing near-field Raman spectroscopy techniques enables the investigation of these challenging samples, even in complex systems, as LIBs. As this thesis is based on the use of near-field Raman spectroscopy techniques for the investigation of interphases in LIBs, the theory behind near-field Raman, as well as different variants, will be addressed in the next chapter.[30,125,133]

Despite its intrinsic limitations, *conventional* Raman spectroscopy is a powerful technique and well established in battery research, with a broad range of possible applications.[134–141]

2.4.2. Near-field Raman Spectroscopy

As already mentioned in the previous chapter, near-field Raman spectroscopy techniques are powerful tools, combining the advantages of *conventional* Raman spectroscopy with increased signal intensities and high surface sensitivity. These properties make these Raman variants ideal candidates for the investigation of interphases in LIBs under *in situ* or

even *operando* conditions. Over time different near-field Raman techniques have been developed, which will be presented and discussed in detail in this chapter.

The near-field Raman effect was discovered in 1974 by the group of Fleischmann, which reported a notably increased Raman signal intensity of pyridine on a roughened Ag foil.[142] While the observed effect was initially assumed to stem from an increased number of pyridine molecules on the metal surface due to the higher surface area, the authors realized that this was not sufficient in explaining the observed signal amplifications. Instead, the observed signal enhancing effect was caused by the plasmonic activity of metals.

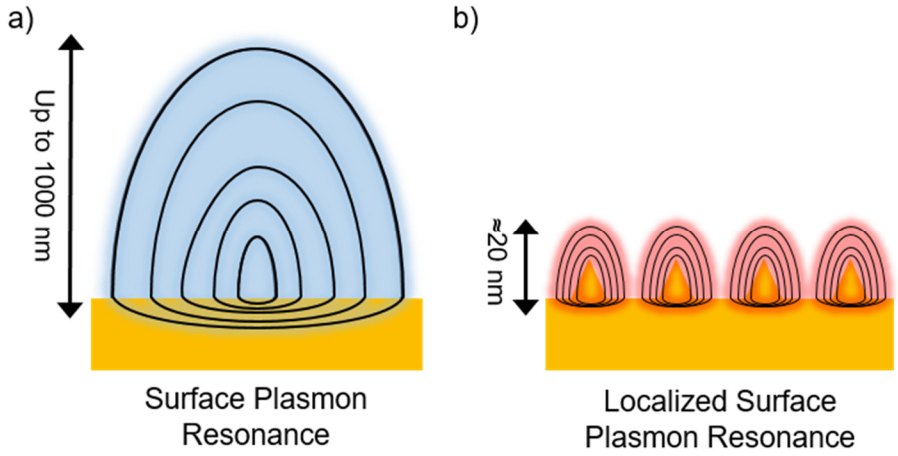

Figure 5: Schematic illustration of the surface plasmon effect, highlighting the difference between **a)** the surface plasmon resonance, occurring on smooth metal surfaces, and **b)** the localized surface plasmon resonance on a nanostructured metal substrate. Arrows on the side represent the estimated size of the surface plasmon above the respective substrate.

The plasmonic activity is caused by delocalized electrons in the conduction band of the respective metal forming an electron cloud above the metal surface. Upon irradiation of the metal with a light source, these electrons will start to collectively oscillate, which is called surface plasmon resonance (**Figure 5a**). On a smooth metal surface, this electron cloud can freely oscillate lateral to the substrate, resulting in no enhancement of the Raman signal, as irradiating photons are only absorbed. However, on roughened or nanostructured surfaces the plasmons oscillate perpendicular to the substrate due to interactions of vertically and laterally moving plasmons. In contrast to the smooth surface, where plasmons are distributed equally over the substrate, plasmons are concentrated on “hot-spots” in the case of nanostructured substrates, giving the name localized surface plasmon resonance (LSPR, **Figure 5b**). In addition, the LSPR also enables the scattering of irradiating photons, allowing the Raman scattering process to be detected. When it comes to the actual enhancement of the Raman signal intensity, two main theories are considered: electromagnetic and charge transfer enhancement.[125,127,133,143]

For the electromagnetic enhancement, the analyte molecule has to be in proximity to the substrate surface, allowing the interaction of the surface plasmons with the analyte molecules electrons. This interaction of the electrons drastically increases the polarization

around the molecule, greatly enhancing the efficiency of the Raman scattering process and thus enhancing Raman signal intensities. For the charge transfer or chemical enhancement, the analyte molecule has to form a chemical bond to the substrate. It is believed that the formation of this bond results in the formation of additional electronic states, which are resonant with the Raman scattering. Upon irradiation, the emitted photon is absorbed into the metal, resulting in the intermediate transfer of an electron to the bonded molecule and back to the metal. Due to this electron transfer the polarizability of the analyte molecule greatly increases, resulting in enhanced Raman signal intensity.[125,127,133]

While both theories greatly differ from their working principle, they have one key aspect in common, making them hard to distinguish. For both approaches, the analyte molecule has to be in very close proximity to the surface of the substrate, hence the name near-field Raman spectroscopy. Either because it is bonded to the surface, or because it has to be surrounded by the cloud of oscillating surface plasmons, which only provides sufficient electromagnetic enhancement up to a distance of 20 nm from the substrate. This fact makes the different near-field Raman spectroscopy techniques very sensitive for the investigation of surface processes or the characterization of thin films, *e.g.* interphases.[125,144]

In theory, the near-field effect can be observed using every metal as substrate. However, in practice, there are some key properties which greatly affect the efficiency of near-field Raman spectroscopy. Most important, all surface plasmons have a resonance frequency, depending on the metal substrate, in which irradiating photons are absorbed most efficiently, resulting in the strongest Raman signal enhancement. The surface plasmons of Au and Ag for example, oscillate in frequencies matching the visible light. As these frequencies correspond to the laser systems, which are typically used for Raman spectroscopy, Au and Ag substrates are commonly used for near-field Raman spectroscopy, exhibiting the greatest Raman signal enhancement. Nevertheless, not only the metal determines the plasmon resonance frequency. The properties of the substrates' surface, *e.g.* the structure of the roughened substrate or the size and form of nanoparticles (NPs), greatly influence the plasmon resonance frequency, allowing extensive tuning of the near-field substrates.[125,145]

Over time, different near-field Raman spectroscopy techniques have been developed, which can be differentiated by the substrate used to obtain signal enhancement. The first technique, which was also used by the Fleischmann group in the initial discovery of the near-field Raman effect, is called surface enhanced Raman spectroscopy (SERS). For SERS, roughened or nanostructured foils or deposited thin-films from noble metals, as Au, Ag or Cu, can be utilized, providing the necessary LSPR for Raman signal enhancement (**Figure 5b**). As the preparation of these substrates and the implementation into optical cells is straightforward, SERS is the most commonly used near-field Raman spectroscopy

technique.[30,146] SERS also plays a vital role in the characterization of interphases in LIBs, as demonstrated multiple times in the literature.[147–150] As an example, Li *et al*. investigated the SEI formed on an Ag electrode, which served as SERS substrate at the same time. The Ag electrode was discharged in a carbonate-based electrolyte (1 $_M$ $LiPF_6$ in EC:DEC; 1:1) until reaching a potential of 0 V *vs.* $Li|Li^+$. In the obtained SER spectra, Li_2CO_3, LiOH, and semi-carbonate species were identified as interphase composition products.[151] Nevertheless, SERS investigations are dependent on the use of the aforementioned substrates for signal enhancement, rendering the investigation of interphases on real electrodes and therefore, under real working conditions, impossible. Other near-field Raman spectroscopy variants are able to overcome these limitations. One possible alternative is tip-enhanced Raman spectroscopy (TERS, **Figure 6a**). For TERS, Raman spectroscopy is combined with atomic force microscopy (AFM). Here, instead of a metal foil, a sharp Au or Ag tip is used as substrate, providing a very localized LSPR when irradiated. Because of this highly localized Raman signal enhancement, the spatial resolution of TERS is also very high, allowing mapping of different (electrode-)samples with a great resolution of <10 nm.[30,143,146,152,153] The possibilities of TERS for the characterization of interphases were demonstrated by Nanda *et al*., investigating the interphase formed on a silicon electrode by degradation of a carbonate-based electrolyte (1 $_M$ $LiPF_6$ in EC:DEC; 1:1). In their study, the authors were able to track the formation of a mosaic like SEI, as suggested by previous models (**Chapter 2.1**). Moreover, changes in the interphase composition were monitored over multiple galvanostatic charge/discharge cycles. In the initial cycles, mostly semi-carbonate species and PEO-type oligomers were identified in the interphase composition, whereas it was dominated by carboxylates and lithium phosphate-species at a later stage.[153]

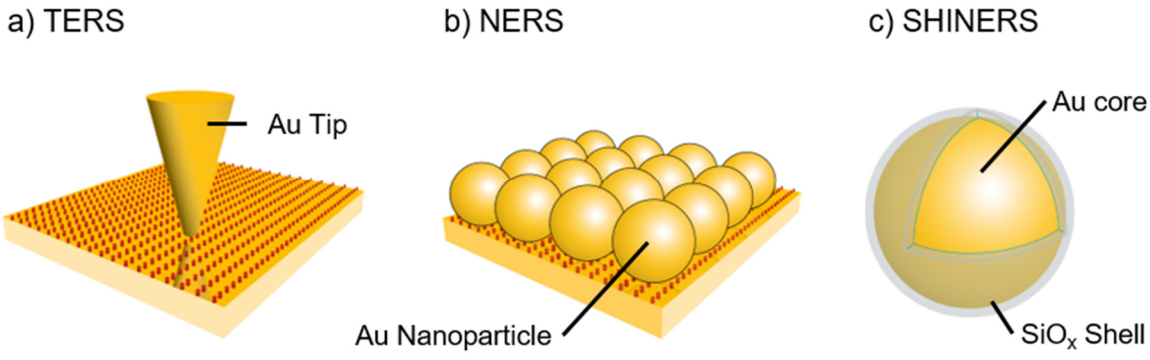

Figure 6: Schematic representation of the different near-field Raman spectroscopy techniques, developed from the initial surface enhanced Raman spectroscopy configuration. **a)** Tip enhanced Raman spectroscopy (TERS), **b)** nanoparticle enhanced Raman spectroscopy (NERS), and **c)** depiction of an Au-nanoparticle coated with a SiO_x shell, as commonly used for shell isolated nanoparticle enhanced Raman spectroscopy (SHINERS). SHINERS experimental configuration resembles the configuration presented for NERS. This figure is adapted with permission from [133].

Despite these promising insights into interphase formation mechanisms and composition, TERS studies on interphases in LIBs are scarce, due to the complex combination of Raman

and AFM, further complicated by the challenging experimental conditions of LIBs. Moreover, TERS signal enhancement is rather weak, compared to other near-field Raman spectroscopy techniques, as LSPR is only provided by one sharp tip, drastically reducing its sensitivity for low concentrated surface species.[152–154]

In nanoparticle enhanced Raman spectroscopy (NERS, **Figure 6b**), which in the literature is often also referred to as SERS, this particular downside is overcome by the use of Au or Ag NPs, introduced to the samples surface prior to the experiment. Instead of a single tip as in TERS, every individual NP serves as an LSPR source in NERS, resulting in a plethora of signal enhancing hot spots on the sample, drastically increasing the sensitivity. In addition, it was found that the LSPR is especially strong on the junction between individual plasmonic active NPs, providing additional signal enhancement.[125,127,133,144,155] As the resonance frequency of the plasmons is greatly influenced by the size of the nanoparticles, the window of suitable wavelengths for efficient excitation is rather small. However, despite being somewhat localized due to the structure of the substrate, the surface plasmons are able to roam between different NPs, if they are in close proximity (<5 nm). Through this effect, the window of suitable wavelengths can be notably widened, as every connected NP provides additional suitable wavelength for efficient LSPR.[125]

While the implementation of NERS successfully solved the sensitivity issue of TERS, this comes at the lack of spatial resolution. Moreover, the application of NERS for the investigation of interphases in LIBs is challenging, as the introduced NPs can spark artificial interphase formation reactions, distorting obtained information. In addition, the introduced NPs are vulnerable to the harsh conditions in operating LIBs, leading to their degradation *via* oxidation or lithiation, which quenches their plasmonic activity. The study of Piernas-Muñoz *et al*., is a good example for the use of NERS for interphase characterization in LIBs.[156] In their study, the authors introduced Au NPs *via* electrodeposition on a silicon electrode, enabling the identification of organic lithium compounds, olefinic species, and organophosphates as degradation products of a carbonate-based electrolyte (1.2 $_M$ $LiPF_6$ in EC:EMC; 3:7).

Shell-isolated nanoparticle enhanced Raman spectroscopy (SHINERS, **Figure 6c**) is the logic successor of NERS, introducing a protective coating around the employed NPs, usually comprised of Al_2O_3 or SiO_2. These protective shells increase the inertness of the NPs, minimizing the risk of artificially catalyzed reactions and NP degradation. Most importantly, the coating prevents direct contact of the analyte with the NP, ensuring a correlation between the obtained Raman signal and the probed sample and not of an additional bond between analyte and substrate.[30,33,146,152,154,155,157,158] By addressing these challenges, SHINERS is an ideal technique for the investigation of interphases in LIBs, combining high sensitivity with substrate generality. In addition, by adjustable synthesis of

NP size and shape, the enhancing effect can be tailored corresponding to the respective sample and the available Raman system.[30,33,146,152,154,155]

Nevertheless, studies employing SHINERS for interphase characterization are still scarce, as SHINERS is a fairly new technique. The potential of SHINERS was demonstrated by Gajan *et al*., investigating the SEI formed by a carbonate-based electrolyte (1 $_{M}$ $LiPF_6$ in EC:DEC; 1:1) on a tin electrode. The authors of the study identified semi-carbonate species like lithium ethylene mono-carbonate (LEMC) and diethyl-2,5-dioxahexane carboxylate (DEDOHC) as major interphase components. In addition, potential dependent dissolution and reformation of DEDOHC was observed during the *operando* monitoring of the electrode surface, expressing interphase instability during operation.[32]

Studies presented by other groups in the recent years only focus on the anode.[159–163] Systematic investigations are lacking and to this date the only systematic investigations were performed as part of this work and related publications. These contents will be presented over the following chapters.[28,29]

3. Motivation

LIBs are the most promising technology for the storage of renewably sourced energy, for the electrification of the transport sector and for the reduction of man-made global emissions. Despite great advances in the last years, LIBs still have to be improved notably in terms of safety, cost, and energy density. The implementation of novel electrode materials to increase key properties of LIBs is hindered by the formation of instable and ineffective interphases on anode and cathode, resulting in continuous electrolyte decomposition and active material degradation, limiting performance and lifetime of the cells. Stabilization of these interphases through the introduction of specialized film-forming additives holds great promise, nonetheless, a deep understanding of interphase compositions and formation mechanisms under real working conditions is necessary to systematically develop new and tailored additives. Although there is a wide range of available interphase characterization methods, at the moment only vibrational spectroscopy techniques like Raman spectroscopy are suitable for investigations under these challenging conditions. Still, due to intrinsic limitations, *conventional* Raman spectroscopy fails to detect small sample quantities, like interphases. To overcome this constraint, near field Raman spectroscopy variants, like SHINERS, can be employed to realize *operando* investigation of interphases in LIBs.

Based on the challenges outlined above, two main areas of focus can be defined for this thesis. The first is the modification of interphases *via* the implementation of promising film-forming electrolyte additives. The second is the analysis and characterization of the additive-derived interphases. Accordingly, the following objectives shall be pursued in this thesis:

- Optimization of the SHINERS technique for interphase characterization in LIBs.
- Validation of the SHINERS technique on the base of an established LIB-system.
- Implementation of film-forming additives for the stabilization of interphases in high voltage LIBs with next-generation electrode materials.
- Characterization of the additive-derived interphases by *operando* SHINERS.
- Identification of relations between additive structure, interphase composition and cell performance.
- Elucidation of interphase formation mechanisms.

Following the formulated objectives, the structure of the thesis can be divided into three parts, as depicted in **Figure 7**.

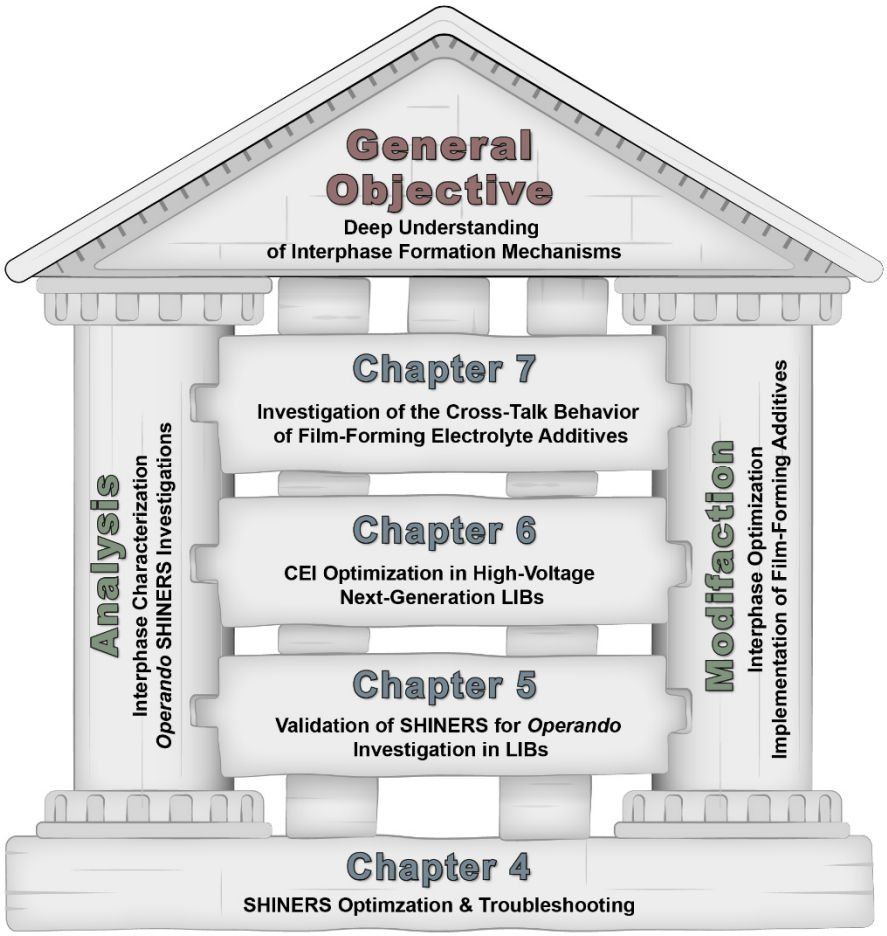

Figure 7: Overview of the proposed structure of this thesis. Two areas of focus, interphase modification and analysis, make up the main work performed during this thesis. The three main chapters of this thesis, **Chapters 5 – 7** bridge the areas of focus.

The first part of this thesis (**Chapter 5**) is focused on the implementation of the SHINERS technique into the LIB system. To validate the functionality of SHINERS for the *operando* characterization of interphases, a successful proof-of-concept study is the main goal of this particular chapter. NMC111||graphite cells with a carbonate-based electrolyte serve as reference system, for the investigation of thiophene as CEI-forming additive. Finally, the formation of a thiophene-based interphase is captured by *operando* SHINERS measurements.

The second part (**Chapter 6**) of this thesis is aimed at the development of a suitable electrolyte formulation for the stabilization of the CEI on next-generation NMC811 cathodes in a commercial high-voltage application. To stabilize the CEI, different thiophene-based derivatives are investigated upon their film-forming properties. In the following, the interphase derived from promising additive candidates is characterized using *operando* SHINERS, to elucidate the composition of the additive-derived CEI and to understand the underlying formation mechanisms.

The focus of the third part (**Chapter 7**) is on the cross-talk behavior of film-forming electrolyte additives. Here, different ethylene carbonate-based electrolyte additives will be

investigated and the formed SEI investigated by *operando* SHINERS. Detailed analysis, as well as additional experiments are performed to unravel the cross-talk mechanism of vinylethylene carbonate (VEC), accounting for the observed phenomena during electrochemical characterization.

In addition to the main chapters presented above, a detailed supplementary chapter (**Chapter 4.2.5**) on the synthesis and characterization of NPs for SHINERS is presented. This section of the thesis will also address the experimental limitations of SHINERS, as well as additional experiments performed during this thesis regarding the stability of NPs, hoping to aid future users of this particular technique.

4. Materials and Experimental Methods

This chapter provides a summery over the materials and experimental methods and techniques which have been employed within this thesis. Segments of this chapter have been published and are used with permission.[28,29,159]

4.1. Materials

Chemicals and materials that have been used within this thesis are listed in **Table 1** below.

Table 1: Summary of chemicals and materials used in this thesis, including supplier and purity.

Substance / Material	Supplier	Purity
Electrolyte Preparation		
3,3-Bithiophene	TCI	> 98%
3,4-Dibromothiophene	TCI	> 98%
3-Bromothiophene	TCI	> 98%
3-Cyanothiophene	TCI	> 98%
3-Methoxythiophene	TCI	> 98%
3-Phenylthiophene	TCI	> 98%
3-Thiophene boronic acid	Sigma Aldrich	> 98%
3-Thiophene carboxylic acid	Activate Scientific	> 98%
Chloroethylene carbonate (ClEC)	ABCR	> 98%
Diethyl carbonate (DEC)	E-Lyte Innovations	Battery grade
Ethylene carbonate (EC)	E-Lyte Innovations	Battery grade
Etyhl methyl carbonate (EMC)	E-Lyte Innovations	Battery grade
Fluoroethylene carbonate (FEC)	ABCR	> 98%
$LiPF_6$	E-Lyte Innovations	Battery grade
Thiophene	Sigma Aldrich	> 99%
Thiophene-3-ol	BLD Pharm	> 98%
Vinylene carbonate (VC)	E-Lyte Innovations	Battery grade
Vinylethylene carbonate (VEC)	ABCR	> 99%
Cell Preparation		
2032 Coin Cell Housing	Hohsen Corporation	-
Celgard 2500 (polypropylene)	Celgard	-
Graphite Electrode sheets (95 wt.%, 1.2 mAh cm^{-2})	CustomCells GmbH	Battery grade
Li-metal foil	Albemarle Corporation	Battery grade

NMC111 Electrode sheets (90 wt.%, 1.0 mAh cm^{-2})	CustomCells GmbH	Battery grade
NMC111||Graphite Pouchcells	LiFUN Technology	Battery grade
NMC622||Graphite Pouchcells	LiFUN Technology	Battery grade
NMC811||Graphite Pouchcells	LiFUN Technology	Battery grade
Polyethylene terephthalate foil (Mylar® foil)	PPI Adhesive products	-
Whatman GF/D (glass fiber)	Whatman	-
Nanoparticle Synthesis		
3-Aminopropyltrimethoxysilane (APTMS)	Sigma Aldrich	> 97%
3-Aminopropyltriethoxysilane (APTES)	Sigma Aldrich	> 99%
$AgNO_3$	Sigma Aldrich	> 99.99%
$AuCl_3$	Sigma Aldrich	> 99.99%
Hydrochloric acid (6 $_M$)	Sigma Aldrich	Analytical grade
Hydroxylamine hydrochloride	Sigma Aldrich	> 99.99%
L-ascorbic acid	Sigma Aldrich	> 99%
NaOH solution (50%)	Sigma Aldrich	Reagent grade
Sodium citrate	USP	USP reference standard
Sodium silicate	Sigma Aldrich	Reagent grade
Further Chemicals		
Aluminum mesh	EL-CELL	Battery grade
Copper mesh	EL-CELL	Battery grade
Et_2O	SPS, PureSolv MD7	-
Gold foil (5 x 5 x 0.5 mm)	ChemPUR	> 99.99%
Hydrochloric acid (37%)	Merck	Analytical grade
Isopropanol	Acros Organics	> 99.8%
KCl	AppliChem	> 99.5%
Milli-Q Water	Merck	18.2 MΩ cm^{-1}
Naphthalene	TCI	> 98%
Nitric acid (65%)	Fischer Scientific	-
Pyridine	Sigma Aldrich	> 99.9%
THF	SPS, PureSolv MD7	-

4.2. Experimental Methods

4.2.1. Electrolyte Preparation

In this thesis, various electrolyte formulations were prepared. In general, these formulations were prepared using a carbonate-based baseline electrolyte. In the first part of this thesis (**Chapter 5**) the baseline electrolyte (**BE 1**) consisted of 1 $_M$ $LiPF_6$ dissolved in EC:DEC (1:1 by weight). In the second and third part (**Chapters 6** and **7**) the baseline electrolyte was modified (**BE 2**), consisting of 1 $_M$ $LiPF_6$ dissolved in EC:EMC (3:7 by weight). For the preparation of additive-containing electrolyte formulations, the employed additives were added in the desired concentration to the respective baseline electrolyte. In addition, the amount of $LiPF_6$ was adjusted, to retain a concentration of 1 $_M$. If necessary, utilized additives were dried for 24 h at 80 °C under reduced atmosphere. Electrolytes were prepared in an argon-filled glovebox (MBraun, H_2O and O_2 < 1 ppm), and stored either in an argon-filled glovebox or a dry room (dew point < –50 °C).

4.2.2. Cell Preparation

For electrochemical analysis of the prepared electrolyte formulations different cells were prepared.

For galvanostatic charge/discharge experiments different cell-types were utilized throughout this thesis. For the galvanostatic cycling experiments, presented in **Chapter 5**, 2032-type NMC111||graphite coin-cells were prepared. NMC111 and graphite electrodes with diameters of 14 mm and 15 mm, respectively, were punched out from commercially available electrode sheets. Before cell assembly, the electrodes were dried at 120 °C for 12 h at reduced atmosphere. During cell assembly a 16 mm circular Celgard 2500 separator was placed between the electrodes, wetted with 60 µL of electrolyte. Coin-cell assembly was performed in a dry room. For the galvanostatic cycling experiments, presented in **Chapters 6** and **7**, commercially available NMC811||graphite and NMC622||graphite pouch-cells were utilized. Before cell assembly, the pouch-cells were cut-open and dried for 24 h at 80 °C under reduced atmosphere. The cells were filled with 700 µL of electrolyte and sealed at 165 °C for 5 s at 15% of the ambient pressure, using a GN-HS200V pouch-cell sealer (Gelon LIB Co.). In **Chapter 7**, for de-gassing after cell formation, the pouch-cells were opened and re-sealed at the cell stack as described above.

Additional 2032-type coin-cells prepared for the determination of electrode degradation, presented in **Chapter 7**, were assembled as described above for **Chapter 5**. However, instead of preparing electrodes from a pristine electrode sheet, the utilized electrodes were taken from pouch-cells after reaching 50% state-of-health (SoH). In these coin-cells, the

electrochemically aged electrodes were paired with pristine counter parts. In general, four cells were prepared for every investigated electrolyte formulation.

For potentiostatic electrolyte characterization *via* cyclic voltammetry (CV) experiments, T-type Swagelok® cells were prepared, allowing for precise control of the electrode potential, due to an additional reference electrode. For continuity of the results, the electrodes utilized for the CV measurements are the same electrodes as employed for the galvanostatic cycling experiments. For the cells presented in **Chapter 5**, 12 mm circular electrodes were punched out from electrode sheets. For the cells in **Chapters 6** and **7**, first the cell stack was retrieved from the respective pouch-cells. Subsequently, the active material coating was removed from one side of the double-coated electrodes using THF. Afterwards, 12 mm circular electrodes were punched out from the obtained electrode sheets. Prior to cell assembly, all prepared electrodes were dried at 90 °C for 24 h at reduced atmosphere. To ensure electronic insulation, the inside of the Swagelok cells was covered with Mylar® foil. Working and counter electrode (WE and CE) were separated using a 13 mm Whatman GF/D glass fiber separator, while a 10 mm Whatman separator was used for the reference electrode (RE). The separators were soaked with 120 µL and 80 µL of electrolyte, respectively. For electrolyte characterization under oxidative conditions, NMC electrodes were employed as WEs, paired with graphite CEs. For electrolyte characterization under reductive conditions, graphite WEs were paired with Li-metal CEs. In all cases, Li-metal was used as RE. Preparation of the Swagelok® cells was performed in an argon-filled glovebox.

4.2.3. Electrochemical Characterization

4.2.3.1. Galvanostatic Charge/Discharge Cycling

To determine the effect of the prepared electrolyte formulations on the electrochemical performance of the chosen cell-system, galvanostatic charge/discharge cycling experiments were performed in a voltage range from 4.50 V to 2.80 V. The employed cycling routine was modified in every chapter, as described in the following.

In **Chapter 5**, after cell assembly, the cells were rested for 24 h to ensure sufficient electrode wetting. Afterwards, the cells were formatted, performing 3 charge/discharge cycles at a C-rate of C/10 and C/3 using constant current/constant voltage (CCCV) steps. Further cycling of the cells was performed at a C-rate of 1 using constant current (CC) steps until reaching 80% SoH. The C-rate was calculated based on the specific capacity of the employed NMC111 cathode.

In **Chapter 6**, after cell assembly, the cells were rested for 24 h to ensure sufficient electrode wetting. Afterward, the cells were formatted, performing 3 charge/discharge cycles at a C-rate of C/10 and C/3 using CCCV steps. Further cycling of the cells was performed at a C-rate of 1 C using CC-steps until reaching 50% SoH. The C-rate was calculated based on the nominal capacity (200 mAh) of the employed pouch-cells.

In **Chapter 7**, after cell assembly, the cells were pre-polarized for 12 h by applying a constant voltage of 1.50 V. Afterward, the cells were formatted, performing two CCCV charge/discharge cycles at a C-rate of C/10. After formation, the cells were de-gassed, reconnected, rested for an additional 12 h, before further charge/discharge cycling at a C-rate of 1 C using CC steps until reaching 50% SoH. The C-rate was calculated based on the nominal capacity (200 mAh) of the employed pouch-cells.

All galvanostatic charge/discharge cycling experiments were performed at 20 °C using a MACCOR 4000 series battery tester. For galvanostatic cycling of the pouch cells, a specially designed cell-holder was used, allowing the application of a constant pressure (2 bar) onto the cells during cycling.[164]

4.2.3.2. Potentiostatic Investigation

Potentiostatic investigation (cyclic voltammetry) of the prepared electrolyte formulations were conducted on an Autolab potentiostat/galvanostat (Metrohm) with a sweep rate of 150 µV s^{-1}, controlled using Nova 2.1 (Metrohm). Cells with an NMC WE were tested in a potential range of 2.80 V *vs.* Li|Li^+ and 4.50 V *vs.* Li|Li^+ or 5.00 V *vs.* Li|Li^+, while cells with a graphite electrode were tested between 2.00 V *vs.* Li|Li^+ and 0.05 V *vs.* Li|Li^+. Before the experiments, the prepared cells were rested for 10 h. All CV investigations were carried out in Swagelok® T-type cells, assembled as described above.

4.2.3.3. Electrochemical Impedance Spectroscopy

Within **Chapters 5** and **7** EIS measurements were performed using commercially available pouch-cells prepared as described above. EIS measurements were conducted using an Autolab potentiostat/galvanostat, controlled by Nova 2.1. The pouch-cells were galvanostatically charge/discharge cycled at a C-rate of C/2. EI spectra were taken at a cell voltage of 3.80 V in every charge and discharge half-cycle, corresponding to a state of charge of 50%, in a frequency range of 0.01 Hz to 100000 Hz with 15 frequency points per decade.

4.2.4. Raman Investigation

All Raman investigation performed in this thesis were carried out on a confocal Raman microscope (LabRam HR evolution, Horiba Scientific) equipped with an air-cooled CCD detector and 600 g mm^{-1} grating. Samples were excited using a blue (442 nm), green (532 nm) or red (633 nm) laser, with a power output of 8 mW, 12.20 mW, and 10.50 mW at the objective. Laser power, acquisition time and spectra accumulations were adjusted for every sample and every measurement. Therefore, detailed information on these specific properties will be noted in the figure description of every displayed Raman spectrum. Handling of the Raman spectrometer and curation of the obtained spectra was performed using the LabSpec 6.7.2.1 software (Horiba Scientific). Before every Raman experiment, the system was calibrated onto the band of *c*-Si around 520.70 cm^{-1}.

For *in situ* / *operando* SHINERS experiments, galvanostatic charging of the assembled optical cells was carried out using an Autolab potentiostat/galvanostat PGSTAT204 (Metrohm). The cells were charged to a cell voltage of 4.50 V at a C-rate of C/3, calculated based on the capacity of the WE. Charging was stopped at defined cell voltages to perform Raman measurements, to avoid voltage drops, a constant voltage was applied during spectra acquisition. Note that in the experiments presented in **Chapter 6** a Li-metal RE was introduced to the optical cell for precise control of the WE potential. Therefore, in this chapter the term “potential” will be used.

For SERS investigations, potentiostatic charging of the optical cells was performed using an Autolab potentiostat/galvanostat PGSTAT204 (Metrohm), up to a WE potential of 4.50 V *vs.* $Li|Li^+$. For potentiostatic charging, a linear sweep voltammetry experiment was performed with a sweep rate of 150 µV s^{-1}. Raman measurements were carried out at defined WE potentials. To avoid potential drops a constant voltage was applied during the measurements.

4.2.5. Raman Sample Preparation

The controlled synthesis of NPs with different sizes and out of different metals is crucial to tune the properties of SHINRES technique, to achieve optimum signal enhancement. Thus, NP synthesis is a distinct aspect of the preparation of SHINERS samples in this thesis. Therefore, the synthesis of Au and Ag NPs in different sizes will be described in detail in the following. In addition, a section regarding the characterization of the prepared NPs and the sample preparation for SHINERS and SERS measurements is added. Moreover, this segment contains a brief discussion of technical and intrinsic challenges of SHINERS in LIB research.

4.2.5.1. Nanoparticle Synthesis

All glassware used for the synthesis of NPs was carefully cleaned with *aqua regia* and boiled with Milli-Q water beforehand. The protocols for Au NP synthesis were adapted from.[165]

4.2.5.2. Au Nanoparticles

4.2.5.2.1. 55 nm Au Nanoparticle Synthesis

In a round-bottom flask an $AuCl_3$ solution (100 mL, 0.01 wt.%) was brought to a boil. A freshly prepared sodium citrate solution (700 µL, 1 wt.%) was added quickly. The obtained solution was boiled for further 30 min, before cooling to room temperature (RT). At this point, the obtained NPs have a diameter of 55 nm and are stable in the reagent stock solution for up to 1 month. For silica coating of the NPs, 30 mL of the 55 nm stock solution were added to a round-bottom flask. An APTMS solution (400 µL, 1 $_{mM}$) was added dropwise under vigorous stirring. The obtained solution was stirred for 15 min at RT. Afterward, a sodium silicate solution (3.20 mL, 0.54 wt.%, pH = 10; adjusted with HCl) was added. The resulting mixture was stirred at RT for 3 min, before stirring for 60 min at 90 °C. Finally, the reaction mixture was cooled in an ice-bath. At this point the NP coating exhibits a thickness of 2 nm – 4 nm. For purification of the coated NPs, the mixture was centrifuged for 10 min at 5000 rpm at 10 °C. The supernatant was decanted and replaced with Milli-Q water. This purification step was repeated 3 times. The prepared NPs were stored in a fridge at 6 °C for a maximum of 2 weeks.

4.2.5.2.2. 120 nm Au Nanoparticle Synthesis

In a round-bottom flask an $AuCl_3$ solution (100 mL, 0.01 wt.%) was brought to a boil. A freshly prepared sodium citrate solution (1 mL, 1 wt.%) was added quickly. The obtained solution was boiled for further 30 min, before cooling to RT, yielding NPs with a diameter of 40 nm, stable for up to 1 month in the reagent stock solution. In the next step, 4 mL of the 40 nm stock solution were added to a round-bottom flask and diluted with 53 mL Milli-Q water. Sodium citrate solution (900 µL, 1 wt.%) was added, before stirring the resulting mixture for 3 min at RT. $AuCl_3$ solution (900 µL, 1 wt.%) was added and the resulting mixture stirred for 8 min. Afterward, hydroxylamine hydrochloride solution (1.40 mL, 0.01 $_{M}$) was slowly added dropwise under vigorous stirring. The reaction mixture was stirred for a minimum of 5 min. At this point the obtained NPs exhibit a diameter of 120 nm.

For silica coating of the NPs, 15 mL of the 120 nm stock solution were added to a round-bottom flask and diluted with Milli-Q water (15 mL). An APTES solution (500 µL, 0.5 $_{mM}$) was added slowly dropwise under vigorous stirring. The obtained solution was stirred for another

20 min at RT. Afterward, a sodium silicate solution (2.80 mL, 0.54 wt.%, pH = 10; adjusted with HCl) was added. The resulting mixture was stirred at RT for 3 min, before stirring for 60 min at 90 °C. Finally, the reaction mixture was cooled in an ice-bath. At this point the NP coating exhibits a thickness of 2 – 4 nm. For purification of the coated NPs, the mixture was centrifuged for 10 min at 2300 rpm at 10 °C. The supernatant was decanted and replaced with Milli-Q water. This purification step was repeated 3 times. The prepared NPs were stored in a fridge at 6 °C for a maximum of 2 weeks.

4.2.5.2.3. 20 nm Au Nanoparticle Synthesis

The synthesis of 20 nm Au NPs follows the same protocol as described for 55 nm Au NPs. However, the amount of sodium citrate solution added to the reaction mixture was increased to 1.95 mL.

4.2.5.3. Ag Nanoparticles

4.2.5.3.1. 12 nm Au Seed Synthesis

To ensure a narrow size distribution of the synthesized Ag NPs, it proved to be necessary to grow the NPs around a seed with a controlled size. For this purpose, 12 nm Au seeds were utilized in this thesis. For the synthesis of the seeds an $AuCl_3$ solution (100 mL, 0.01 wt.%) was added to a round-bottom flask. The solution was brought to a boil and a sodium citrate solution (3 mL, 1 wt.%) was added quickly. The solution was boiled for 40 min under constant stirring before cooling to RT. The synthesized seeds are stable in the reagent solution for 1 month.

4.2.5.3.2. 100 nm Ag Nanoparticle Synthesis

In a round-bottom flask 500 µL of the 12 nm Au seed solution was diluted with Milli-Q water (20 mL). Sodium citrate solution (1 mL, 1 wt.%) and L-ascorbic acid solution (3 mL, 0.01 $_M$) were added and the obtained solution was stirred for 5 min at RT. An $AgNO_3$ solution (2.40 mL, 0.01 $_M$) was added with a speed of 15 mL min^{-1}. The obtained solution was brought to a boil and stirred for 2 h. At this point the obtained NPs exhibit a diameter of 100 nm. For silica coating 9 mL of the 50 nm Ag NP solution were diluted with Milli-Q water (21 mL). The pH of the solution was adjusted to a value of 5 by adding H_2SO_4. Afterward, an APTMS solution (400 µL, 1 $_{mM}$) was added dropwise. The obtained solution was stirred for 15 min, before adding a sodium silicate solution (3.20 mL, 0.54 wt.%). The obtained mixture was stirred vigorously for 3 min. By the addition of a NaOH solution (0.50 $_M$) the pH value of the reagent mixture was increased to a value of pH = 11.5, before bringing the mixture to a boil. To obtain a silica-shell thickness of 3 nm the solution was boiled under constant stirring for 90 min. Afterward, the mixture was cooled down in an ice-bath.

Purification of the obtained Ag NPs was performed *via* centrifugation for 10 min at 2300 rpm at 10 °C. The supernatant was decanted and replaced with Milli-Q water. This purification step was repeated 3 times. The prepared NPs were stored in a fridge at 6 °C for a maximum of 2 weeks.

4.2.5.3.3. Synthesis of Ag Nanoparticles with different sizes

The synthesis of Ag NPs with various sizes mainly follows the protocol as described for the NPs with a diameter of 100 nm. NP size can be controlled directly by the volume of $AgNO_3$ solution added to the reaction mixture. The necessary volume of $AgNO_3$ solution to synthesize the respective NP size is presented in **Table 2** below.

Table 2: Necessary volume of $AgNO_3$ solution added to the reaction mixture to achieve formation of Ag NPs with targeted diameters.

Ag NP diameter / nm	V_{AgNO3} / mL
20	0.10
28	0.20
36	0.30
50	0.47
70	0.70

4.2.6. Nanoparticle Characterization

The size of the synthesized NPs was controlled *via* SEM investigation, as shown in **Figure A1** and **Figure A2**. Here silica coated Au NPs with a targeted size of 55 nm and 120 nm, respectively, were drop cast onto different electrodes. As depicted in the figures, the measured diameter of the NPs is in very good agreement with the targeted size, especially if the silica-shell thickness of 2 nm – 4 nm is considered.

For confirmation of a complete coating of the synthesized NPs, NPs were drop cast onto a Si-wafer. The wafer was dried under reduced atmosphere for 10 minutes to remove solvent residues. Afterward, the wafer was infused with an aqueous pyridine solution (0.01_{M}) and covered with a quartz optical window. The prepared wafer then was investigated *via* Raman spectroscopy. As shown in **Figure A3**, the spectrum of NPs with a complete coating only shows a band corresponding to the Si-wafer. In contrast, the spectrum of the incompletely coated NPs exhibits additional bands around 1012 cm^{-1} and 1037 cm^{-1}. These bands can be ascribed to the coordination of pyridine molecules to the Au core of the NPs, revealing pinholes in the silica shell. In addition to SEM investigation, NPs were characterized using UV/Vis spectroscopy. These investigations not only provide information on size distribution of the synthesized batch of NPs, but also on the absorption maxima of the respective NPs.

As described in **Chapter 2.4.2**, the LSPR strongly correlates with plasmon absorption efficiency of the substrate and thus the size of the NPs. Determining the absorption maxima of the NPs *via* UV/Vis allows a straightforward selection of NPs for maximum signal enhancement, respecting the available laser sources of the utilized Raman system. UV/Vis measurements were carried out on a UV-2450 UV/Vis spectrometer (Shimadzu) using quartz cuvettes (QS, Hellma Analytics) with a 10 mm path length. Spectra were recorded from 900 nm to 200 nm using UVProbe2.33 software (Shimadzu).

Figure A4 depicts the absorption maxima of Au NPs with various sizes between 20 nm and 120 nm. The absorption maxima shift to higher wavelengths with increasing NP diameter. Considering that only Au NPs with a size of 55 nm and 120 nm were utilized for SHINERS interphase investigation in this thesis, **Figure A4** nicely demonstrates that these NPs are mostly suitable for the red laser (633 nm). While the green laser (532 nm) only shows minor overlapping with the absorption curves, the blue laser (442 nm) is completely unsuited for the enhancement with Au NPs. A practical example of this effect is shown in **Figure A5**, displaying SHINER spectra taken from the surface of a Si-wafer in the presence 120 nm Au NPs. The spectra were recorded during the characterization of the interphase formed by a *γ*-butyrolactone-based (1 $_{M}$ $LiBF_4$, E-Lyte Innovations, battery grade; GBL, Sigma Aldrich, 99%) electrolyte with a red and a green laser. It is clear to see that the spectrum recorded with a green laser only exhibits bands assigned to the GBL electrolyte. In contrast, the red laser spectrum additionally shows several prominent bands which can be assigned to interphase formation products. This example outlines the importance of employing the right NP size for the chosen laser system, as signal enhancement and thus interphase analysis is only possible with the right combination.

While the blue laser is not suitable for the Au NPs, Ag NPs are a good match, as shown in **Figure A6**. Nevertheless, **Figure A6** also outlines the main challenge of Ag NP synthesis. While the small NPs (up to a diameter of 70 nm) show a narrow absorption curve, bigger size NPs exhibit a broad curve, indicating a wide NP size distribution. The uneven NP size distribution of the bigger Ag NPs is caused by the slow reaction kinetics of the Ag reduction during NP synthesis. While the use of Au seeds overcomes the issues of inhomogeneous Ag NP nucleation, the synthesis of Ag NPs with a big diameter and a narrow size distribution is not possible *via* citrate reduction. An example for the necessity of Au seeds for successful Ag NP synthesis is depicted in **Figure A7**, exhibiting the UV/Vis absorption curves of Ag NPs, synthesized without Au seeds, clearly showing broad absorption curves, even for Ag NPs with a smaller diameter.

4.2.7. SERS and SHINERS Sample Preparation

In this thesis two near-field Raman spectroscopy techniques were employed, SERS and SHINERS, requiring different sample preparation approaches.

For SERS sample preparation, an electrochemically roughened Au foil was utilized. For roughening, first the foil was cleaned with isopropanol and Milli-Q water in an ultrasonic bath. In the next step, the foil was annealed to revert previous roughening. Using a propane gas burner, the foil was brought to a yellow glow repeatedly for 2 min to 3 min. For the actual roughening the Au foil was hung in an aqueous KCl solution (0.10 $_M$, Milli-Q water), which has been bubbled with N_2 for 30 min to remove ambient oxygen. Additionally, Pt-electrodes were introduced to the KCl bath, serving as CE and (*quasi*-)RE. The prepared system was cycled between -0.30 V *vs.* Pt and 0.90 V *vs.* Pt at a sweep rate of 250 mV s^{-1}. At the upper and lower vertex potential, a delay of 10 s and 2 s was applied, respectively. This process was repeated 25 times. After roughening, the Au foil was rinsed thoroughly with Milli-Q water, dried in an N_2 stream and further dried in an oven (Binder) at 60 °C, before application.

For SHINERS sample preparation, coated NPs with a selected diameter were synthesized as described above. Usually SHINERS samples were prepared *via* drop casting of solution of the NPs onto varying substrates, with the exception of electrochemically aged and Li-metal electrodes. For these samples the coated NPs were transferred from the aqueous reaction solution into an organic medium (isopropanol) *via* centrifugation. A systematic SEM investigation was performed to determine the optimized amount of NPs added to the electrode surface. Adding a total of 500 µL (5 x 100 µL) of concentrated NP solution yielded a satisfying coverage of the substrate surface with NPs. As shown in **Figure A8**, NPs are distributed over multiple crystals, sticking directly to the surface of the active material. In addition, small hot-spots are formed, where multiple NPs are close together, allowing for increased signal enhancement. Nevertheless, NP coverage is still loose enough to not interfere notably with the electrochemical activity of the electrode. After drop casting of the NPs onto the electrode surface, the prepared sample was dried for 12 h at 90 °C under reduced atmosphere.

In cases were the sample did not allow for direct drop casting of the NPs, *e.g.* due to the reactivity of Li-metal or the sensitivity of the interphase on electrochemically aged electrodes, NPs were introduced onto the surface of an optical quartz window. Similar to the regular electrode samples, 5 x 100 µL of concentrated NP solution were added to the window. However, here NPs were not transferred to an organic medium, as the higher surface tension of the aqueous medium allows for a more concentrated application of NPs. After drop casting, the prepared optical windows were dried at 60 °C for 1 h and for further

10 min under reduced atmosphere. For Raman measurements the sensitive samples were brought into direct contact with the NPs on the window, enabling SHINERS enhancement.

4.2.8. Cell and Electrode Configurations

Most Raman measurements conducted during this thesis were performed under *in situ* or *operando* conditions. These conditions require an adequately working electrochemistry in the optical cells, to ensure similar parameters compared to the cells used for galvanostatic charge/discharge cycling experiments. As SHINERS interphase investigations were performed on multiple electrode materials, including positive and negative electrodes, the development of different cell and electrode configurations was necessary. In general, all presented Raman investigations were performed in the airtight ECC-STD optical cell (EL-CELL, **Figure A9a**), allowing the contacting of 3 electrodes. This is especially valuable as this enables the introduction of an RE, to precisely monitor the WE potential during measurements. The different configurations employed in this work are depicted in **Figure A9** and will be described in detail in the following.

For interphase investigations on the surface of typical cathode active materials (electrode connected as WE), a simple “sandwich” configuration was employed (**Figure A9b**). Here, the WE was placed directly on top of the CE, with both electrode’s active material facing upwards to the optical window. WE and CE were separated using a Celgard 2500 separator. Additionally, an aluminum mesh was placed on top of the WE to ensure sufficient electrolyte wetting and diffusion.

For interphase investigations on the surface of typical anode materials (electrode connected as WE), the before presented “sandwich” configuration was not suitable. It was observed that often, instead of lithiation of the active material, Li was plated onto the backside of the anode current collector. Li-plating was probably induced by exceeding over voltages, caused by extended Li-ion diffusion pathways. To enable proper electrochemistry the “donut” configuration was employed (**Figure A9c**). Here, the CE is placed on top of the WE. However, in this case, the active material side of the CE faces downwards in the direction of the WE active material, allowing faster Li-ion diffusion. To enable observation of the WE surface, a hole is punched into the center of the CE and the separator.

While the configurations described above enable stable chemistry for either anode or cathode Raman investigation, the observation of both WE and CE surface during the same experiment is not possible. To overcome this challenge, the “side-by-side” configuration can be employed (**Figure A9d**), where both electrodes are placed next to each other. Here the active material of both WE and CE are facing towards the optical window, allowing simultaneous observation. Although a flexible investigation of both electrodes’ surfaces is

allowed, the configuration often struggles with reliable electrochemistry. In addition, preparation of the cell is challenging, due to limited space in the optical cell. In all presented cell configurations, the RE is placed on the side at the outer edge of the cell.

4.3. Challenges of SHINERS

During the detailed investigation of the SHINERS technique as part of this work, measurements of the anode side proved to be difficult.

The author of this thesis hopes that this segment might help other users of the SHINERS technique, upon encountering similar phenomena. Nevertheless, it has to be emphasized that, despite this limitation, SHINERS is a very powerful technique providing crucial information on interphase formation mechanisms and compositions, and still has a lot of potential for improvement.

In almost all performed experiments, a notable loss of features in the spectrum and a diminished signal to noise ratio, caused by a severe increase in the fluorescent background, hindered data interpretation. In all cases, the effect of this phenomenon directly correlated with the duration of the experiment, as well as the anode potential. The phenomenon was more pronounced for decreasing anode potential, and is presumably caused by two main aspects, which must not be viewed as alternatives but as complementary.

The first aspect is the instability of Au NPs at low potentials, where they are prone to lithiation reactions. This degradation likely explains the observed decrease in signal intensity in the context of the decreasing anode potential. In addition, the loss of the SHINERS effect correlates well with the increasing fluorescence, not anymore being overruled by SHINERS enhancement. In theory, the protective SiO_2 coating should prevent NP degradation. However, similar to Au, SiO_2 is susceptible to lithiation. **Figure A10** shows the results of an additional experiment, determining the effect of the SiO_2 coating on the lithiation of Au NPs. In this experiment, Au NPs were introduced to the surface of a Cu electrode. In a Swagelok® T-type cell, the Cu electrode was paired against a Li-metal CE and Li was plated onto the Cu electrode. This experiment was performed with SiO_2-coated and uncoated Au NPs, as well as a bare Cu electrode for reference. The potential response shows a distinct influence of the coating on the lithiation of the NPs, notably decreasing the Li-uptake. Nevertheless, the results clearly show lithiation of the coated NPs, being in good agreement with the phenomena observed during the SHINERS measurements.

The second aspect is the thickness of the formed interphase. As the thickness of the SEI can reach several hundreds of nanometers, it is plausible that the NPs introduced to the surface of the electrodes before interphase formation are simply buried under the evolving SEI, quenching the SHINERS effect. This explanation is also in good agreement with the

observation of aggravated signal loss at low anode potentials, where enhanced interphase growth is expected. While the use of NPs with a bigger diameter would be a logical approach, it has to be considered that bigger NPs are less chemically stable, enhancing the risk of NP degradation.

It further has to be noted that the described phenomena were not observed during cathode-side investigations. As the Au NPs are stable towards higher potentials and the CEI is typically notably thinner, compared to the SEI, this finding further supports the previous assumptions.

4.4. Additional Characterization Techniques

4.4.1. Scanning Electron Microscopy

SEM investigations were carried out on an Auriga electron microscope (Carl Zeiss Microscopy) with a 3 kV accelerating voltage. Electrode samples were prepared from electrochemically aged electrodes, extracted from optical and pouch cells. Before SEM investigation the electrodes were rinsed 3 times with 100 µL EMC and dried under reduced atmosphere. To avoid sample contamination, sample preparation was performed in an argon-filled glovebox. The samples were transferred to the microscope chamber using an airtight vessel. SEM images presented in this thesis were recorded by Lars Frankenstein, Sebastian Kühn, Friederike Reißig, and Verena Küpers. Sample preparation, SEM image treatment and data interpretation were performed by the author of this thesis.

4.4.2. Electron-Dispersive X-Ray Spectroscopy

EDX analysis was carried out on an Auriga electron microscope, equipped with an EDX detector (Oxford Instruments) and an accelerating voltage of 10 kV. Samples were prepared as described for SEM investigations. EDX measurements were performed by Lars Frankenstein, Sebastian Kühn, and Friederike Reißig. Sample preparation, EDX image treatment and data interpretation were performed by the author of this thesis.

4.4.3. Focused Ion Beam – Secondary Ion Mass Spectrometry

Focused ion beam – secondary ion mass spectrometry (FIB-SIMS) analysis of electrochemically aged electrodes was performed using a fibTOF detector. The time-of-flight (TOF) mass detector is integrated into a FIB-equipped SEM microscope. For ion sputtering, an ion gun with $^{69}Ga^{+}$ ions was employed with a FIB current of 30 keV and 1 nA. FIB-SIMS electrode samples were extracted from galvanostatically charge/discharge cycled pouch cells, after reaching their respective end of life at 50% SoH and dried under reduced atmosphere. Sample preparation and storage was conducted in an argon-filled

glovebox. FIB-SIMS measurements were performed by Lex Pillatsch and Valentine Grimaudo from TOFWERK AG. Sample preparation, FIB-SIMS image creation and data interpretation was performed by the author of this thesis.

4.4.4. Gas Chromatography

Gas chromatography (GC) investigations coupled with mass spectrometry (MS) were performed of the electrochemically aged electrolyte. For sample preparation, pouch cells were prepared as described above and filled with the respective electrolyte. After performing 100 galvanostatic charge/discharge cycles, following the standard procedure, the cells were transferred to an argon-filled glovebox. The cell stack was extracted and the electrodes separated. Separator and negative electrode were placed in a centrifugation system and centrifuged at 8000 rpm for 30 min at 20 °C (MEGA STAR 600R centrifuge, VWR).[166] The extracted electrolyte was diluted with dichloromethane (1:100, *v:v*) and stored at 5 °C for 12 h to precipitate $LiPF_6$. GC-MS investigations were performed on a GCMS-QP2010 Ultra (Shimadzu, AOC5000 Plus autosampler), equipped with a nonpolar column (Supelco SLB-5 ms, 30 m x 0.25 mm. 0.25 µm, Sigma Aldrich). For the measurements, the GC injector was set to 250 °C and a sample volume of 1 µL injected. The initial oven temperature was set to 40 °C for 1 min. Afterward, the temperature was increased to 60 °C at a rate of 3 K min^{-1} and further increased to 260 °C at a rate of 30 K min^{-1}, holding the final temperature for 2 min. For the MS, the ion source was operated in electron ionization mode with 70 eV, while the detector voltage was set following a weekly auto-tune. The quadrupole mass detector was operated in scan mode in a *m/z* range from 20 to 350. GC-MS investigations were performed by Christoph Peschel. Sample preparation was performed by Angela Griggio. Interpretation of the data was performed by the author of this thesis.

4.4.5. Gas Chromatography with High Resolution-Accurate Mass

In addition to the GC-MS investigations, supplementary high resolution-accurate mass (HRAM)-MS analysis was performed of selected samples, using a Q Exactive GC Orbitrap GC-MS/MS system (TRACE 1310 GC and TriPlus RSH autosampler, all Thermo Fischer). MS resolution was set to 60,000 (full-width half maximum at *m/z* 200). Chromatographic separation was performed as described for the regular GC-MS investigations. Chemical ionization was performed with ammonia (3.5 purity) and experimental parameters applied following Peschel *et al*.[167] GC-HRAM-MS investigations were performed by Christoph Peschel. Sample preparation was performed by Angela Griggio. Interpretation of the data was performed by the author of this thesis.

4.4.6. Nuclear Magnetron Resonance Spectroscopy

$^{13}C\{^{1}H\}$ cross polarization magic angle spinning (CP-MAS) NMR spectra were recorded using a 14.1T AVANCE NEO NMR spectrometer (Bruker), equipped with a 3.2 mm double resonance MAS probe tuned to ^{1}H and ^{13}C with respective rf-powers of 100 kHz and 85 kHz, while MAS rotor spinning at 15 kHz. During the measurements, high power decoupling (100 kHz, spinal64) and a 2 ms contact time were applied. 16,000 transients were acquired with a delay cycle of 4 s. All spectra were acquired and processed with TopSpin 4.2 (Bruker) and referenced to α-glycine. NMR spectrum acquisition and processing were performed by Johannes Thienenkamp. Sample preparation and data interpretation was conducted by the author of this thesis.

4.4.7. Quantum Chemistry and DFT Calculations

Quantum chemistry (QC) calculations were performed, using the Gaussian 16 package at the accurate, but computationally expansive, G4MP2 level of theory (typical error of 1 kcal mol^{-1} or 0.04 V).[168,169] Molecular structures of educts, products, and intermediates of the modeled reactions were created by Avogadro.[170] Using CREST, conformers with the lowest energy were obtained at the semi-empirical xtb level of theory.[171–174] Additional conformers were generated *via* Open Babel or by hand.[175]

Electrochemical oxidation potentials (E_{ox}) were calculated *via* the Nernst equation:

$$E_{Ox} = \frac{\Delta G_{Ox}}{nF} \quad (1)$$

Here, ΔG_{Ox} equals the difference in free energy in eV, n gives the number of transferred electrons per elementary step, and F equals the Faraday's constant (26.80 A h mol^{-1}). Note that for calculated electrochemical reduction potentials the sign of the equation changes. For correlation of the calculated potentials to the $Li|Li^{+}$ scale, relevant for the experimental values, a constant shift of -1.40 V was applied.[176,177] To mimic the intermolecular environment, an implicit solvation model was applied for all calculations. For the G4MP2 and xtb level of theory calculations, the SMD and GBSA solvation models were employed, featuring built-in parameters for acetone, resembling a similar dielectric constant compared to liquid carbonate-based electrolytes.[173,177–180] In addition to the QC calculations density functional theory (DFT) calculations were performed to predict Raman spectra. The DFT calculations were carried out using the Gaussian 16 package. Molecule geometries were optimized using the B3LYP DFT and the 6-311++G(3df,2p) basis set. Similar to the QC calculations a SMD implicit solvation model was employed, with built-in parameters for acetone, to mimic the effect of the surrounding molecular environment.[177] QC calculations

were performed by Diddo Diddens. DFT calculations were performed by Matthias Weiling. Data interpretation was performed by the author of this thesis.

4.5. Synthesis

4.5.1. Synthesis of the VEC Reduction Product

In **Chapter 7** the product of the reductive decomposition of VEC was synthesized to gain information on the observed cross-talk phenomenon. The synthesis was inspired by the approach by Lucht *et al.* Naphthalene (4.09 g, 0.03 mol) was dissolved in THF (dry, 50 mL).[181] Li-metal (0.20 g, 0.03 mol) was added to the solution. The obtained mixture immediately turned into a dark green color and was stirred for 12 h at room-temperature. VEC (3.31 g, 0.03 mol) was added to the reagent solution. Upon VEC addition, the reaction mixture turned into a red-yellowish color. After stirring the mixture for 12 h at RT, the solvent was removed by high vacuum. The obtained crude product was washed with Et_2O (5 x 20 mL) and dried under high vacuum for 24 h. The final product was obtained as a yellow powder.

$^{13}C\{^1H\}$ CP-MAS NMR: δ (ppm) = 227, 213 (C=O); 170, 160 (R-COO or R-OCOO); 136, 127, 114 (C=C); 68 (R-CO^-); 38, 30, 13 (R-CH).

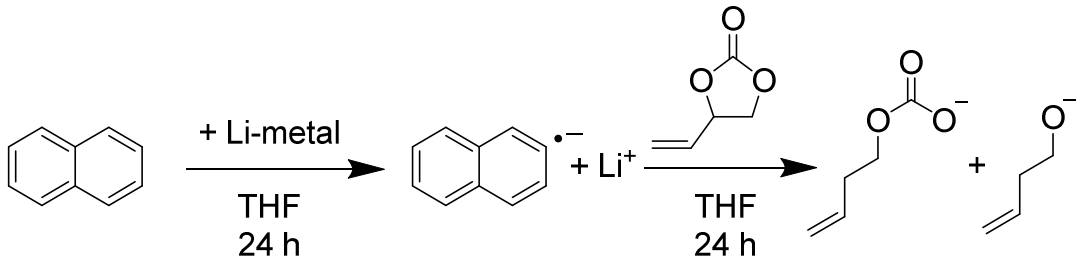

Figure 8: Synthesis route for the VEC decomposition product using Li-naphthalenide to resemble the reactivity of a lithiated graphite electrode. In addition, the structures of the proposed reaction products are depicted, based on the results of the $^{13}C\{^1H\}$ CP MAS NMR analysis

5. Implementation of SHINERS for Interphase Investigation in High-Voltage LIBs – a Proof-of-Concept

Major segments of this chapter have been published in

F. Pfeiffer, D. Diddens, M. Weiling, M. Baghernejad; Study of a High-Voltage NMC Interphase in the Presence of a Thiophene Additive Realized by *operando* SHINERS; *ACS Appl. Mater. Interfaces*, **2023**, 15, 5, 6676–6686.[28]

and are reproduced or adapted with permission.

5.1. Introduction

Increasing the operational voltage through the implementation of next-generation cathode materials like Ni-rich NMC, is a straightforward approach to enhance the energy density of LIBs.[10–12] On the contrary, instability and mechanical degradation of the electrodes, as well as aggravated electrolyte decomposition, caused by the harsh voltage conditions, lead to rapid LIB performance deterioration.[19–21] While the introduction of film-forming electrolyte additives is a promising approach to mitigate LIB failure mechanisms, SOTA electrolyte additives fail to facilitate the formation of interphases, capable to cope with these new challenges.[3,6,13] This raises the need for novel electrolyte formulations employing new functional film-forming additives. To ensure a target driven development of promising new electrolyte additives, a deep understanding of the composition of additive-induced interphases and the underlying interphase formation mechanisms is necessary. In an ideal case, these information are retrieved under real working conditions, allowing a dynamic insight into the evolving interphases.[5,6,26] Obtaining information under these challenging conditions puts severe limitations onto the experiments, greatly limiting the number of available techniques. Vibrational spectroscopy techniques, especially Raman spectroscopy, are ideal candidates for *in situ* or *operando* investigations of LIBs, benefiting from simple sample preparation, high resolution and sensitivity, and a straightforward combination with electrochemistry. In addition, these techniques are very robust and can be considered non-destructive, accounting for their widespread application in battery research.[30–32] While *conventional* Raman spectroscopy is often employed for the characterization of electrolytes and electrode materials, it is not suitable for interphase analysis, due to intrinsic limitations (**Chapter 2.4**). In contrast, near-field Raman spectroscopy variants like SHINERS are capable of realizing the detection of nanometric thin interphases, providing great signal enhancement and an increased surface sensitivity.[30,33–35] As SHINERS is a fairly new technique, studies employing SHINERS for interphase characterization are still scarce and unsystematic. In addition, reported studies were only focused on the anode side so far.[30,32,160,161]

The main objective of this chapter is the successful implementation of SHINERS into an already established LIB system, proving the practicability of SHINERS and the developed experimental set-up, to allow systematic interphase investigation and to understand the formation of an additive-induced interphase. Literature known thiophene (THP) as CEI-forming electrolyte additive was chosen as a model system.[24,28,29,79–82] Employing *operando* SHINERS, it was possible to capture the polymerization of the THP additive on the surface of a NMC111 cathode, highlighting the ability of SHINERS for dynamic interphase investigation. In addition, it was possible to elucidate the THP polymerization mechanism, based on the results of the performed *operando* SHINERS investigation, correlating to the results of the accompanying electrochemical characterization.

5.2. Electrochemical Investigation of THP-Containing LIBs

Galvanostatic charge/discharge cycling experiments were performed in 2032-type high-voltage NMC111||graphite coin cells, to determine the effect of THP as electrolyte additive on the electrochemical performance. The key data are summarized in **Table 3**, and discussed in detail in the following.

Based on the use of BE 1 (1 $_M$ $LiPF_6$ in EC:DEC 1:1 by weight), different electrolyte formulations with varying THP concentrations ranging from 0.01 $_M$ to 0.12 $_M$ were prepared. Initial charge/discharge cycling experiments of all prepared electrolyte formulations showed a distinct influence of the additive concentration on the performance and cycle life of the cell. As displayed in **Figure A11a**, concentration of 0.10 $_M$ THP was identified as optimum, showing an improvement of the electrochemical performance, compared to the cells cycled in the presence of BE 1 (**Figure 9a**), as well as the electrolyte formulations containing other THP concentrations. While the BE 1 cells exhibited a notably higher discharge capacity at the first cycle after formation (≈150 mAh g^{-1}), they suffered from a severe capacity fading, known for NMC cathodes at high operational voltages, reaching 82% state-of-health (SoH) after ≈100 cycles (**Figure 9b**). In contrast, cells with an optimized concentration of THP exhibited lower discharge capacities (≈139 mAh g^{-1}), but decreased capacity fading, remaining at a SoH of 94% after 100 cycles, and reaching 90% SoH after 210 cycles (**Figure A12**).

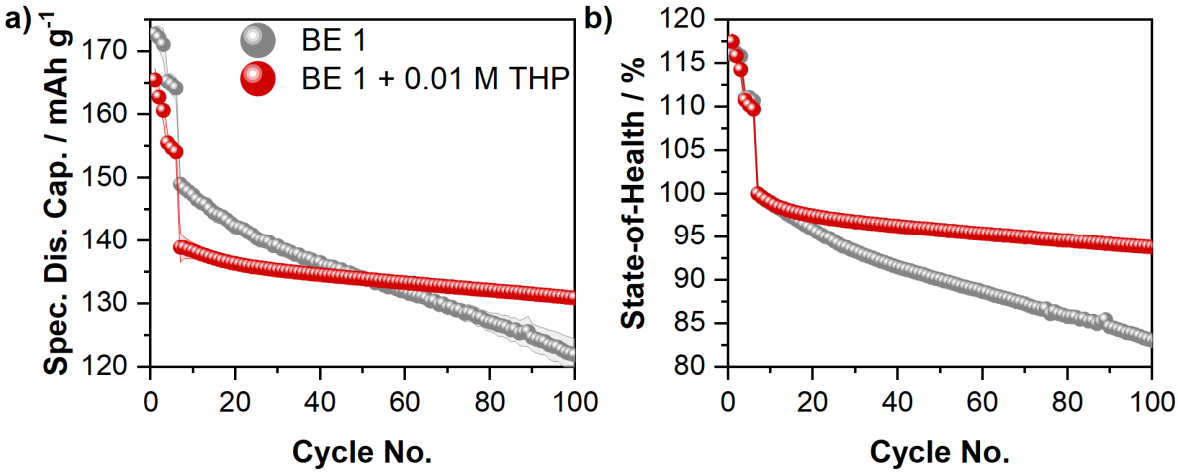

Figure 9: **a)** Specific discharge capacities (Spec. Dis. Cap.) obtained from galvanostatic charge/discharge cycling at a C-rate of 1 C in a voltage range of 2.80 V – 4.50 V of NMC111||graphite coin cells, cycled in the presence of the BE 1 (1 $_{M}$ $LiPF_6$ in EC:DEC 1:1 by weight; **grey**) and the BE 1 + 0.10 $_{M}$ thiophene (THP, **red**). Cell formation was performed by 3 charge/discharge cycles at a C-rate of C/10, followed by 3 charge/discharge cycles at a C-rate of C/3. Graph redrawn from [28]. **b)** State-of-health of the NMC111||graphite coin cells. Note that the state-of-health is calculated based on the 7th cycle, being the first one performed at a C-rate of 1 C.

In addition, Coulombic efficiencies (CEs) of the cells cycled with the THP-containing electrolyte formulations were notably lower, reaching a CE of 71% compared to a CE of 84% for the BE 1 cells in the first formation cycle (**Figure 10a**). The decreased CE was attributed to additional charge consumption in the presence of THP, indicating additive degradation. During the following formation cycles, THP-containing cells still exhibit lower CEs, however, CE values were more similar to the baseline cells (95% *vs.* 97%). Nevertheless, for higher cycle numbers (> 10 cycles) THP-containing cells showed higher CEs of 99.8% compared to 99.6% reached for the BE 1 cells, suggesting decreased parasitic reactions in the presence of THP.

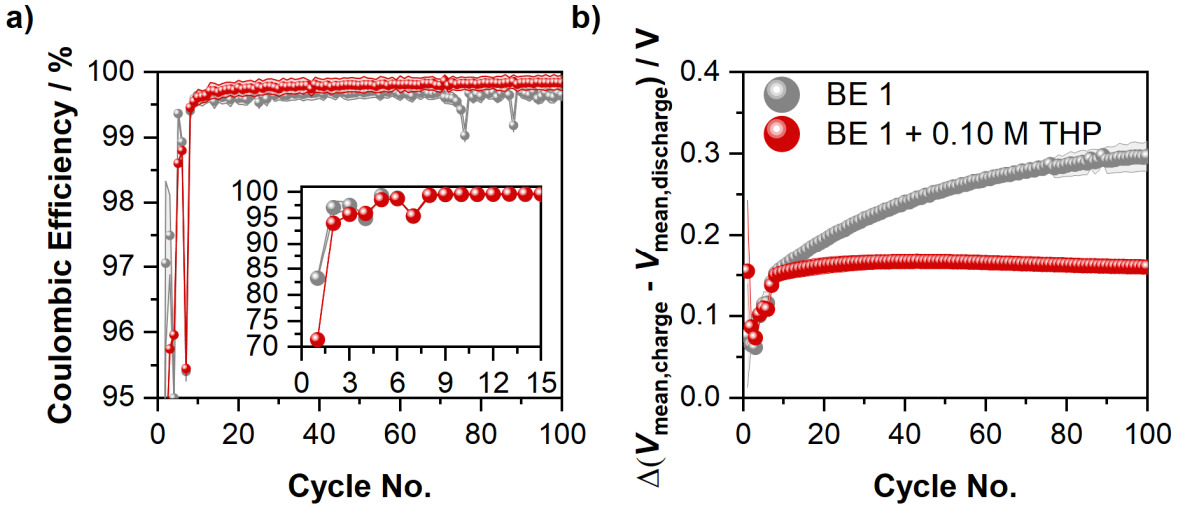

Figure 10: **a)** Coulombic efficiencies calculated for NMC111||graphite coin cells galvanostatically charge/discharge cycled at a C-rate of 1 C in a voltage range of 2.80 V – 4.50 V of, cycled in the presence of the BE 1 (1 $_{M}$ $LiPF_6$ in EC:DEC 1:1 by weight; **grey**) and the BE 1 + 0.10 $_{M}$ thiophene (THP, **red**). **b)** Differential voltage (ΔV) analysis of the NMC111||graphite coin cells, cycled in the presence of BE 1 and BE 1 + 0.10 $_{M}$ THP. Note that the displayed ΔV value corresponds to the difference between the mean charge and the mean discharge voltage. Figure adapted from [28].

The data obtained during the galvanostatic charge/discharge cycling was further evaluated *via* differential voltage (Δ*V*) analysis. Here Δ*V* equals the difference between the mean charge and the mean discharge voltage, providing a robust tool to determine the cell's internal resistance. During formation, cells containing the BE 1 and the BE 1 + 0.10 $_M$ THP exhibited similar Δ*V* values (**Figure 10b**). Only in the first formation cycle THP cells showed an increased Δ*V* value of 150 mV, compared to 60 mV calculated for the baseline cells. During continuous charge/discharge cycling however, a contrary behavior was observed. Here the Δ*V* value of the THP-containing cells remained almost constant, increasing from 138 mV at the first cycle after formation to a value of 160 mV at the 100th cycle. In contrast, for the BE 1 cells, a notable increase from 141 mV to 297 mV was recorded. This severe increase in the internal resistance was attributed to uncontrolled interphase formation, caused by ongoing electrolyte decomposition, while the presence of THP seems to mitigate this effect. The results of the Δ*V* analysis was further supported by EIS experiments (see **Figure A13**) confirming the observed trend of a notably reduced growth of the internal resistance in the presence of THP.

Table 3: Key data of the galvanostatic charge/discharge investigation of NMC111||graphite coin-cells, cycled in the presence of BE 1 (1 $_M$ $LiPF_6$ in EC:DEC 1:1 by weight) and BE 1 + 0.10 $_M$ THP. Shown are the discharge capacity, the state-of-health (SoH), Coulombic efficiency (CE), and *ΔV* at selected cycles numbers. Note that the 7th cycle equals the first cycle after formation.

Electrolyte	Capacity 7th Cycle	SoH 100th Cycle	CE 1st Cycle	CE 10th Cycle	Δ*V* 1st Cycle	Δ*V* 7th Cycle	Δ*V* 100th Cycle
BE 1	150 mAh g^{-1}	82%	84%	99.6%	60 mV	141 mV	297 mV
BE 1 + 0.10 $_M$ THP	139 mAh g^{-1}	94%	71%	99.8%	150 mV	138 mV	160 mV

The results of the galvanostatic cycling experiments clearly indicate the formation of an additive-derived interphase in the presence of THP. THP-derived interphase formation accounted for the lower initial discharge capacity in the THP-containing cells, due to increased electrode resistance and additional charge consumption. However, effective interphase formation also accounted for the reduced capacity fading, by suppressing electrode and electrolyte degradation, indicated by the higher CEs and constant Δ*V* values during ongoing charge/discharge cycling. This conclusion can also be correlated directly to the observed trends during the galvanostatic cycling of cells containing the BE 1 + different THP concentrations. As shown in **Figure A11**, low cycling performances were observed for low THP concentrations, high performances for medium THP concentrations, and a low

performance for high THP concentrations, further strengthening the assumption of the formation of a THP-derived interphase. The addition of low THP concentrations resulted in the formation of an insufficient interphase, ineffective in suppressing electrolyte decomposition and thus mitigating capacity fading. On the contrary, the addition of a high THP concentration resulted in aggravated interphase formation, severely increasing the internal resistance and thus lowering the cycling performance. Only for an optimized THP concentration, an effective compromise between additional resistance and degradation protection was achieved, resulting in enhanced electrochemical performance.

As galvanostatic charge/discharge cycling experiments indicate the formation of a THP-derived interphase, additional investigations were performed to further characterize this particular interphase and to gain insights into its formation. The CVs obtained from NMC111||graphite Swagelok® cells in the presence of BE 1 and BE 1 + 0.10 $_{M}$ THP exhibit notable differences (**Figure 11**) for the employed electrolyte formulations.

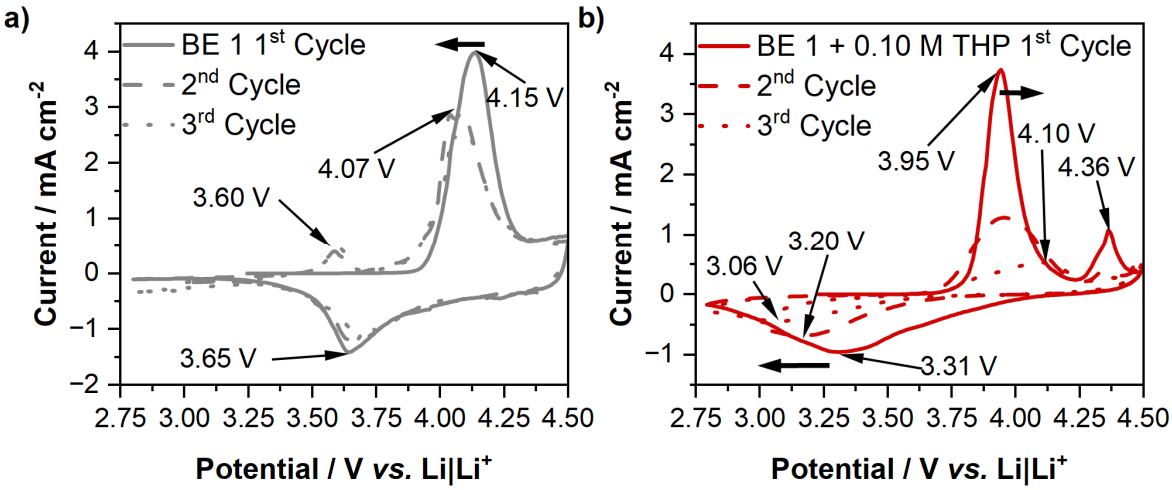

Figure 11: Cyclic voltammograms of NMC111||graphite T-type Swagelok® cells with Li-metal reference electrodes obtained in the presence of **a)** BE 1 (1 $_{M}$ $LiPF_6$ in EC:DEC 1:1 by weight; **grey**) and **b)** BE 1 + 0.10 $_{M}$ THP (**red**). Cyclic voltammetry was performed in a potential range of 2.80 V – 4.50 V *vs.* $Li|Li^+$ with a scan rate of 150 µV s^{-1}. In total 3 charge/discharge cycles were performed marked by full, dashed, and dotted lines in the depicted voltammograms. Important peaks, discussed in the main text, are highlighted by arrows and the peak potential is noted. Distinct peak shifts are highlighted by bold arrows. Figure adapted from [28].

For BE 1, the first CV cycle showed only peaks assigned to Li-ion extraction from the NMC material in the anodic part, and the subsequent re-insertion of Li-ions in the cathodic part at 4.15 V *vs.* $Li|Li^+$ and 3.65 V *vs.* $Li|Li^+$, respectively. In the second and third CV cycle the anodic peak was slightly shift to a lower potential of 4.07 V *vs.* $Li|Li^+$. Furthermore, peak intensity slightly decreased, while the corresponding peak on the cathodic side did not show distinct differences compared to the first cycle. In addition, a new peak was observed in the anodic scan for the second and third cycle at 3.60 V *vs.* $Li|Li^+$. As no additional peak was observed on the cathodic side, and the peak on the anodic side only appeared after the first complete cycle, it might be attributed to the oxidation of electrolyte decomposition products,

migrated from the graphite anode in a sort of cross-talk phenomenon. Similar, for the THP-containing cell peaks attributed to the extraction and re-insertion of Li-ions were observed for the first cycle, however, at slightly shifted potentials of 3.95 V *vs.* Li|Li$^+$ and 3.31 V *vs.* Li|Li$^+$. Moreover, an additional distinct peak was observed in the presence of THP at 4.35 V *vs.* Li|Li$^+$. Within the second CV cycle, notable differences were observed. While the potentials of the peaks on the anodic side remained, peak intensity severely decreased. On the cathodic side, the Li-ion re-insertion peak intensity decreased and shifted to 3.20 V *vs.* Li|Li$^+$. The third cycle exhibited further decreasing peak intensities and broadening of the peaks ascribed to Li-ion reactions. In addition, peak positions shifted to 4.10 *vs.* Li|Li$^+$ and 3.06 V *vs.* Li|Li$^+$. CV results further strengthen the assumption of THP-induced interphase formation, mainly through the additional peak at 4.36 V *vs.* Li|Li$^+$, which can be attributed to oxidation of the THP additive. In addition, peak broadening, severe loss of peak intensity and increasing peak to peak separation (BE 1: 500 mV → 450 mV; BE 1 + 0.10 $_M$ THP: 650 mV → 750 mV → 1000 mV), further indicated interphase formation in the presence of THP. All of these effects were attributed to the presence of a THP-derived interphase, interfering with Li-ion diffusion. These findings are in good agreement with the results of the galvanostatic cycling experiments, also indicating interphase formation in the presence of THP.

Moreover, CV analysis reveals that formation of the THP-derived interphase occurs especially during the first cycle, as the intensity of the peak, attributed to THP oxidation, notably decreases in the subsequent cycles. A similar trend was also demonstrated by d*Q*/d*V vs*. voltage analysis (**Figure A14**). For the THP-containing electrolyte, the d*Q*/d*V vs*. voltage plot exhibited a prominent peak at a voltage of 4.35 V in the first cycle, corresponding to THP oxidation, as no similar peak was observed for the BE 1 cell. For the second cycle d*Q*/d*V vs*. voltage this peak vanished, being in good agreement with the discussed CVs. These findings were further supported by the voltage – capacity histograms, shown in **Figure A15b**. For the first cycle BE 1 + 0.10 $_M$ THP histogram, a distinct plateau starting at a cell voltage of 4.32 V was observed, being in good agreement with the THP-oxidation peak observed in the CV. In addition, the first cycle THP histogram exhibits a large voltage hysteresis outlining charge consumption, caused by additive oxidation. In the second cycle histogram, the observed plateau, as well as the voltage hysteresis, are notably shorter, indicating that the majority of THP is oxidized within the first cycle. Note that for the baseline histogram no additional plateau was observed. The voltage – capacity histograms of the 50th cycle further highlight the effect of the presence of THP on the electrochemical performance of the cells, exhibiting a notably lower voltage hysteresis, compared to the BE 1 cells, indicating reduced parasitic reactions and overvoltages, probably caused by formation of an effective interphase.

5.3. Surface Investigations by SEM and EDX

To further confirm the formation of an interphase in the presence of THP, the surface of NMC111 cathodes, taken from cells cycled in the presence of the THP-containing electrolyte was investigated *via* SEM. In addition, SEM images were obtained from pristine electrodes and electrodes taken from BE 1 cells, to fully capture the effect of THP. As shown in **Figure 12**, notable differences were observed for the sampled electrode surfaces.

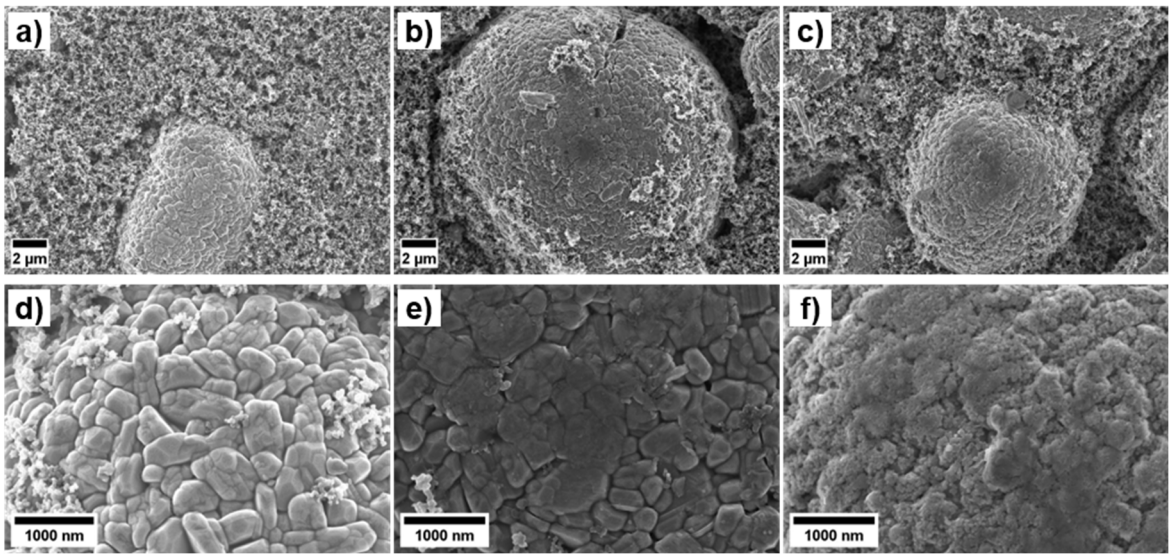

Figure 12: SEM images obtained from the surface of different NMC111 cathodes. **a)** and **d)** display SEM images of a pristine electrode. **b)** and **e)** show the SEM images of an electrode electrochemically aged in the presence of BE 1 (1 $_M$ $LiPF_6$ in EC:DEC 1:1 by weight), while **c)** and **f)** depict the surface of an electrode electrochemically aged in the presence of BE 1 + 0.10 M THP. Figure adapted from [28].

The comparison of the SEM images obtained from the BE 1 cathode with the pristine electrode, shows a distinct influence of the galvanostatic charge/discharge cycling on the electrode surface. For the BE 1 electrode, first signs of particle cracking were already observed. Furthermore, the formation of a non-uniform, discreet, mostly transparent interphase was observed, covering only small patches of the active material. In contrast, the electrodes taken from a THP-containing cell clearly show the distinct formation of a bulky, cauliflower-like interphase, covering the entirety of the active material. Additional EDX measurements of the same electrode samples exhibited the presence of sulfur on the whole electrode sample (**Figure A16**). However, a particular concentration of sulfur was found on the active material particles, which already showed prominent interphase formation in the aforementioned SEM image. In combination with the results of the electrochemical investigation, the performed surface characterization demonstrated increased CEI formation in the presence of THP, accounting for the enhanced cycling performance. In addition, these results further substantiate that the formed interphase is derived from the THP additive.

5.4. Interphase Characterization *via Operando* SHINERS

While the previous investigations clearly show the formation of a THP-derived CEI, an analysis of the composition of the formed interphase and the underlying formation processes is still missing, crucial to deeply understand interphase formation mechanisms. To unravel these remaining questions, *operando* SHINERS measurements were performed in a NMC111||graphite cell in the presence of BE 1 and BE 1 + 0.10 $_M$ THP, using the "sandwich"-configuration, where both electrodes face the window of the optical cell (**Chapter 4.2.8**).

As expected from SEM investigation, SHINERS measurements performed on the surface of the NMC111 electrode do not capture prominent interphase formation, showing almost no additional bands upon increasing cell voltage (**Figure A17**). Prominent bands captured in the BE 1 spectrum at a voltage of 4.50 V mostly correspond to the electrode active material. In particular, the band around 557 cm^{-1} corresponds to Ni-O lattice vibrations of the NMC material, while the dominant bands around 1355 cm^{-1} and 1574 cm^{-1} can be assigned to the D and G-band of the graphitic conductive agent.[28] Only the band around 846 cm^{-1} can be attributed to interphase formation, only observed at high voltages. This band can be ascribed to C-H deformation vibrations, indicating the presence PEO-type or semi-carbonate species,[28,32] formed from BE decomposition products.

In contrast, the spectra obtained in the presence of an optimized concentration of THP exhibit distinct additional bands at a cell voltage of 4.50 V, ascribed to interphase formation (**Figure A18**). Similar to the BE 1 spectra, the spectrum recorded at the open circuit voltage (OCV) is dominated by bands corresponding to the NMC active material around 600 cm^{-1}, and the graphitic conductive agent around 1347 cm^{-1} and 1580 cm^{-1}. While the graphitic bands remain in the spectrum recorded at 4.50 V, the NMC-ascribed band diminished. Instead, a band around 559 cm^{-1} arises, which can be attributed to NMC lattice vibrations as well. This change can be attributed to phase transition processes within the NMC material during delithiation. In addition, several new bands were observed, which are directly ascribed to interphase formation. Bands between 644 cm^{-1} and 737 cm^{-1} correspond to C-C and C-S-C ring deformation vibrations, while the band around 846 cm^{-1} band is attributed to C-H deformation vibrations. The band around 1086 cm^{-1} can be ascribed to C-C stretching or C-H wagging vibrations. Furthermore, bands around 1174 cm^{-1} and 1232 cm^{-1} correspond to anti and regular C-C stretching vibrations. The bands around 1432 cm^{-1} and 1495 cm^{-1}, dominating the spectrum, is assigned to the regular and anti C=C stretching vibrations of aromatic molecules. A comparison of the BE 1 spectrum and the BE 1 + 0.10 $_M$ THP spectrum, taken at the voltage of 4.50 V clearly outlines that most of the newly arising peaks can be directly attributed to the THP additive (**Figure 13**).[28]

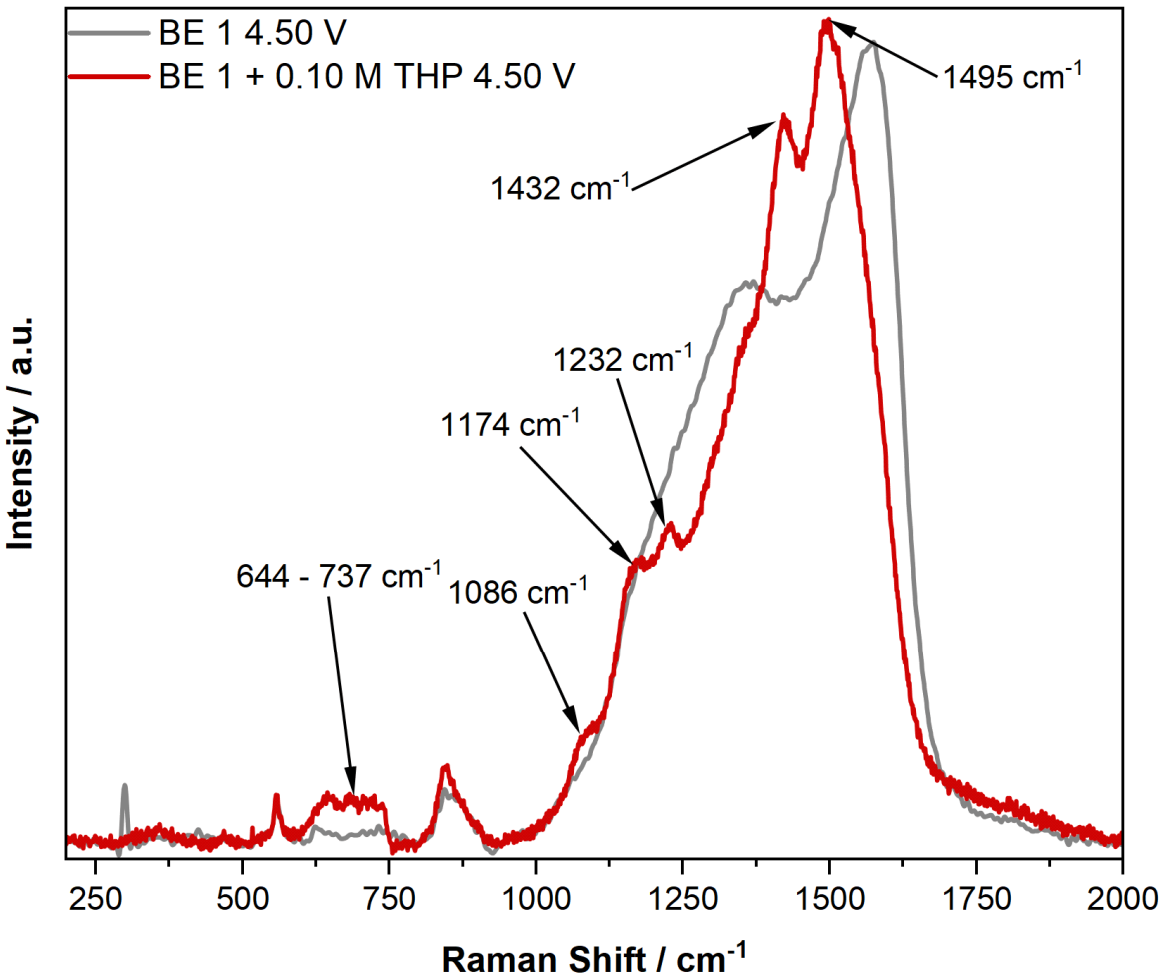

Figure 13: *Operando* SHINER spectra taken from the surface of an NMC111 electrode in the presence of BE 1 (1 M $LiPF_6$ in EC:DEC 1:1 by weight; **grey**) and BE 1 + 0.10 M THP (**red**). For the SHINERS measurement the NMC electrode was connected as working electrode, paired against a graphite counter electrode. Galvanostatic charging was performed at a C-rate of C/3. Au SHINs with a diameter of 55 nm were introduced to the electrode surface before the cell assembly. Spectra were recorded at the cut-off voltage of 4.50 V. For spectrum acquisition the samples were excited using a 633 nm laser, adjusted to a power output of 1.05 mW. Spectra were acquired over two accumulations of 50 s. Important, newly arising bands observed in the spectra are highlighted by arrows. In addition, band positions are noted. Figure adapted from [28].

Especially the bands around the area of 644 cm^{-1} and 737 cm^{-1}, as well as the bands around 1432 cm^{-1} and 1495 cm^{-1} are characteristic for polythiophene, as shown in the literature.[182–184] Therefore, the performed *operando* SHINERS investigations has proven the formation of a THP-derived CEI on the surface of the NMC111 cathode, as already indicated by electrochemical and surface investigations prior. In addition, based on the band intensities, the SHINER spectra suggest that the formed CEI is mostly comprised of polythiophene. However, the SHINER spectra also imply the formation of a co-polymer formed by EC and THP, indicated by the band around 1174 cm^{-1}. While being ascribed to C-C stretching vibrations, this band could be matching to polythiophene. Nevertheless, this band could also be ascribed to the decomposition products of carbonate-based solvents, as shown in other studies.[32]

5.5. Mechanistic Investigation of CEI Formation *via Operando* SHINERS and Quantum Chemistry Calculations

As described in the previous segment, *operando* SHINERS investigations finally revealed the formation of a THP-derived CEI, comprising mostly of polythiophene. However, questions regarding the interphase formation mechanism and the suggested formation of a co-polymer still remained. In a first step, an additional *operando* SHINERS experiment was conducted, using Li-metal as CE. Note that due to the low scan rate the Li-metal electrode functions also as a (*quasi*-)RE. This enables a precise monitoring of the cathode potential, capturing the potential-depended interphase formation.

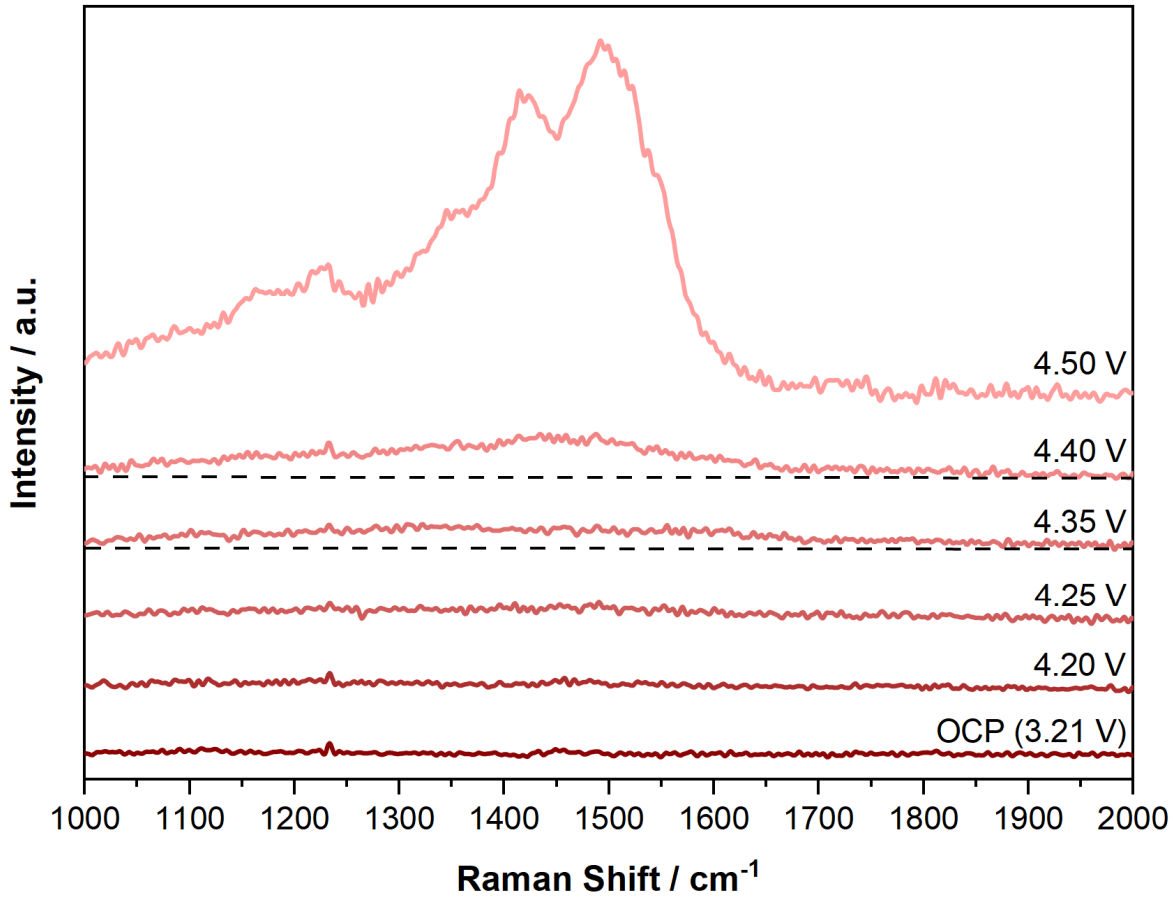

Figure 14: *Operando* SHINER spectra taken from the surface of an NMC111 electrode in the presence of BE 1 (1 M $LiPF_6$ in EC:DEC 1:1 by weight) + 0.10 M THP. For the SHINERS measurement the NMC electrode was connected as working electrode, paired against a Li-metal counter electrode. Potentiostatic polarization of the cathode was performed at a scan rate of 150 µV s^{-1}. Au SHINs with a diameter of 55 nm were introduced to the electrode surface before the cell assembly. For spectrum acquisition the samples were excited using a 633 nm laser, adjusted to a power output of 1.05 mW. Spectra were acquired over two accumulations of 50 s. Spectra were recorded at different potentials, marked in the depicted spectra referenced against $Li|Li^+$. In addition, dashed lines represent the respective spectra background to highlight changes in the background intensity. Figure adapted from [28].

As shown in **Figure 14**, first signs of interphase formation start at a potential of 4.35 V *vs.* $Li|Li^+$, demonstrated by an increase in the background intensity in the area between 1300 cm^{-1} and 1600 cm^{-1}. Background intensity further increased with increasing cathode

potential (4.40 V *vs.* Li|Li$^+$), indicating continuous CEI formation. At the cut-off potential of 4.50 V *vs.* Li|Li$^+$, the obtained spectra exhibit the same bands, as observed within the initial SHINERS experiment, ascribed to the formation of the polythiophene-based CEI. These findings are in good agreement with the results of the performed electrochemical investigations, also suggesting THP oxidation around 4.35 V *vs.* Li|Li$^+$.

Additionally, QC calculations for the assumed oxidative polymerization of THP were performed to gain fundamental insights into the interphase formation mechanisms. The proposed polymerization mechanism is depicted in **Figure 15** below.

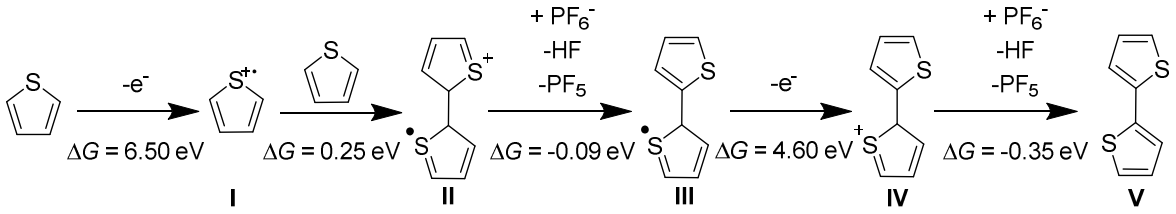

Figure 15: Proposed reaction mechanism for the oxidative electro-polymerization of thiophene. Calculated differences in free energy (Δ*G*, computed at 298 K) are given for every reaction step in electron volts (eV). Figure adapted from [28].

In the first step (**I**), a THP molecule is oxidized, forming a radical. For this step a free energy difference of Δ*G* = 6.50 eV was calculated. Note that this value is equivalent to a potential *vs.* Li|Li$^+$ given in volts, as only one electron is transferred per elementary reaction. Moreover, this potential corresponds to a value of 5.10 V *vs.* Li|Li$^+$, which is notably lower, compared to the oxidation potential of single EC molecules, calculated at 5.70 V *vs.* Li|Li$^+$. This is in good agreement with the observations of the other experiments performed within this study, outlining THP oxidation prior to BE 1 oxidation. In the second step (**II**), the formed radical may encounter a second THP molecule, forming a radical dimer cation. Dimerization corresponds to a free energy difference of Δ*G* = 0.25 eV. The dimer cation is further stabilized through deprotonation, *e.g.* by an PF_6^- anion (**III**), resulting in a slight free energy gain of Δ*G* = -0.09 eV. After deprotonation, the radical dimer is further oxidized (**IV**). In comparison to the initial THP oxidation, a notably lower free energy difference of Δ*G* = 4.60 eV was calculated, corresponding to 3.20 V *vs.* Li|Li$^+$, for the oxidation of the THP-dimer. Similar to (**III**), the obtained closed-shell dimer cation is further stabilized *via* deprotonation (**V**). For this step a distinct gain in free energy of Δ*G* = -0.35 eV was calculated. The total free energy difference for the whole polymerization reaction was calculated to a value of Δ*G* = 10.90 eV. This equals a value of Δ*G* = 5.45 eV per elementary step (note that two electrons were transferred in total), corresponding to a potential of 4.05 V *vs.* Li|Li$^+$. In respect to the assumptions and simplifications given for the conducted calculations, the QC results are in good agreement with the polymerization potential, experimentally determined *via operando* SHINERS and CV. In addition, the QC calculations

highlight that subsequent oxidations of polythiophene occur at a relatively low potential, indicating a cascade-like polymerization of the THP additive, after initial dimerization. This matches SHINERS findings, showing a severe increase in interphase formation after initial interphase nucleation.

Besides THP polymerization, the possibility of a copolymer formation of EC and THP was investigated *via* QC calculations. The proposed reaction mechanism is depicted in **Figure A19**. Similar to THP polymerization, the first reaction step contains oxidation of an EC molecule, forming a radical cation, which is subsequently deprotonated, *e.g.* by a PF_6^- anion. For this step a potential of 5.70 V *vs.* Li|Li^+ was calculated. In the next step, the formed EC radical encounters a THP molecule. For the dimerization transition state an energy barrier of $\Delta G^‡$ = 0.56 eV was calculated. Final dimerization is accompanied by a gain in free energy of ΔG = -0.59 eV. In general, the QC calculations show that the formation of the EC and THP co-polymer is thermodynamically possible. Nevertheless, the high initial oxidation potential of EC renders THP polymerization more favorable. Due to the high surplus of EC in the electrolyte however, co-polymerization is still plausible. These findings are in good agreement with the *operando* SHINERS investigations, showing the EC-THP copolymer as a minor interphase component, indicated by the band around 1174 cm^{-1}.

Besides QC calculations of THP polymerization and EC-THP co-polymerization, additional investigations were conducted to shine light on the polymerization of EC. Here two different mechanisms, a radical and an anionic reaction, were considered **Figure A20**. For the radical pathway, formation of an EC radical *via* oxidation and deprotonation was suggested for the first reaction step, giving a potential of 5.70 V *vs.* Li|Li^+. For the subsequent encounter with another EC molecule an energy barrier of $\Delta G^‡$ = 1.58 eV was calculated. For the following polycarbonate formation, only a minor energy gain of ΔG = -0.02 eV was calculated, rendering the radical EC polymerization thermodynamically unlikely. For the anionic mechanism, a nucleophilic attack of a F^- anion at a single EC molecule is assumed in the first step, giving a calculated energy barrier of $\Delta G^‡$ = 0.78 eV. Following the F^- attack, EC undergoes a ring opening process, leading to the formation of a linear carbonate with a negatively charged carbonate group, giving a stabilizing energy gain of ΔG = -0.10 eV. Subsequently, the formed carbonate anion can further react with other EC molecules *via* nucleophilic attacks, starting polycarbonate formation. While the QC calculations clearly show that polythiophene formation is thermodynamically favored, EC polymerization *via* the anionic mechanism is realistic, due to the high surplus of EC molecules in the electrolyte. Furthermore, as the initiating F^- anion is a side-product of THP polymerization, it could be concluded that EC polymerization could occur around the same cathode potential of

4.35 V *vs.* Li|Li^+, accounting for the band observed around 846 cm^{-1} in both BE 1 and BE 1 + 0.10 $_M$ THP SHINER spectra.

5.6. Conclusion

In this chapter, THP was employed as CEI-forming electrolyte for high-voltage LIBs. Through electrochemical investigations, the effect of an optimized THP concentration in the electrolyte formulation was characterized. The results showed a distinct improvement of the galvanostatic charge/discharge cycling performance in the presence of THP. In addition, further investigations indicated formation of a THP-derived interphase, formed at an elevated cathode potential of 4.35 V *vs.* Li|Li^+. This suggestion was further supported by surface investigations performed by SEM, visualizing a distinct interphase formation in the presence of THP. Additional EDX measurements highlighted the THP-derivation of the formed interphase, outlining the concentration of sulfur on CEI-covered active material particles. *Operando* SHINERS investigations finally proved the formation of a THP-derived CEI, showing the distinct formation of polythiophene on the surface of the cathode. Moreover, SHINERS investigations demonstrated that polythiophene is the major component of the formed CEI. Nevertheless, additional electrolyte decomposition products, as well as the presence of a copolymer comprising of EC and THP were captured by SHINERS. Besides interphase characterization, *operando* SHINERS investigations allowed the proposal of a reaction mechanisms *via* QC calculations for the polymerization of THP, based on the observed potential-dependent interphase formation.

In addition to the investigated electrochemical performance of the THP-containing cells, as well as the characterization of the additive-derived interphase, this study served as proof-of-concept study. Using a known system, it was not only successful in implementing SHINERS into a LIB set-up, but also in monitoring and capturing the formation of an additive-derived interphase under real working conditions. Moreover, the obtained results were in good agreement with additionally performed electrochemical, surface, and QC calculation investigations, further outlining the potential of the SHINERS technique. With the presented study it was not only possible to present the first CEI investigation performed *via* SHINERS to the battery research community, but also to strongly validate the applicability of the chosen technique to achieve the objectives set for this thesis.

6. Optimization of the NMC811-Electroyte Interphase by Thiophene-derived Additives

Major segments of this chapter have been published in:

Pfeiffer, F., Diddens, D., Weiling, M., Frankenstein, L., Kühn, S., Cekic-Laskovic, I. and Baghernejad, M.; Quadrupled Cycle Life of High-Voltage Nickel-Rich Cathodes: Understanding the Effective Thiophene-Boronic Acid-Based CEI *via operando* SHINERS. Adv. Energy Mater., **2023**, 13, 2300827.

and are reproduced or adapted with permission from [29].

6.1. Introduction

The main objective of the previous **Chapter 5** was to successfully demonstrate the implementation of *operando* SHINERS for the dynamic investigation of evolving interphases in a high-voltage LIB, the focus of this chapter will be more on the optimization of the NMC811-electrolyte interphase, further enhancing cycling performance. Whereas already shown within **Chapter 5**, the use of dedicated CEI-forming electrolyte additives, in this case THP, can notably increase the stability of the cathode, leading to reduced capacity fading and an increased cycle life. Nevertheless, the formation of a THP-derived interphase also resulted in additional internal resistances, especially during the initial cycles. The higher resistance, as well as charge consumption during additive oxidation, resulted in reduced capacities for the THP-containing cells. Through the introduction of different functional groups to the additive structure, key parameters of the additive-derived CEI shall directly be influenced, to achieve an optimized performance and a more beneficial interphase formation. Moreover, the previous study was performed on an established system, using SOTA NMC111 and graphite electrodes, the focus of this particular study will be on a more challenging cell system, employing next-generation Ni-rich NMC811 cathodes. In comparison to NMC111, which is already widely employed in commercial applications, NMC811 exhibits some distinct advantages. NMC811 cathodes offer higher specific capacities, further increasing the energy density of the respective cells.[12,29,185,186] In addition, Ni-rich NMC materials greatly benefit from reduced Co-content, rendering these materials cheaper, less toxic, and more sustainable. However, the use of NMC811 cathodes is greatly hampered by their reduced stability. Compared to NMC111, Ni-rich electrodes suffer from lower thermal stability, as well as a lower cycling stability, leading to severe safety issues and a limited cycle life.[19–21,28,29,185,187] At high-voltage conditions, Ni-rich NMC materials additionally exhibit the dissolution of TM ions into the electrolyte, caused by mechanical degradation and collapse of the material structure, irreversible phase-transitions (Jahn-Teller distortion), or HF etching. Dissolved TM ions are subsequently

deposited on the anode surface, initiating the formation of Li-dendrites, posing the risk of micro-short-circuits, and leading to a dramatic capacity loss, also known as “roll-over failure” in the literature.[20,21,29,159,187] In addition, the cell-format employed in this study will be changed from coin cell to pouch cells, contributing to an increased commercial relevance of this particular study, due to a more realistic cell format and electrolyte to electrode ratio.

Besides interphase optimization, the now established and optimized *operando* SHINERS technique will be employed to characterize the interphase-derived from promising additive candidates, identified during galvanostatic cycling experiments. Thereby, unraveling interphase composition, and shedding light on interphase formation mechanisms and the effect of introduced functional groups on interphase formation and properties, as well as electrochemical performance.

6.2. Optimizing the NMC811-Electrolyte Interphase

6.2.1. Identification of Promising Electrolyte Additive Candidates

Different thiophene-based molecules, featuring a variety of selected functional groups, were introduced within this study to optimize the NMC811-electrolyte interphase. The idea behind the introduction of these functional groups is to directly influence either the formation or key properties of the interphase. For example, the addition of electron withdrawing groups reduces the oxidation potential of the thiophene motif, easing the oxidative polymerization of the additive, while acidic or hydroxyl groups may be present in an anionic form in the additive-derived interphase, influencing Li-transport processes. An overview of the additive molecules investigated within this thesis is depicted in **Figure 16** below.

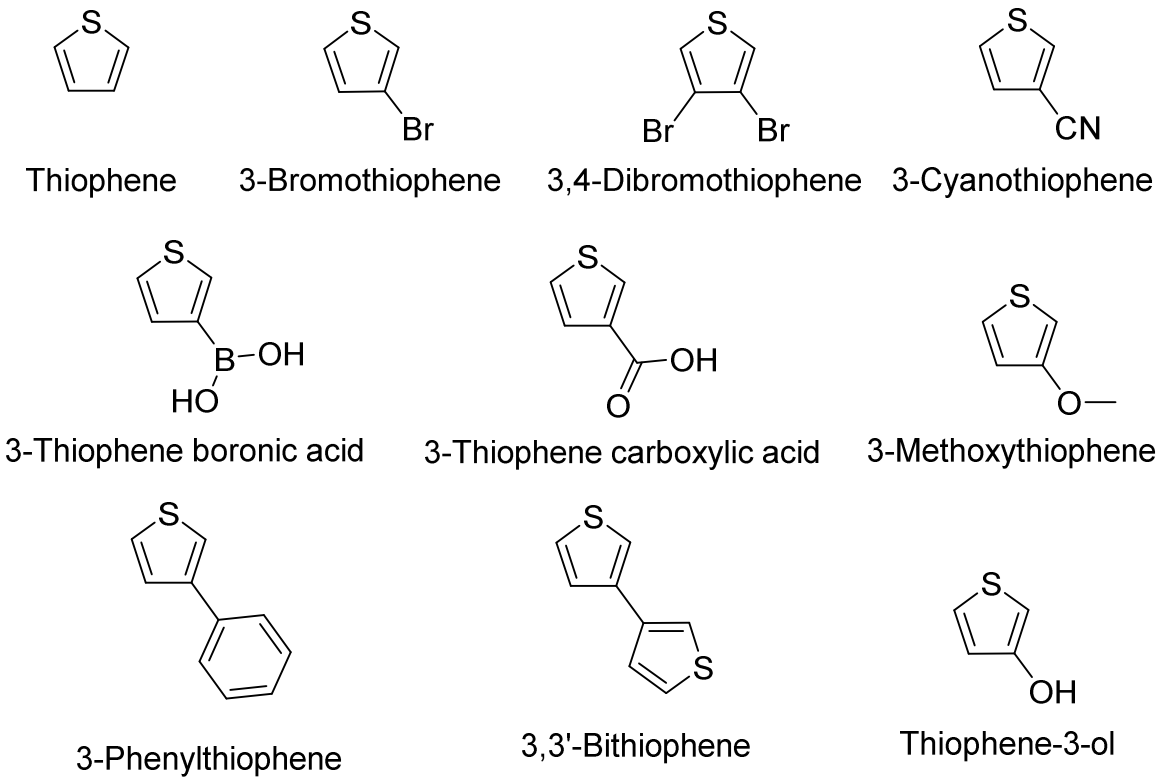

Figure 16: Overview of the thiophene derivatives investigated within this study as CEI-forming electrolyte additives. Given are the molecular structure, as well as the name of the respective molecules. Supplier and purity of the employed additives are noted in **Chapter 4.1**.

All of the molecules depicted in **Figure 16** were employed in galvanostatic charge/discharge cycling experiments, showing a distinct influence on the electrochemical performance compared to the BE 2-containing cells (**Figure 17** and **Figure A21**). For preliminary identification of promising candidates, two additive concentrations (0.04 $_{M}$ and 0.12 $_{M}$) were selected, based upon the results of the previous study with a THP-containing electrolyte in NMC111||graphite coin cells (**Figure A11**). Note that these concentrations are not representing the optimized additive concentration. Instead, they resemble the slightly exceeded upper and lower border of additive concentration, which yielded a positive effect on the cells cycling performance. Employing this matrix highlights trends in the additives influence on the cell, while limiting spent resources. Upon identification of promising candidates, concentration optimization was performed for these particular molecules. **Figure 17** depicts the specific discharge capacities of additive-containing cells exceeding the benchmark performance, while the specific discharge capacities of additive-containing cells falling short to the benchmark performance are presented in **Figure A21**.

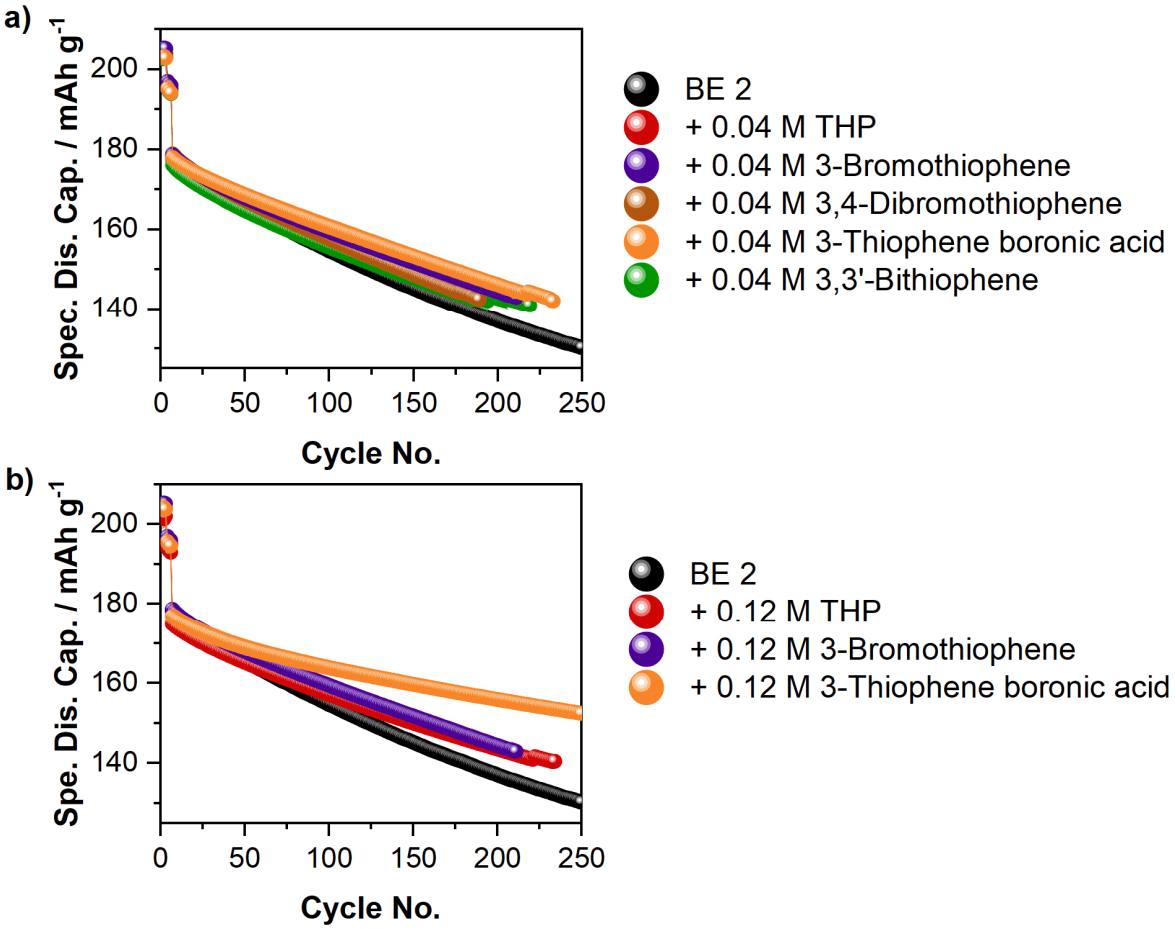

Figure 17: Specific discharge capacities (Spec. Dis. Cap.) obtained from NMC811||graphite pouch cells galvanostatically charge/discharge cycled at a C-rate of 1 C in a voltage range between 2.80 V – 4.50 V. Depicted are the discharge capacities of cells containing different thiophene-based electrolyte additives in the concentration of **a)** 0.04 $_M$ and **b)** 0.12 $_M$, in comparison to the discharge capacities obtained from the cells cycled in the presence of the BE 2 (1 $_M$ $LiPF_6$ in EC:EMC 3:7 by weight; **black**). Note that this figure only depicts the additive-containing cells exhibiting an improved electrochemical performance compared to the BE 2 cells. For the results of the other investigated electrolyte formulation the reader is kindly referred to **Figure A21**.

As shown in **Figure 17**, for the electrolyte formulations containing a 0.04 $_M$ additive concentration an improved cycling performance was recorded for thiophene, 3-bromothiophene, 3,4-dibromothiophene, 3-thiophene boronic acid, and 3,3'-bithiophene. The addition of the molecules to the BE 2 resulted in an increased cycle number until reaching 80% SoH of 25%, 26%, 11%, 38%, and 31%, respectively. The combined results of the galvanostatic cycling experiments for all prepared electrolyte formulations are summarized in **Table A1**. Interestingly, for the additive concentration of 0.12 $_M$, a beneficial effect was only observed for thiophene, 3-bromothiophene, and 3-thiophene boronic acid. Here, the additive-containing electrolyte showed an increased cycle number of 40%, 26%, and 154% until reaching 80% SoH, compared to the BE 2 cells. A detailed analysis of the results of the galvanostatic cycling experiments for all prepared electrolyte formulations is presented in **Table A2**. Concluding from the results of the preliminary testing of the additive-containing electrolyte formulations, first trends of the relation between additive structure and obtained performance can be identified. In general, improved cycling performance was only

observed for additives featuring an electron-withdrawing functional group, while the introduction of additives with an electron-donating group solely resulted in a decreased cycling performance. As a reduced electron density within the aromatic ring decreases the oxidation potential of the molecule, a facilitated oxidative electro-polymerization of the additives could be a valid explanation for the observed phenomenon.[24] This assumption is further strengthened by the fact that the 3,3'-bithiophene-containing electrolyte also exhibited an increased cycling performance. While an additional THP-group *per se* is not electron withdrawing, the QC calculations performed within the previous **Chapter 5**, clearly showed that the oxidation potential of the THP-dimer is notably lower, compared to a single THP molecule. Therefore, a similar effect was observed for the electron-withdrawing groups. However, the performed galvanostatic cycling experiments also included additive molecules that showed a decreased performance, despite the presence of an electron-withdrawing functional group. The possible reasons for this are numerous and a detailed analysis of every investigated additive would greatly exceed the scope of this thesis. Moreover, it has to be considered that no concentration optimization was performed for the additives.Nevertheless, the conducted galvanostatic cycling experiments successfully identified promising additive candidates, showing at least a moderately improved cycling performance compared to the BE 2 cells. Out of these candidates, 3-thiophene boronic acid (3-THP-BOH) clearly showed the greatest improvement and therefore, was selected for further investigations to optimize the NMC811-electrolyte interphase. First, the optimized concentration of the additive was determined, and further used for all investigations conducted within this project. As depicted in **Figure A22**, the addition of a 0.20_{M} concentration of 3-THP-BOH showed the optimum cycling performance, notably outperforming the BE 2 cells. The results of the electrochemical investigations of the cells with an optimized 3-THP-BOH concentration are shown in **Figure 18a** below.

6.2.2. Electrochemical Characterization of the Optimized NMC811-Electrolyte Interphase

In comparison to the BE 2 cells, the cells containing an optimized additive concentration exhibited a slightly lower discharge capacity of 173 mAh g^{-1} *vs.* 178 mAh g^{-1} after the formation cycles (**Figure 18a**). However, due to decreased capacity fading after 75 cycles both electrolyte systems show similar discharge capacities of 162 mAh g^{-1}. With ongoing cycling, the reduced capacity fading of the 3-THP-BOH-containing cells results in a drastically enhanced cycle life, reaching 80% SoH after 650 cycles, effectively quadrupling the cycle life of the BE 2 cells, which reached 80% SoH after 165 cycles. While the total lifetime of the BE 2 cells was limited to about 500 cycles, the additive-containing cells

surpassed 1750 continuous charge/discharge cycles, showing a specific discharge capacity of 115 mAh g^{-1} (69% SoH).

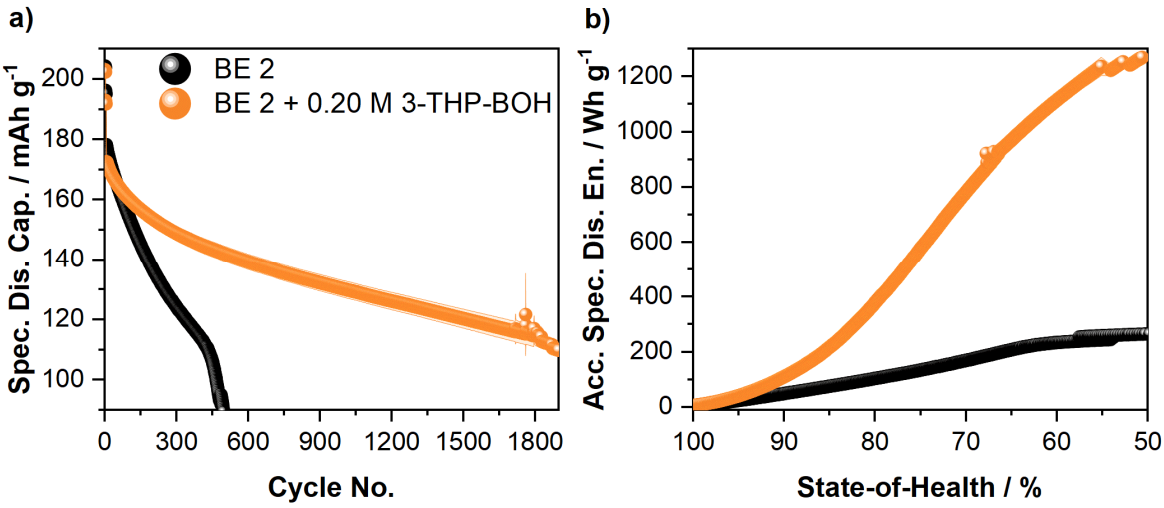

Figure 18: **a)** Specific discharge capacities (Spec. Dis. Cap.) obtained from NMC811||graphite pouch cells galvanostatically charge/discharge cycled at a C-rate of 1 C in a voltage range between 2.80 V – 4.50 V in the presence of the BE 2 (1 M $LiPF_6$ in EC:EMC 3:7 by weight; **black**) and the BE 2 + 0.20 M 3-THP-BOH (**orange**). Note that cycling was performed until reaching a state-of-health of 50%. However, cycling of the additive-containing cells was stopped at a state-of-health of 65%. **b)** Accumulated specific discharge energies (Acc. Spec. Dis. En.) obtained from NMC811||graphite pouch-cells containing the BE 2 and the BE 2 + 0.20 M 3-THP-BOH. Figure redrawn with permission from [29].

Furthermore, the addition of 3-THP-BOH proved to effectively suppress the rapid capacity fading, which was observed for the BE 2 cells after about 450 charge/discharge cycles. This rapid capacity fading can be attributed to the degradation of the cathode and the roll-over failure, caused by the dissolution of TM ions from the cathode active material, greatly limiting NMC cathode use in high-voltage applications. Additive presence also reflected on the obtained CEs during galvanostatic cycling (**Figure A23**). For the first formation cycle a CE of 85% was recorded for the additive-containing cells, notably lower compared to the BE 2 cells, showing a CE of 88% during the initial cycle. This lower CE value can be attributed to charge consumption in the presence of the additive, indicating its degradation. During further cell-formation, the CE of the BE 2- and the 3-THP-BOH-containing cells drastically increased, however, for the additive-containing cells overall lower CEs were observed. The trend was also observed for higher cycle numbers. While both investigated electrolyte formulations exhibited CEs > 99.8%, BE 2 cells slightly exceeded the additive-containing cells, indicating ongoing additive decomposition. Interestingly, for the BE 2 cells, a sharp decline of the CE was observed after 450 charge/discharge cycles, being in good agreement with the drastically decreasing discharge capacity values of the respective cells, indicating the loss of active lithium *e.g.* through lithium plating.

Additional insights into the overall electrochemical performance of the cells containing the investigated electrolyte formulations can be gained by the comparison of the accumulated

specific discharge energies (ADEs) plotted against the SoH (**Figure 18b**). This value allows for a fair comparison of the performance during galvanostatic cycling, representing not only the absolute discharge capacities, but also the rate of capacity fading. Similar to the discharge capacities, the ADEs clearly show the drastically improved performance of the additive-containing cells, reaching 380 Wh g^{-1} and 1270 Wh g^{-1} at a SoH of 80% and 50%, respectively. In contrast, BE 2 cells exhibited ADEs of 105 Wh g^{-1} and 265 Wh g^{-1}, reaching only a third and a fifth of their counterparts' values. To further set the performance of the additive-containing cells into perspective, additional galvanostatic cycling experiments were performed with cells in the presence of 0.10 $_M$ LiDFP. Due to its TM ion scavenging ability and beneficial influence on interphase formation, LiDFP is commonly used, especially in high-voltage applications.[53,187] As shown in **Figure A24**, the addition of LiDFP to the electrolyte formulation reduces capacity fading, increasing the cycle life of the respective cells by 50%. In addition, the rapid capacity fading observed towards the end of cycling is less steep, highlighting the mitigating effect of LiDFP on the roll-over failure. Nevertheless, the introduction of LiDFP is not sufficient to fully suppress the roll-over, and cycling performance is still exceeded by the 3-THP-BOH-containing cells, further outlining the additives' potential.

Further analysis of the data obtained from galvanostatic cycling experiments was conducted *via* Δ*V* analysis, giving insights into the influence of the additive on the cell's internal resistance. As shown in **Figure 19a**, the addition of 3-THP-BOH to the electrolyte results in a distinct effect on the obtained Δ*V* values. For the initial formation cycle, higher values were recorded for the 3-THP-BOH-containing cells, showing a Δ*V* value of 100 mV, compared to the 61 mV recorded for the BE 2 cells. With completed cell formation Δ*V* values increased to 194 mV and 226 mV for the BE 2 and BE 2 + 3-THP-BOH-containing cells, respectively. During continuous galvanostatic charge/discharge cycling, a steady increase of the Δ*V* value was observed for both investigated electrolyte formulations. However, the internal resistance of the BE 2 cells increased in a notably higher rate, reaching a Δ*V* value of 810 mV after 500 charge/discharge cycles, compared to the additive-containing cells remaining at a Δ*V* value of 360 mV after 500 cycles. Even after 1750 cycles, a lower Δ*V* value of 650 mV was recorded for the cells cycled in the presence of 3-THP-BOH. The observed development of the Δ*V* values are in good agreement with the expected interphase-forming behavior of the employed additive and also are in good agreement with the observed cycling performance. Due to the formation of an additive-derived interphase internal resistance of the 3-THP-BOH-containing cells is higher during the initial charge/discharge cycles, resulting in higher overvoltages. In combination with reduced CEs, the interphase formation accounts for the decreased specific discharge capacity.

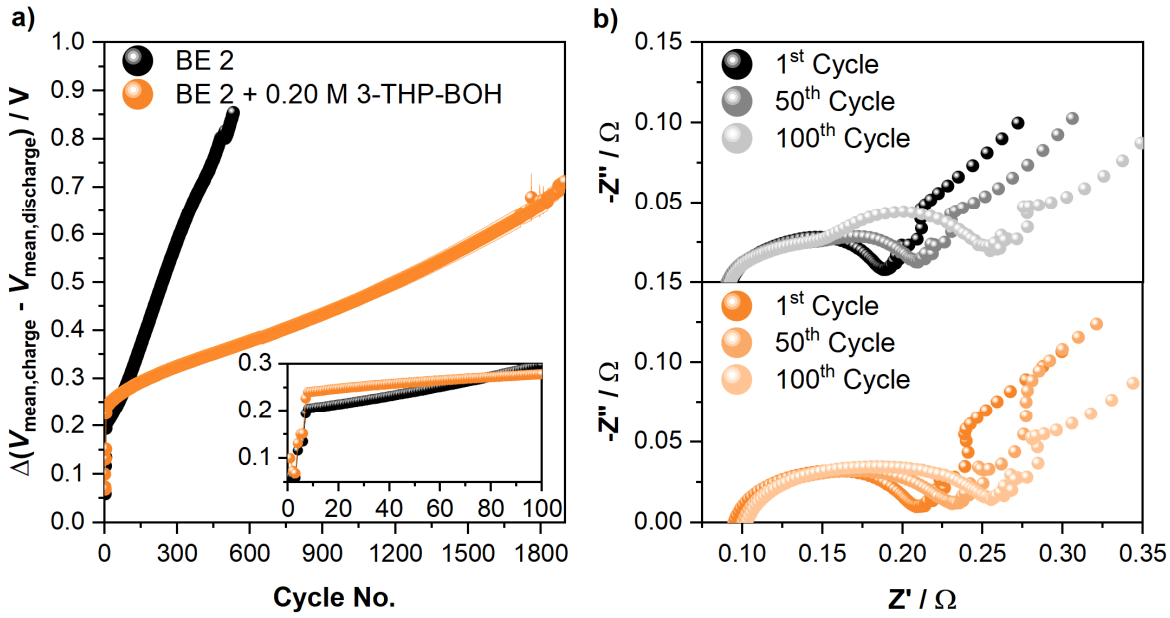

Figure 19: **a)** Differential voltage (ΔV) analysis of the NMC811||graphite pouch cells, cycled in the presence of the BE 2 (1 M $LiPF_6$ in EC:EMC 3:7 by weight; **black**) and the BE 2 + 0.20 M 3-THP-BOH (**orange**) at a C-rate of 1 C in voltage range of 2.80 V – 4.50 V. Note that the displayed ΔV value corresponds to the difference between the mean charge and the mean discharge voltage. **b)** Electrochemical impedance spectra obtained from NMC811||graphite pouch cells galvanostatically cycled in the presence of the BE 2 and the BE 2 + 0.20 M 3-THP-BOH in a voltage range of 2.80 V – 4.50 V at a C-rate of C/2. Impedance spectra were recorded during every charge cycle at 50% state-of-charge for the 1st, the 50th and the 100th cycle. Figure redrawn with permission from [29].

During continuous cycling, beneficial effects, *e.g.* suppressed electrolyte decomposition or electrode degradation of the additive-derived interphase prevail, result in a reduced growth of the cell's internal resistance. This results in a turnover point after 75 cycles, where ΔV values of the 3-THP-BOH containing cells match the ΔV values of the BE 2 cells, and fall drastically short for higher cycle numbers. This trend can also be observed within the galvanostatic cycling performance. Additional investigations of the internal resistance of the cells containing both BE 2 and BE 2 + 0.20 M 3-THP-BOH were conducted *via* EIS, depicted in **Figure 19b**. The obtained results show a higher internal resistance for the additive-containing cells for the 1st and 50th cycle, while a similar resistance was observed for the 100th cycle, being in good agreement with the trends observed for the ΔV analysis.

Similar to the galvanostatic cycling experiments conducted with THP in the previous chapter, the presence of 3-THP-BOH shows a distinct beneficial influence on the electrochemical performance of the respective cells, most likely due to the formation of an additive-derived interphase. To further characterize this interphase and to gain first insights into its formation mechanism, additional analysis of the cycling data was performed. **Figure 20a** depicts the corresponding results of the dQ/dV *vs.* voltage analysis, performed for the first charge/discharge cycle of both investigated electrolyte formulations.

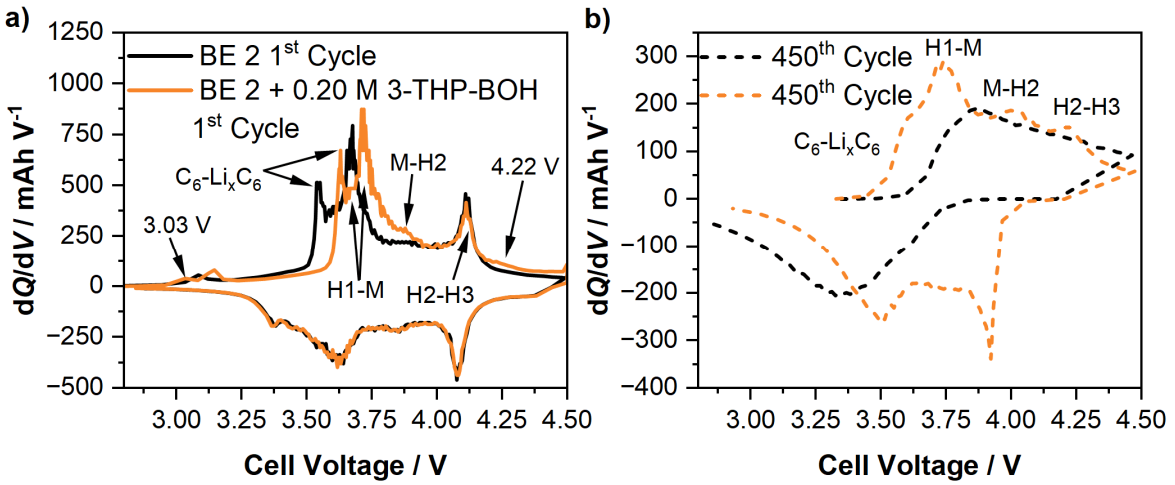

Figure 20: d*Q*/d*V vs*. voltage plots drawn for **a)** the 1st and **b)** the 450th galvanostatic charge/discharge cycle of NMC811||graphite pouch cells in the presence of the BE 2 (1 M $LiPF_6$ in EC:EMC 3:7 by weight; **black**) and the BE 2 + 0.20 M 3-THP-BOH (**orange**). Cycling was performed in a voltage range between 2.80 V and 4.50 V with a C-rate of C/10 and 1 C at the depicted cycles, respectively. Note that the first cycle is marked by a solid line, while the 450th cycle is marked with a dashed line. Important peaks, discussed in the main text, are highlighted by arrows and the peak voltage is noted. Figure redrawn with permission from [29].

As already observed during the cycling experiments, the presence of 3-THP-BOH also shows a distinct influence on the obtained d*Q*/d*V vs*. voltage plots. For the BE 2 cells, most observed features in the spectrum can be assigned to the lithiation of graphite at a voltage of 3.54 V or phase transitions within the NMC lattice structure. Here the H1-M phase transition was observed at 3.67 V, while M-H2 and H2-H3 phase transition occurred at voltages of 3.91 V and 4.11 V, respectively.[188] In addition, a peak at 3.08 V can be ascribed to EC decomposition. For the additive-containing cells the corresponding peaks were observed as well at 3.14 V, 3.63 V, 3.71 V, 3.93 V, and 4.11 V, respectively. Moreover, the spectrum exhibits additional peaks at a voltage of 3.03 V and 4.22 V, attributed to the electrochemical degradation of the additive, indicating interphase formation. The formation of an additive-derived interphase, causing overvoltages through increased internal resistance, is also a valid explanation for the observed peak shifts in the d*Q*/d*V vs*. voltage plot of the 3-THP-BOH-containing cells. This finding is also in good agreement with the previous results of the galvanostatic cycling experiments. For the second and third cycle, the d*Q*/d*V vs*. voltage plot of both investigated electrolyte formulations exhibit the same features at very similar voltages (**Figure A25**). It is worth noting that the additional peaks observed within the first cycle for the additive-containing cells were not observed in the later cycles. This indicates, that additive degradation and thus interphase formation mostly occur within the first formation cycle. The d*Q*/d*V vs*. voltage plot obtained at higher cycle numbers also outline the effect of the presence of 3-THP-BOH on the cathode active material degradation. The BE 2 d*Q*/d*V vs*. voltage plot of the 450th cycle only exhibits broad peaks without clear features, indicating a high degree of cathode active material degradation (**Figure 20b**). In contrast, the aforementioned peaks, corresponding to graphite lithiation

and NMC lattice phase transitions, are still distinct for the additive-containing cells, showing that the formation of the additive-derived interphase effectively reduces cathode active material degradation. Again, this corresponds well with the observed cycling performances, showing suppressed roll-over failure in the presence of 3-THP-BOH. Further insights into the properties of the formed additive-derived interphase can be gathered by comparing the voltage profiles of the initial charge/discharge cycles of the BE 2 and the BE 2 + 0.20 $_{M}$ 3-THP-BOH-containing cells, shown in **Figure 21**.

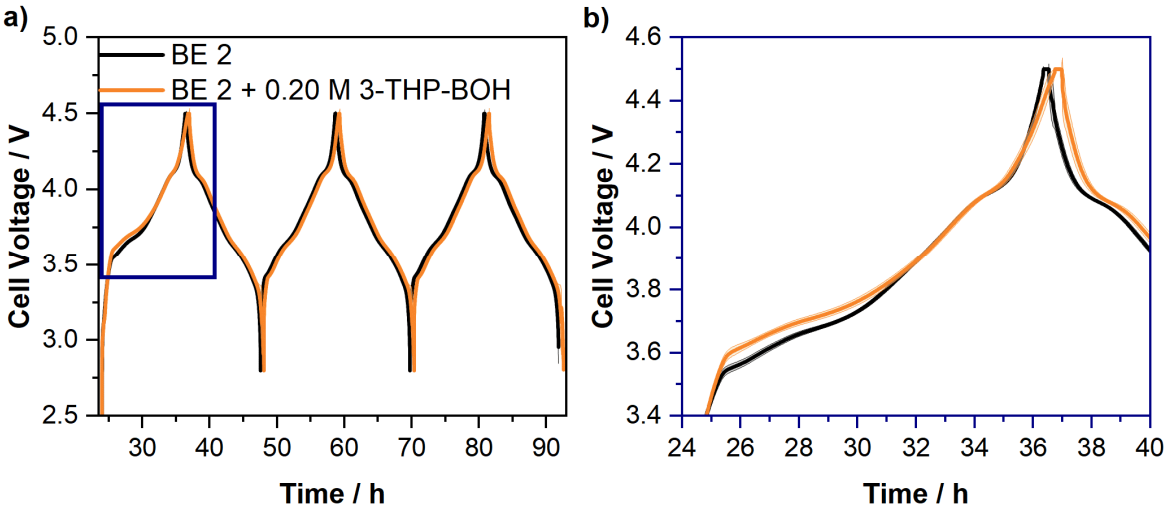

Figure 21: **a)** Voltage *vs*. time profiles of the first three galvanostatic charge/discharge cycles obtained from NMC811||graphite pouch cells cycled in the presence of the BE 2 (1 $_{M}$ $LiPF_6$ in EC:EMC 3:7 by weight; **black**) and the BE 2 + 0.20 $_{M}$ 3-THP-BOH (**orange**). Note that the depicted voltage profile is the average of four individual cells. **b)** Magnification of the initial charge cycle. The chosen inset is representative for the blue box in **a)**. Figure redrawn with permission from [29].

While showing the same characteristic features compared to the BE 2 cells, the voltage profile *vs*. time of the additive-containing cells still exhibits distinct differences. For the first plateau starting at a cell voltage of 3.61 V a notable shift of 70 mV was recorded, in comparison to the BE 2 counterparts. In regards to the previous results of the ΔV and dQ/dV *vs*. voltage analysis, the observed shift can be attributed to increased resistance and overvoltages, caused by the formation of an additive-derived interphase. This assumption is further supported by the finding of increasing voltage shifts for higher additive concentrations. Furthermore, this finding indicates that first steps of interphase-formation have to occur prior to a cell voltage of 3.50 V, to account for the observed effect. Another recorded difference is the slope of the voltage profile between cell voltages of 4.15 V and 4.50 V, which is less steep in the presence of 3-THP-BOH. On the one hand, this can be attributed to parasitic charge-consuming reactions of the additive with other additive or solvent molecules. On the other hand, this voltage region is mainly dominated by material transportation effects.[189] Therefore, the shallow voltage incline can also be attributed to decreased Li-ion transport out of the cathode active material, hindered by the formed interphase. For the voltage profile of the second charge/discharge cycle, no voltage shift of

the plateau around 3.60 V was observed. However, the voltage profile of the additive-containing cell still exhibits the less steep incline above 4.15 V. As d*Q*/d*V* *vs*. voltage analysis indicated that the majority of additive molecules are consumed within the first cycle, this further highlights the influence of the additive-derived interphase on the Li-transport properties. Nevertheless, it has to be assumed that most likely both discussed reasons contribute to the observed effect, as a clear separation is not possible.

In summary, the performed electrochemical investigations clearly show the formation of a beneficial interphase in the presence of 3-THP-BOH, greatly reducing capacity fading and cathode degradation, dramatically enhancing the performance and cycle life of the additive-containing cells. In addition, the obtained results indicate facilitated interphase formation and enhanced interphase properties, reflected in increased electrochemical performance compared to THP through the introduction of the boronic acid functional group.

6.3. Surface Characterization *via* SEM and EDX

While the performed electrochemical investigations strongly indicated the formation of an additive-derived interphase in the presence of 3-THP-BOH, additional characterization experiments were performed *via* SEM and EDX. To gain information on the morphologies and elemental composition of the interphases, electrochemically aged electrodes were taken from NMC811||graphite cells cycled with the BE 2 and the BE 2 + 0.20 $_{M}$ 3-THP-BOH and compared to pristine electrodes as reference. The obtained images from SEM and EDX investigation are depicted in **Figure 22** below and **Figure A26** in the Appendix.

The recorded SEM images express a distinct influence of the presence of 3-THP-BOH on the morphology of the formed interphases on the electrochemically aged NMC811 electrodes. In comparison to the pristine electrodes, the surface of the electrode taken from BE 2 cells did not exhibit the formation of a visible interphase on the NMC particles. In contrast, the clear formation of a smooth interphase was observed for the additive-containing electrolyte. Moreover, the obtained SEM images highlight the homogeneity of the 3-THP-BOH-derived interphase covering the whole surface of the active material, even covering cracks in between the NMC particles. This could contribute to reduced loss of active material due to particle cracking during long term charge/discharge cycling, additionally accounting for the enhanced electrochemical performance.

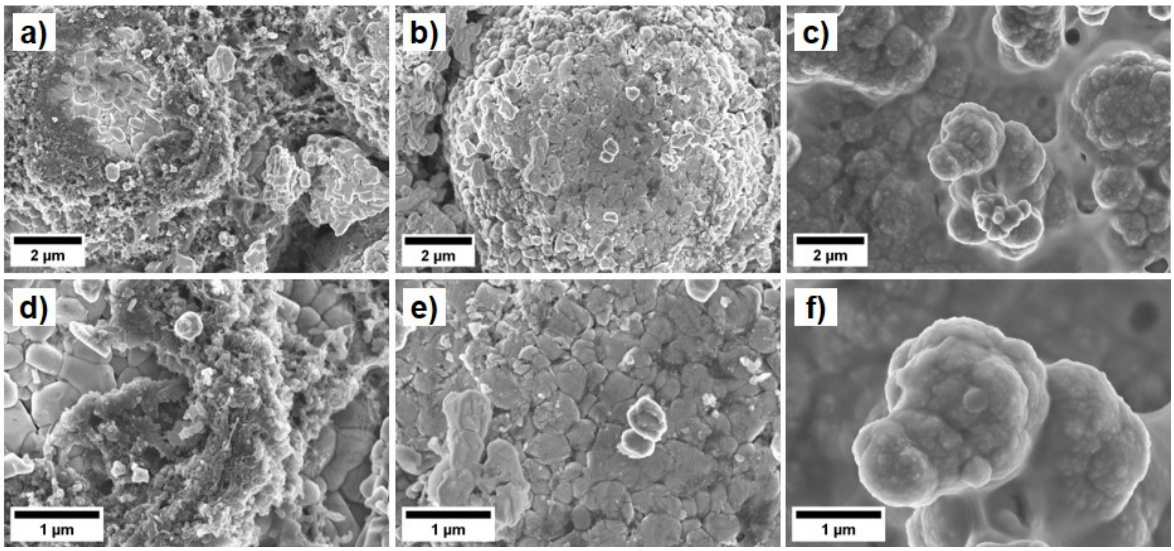

Figure 22: SEM images obtained from the surface of different NMC811 cathodes. **a)** and **d)** display SEM images of a pristine electrode. **b)** and **e)** show the SEM images of an electrode electrochemically aged in the presence of BE 2 (1 $_M$ $LiPF_6$ in EC:EMC 3:7 by weight), while **c)** and **f)** depict the surface of an electrode electrochemically aged in the presence of BE 2 + 0.20 $_M$ 3-THP-BOH. Figure redrawn with permission from [29].

The results of the EDX analysis in **Figure A26** clearly show a notable concentration of boron and sulfur on the surface of the probed NMC811 electrode taken from a 3-THP-BOH-containing cell. In addition, it was observed that the elemental distribution is rather homogenous with no clear spots of concentration, indicating the formation of a uniform interphase, as already suggested from SEM observations. While already indicated by the performed electrochemical investigations, SEM and EDX analysis further suggest the formation of a 3-THP-BOH-based CEI on the surface of the NMC811 electrodes. This is also in good consistency with the obtained EDX results and taking the learnings of the previous study (**Chapter 5**). In addition, the EDX analysis indicates that the boronic acid group remains bond to the thiophenic-backbone during polymerization. If compared to the THP-derived CEI shown in **Figure 12**, which exhibited a cauliflower-like morphology, the 3-THP-BOH-based interphase is notably smoother. This could be attributed to the introduction of the boronic-acid group to the additive's structure and is a plausible reason for the enhanced cycling performance of the 3-THP-BOH-containing cells compared to the THP-based cells (**Figure 17**).

6.4. Characterization of the 3-THP-BOH-Based Interphase *via* *Operando* SHINERS

Electrochemical investigations and surface characterization *via* SEM and EDX strongly indicate the formation of a polythiophene-based interphase in the presence of 3-THP-BOH on the surface of the NMC811 electrodes. However, detailed analysis of the molecular composition of the CEI and insights into the interphase formation are still missing. To shed light on these aspects, *operando* SHINERS investigations were performed on the surface

of NMC811 electrodes in the presence of the BE 2 and the BE 2 + 0.20 $_{M}$ 3-THP-BOH. Using the "sandwich"-configuration, where both electrodes face the window of the optical cell (**Chapter 4.2.8**) in NMC811||graphite cells, SHINERS measurements were performed during galvanostatic charging. In addition, a Li-metal RE was introduced for precise monitoring of the electrode potential. The recorded SHINER spectra for the BE 2 and the BE 2 + 0.20 $_{M}$ 3-THP-BOH taken at the cut-off voltage of 4.50 V *vs.* Li|Li^{+} are depicted in **Figure 23** below. Please note that in the following section only the most important bands will be addressed. For a detailed band assignment and additional spectra, the reader is referred to the Appendix (**Table A3** – **Table A6**, **Figure A27**, **Figure A28**).

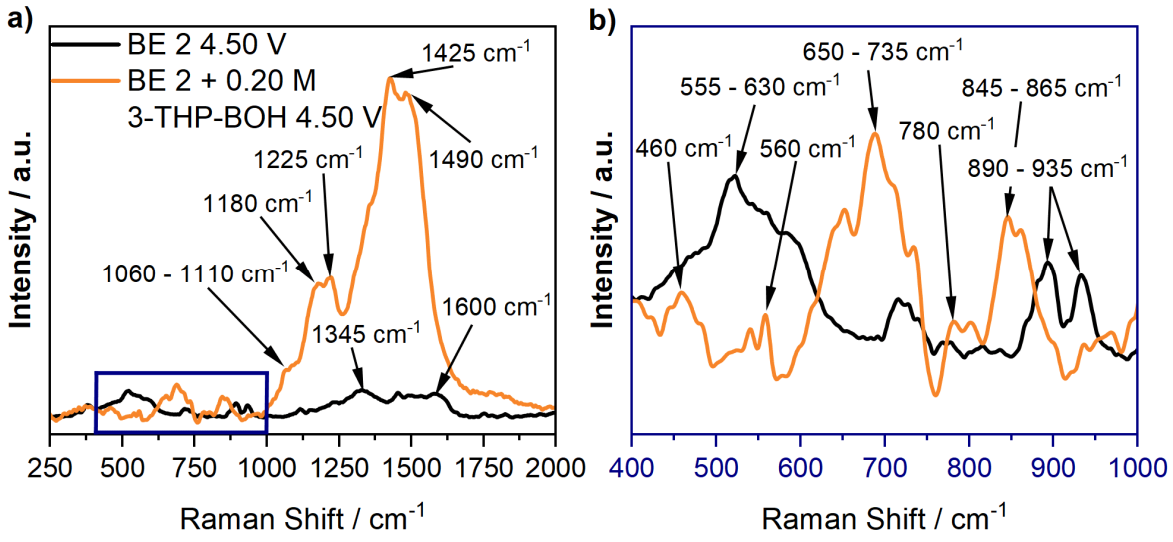

Figure 23: **a)** *Operando* SHINER spectra taken from the surface of an NMC811 electrode in the presence of the BE 2 (1 $_{M}$ $LiPF_6$ in EC:EMC 3:7 by weight; **black**) and the BE 2 + 0.20 $_{M}$ 3-THP-BOH (**orange**). For the SHINERS measurement the NMC electrode was connected as working electrode, paired against a graphite counter electrode. Galvanostatic charge was performed at a C-rate of C/3. Au SHINs with a diameter of 55 nm were introduced to the electrode surface before cell assembly. Spectra were recorded at the cut-off potential of 4.50 V *vs.* Li|Li^{+}. **b)** Enlargement of the spectra shown in **a)** in the Raman shift range of 400 cm^{-1} to 1000 cm^{-1}. The respective inset is represented by a blue box in **a)**. For spectrum acquisition the samples were excited using a 633 nm laser, adjusted to a power output of 1.05 mW. Spectra were acquired over three accumulations of 35 s. Important, newly arising bands observed in the spectra are highlighted by arrows and band positions are noted. Figure redrawn with permission from [29].

The *operando* SHINER spectra taken in the presence of the BE 2 did not exhibit prominent bands, which would indicate the formation of an interphase on the surface of the NMC811 electrodes (**Figure A27**). The spectrum recorded at the cut-off potential of 4.50 V *vs.* Li|Li^{+} only exhibited minor bands around 1010 cm^{-1}, 1150 cm^{-1} and 1505 cm^{-1}, which can be ascribed to the presence of semi-carbonate like components or Li_2CO_3.[29] In contrast, the presence of 3-THP-BOH resulted in the formation of several distinct bands in the recorded SHINER spectra. As these bands were only observed for the additive-containing electrolyte (**Figure 23**), they can be attributed to the expected formation of the 3-THP-BOH-based CEI. At the open circuit potential (OCP, **Figure A28**), the recorded spectrum of the NMC811 surface in the presence of the additive-containing electrolyte is mainly dominated by bands assigned to the electrolyte or the cathode active material. In particular, the broad bands

observed in the region around 555 cm^{-1} – 630 cm^{-1} can be assigned to different NMC lattice vibrations, while the bands around 890 cm^{-1}, 935 cm^{-1}, and 1455 cm^{-1} are attributed to EC and EMC. In addition, the distinct bands around 1345 cm^{-1} and 1600 cm^{-1} correspond to the D- and G-band of the graphitic conductive agent present in the cathode. As already mentioned, after reaching the cut-off potential of 4.50 V *vs.* $Li|Li^+$, the SHINER spectrum exhibited several new bands. While the bands observed for at the OCP around 555 cm^{-1} to 630 cm^{-1} disappeared, new sharp bands were observed around 460 cm^{-1} and 560 cm^{-1}. These bands still correspond to NMC811 lattice vibrations, however, the occurring changes in the bands could be attributed to the de-lithiation of the cathode active material or phase transitions within the lattice structure. In addition, it was also observed that the intensity of the bands, ascribed to the NMC lattice vibrations, notably decrease at high electrode potentials. This could be attributed to the formation of the additive-derived interphase, interfering with the Raman scattering process of the NMC particles. Nevertheless, the reduced skin depth of the Raman scattering process due to the increased electronic conductivity of the delithiated NMC material has to be considered, as well. In addition to the bands ascribed to changes within the electrode active material, newly arising bands were observed which can be directly attributed to the 3-THP-BOH-based CEI. Bands observed in the region around 650 cm^{-1} – 735 cm^{-1} and 780 cm^{-1} can be attributed to C–C and C–S–C ring-deformation vibrations of polythiophene (poly(THP)), while bands around 845 cm^{-1} and 1055 cm^{-1} correspond to the C–H deformation vibrations of poly(THP). The additional band around 1225 cm^{-1} is typically assigned to C–C stretching vibrations and can be attributed to the new C–C bonds in between the polymerized THP monomers. The prominent bands observed around 1425 cm^{-1} and 1495 cm^{-1} are very characteristic for poly(THP) and correspond to the C=C ring and anti-ring stretching, respectively. While all of the discussed bands can be ascribed to the presence of poly(THP), an additional band was observed around 865 cm^{-1}. After comparisons with the reference spectra of pure THP and 3-THP-BOH (**Figure A29**), this band can be attributed to the presence of the boronic acid moiety. The fact that this band is present in the spectrum recorded at the cut-off potential highlights that the boronic acid functionality remains attached to the poly(THP) backbone during polymerization, possibly tuning key properties of the additive-derived interphase. Due to its acidic nature, it can be assumed that the boronic acid group is negatively charged within the electrolyte. In the literature, it was already suggested that the presence of negatively charged surface groups can reduce the resistance of interphases, by coordinating Li-ions and facilitating their transport.[190–192] Therefore, it can be assumed that the boronic acid group functions in a similar manner in this case, accounting for the enhanced cycling performance of the cells containing 3-THP-BOH. This finding is also in good agreement with the results of the SEM and EDX analysis, outlining the formation of a

poly(3-thiophene boronic acid) (poly(3-THP-BOH))-based CEI. Based on the intensity of the bands ascribed to the polymerized additive and the absence of other prominent bands, which could be assigned to alternative interphase components, it can be concluded that the majority of the CEI formed in the presence of 3-THP-BOH consist of poly(3-THP-BOH).

In addition to the characterization of the interphase composition, the full set off the SHINER spectra recorded in the presence of the 3-THP-BOH-containing electrolyte also provides information on the CEI formation mechanism, outlining potential-depended changes within the spectra.

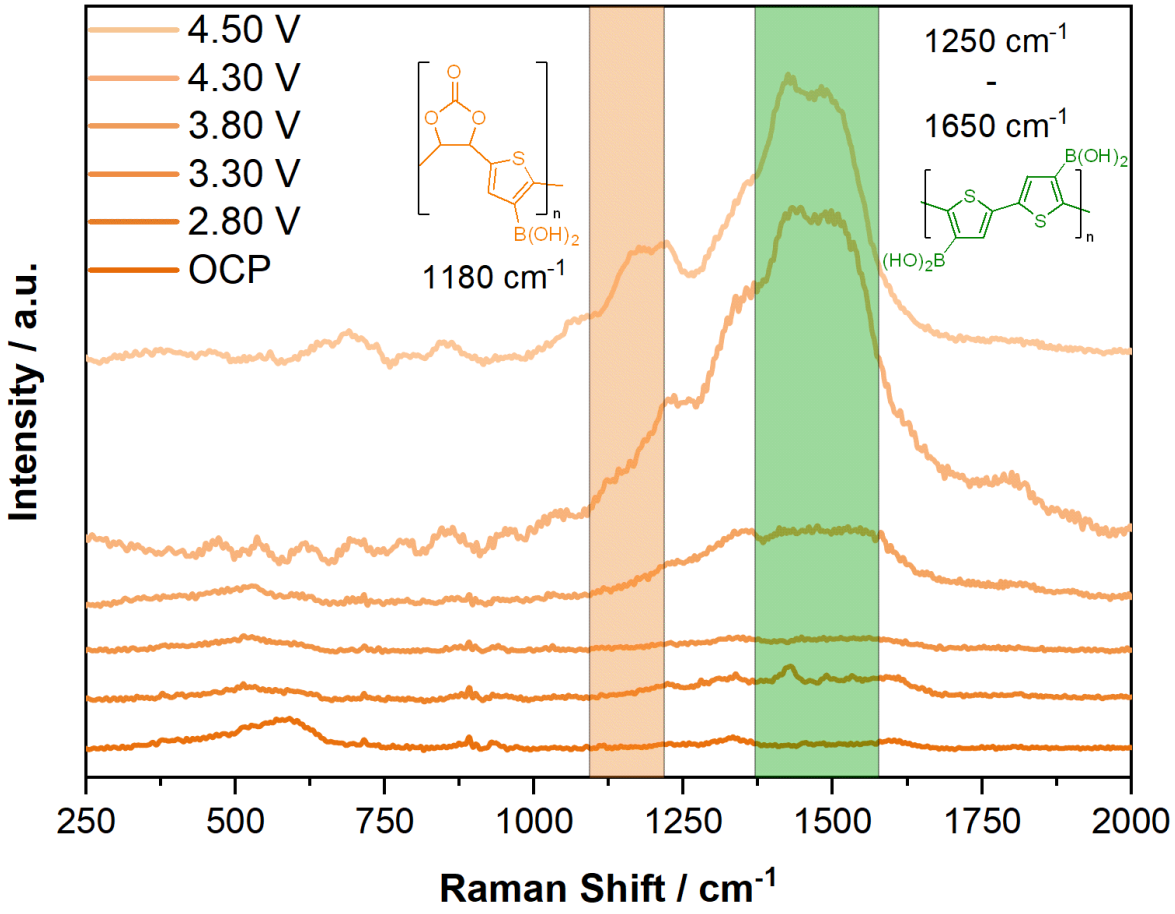

Figure 24: *Operando* SHINER spectra taken from the surface of an NMC811 electrode in the presence of the BE 2 (1 $_M$ $LiPF_6$ in EC:EMC 3:7 by weight) + 0.20 $_M$ 3-THP-BOH. For the SHINERS measurement, the NMC electrode was connected as working electrode, paired against a Li-metal counter electrode. Galvanostatic charge was performed at a C-rate of C/3. Au SHINs with a diameter of 55 nm were introduced to the electrode surface before the cell assembly. Spectra were recorded at different potentials against $Li|Li^+$, marked in the depicted spectra. For spectrum acquisition, the samples were excited using a 633 nm laser, adjusted to a power output of 1.05 mW. Spectra were acquired over three accumulations of 35 s. Important, newly arising bands observed in the spectra are highlighted by colored boxes and band positions or regions are noted. In addition, molecular structures of the attributed molecules are depicted. Figure redrawn with permission from [29].

As shown in **Figure 24**, first indications of the formation of poly(3-THP-BOH) can already be observed at relatively low potentials of 2.80 V *vs*. $Li|Li^+$, demonstrated by an increase in the background intensity between 1250 cm^{-1} and 1650 cm^{-1}. In addition, the characteristic bands around 1425 cm^{-1} and 1490 cm^{-1} were observed at this potential as well. With

increasing electrode potential, background intensity further increased, with a very sudden increase between 3.30 V *vs*. Li|Li^+ and 3.80 V *vs*. Li|Li^+ and an additional increase until reaching 4.30 V *vs*. Li|Li^+. The SHINER spectra obtained at electrode potentials of 4.30 V *vs*. Li|Li^+ and 4.50 V *vs*. Li|Li^+ did not exhibit additional increasing background intensity or newly arising bands. However, a band around 1180 cm^{-1}, only observable as a shoulder at 4.30 V *vs*. Li|Li^+, became notably more distinct at high electrode potentials. It has to be noted that this band cannot be directly ascribed to poly(3-THP-BOH). Instead, this band is typically ascribed to the presence of semi-carbonates. Nevertheless, following the conclusions from **Chapter 5.4**, this band can most likely be attributed to the formation of a co-polymer, consisting of EC and the additive molecule, forming only at high electrode potentials.

Besides potential-dependent *operando* SHINERS measurements, a time-dependent SHINERS experiment was performed to monitor changes in the CEI composition at high electrode potentials. The spectra were obtained from the surface of a NMC811 electrode galvanostatically charged to 4.50 V *vs*. Li|Li^+ in the presence of the BE 2 + 0.20 $_M$ 3-THP-BOH. Afterwards, the potential was held for 60 min and spectra recorded in defined intervals. As shown in **Figure A30**, no distinct changes were observed in the spectra with increasing time, indicating high stability of the 3-THP-BOH-derived interphase towards high potentials.

As depicted in **Figure 25**, the performed *operando* SHINERS investigations demonstrate the formation of an additive-derived interphase on the surface of NMC811 electrodes in the presence of 3-THP-BOH. Moreover, the SHINERS measurements identify poly(3-THP-BOH) as main CEI component. In addition, the *operando* SHINERS investigations allow first insights into the interphase formation mechanism, highlighting first occurrence of additive polymerization already at low electrode potentials of < 2.80 V *vs*. Li|Li^+. However, the majority of CEI formation takes place above an electrode potential of approximately 3.50 V *vs*. Li|Li^+, indicated by a strong increase in the background intensity and the arising of prominent, characteristic bands.

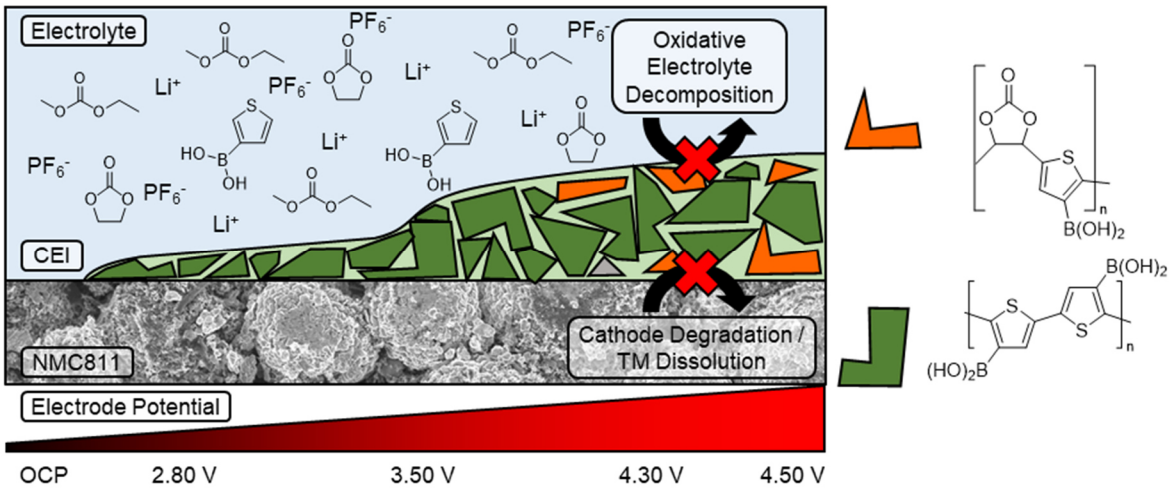

Figure 25: Schematic overview of the proposed potential-dependent CEI formation on the surface of an NMC811 electrode in the presence of the BE 2 (1 M $LiPF_6$ in EC:EMC 3:7 by weight) + 0.20 M 3-THP-BOH, based on the obtained *operando* SHINERS results. Note that the depicted electrode potential increases from left to right. Denoted potentials are referenced against Li|Li^+ and correspond to the recorded SHINER spectra. The presence of poly(3-THP-BOH) is indicated by **green** blocks, while the EC-3-THP-BOH copolymer is indicated by **orange** blocks and other interphase components by **grey** blocks. Figure redrawn with permission from [29].

These findings are in good agreement with the results of the d*Q*/d*V* *vs*. voltage analysis shown in **Figure 20**, which also indicated additive decomposition reactions at lower, as well as higher cell voltages. To further investigate the interphase formation mechanism, QC calculations were performed, based on the experimental results.

6.5. Unraveling the Interphase Formation Mechanism *via* Quantum Chemistry Calculations

Additional QC calculations were performed to gather information on the formation mechanism of the additive-derived interphase, shown by electrochemical investigations and SHINERS analysis. The proposed reaction mechanism for the electro-polymerization of 3-THP-BOH is depicted in **Figure 26** below.

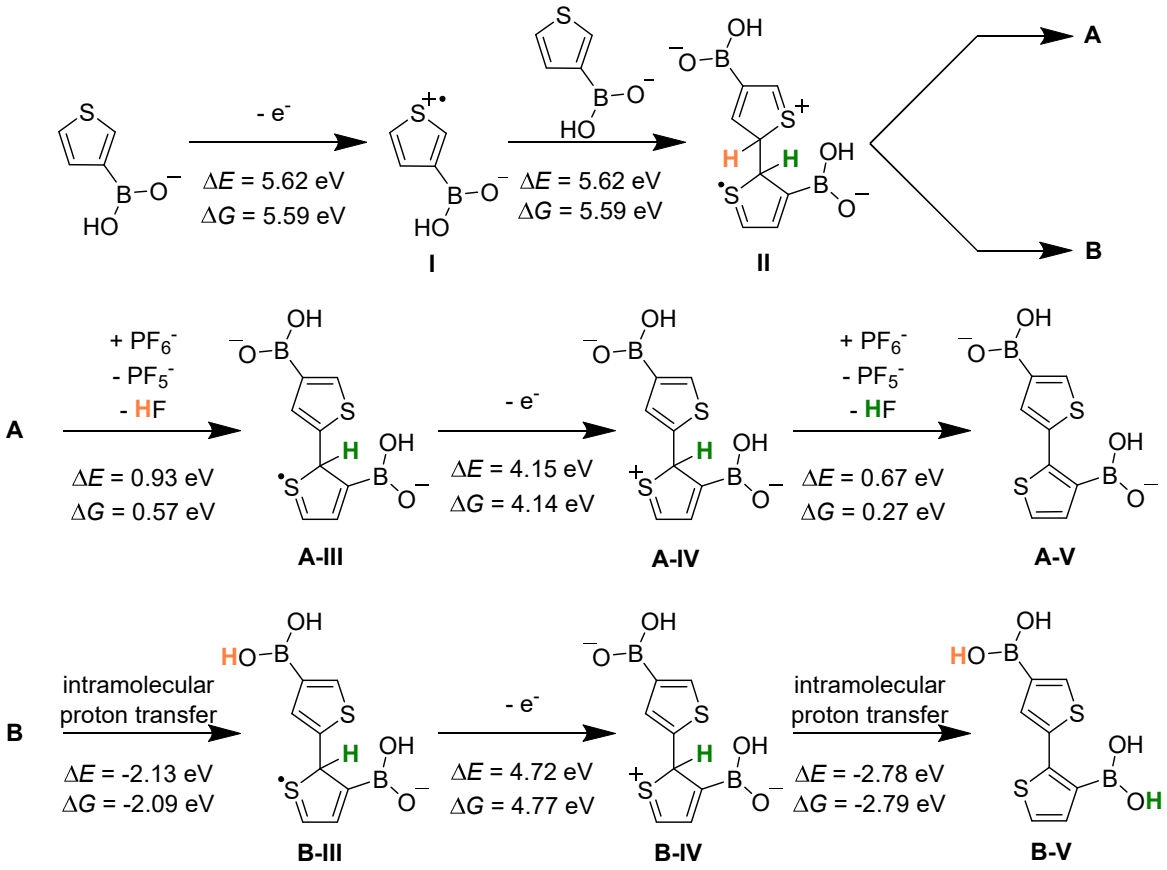

Figure 26: Suggested reaction mechanisms for the electro-polymerization of 3-THP-BOH. Shown are two alternative reaction routes **A** and **B**, characterized by alternative deprotonation options. The figure also provides the energy differences (Δ*E*, computed at 0 K) and the free energy difference (Δ*G*, computed at 298 K) calculated for each step. The determined energy values are given in electron volts (eV). Note that a value of 1.40 V has to be subtracted from the calculated energies to determine the potential on the experimental relevant Li|Li$^+$ scale. Figure redrawn with permission from [29].

In the first step (**I**) of the proposed mechanism a single 3-THP-BOH molecule is oxidized, giving a calculated change in the free energy of Δ*G* = 5.59 eV or an oxidation potential of 4.19 V *vs*. Li|Li$^+$, forming a radical. Note that for the calculations it was assumed that the 3-THP-BOH molecule is in a semi-deprotonated state, due to its moderate acidity. The calculated oxidation potential for the single 3-THP-BOH molecule is notably lower, compared to a single EC molecule (5.70 V *vs*. Li|Li$^+$), emphasizing additive decomposition prior to bulk electrolyte oxidation. Moreover, the calculations show earlier additive oxidation compared to single THP molecules (5.10 V *vs*. Li|Li$^+$), highlighting the effect of the introduced boronic acid group on facilitated oxidation. Following the oxidation, the formed radical may encounter a second 3-THP-BOH molecule forming a dimer with a free energy difference of Δ*G* = 0.63 eV (**II**). For the subsequent deprotonation of the formed dimer (**III**), two possible alternatives were considered. For the first variant (**A**), deprotonation occurs *via* an external anion, *e.g.* a PF_6^- anion, resulting in an increase of the free energy (Δ*G* = 0.57 eV). After deprotonation, the radical dimer is further oxidized (**A-IV**), giving a change in the free energy of Δ*G* = 4.14 eV. Following the second oxidation, the dimer is further deprotonated by an external anion (**A-V**), resulting in an increase in the free energy of

ΔG = 0.27 eV. For the overall electro-polymerization of 3-THP-BOH following the A route, a total free energy of ΔG = 11.20 eV was calculated, equaling 5.60 eV per transferred electron and a reaction potential of 4.20 V *vs*. Li|Li^+. For the second variant (**B**), an intramolecular proton transfer to one of the semi-deprotonated boronic acid groups was suggested, instead of external deprotonation. For this step a major gain in free energy of ΔG = -2.09 eV was calculated. For the subsequent radical dimer oxidation (**B-IV**) a slightly higher free energy difference of ΔG = 4.77 eV was calculated. However, for the final deprotonation (**B-V**), again *via* intramolecular proton transfer, a distinct free energy gain of ΔG = -2.79 eV was obtained. Due to the major gains in free energy during the deprotonation steps a total free energy of ΔG = 6.57 eV (3.29 eV per transferred electron; oxidation potential of 1.89 V *vs*. Li|Li^+) was calculated for the overall reaction following the B route, notably lower compared to the A variant. Based upon the performed QC calculations, the thermodynamically favored route **B** is more plausible. However, it has to be considered that the calculated oxidation potential of a single 3-THP-BOH is notably higher, compared to the overall reaction potential. In addition, it is not clear that all monomer molecules are semi-deprotonated under experimental conditions, possibly resulting in mixed polymerization mechanisms. Also, semi-deprotonated 3-THP-BOH molecules could coordinate Li-ions, which would increase the oxidation potential of the respective molecules. Therefore, it is suggested that the formation of the polymeric interphase only occurs at low rates at lower electrode potentials, and accelerates with increasing potentials, closing in on the oxidation potential of the single 3-THP-BOH molecule. This suggestion is in very good agreement with the performed *operando* SHINERS measurements shown in **Figure 24**, indicating initial interphase formation already at electrode potentials lower than 2.80 V *vs*. Li|Li^+. However, major interphase formation was only observed at potentials above 3.50 V *vs*. Li|Li^+.

In addition to the investigation of the electro-polymerization of the additive, QC calculations were employed to clarify the possible co-polymerization of 3-THP-BOH with EC, captured by SHINERS measurements. For the suggested co-polymerization, a reaction mechanism similar to the electro-polymerization of 3-THP-BOH (**Figure 26**) and the THP-analogue (**Chapter 5.5**) was considered. The proposed mechanism is depicted in **Figure A31**. In the first step (**I**), EC gets oxidized forming a radical cation, which is subsequently deprotonated by a PF_6^- anion. For the initial EC oxidation, a potential of 5.70 V *vs*. Li|Li^+ was calculated. Following the oxidation, the formed EC radical may encounter a semi-deprotonated 3-THP-BOH molecule (**II**). For entering the dimerization transition state an energy barrier of $\Delta G^‡$ = 0.44 eV was calculated, followed by a stabilizing free energy gain of ΔG = -0.72 eV (**III**). After dimerization the obtained molecule can be further oxidized, resulting in the formation of the copolymer observed during SHINERS measurements. The performed QC calculations demonstrate that the formation of the copolymer is thermodynamically feasible.

However, they also outline that the formation of poly(3-THP-BOH) is clearly energetically favored, making up the majority of the formed interphase. This is in very good agreement with the results of the *operando* SHINERS investigations, showing formation of poly(3-THP-BOH) already at low electrode potentials, while copolymer formation was only observed close to the cut-off potential of 4.50 V *vs*. Li|Li^+. In addition, based on band intensities it can be concluded that the copolymer is only formed on a low scale.

6.6. Conclusion

Combined investigation *via* galvanostatic cycling and *operando* SHINERS measurements successfully showed that the introduction of 3-thiophene-boronic acid (3-THP-BOH) results in the formation of an effective additive-induced CEI, greatly enhancing the electrochemical performance and the cycle life of the respective high-voltage NMC811||graphite pouch cells. The cells containing an optimized concentration of 3-THP-BOH exhibited a quadrupled cycle life in comparison to the BE 2 cells, as well as reduced capacity fading. Moreover, while the benchmark cells suffered from roll-over failure, the 3-THP-BOH-derived CEI successfully suppressed this rapid capacity loss. *Operando* SHINERS investigations, supported by SEM and EDX analyses, captured not only the presence of a polymeric interphase on the cathode surface, but also showed the presence of the introduced functional group within the polymeric CEI, identifying poly(3-THP-BOH) as major CEI component. In addition, SHINERS results also suggest the formation of a copolymer, consisting of EC and 3-THP-BOH, forming only at high electrode potentials. *Operando* SHINERS measurements further enabled a dynamic tracking of the evolving interphase, demonstrating marginal interphase formation already at potentials lower than 2.80 V *vs*. Li|Li^+ and enhanced CEI growth at higher electrode potentials. Based on these findings, the postulation of a reaction mechanism for the electro-polymerization of 3-THP-BOH was possible, supported by highly accurate QC calculations.

7. Unraveling the Cross-Talk Mechanism of Ethylene Carbonate-based Electrolyte Additives

Major segments of this chapter have been published in:

Pfeiffer, F., Griggio, A., Weiling, M., Wang, J-F., Reißig, F., Peschel, C., Pillatsch, L., Warrington, S., Nowak, S., Grimaudo, V., Wright, I., Baghernejad, M.; Tracing the Cross-Talk Phenomenon of Vinylethylene Carbonate to Unveil its Counterintuitive Influence as an Electrolyte Additive on High-Voltage Lithium-Ion Batteries, Adv. Energy Mater., **2024**, 14, 2402187.

and are reproduced or adapted with permission from [159]. Galvanostatic charge/discharge cycling experiments and SHINERS measurements of the graphite surface presented in this chapter were conducted by Angela Griggio. Interpretation and curation of the data was performed by the author of this thesis.

7.1. Introduction

In the previous chapters selected thiophene-based electrolyte additives were introduced with the intention of facilitating CEI formation. However, it has to be considered that in reality it is not certain that the employed electrolyte additives only affect the targeted electrode, especially in the complex system of LIBs. In fact, an interaction between anode and cathode and the transfer of molecules between the two sides is already known in literature. Although, this so called “cross-talk” phenomenon often only considers the transfer of metal ions or inorganic species between the electrodes during operation.[21,23,187] Nevertheless, the question to what extent electrolyte additives or the respective degradation products directly participate in this cross-talk remains, as the investigation of this phenomenon requires a complex experimental set-up.[193,194] As demonstrated in the precedent chapters of this thesis, *operando* SHINERS has proven to be a very potent technique for the characterization of interphases in high-voltage LIBs, allowing the determination of interphase composition and formation mechanisms. In addition, due to the flexibility and robustness of SHINERS, it allows the monitoring of anode and cathode surface, making it an ideal candidate for the investigation of the cross-talk phenomenon. To systematically approach this complex question, EC-based film-forming electrolyte additives, which are typically employed to modify the SEI, were introduced into high-voltage NMC622||graphite pouch cells, revealing a notably enhanced cycling performance in the presence of VEC. Initial experiments indicated that instead of the anode, processes on the cathode mainly affect the performance of the respective cells, fueled by a cross-talk phenomenon. O*perando* SHINERS and SERS investigations and additional experiments captured the

transfer of additive degradation products, resulting in the formation of a polymeric CEI, unraveling the effect of the employed additive on the galvanostatic cycling performance.

7.2. Electrochemical Characterization of the Electrochemical Performance of EC-derived Electrolyte Additives

Selected electrolyte additives, namely FEC, ClEC, VC and VEC, were introduced to the BE 2 electrolyte and galvanostatically investigated in high-voltage NMC622||graphite pouch cells. All of these employed molecules are based on the EC-motif, derivatized by the addition of different functional groups. While FEC and VC are already commonly used in commercial LIB applications, ClEC and VEC are lesser known. In the first step, the optimized additive concentration was determined for every considered electrolyte additive. The obtained specific discharge capacities are shown in **Figure A32**. The preliminary concentration optimization revealed highest electrochemical performance for 0.75 $_{M}$ FEC, ClEC, and VC. In contrast, for VEC an optimum cycling performance was observed for a concentration of 0.30 $_{M}$, notably lower compared to the alternative candidates. A comparison of the results of the galvanostatic charge/discharge cycling experiments of the optimized concentrations for all considered electrolyte additives is depicted in **Figure 27**. The presence of the different additives has distinct effects on the electrochemical performances obtained from the respective cells, ranging from decreased to strongly enhanced results during the galvanostatic charge/discharge cycling experiments. An overview of the key parameters obtained from galvanostatic cycling is summarized in **Table 4**.

Table 4: Key data of the galvanostatic charge/discharge investigation of NMC622||graphite pouch cells, cycled in the presence of the BE 2 (1 $_{M}$ $LiPF_6$ in EC:EMC 3:7 by weight) and BE 2 + the optimized additive concentrations. Listed are the number of performed cycles until a 50% SoH, the average Coulombic efficiency (CE), the ΔV value at a 50% SoH, and the accumulated specific discharge energies (ADE) recorded at 80% and 50% SoH. Percental changes in the obtained values are calculated in comparison to the BE 2 cells. The shown values were obtained from **Figure 27** and **Figure A33.** Table redrawn with permission from [159].

Electrolyte	Cycle life	Ø CE / %	Δ*V* / mV	ADE_{80} / Wh g^{-1}	ADE_{50} / Wh g^{-1}
BE 2	412	99.9	578	70	174
+ 0.75 $_{M}$ FEC	409 – 1%	99.8 – 0.1%	523 – 11%	97 + 39%	177 + 2%
+ 0.75 $_{M}$ ClEC	420 + 2%	99.6 – 0.3%	716 + 19%	98 + 40%	166 – 5%
+ 0.75 $_{M}$ VC	531 + 29%	99.9 – 0.1%	663 + 13%	44 – 37%	197 + 14%
+ 0.30 $_{M}$ VEC	1928 + 368%	99.9 ± 0%	537 – 8%	169 + 141%	734 + 322%

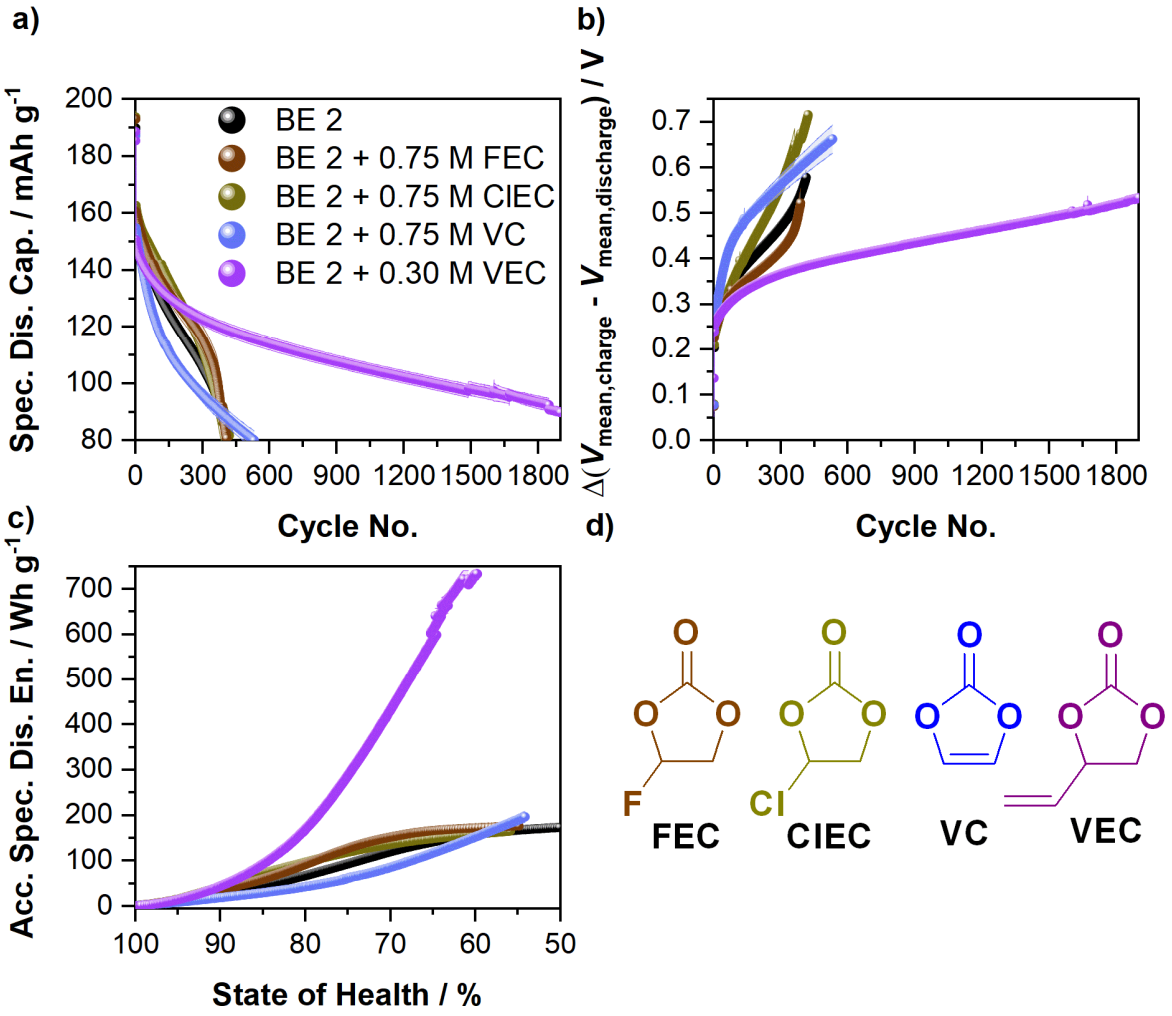

Figure 27: Overview of the results of the galvanostatic cycling experiments obtained from NMC622||graphite pouch cells charge/discharge cycled at a C-rate of 1 C in a voltage range between 2.80 V – 4.50 V in the presence of the BE 2 (1 $_M$ $LiPF_6$ in EC:EMC 3:7 by weight, **black**) and the BE 2 + the optimized concentrations of FEC (**brown**), ClEC (**dark yellow**), VC (**blue**), and VEC (**purple**). Shown are **a)** the specific discharge capacities (Spec. Dis. Cap.) obtained from NMC622||graphite pouch cells, **b)** the differential voltage (ΔV) analysis, **c)** the accumulated specific discharge energies (Acc. Spec. Dis. En.), and **d)** the molecular structure of the employed electrolyte additives. Figure redrawn with permission from [159].

Figure 27a depicts the recorded specific discharge capacities for the NMC622||graphite cells, containing the considered electrolyte formulations with optimized additive concentrations. For the BE 2 cells, an initial specific discharge capacity of 159 mAh g^{-1} was obtained after formation, decreasing to 80 mAh g^{-1}, equaling 50% SoH, at the 412th cycle. It is worth noting that after about 380 cycles a dramatic increase in the capacity fading was observed. In accordance with a similar effect observed for the NMC811 cathodes in **Chapter 6** prior, this phenomenon can be ascribed to the roll-over failure. The severe degradation of the cathode active material leads to the dissolution of TM ions into the electrolyte and their deposition on the anode's surface. This initiates the formation of Li dendrites, resulting in the loss of active Li, additional electrolyte decomposition and the risk of micro short circuits. For the FEC- and ClEC-containing cells, initial specific discharge capacities of 160 mAh g^{-1} and 163 mAh g^{-1} were recorded, slightly higher in comparison to

the BE 2 cells. With ongoing cycling, the FEC- and ClEC-containing cells exhibited a lower rate of capacity fading, resulting in increased discharge capacities. Similar to the BE 2 cells, the cells containing the EC-halides exhibited severe capacity fading after surpassing 340 and 310 charge/discharge cycles, respectively. Despite higher discharge capacities during lower cycle numbers the FEC- and ClEC-containing cells exhibit a similar cycle life of 409 and 420, respectively, comparable to the BE 2 cells. For the cells containing the VC-based electrolyte, a contrary behavior was observed. While showing a notably lower initial discharge capacity of 155 mAh g^{-1} and a higher rate of capacity fading during moderate cycle numbers, no roll-over failure was observed towards the end of the cells cycle life. Evading this severe capacity fading, overall cycle life of the VC-containing cells was increased by approximately 100 cycles, reaching a SoH of 50% after 531 consequent charge/discharge cycles. The cells cycled in the presence of the VEC-containing electrolyte demonstrated a notably enhanced electrochemical performance, while the other investigated electrolyte formulations only exhibited marginal improvements. Similar to the VC-cells, the VEC-containing cells exhibited a lower initial discharge capacity of 150 mAh g^{-1}. Nevertheless, capacity fading during ongoing charge/discharge cycling was notably lower, compared to the BE 2, FEC- and ClEC-containing cells. Moreover, no roll-over failure was observed in the presence of VEC, resulting in a drastically increased cycle life. While the cells containing the other investigated electrolyte formulations reached a 50% SoH after about 400 to 500 cycles, the VEC-containing cells exhibited 89 mAh g^{-1}, equaling a 60% SoH, after 1900 charge/discharge cycles, greatly outperforming the alternative electrolyte formulations.

The additive's effect on the electrochemical performance during galvanostatic cycling also reflects on the calculated CEs, depicted in **Figure A33**. While a CE of 88% was recorded for the first charge/discharge cycle of the BE 2 cells, a higher CE of 89% was recorded for the FEC- and VC-containing cells. In contrast, the ClEC- and VEC-containing cells exhibited lower first cycle CEs of 83% and 86%, respectively. The CEs recorded for the 2nd and 3rd cycle of the VEC-containing cells undercut the CEs calculated for their counterparts by about 1%, indicating additional charge-consuming reactions occurring in the presence of VEC. Despite exhibiting notable difference during the formation cycles, the CEs recorded during the continuous charge/discharge cycling exhibit similar average CE values of approximately 99.9% for all investigated electrolyte formulations, with the ClEC-containing cells being the only exception, showing an average CE of 99.6%. Despite the similar CE values recorded during cycling, it has to be highlighted that the CE values exhibited by the additive-containing cells are slightly lower, compared to the BE 2 cells, indicating continuous parasitic reactions due to *e.g.* additive degradation. In addition, it is worth noting that the

BE 2, the FEC- and the ClEC-containing cells exhibit a distinct decrease of the CEs towards the end of their cycle-life, mimicking the severe capacity fading observed in **Figure 27a**.

Investigating the additive's influence on the cells internal resistance is also an important aspect, regarding the evaluation of the electrochemical performance. In accordance with the previous chapters, Δ*V* analysis was performed to estimate the internal resistance of the investigated cells (**Figure 27b**). After formation, a Δ*V* value of 205 mV was recorded for the BE 2-containing cells. While the cells containing the FEC- and ClEC-based electrolyte formulations exhibited similar values of 225 mV and 210 mV, notably higher Δ*V* values of 250 mV and 240 mV were obtained for the VC and VEC cells, respectively. These findings are in accordance with the initial discharge capacities, observed during galvanostatic cycling. BE 2-, FEC- and ClEC-containing cells showed higher initial capacities matching the lower internal resistances. In contrast, the higher Δ*V* values exhibited by VC- and VEC-containing cells result in enhanced over-voltages and thus, decreased initial discharge capacities. During continuous galvanostatic charge/discharge cycling, different trends for the growth of the internal resistance were observed for every considered electrolyte formulation. The BE 2-, and the FEC-containing cells exhibited a similar behavior, showing a moderate increase in the Δ*V* values after the formation cycles. However, towards the end of their respective cycle life, a sharp increase in the internal resistance was observed, resulting in a final Δ*V* value of 578 mV for the BE 2 cells and 523 mV for the FEC-containing cells at a 50% SoH. This sharp increase in the recorded Δ*V* values is in good agreement with the trends exhibited by CEs and the cycling performance of these electrolyte formulations, showing a severe deterioration of the electrochemical performance. As already mentioned, these effects could be attributed to the degradation of the cathode active material and especially the formation of Li dendrites, causing additional interphase formation, further increasing the cells' internal resistance. While the ClEC-containing cells exhibit a similar cycling performance compared to the BE 2 and the FEC cells, the obtained Δ*V* values show an almost linear increase during continuous charge/discharge cycling, differing from their counterparts. In addition, the Δ*V* value of 716 mV recorded at 50% SoH for the cells cycled in the presence of ClEC is notably higher, compared to the other investigated electrolyte formulations. The observed phenomenon could be attributed to continuous electrolyte decomposition, leading to uncontrolled interphase growth, due to the formation of an ineffective SEI. The Δ*V* values observed for the VC-containing cells directly mimic the obtained discharge capacities. After the formation cycles, the internal resistance of the VC cells greatly increases, accounting for the high rate of capacity fading observed during the first 200 charge/discharge cycles. Nevertheless, for higher cycle numbers, the VC-containing cells exhibit a notably lower growth of the internal resistance, directly reflecting on the obtained discharge capacities. At 50% SoH the VC cells exhibit a Δ*V* value

of 663 mV. In comparison to the other considered electrolyte formulations, the cells cycled in the presence of VEC exhibited the lowest growth of internal resistance, reaching a Δ*V* value of 537 mV at 50% SoH. This value is notably lower, compared to the BE 2, ClEC, and VC cells, and only slightly higher than the Δ*V* value recorded for the FEC cells. It has to be emphasized that the Δ*V* value for the VEC-containing cells was obtained after more than 1900 cycles, while the cell cycled in the presence of the other electrolyte formulations barley surpassed 400 or 500 cycles, respectively. In addition, the recorded Δ*V* values for the VEC-containing cells increase linearly, not exhibiting drastic changes on the growth of the internal resistance. In accordance with the obtained discharge capacities, it is suggested that the presence of VEC results in the formation of an effective interphase, suppressing electrolyte decomposition and the roll-over failure.

Similar to the previous chapter, a final evaluation of the considered electrolyte formulations was performed by analyzing the obtained ADEs, shown in **Figure 27c**. This analysis is especially valuable in this context, as the electrochemical performance of cells containing the investigated electrolyte formulations strongly divert, exhibiting different rates of capacity fading, different cycle numbers and roll-over failures. For the cells containing the BE 2, a value of 174 Wh g^{-1} was obtained at 50% SoH. This value is similar to the values obtained for the FEC- and ClEC-containing cells, exhibiting ADEs of 177 Wh g^{-1} and 166 Wh g^{-1}, respectively, accounting for the higher initial discharge capacities and the stronger capacity fading towards the end of cycling. Due to the prolonged cycle life, the VC-containing cells showed an increased ADE of 197 Wh g^{-1}. For the cells cycled in the presence of VEC an ADE of 734 Wh g^{-1} was obtained, greatly outperforming the other electrolyte systems, accounting for the lower rate of capacity fading and drastically prolonged cycle life. Considering 50% SoH as end of cycle life reveals important details on cathode degradation and long-term cycling effects, typically 80% SoH is considered as end of life criterium, especially in commercial applications. While the ADEs obtained at 50% SoH showed similar or enhanced values for the additive-containing cells, the ADEs recorded at 80% SoH show different trends. Here, FEC- and ClEC-containing cells show a distinctly enhanced performance, exhibiting ADEs of 97 Wh g^{-1} and 98 Wh g^{-1}, compared to the 70 Wh g^{-1} obtained from the BE 2 cells. Opposing to the previous consideration, at 80% SoH the VC-containing cells exhibit a strongly decreased ADE of 44 Wh g^{-1}, caused by the strong capacity fading and high internal resistances. Despite the variated SoH, the cells cycled in the presence of VEC still show a distinct improvement compared to all other considered electrolyte formulations, giving an ADE of 169 Wh g^{-1} at 80% SoH.

To gain first insights into the interphase formation abilities of the investigated electrolyte additives CV measurements were performed in a three-electrode system using graphite as

WE, and Li-metal as CE and RE. The obtained CVs are depicted in **Figure 28** below, and show the CV of the 1st and 2nd cycle in comparison to the CV recorded for the BE 2.

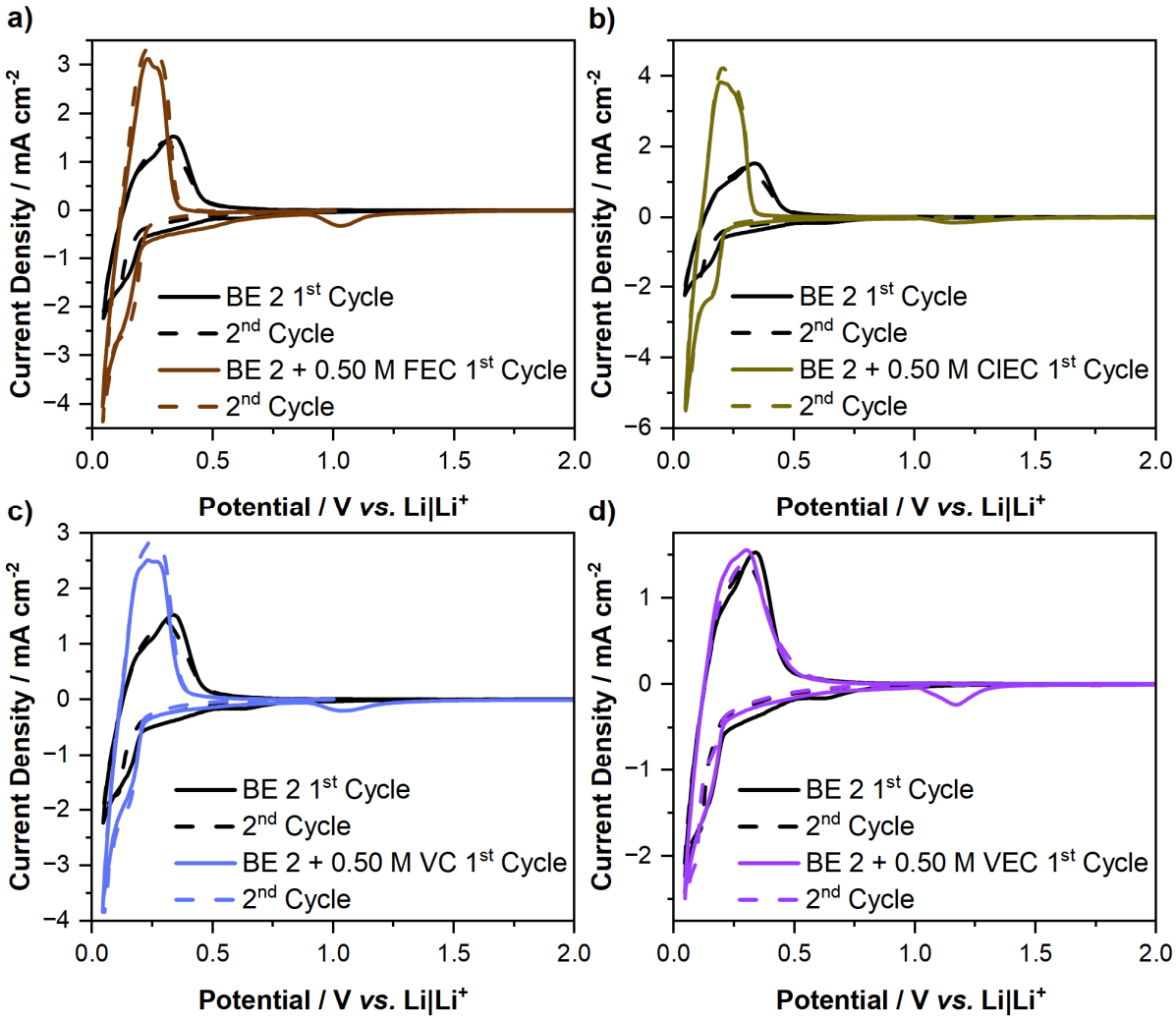

Figure 28: Cyclic voltammograms (CVs) of graphite||Li-metal T-type Swagelok® cells with Li-metal reference electrodes obtained in the presence of the BE 2 (1 $_M$ $LiPF_6$ in EC:EMC 3:7 by weight, **black**) and the different electrolyte additive-containing electrolyte formulations. Shown are the CVs recorded for **a)** FEC (**brown**), **b)** ClEC (**dark yellow**), **c)** VC (**blue**), and **d)** VEC (**purple**) in comparison to the BE 2 CVs. Cyclic voltammetry was performed in a potential range of 2.80 V – 4.50 V *vs.* $Li|Li^+$ with a scan rate of 150 µV s^{-1}. In total 2 charge/discharge cycles were performed, marked by full and dashed lines in the depicted voltammograms. Figure redrawn with permission from [159].

As expected, for all additive-containing electrolyte formulations an additional peak was observed during the cathodic scan. Due to this peak's absence from the BE 2 CV, it can be attributed to the reductive degradation of the respective additive molecules. It is also worth noting that these peaks were recorded at higher potentials of 1.03 V *vs.* $Li|Li^+$, 1.16 V *vs.* $Li|Li^+$, 1.05 V *vs.* $Li|Li^+$, and 1.17 V *vs.* $Li|Li^+$ for the FEC-, ClEC-, VC-, and VEC-containing electrolyte formulations, than the peak ascribed to the reduction of EC, observed at a potential of 0.64 V *vs.* $Li|Li^+$ in the BE 2 CV. This indicates degradation of the electrolyte additives and thus formation of an additive-derived SEI prior to reductive decomposition of the bulk electrolyte. Moreover, it was found that the additive degradation peak was only

observed within the first CV cycle. This further suggests that the majority of the additive molecules are consumed during the first charge/discharge cycle.

The performed electrochemical investigation of the considered electrolyte formulations revealed a clear influence of the respective electrolyte additives on the cycling performance of the employed high-voltage NMC622||graphite pouch cells. As expected, CV measurements indicated reductive decomposition and therefore, SEI formation prior to bulk electrolyte degradation. However, the cells containing an optimized concentration of the common electrolyte additives FEC and VC, showed little to no improvement of the obtained cycling performance compared to the BE 2 cells. Instead, especially the FEC- and also ClEC-containing cells were greatly limited by roll-over failure, resulting in a strong capacity fading. Out of the introduced electrolyte additives only VEC exhibited a distinct enhancement of the electrochemical performance, notably outperforming the other considered electrolyte formulations. The performed CV measurements, the obtained specific discharge capacities and the conducted ΔV analysis indicate the formation of an efficient interphase, in the presence of VEC, suppressing electrolyte degradation and the roll-over failure, observed for BE 2-, FEC-, and ClEC-containing cells. To fully elucidate the interphase formation mechanisms and interphase composition, further investigations were necessary.

7.3. GC-MS Investigation of the Aged Electrolyte

To gain additional insights into the interphase formation mechanism was the investigation of the electrochemically aged electrolyte, extracted after 100 charge/discharge cycles from the NMC622||graphite pouch cells. Electrolyte investigation was carried out by GC-MS, and the recorded chromatograms for all considered electrolyte formulations are shown in **Figure 29**. The chromatogram of the electrochemically aged BE 2 is dominated by peaks ascribed to the main electrolyte solvents EC and EMC. In addition, distinct peaks were identified, ascribed to the linear carbonates dimethyl carbonate (DMC) and diethyl carbonate (DEC). Moreover, the chromatogram exhibits the presence of carbonate oligomers (oxa-hexane carboxylates (‘OHCs)) with increasing chain length. While the presence of DMC and DEC can be ascribed to the transesterification of EMC, ‘OHCs originate from the reductive decomposition of EC. The distinct presence of these molecules in the electrochemically aged electrolyte indicates the formation of an ineffective SEI in the presence of the BE 2, not able to effectively prevent the reductive decomposition of the bulk electrolyte. The recorded chromatograms of the FEC-, ClEC-, and VC-containing electrolytes exhibit great similarities.

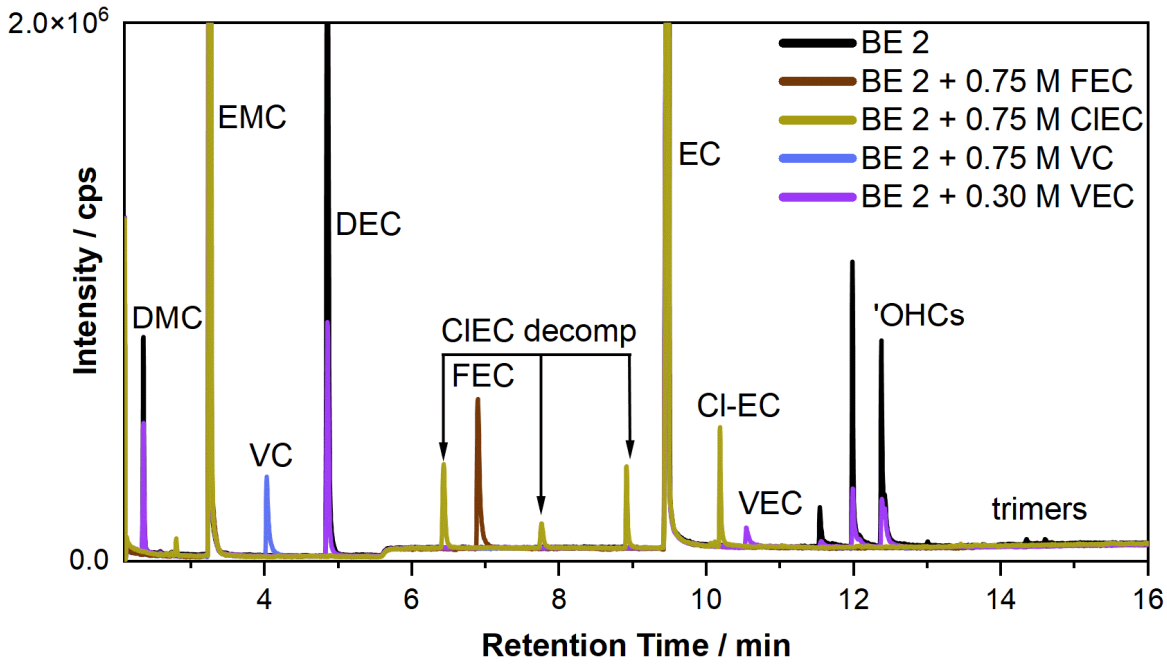

Figure 29: Comparison of the gas chromatograms recorded from the investigated electrolyte formulations electrochemically aged in NMC622||graphite pouch cells. The respective electrolytes were extracted after 100 galvanostatic charge/discharge cycles. Peak identification was performed *via* mass spectrometry and peaks are assigned in the respective chromatograms. Depicted are the chromatograms of the electrochemically aged BE 2 (1 $_{M}$ $LiPF_6$ in EC:EMC 3:7 by weight; **black**) and the additive-containing electrolyte formulations at the optimum electrolyte additive concentration for FEC (**brown**), ClEC (**dark yellow**), VC (**blue**), and VEC (**purple**). The individual chromatograms are depicted in **Figure A34**. Figure redrawn with permission from [159].

All chromatograms are dominated by the EC- and EMC-ascribed peaks. Furthermore, for all electrolytes the distinct presence of additive residues was observed, demonstrating that despite 100 consecutive charge/discharge cycles the additives have not been fully consumed. Interestingly, only for the ClEC-containing electrolyte formulation additive decomposition products were identified within the extracted electrolyte. These decomposition products were further investigated by GC-HRAM-MS, and are discussed in the Appendix (**Figure A35**). Most importantly, the electrochemically aged FEC-, ClEC-, and VC-containing electrolyte formulations did not exhibit notable concentrations of the reductive electrolyte decomposition products, identified for the BE 2 cells. This indicates the formation of a more effective SEI in the presence of these electrolyte additives. In contrast, the aged electrolyte extracted from the VEC-containing cells exhibited a distinct presence of transesterification and EC-degradation products. While the results of the electrochemical investigation demonstrate a drastically improved cycling performance in the presence of VEC, ascribed to beneficial interphase formation, the results of the GC-MS measurements present a distinct contrast. Instead of further outlining the formation of an effective interphase suppressing electrolyte decomposition, they actually outline the formation of an ineffective SEI, resulting in continuous electrolyte degradation.

7.4. SEI Characterization *via Operando* SHINERS

Following the contradictory results of the GC-MS investigation, *operando* SHINERS measurements of the graphite surface in the presence of all considered electrolyte formulations with an optimized additive concentration were performed to gain insights into the composition of the formed SEIs. The recorded SHINER spectra are depicted in **Figure 30** below. In the following discussion of the SHINERS investigation only important and characteristic bands will be mentioned to enhance clarity of the segment. For a complete assignment of all identified bands and the full range spectra, the reader is kindly referred to **Table A7** – **Table A11** and **Figure A36** – **Figure A40** in the Appendix.

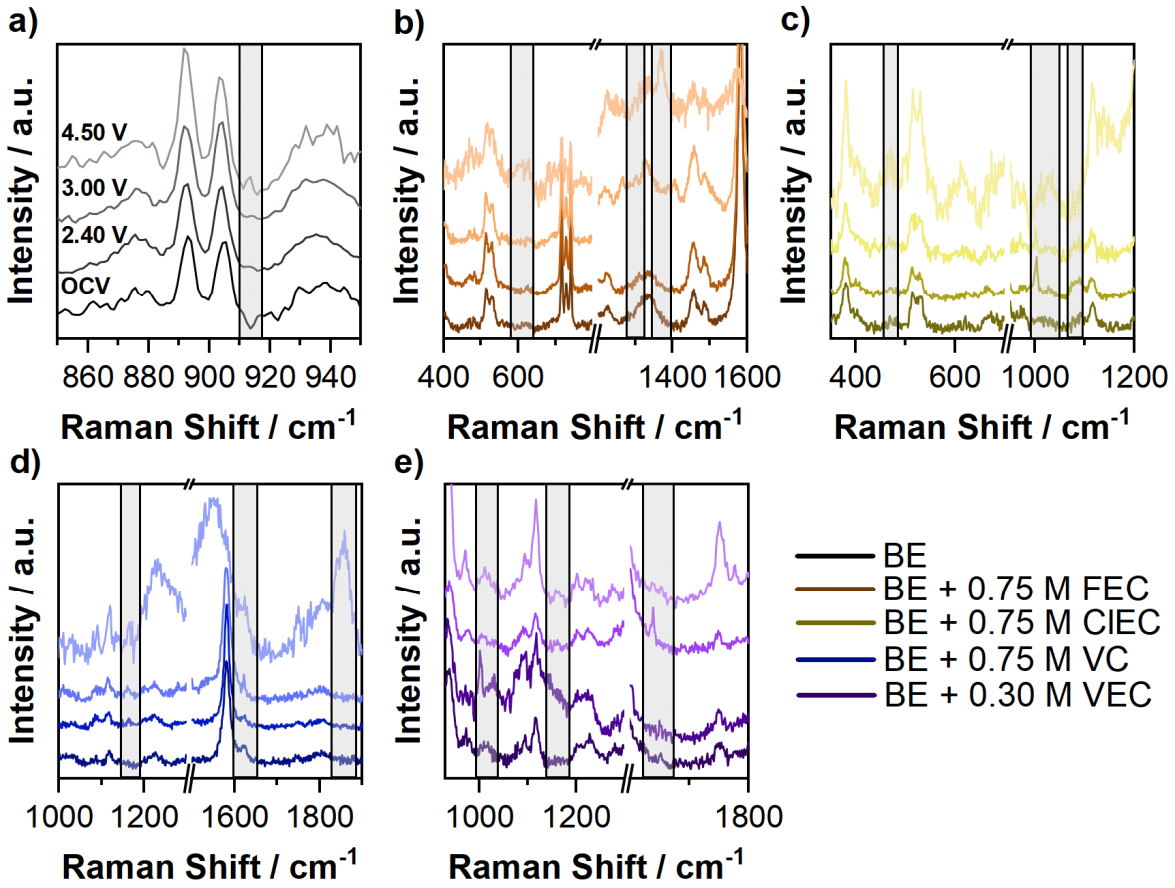

Figure 30: *Operando* SHINER spectra taken from the surface of a graphite electrode in the presence of the BE 2 (1 M $LiPF_6$ in EC:EMC 3:7 by weight) and the additive-containing electrolytes. For the SHINERS measurement, the graphite electrode was connected as working electrode, paired against a NMC622 counter electrode. Galvanostatic charge was performed at a C-rate of C/3. Au SHINs with a diameter of 55 nm were introduced to the electrode surface before cell assembly. Spectra were recorded at different cell voltages, denoted in the spectra and indicated by the intensity of the color. Spectra were recorded in the presence of **a)** the BE 2 (**black**) **b)** FEC (**brown**), **c)** ClEC (**dark yellow**), **d)** VC (**blue**), and **e)** VEC (**purple**). For spectrum acquisition, the samples were excited using a 633 nm laser, adjusted to a power output of 1.05 mW. Spectra were acquired over three accumulations of 35 s. Important newly arising bands observed in the spectra are highlighted by grey boxes. Figure redrawn with permission from [159].

For the BE 2 only one characteristic band was identified in the SHNER spectra taken from the surface of the graphite electrode (**Figure 30a**). This band was observed around 913 cm^{-1} and is typically assigned to O–C–O vibrations of diethyl-2,5-dioxahexane

dicarboxylate (DEDOHC), a common decomposition product of EC. In addition, it was observed that the band intensity increases with decreasing anode potential, being in good agreement with the assignment.

In contrast, the SHINER spectra recorded in the presence of the FEC-containing electrolyte exhibit multiple characteristic bands around 626 cm^{-1}, 1301 cm^{-1}, and 1370 cm^{-1} (**Figure 30b**). While the band around 626 cm^{-1} was observed already at low cell voltages, the other bands only arose at higher voltages, becoming distinct at the cut-off voltage of 4.50 V. According to the literature, all mentioned bands can be attributed to C–F stretching and deformation vibrations,[195] characteristic for the FEC molecule or its possible decomposition products. Alternative assignments are plausible, being in good agreement with the expected FEC degradation products. For example, the band around 626 cm^{-1} could alternatively be ascribed to LiOH, while both bands around 1301 cm^{-1} and 1370 cm^{-1} could correspond to the C=O stretching vibrations of semi-carbonate like structures. Interestingly, the band observed around 1370 cm^{-1} could be attributed to the C–C stretching vibrations of polyTHP or poly(furan). Moreover, this band is an exact match with the reference spectrum recorded from pure FEC (**Figure A37**). According to these assignments, the presence of the band around 1370 cm^{-1} could indicate the formation of poly(FEC), already presented in different studies.[73,74,196]

The SHINER spectra recorded from the surface of the graphite electrode in the presence of the ClEC-containing electrolyte show several characteristic bands around 470 cm^{-1}, 1003 cm^{-1}, 1030 cm^{-1}, and 1080 cm^{-1} (**Figure 30c**). Similar to the FEC-sample, most of the observed bands can be attributed to the formation of semi-carbonate-like structures, but alternative assignments are plausible. For example, the band around 470 cm^{-1} is typically attributed to semi-carbonates, but also an attribution to C–Cl stretching vibrations is also possible. Following these assignments, it is suggested that this band is attributed to the presence of a chlorinated semi-carbonate, as the formation of these species has already been highlighted by GC-MS investigation. The bands around 1003 cm^{-1}, 1030 cm^{-1}, and 1080 cm^{-1} can be ascribed to the C–O stretching vibrations of organic carbonates or Li_2CO_3, corresponding to the presence of typical additive or electrolyte solvent degradation products. In addition, the bands around 1003 cm^{-1} and 1080 cm^{-1}, can also be attributed to poly(VC), indicating additive polymerization, similar to FEC discussed prior.[73,74,196] While the bands around 470 cm^{-1} and 1030 cm^{-1} show increasing band intensities with higher cell voltages, a contrary behavior was observed for the bands around 1003 cm^{-1} and 1080 cm^{-1}, exhibiting decreasing band intensities for higher cell voltages. This phenomenon could be attributed to the partial dissolution of the formed SEI, as reported by Gajan *et al*.[32]

Only two characteristic bands around 1161 cm^{-1} and 1854 cm^{-1} were identified in the SHINER spectra obtained in the presence of VC (**Figure 30d**). The band around 1161 cm^{-1} can be ascribed to the presence of semi-carbonate like structures. It was observed at low cell voltages and showed an increasing band intensity with higher cell voltages. In contrast, the band around 1854 cm^{-1} was only observed for the cut-off voltage of 4.50 V and corresponds to Li_2C_2, a known decomposition product of lithiated organic molecules. It is worth noting that out of all spectra recorded from interphases of the different considered additive-containing electrolyte formulations, the SHINER spectra recorded in the presence of VC exhibit the least characteristic bands. This can be explained by the lack of characteristic functional groups in the VC molecule, which would discriminate the additive decomposition products from the degradation products of the electrolyte solvent molecules. Moreover, none of the characteristic bands were ascribed to the presence of poly(VC), which would have been expected to be present.

The SHINER spectra recorded from the graphite electrode surface in the presence of the VEC containing electrolyte showed characteristic bands around 1009 cm^{-1}, 1162 cm^{-1}, 1639 cm^{-1}, and 1651 cm^{-1} (**Figure 30e**). The bands around 1009 cm^{-1} and 1162 cm^{-1} were only observed for higher cell voltages and can be attributed to the presence of semi-carbonate like structures, originating from additive or electrolyte decomposition. In contrast, the band observed around 1651 cm^{-1} can be directly attributed to the VEC molecule, corresponding to the C=C stretching vibrations of its vinyl group. With increasing cell voltage, the band around 1651 cm^{-1} diminished. Instead, a new, sharp band arises around 1639 cm^{-1}. Due to its proximity to the original 1651 cm^{-1} band and the finding that the 1639 cm^{-1} band arises upon diminishing of the original band, it can be attributed to a VEC decomposition product. Additionally, performed DFT calculations emphasize that this band shift can actually be attributed to the ring-opening reaction of VEC (**Table A12**). At high cell voltages of 4.50 V, the intensity of the 1639 cm^{-1} band strongly decreases. While the band around 1651 cm^{-1} can be identified again, yet it does not exhibit its original intensity, thus indicating dissolution of the ring-opened VEC degradation product from the surface of the graphite electrode, instead of adsorption and desorption effects. Dissolution of the VEC decomposition product might additionally contribute to the ineffectiveness of the SEI formed in the presence of VEC, as indicated by GC-MS measurements.

All in all, the performed SHINERS experiments did not provide a valid explanation for the observed trends during galvanostatic cycling, despite identifying distinct characteristic bands for every considered electrolyte formulation. Instead, the SHINER spectra indicated mostly similar SEI compositions, only pointing out an increased formation of semi-carbonates in the presence of the introduced electrolyte additives.

7.5. Revealing the Formation of a VEC-derived CEI

The previous investigations clearly show improved electrochemical performance of the employed NMC622||graphite pouch cells in the presence of VEC. Despite the initial aim to optimize the graphite-electrolyte interphase, GC-MS investigations demonstrated the formation of an ineffective SEI for VEC-containing cells. Also, SHINERS characterization of the additive-derived interphases did not unravel the observed phenomena. As the reason for the enhanced performance cannot be found on the anode side, logically the cathode side has to be considered. Especially, as the employed NMC cathodes show great instabilities at the high voltage conditions, which were applied during the galvanostatic cycling experiments in this study. The NMC instability is already indicated in the roll-over failure observed for the BE 2-, FEC-, and ClEC-containing cells. Therefore, cathode degradation is expected to be the main reason behind the differences in the cycling performance and hence, additional galvanostatic cycling experiments were performed to investigate whether VEC protects the active material on the cathode. For these cycling experiments, the graphite anode and the NMC622 cathode were removed from the pouch cells after galvanostatic charge/discharge cycling at their respective end of life (50% SoH). 14 mm and 15 mm circular electrodes were punched from the extracted anodes and cathodes, respectively. In coin-cells, these aged electrodes were paired with pristine counterparts and galvanostatically cycled in the presence of the BE 2. Electrodes were extracted from the BE 2-, the FEC-, and the VEC-containing cells. The obtained discharge capacities are depicted in **Figure A41**. For the electrodes extracted from the BE 2 cells, very opposing results were obtained. While the cell with an aged graphite electrode, paired with a pristine NMC622 cathode, exhibited specific discharge capacities of around 160 mAh g^{-1}, only discharge capacities below 10 mAh g^{-1} were obtained from the cell with an aged NMC622 cathode. This finding clearly outlines the degradation of the cathode active material during galvanostatic cycling, accounting for the degrading cycling performance, whereas the graphite anode remains mostly intact. For the electrodes extracted from the additive-containing cells, similar trends were observed, showing discharge capacities of about 160 mAh g^{-1} for the cells with the aged graphite electrodes, while the cells containing the aged cathodes exhibited notably lower discharge capacities (**Figure A42**). However, for the coin cells containing the aged cathodes, notable differences were observed. While the cells with the cathodes extracted from the original BE 2 pouch cells exhibited very low discharge capacities, higher capacities of about 20 mAh g^{-1} and 50 mAh g^{-1} were obtained for the cathodes extracted from the FEC- and VEC-containing cells, respectively (**Figure A42b**). These findings are in good agreement with the galvanostatic cycling results, showing suppressed cathode degradation / roll-over failure in the presence of VEC, accounting for the higher discharge capacities obtained from the aged

cathodes. This further supports the assumption that the cathode side is the factor determining the performance in the chosen cell system.

To further investigate the effect of VEC on the cathode side, additional CV experiments were performed with an NMC622 WE, a graphite CE, and a Li-metal RE in the presence of the BE 2 and the VEC-containing electrolyte. The CVs recorded for the 1st and 2nd charge/discharge cycle are depicted in **Figure 31** below.

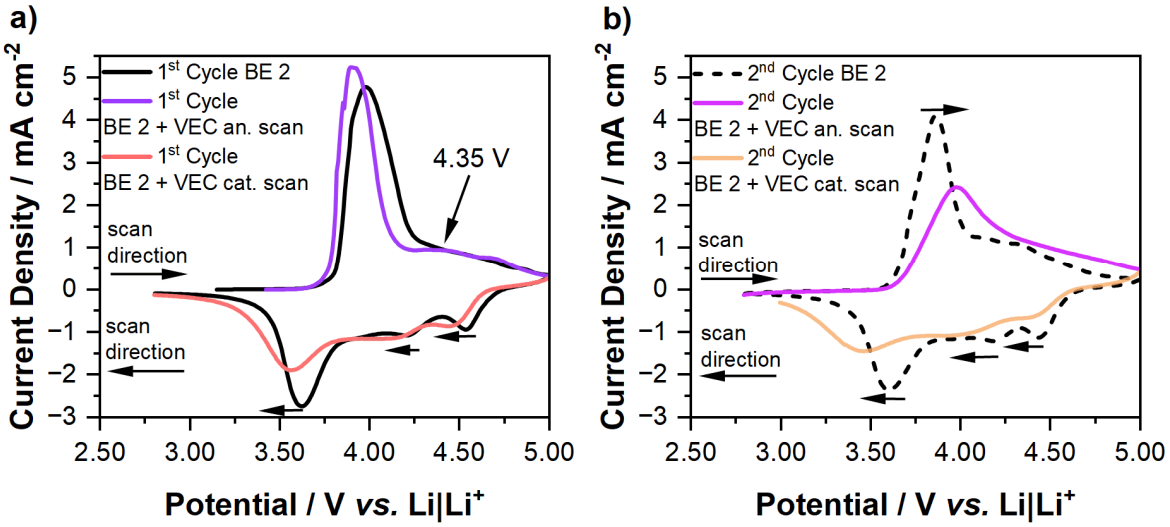

Figure 31: Cyclic voltammograms (CVs) of NMC622||graphite T-type Swagelok® cells with Li-metal reference electrodes obtained in the presence of the BE 2 (1 M $LiPF_6$ in EC:EMC 3:7 by weight, **black**) and the BE 2 + 0.30 M VEC (**colored**). Depicted are the **a)** 1st and **b)** 2nd scan. In addition, for the VEC-containing electrolyte the scans are separated into the anodic (an.; **purple**) and cathodic (cat.; **red**) scan. Cyclic voltammetry was performed in a potential range of 2.80 V – 5.00 V *vs.* Li|Li+ with a scan rate of 150 µV s^{-1}. Important peaks and the characteristic potential shift of bands observed for the CVs of the VEC-containing electrolyte formulation are highlighted by arrows and the recorded potential. Figure redrawn with permission from [159].

During the initial anodic scan, the obtained voltammograms of the BE 2 and the VEC cell exhibit strong similarities. Nevertheless, an additional broad peak can be observed at a high potential of 4.35 V *vs.* Li|Li+ in the presence of VEC, indicating oxidative reactions of the additive. In the following cathodic scan, a distinct shift of the peaks, ascribed to the NMC phase transition upon lithiation, towards lower potentials was observed. For the second CV cycle, all observed features exhibited a notable shifting and broadening, indicating the formation of a resistive interphase on the cathode surface in the presence of VEC. It is worth noting that a similar behavior was not observed during the CV experiments conducted for the other investigated electrolyte additives (**Figure A43**).

To further clarify interphase presence and gain insights into the morphologies of the formed interphases both on anode and cathode, SEM investigations were performed of the surface of NMC622 and graphite electrodes. These electrodes were taken from NMC622||graphite pouch cells after completed formation, as well as from pristine electrodes as reference. This was conducted for every investigated electrolyte formulation. The recorded SEM images are depicted in **Figure 32** and **Figure 33**.

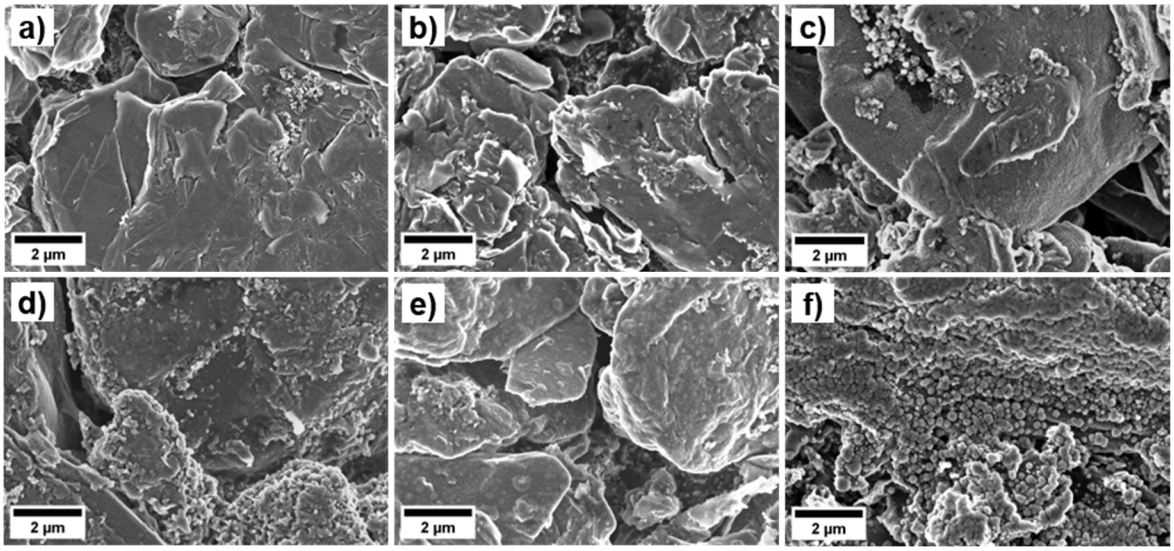

Figure 32: SEM images of the surface of a graphite electrode extracted from NMC622||graphite pouch cells after formation. The respective cells were cycled in the presence of **b)** the BE 2 (1 $_M$ $LiPF_6$ in EC:EMC 3:7 by weight) and the BE 2 + the optimized additive concentrations: **c)** FEC, **d)** ClEC, **e)** VC, and **f)** VEC. **a)** shows the pristine graphite electrode as reference. Figure redrawn with permission from [159].

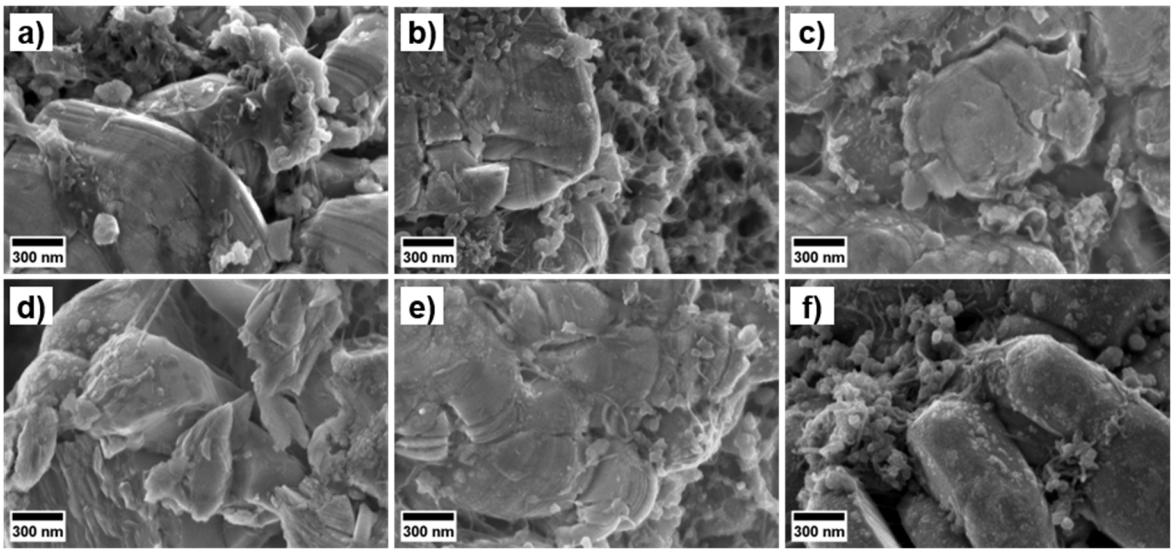

Figure 33: SEM images of the surface of an NMC622 electrode extracted from NMC622||graphite pouch cells after formation. The respective cells were cycled in the presence of **b)** the BE 2 (1 $_M$ $LiPF_6$ in EC:EMC 3:7 by weight) and BE 2 + the optimized additive concentrations: **c)** FEC, **d)** ClEC, **e)** VC, and **f)** VEC. **a)** shows the pristine NMC622 electrode as reference. Figure redrawn with permission from [159].

The SEM images recorded from the graphite electrodes for all considered electrolyte formulations exhibit a prominent interphase formation (**Figure 32**). Nevertheless, interphase morphologies strongly vary. For BE 2 the formation of a uniform SEI was observed, covering the majority of the electrodes' surface. The interphase formed in the presence of FEC appears denser and smoother, compared to BE 2. In contrast, the SEI formed on the graphite electrode, which was cycled in the presence of the ClEC-containing electrolyte, looks brittle and less uniform and formed several overlapping patches on the graphite particles. Similar to the ClEC-derived SEI, the interphase formed in the presence VC appears patchy and less uniform, however, the morphology resembles the SEI observed

for the BE 2 cell. For the SEI formed in the presence of VEC, distinct differences were observed in the morphology. Here the interphase exhibits a mossy texture, instead of the mostly smooth and uniform interphases exhibited by the other electrolyte formulations. In addition, the VEC-derived interphase appears to be very brittle, allowing the direct observation of the anode active material through prominent gaps between the SEI patches. This incomplete coverage could be attributed to the dissolution of the VEC decomposition product, indicated by SHINERS investigations (**Figure 30e**). Moreover, the direct exposure of anode surface to the electrolyte could account for the ongoing electrolyte decomposition, which was revealed by GC-MS measurements. In contrast to the SEM images obtained from the graphite electrodes, the SEM images recorded from the NMC cathodes mostly do not exhibit the formation of an interphase (**Figure 33**). Only for the VEC sample interphase formation on the cathode was captured. The recorded SEM images exhibit a rough and patchy interphase covering a majority of the active material surface, clearly demonstrating CEI formation in the presence of VEC. These findings further validate the results of the previous experiments, which already indicated the VEC-induced formation of an interphase on the cathode.

In addition to the SEM investigations, graphite electrodes were further investigated *via* ToF FIB-SIMS, shining light on the in-depth elemental distribution of Mn and different Li-species, including Li, LiF, and Li_2O, on the anode surface. For the analysis, the electrochemically aged graphite electrodes were extracted from NMC622||graphite pouch cells cycled in the presence of all investigated electrolyte formulations after their respective end of life (50% SoH). Mn was chosen for elemental analysis to resemble the deposition of TM ions originating from the cathode active material, while the presence of Li-species can be attributed to SEI formation due to electrolyte degradation. In **Figure 34**, the elemental distribution for the overall Li-species and Mn are depicted for the graphite electrodes cycled in the presence of the BE 2 and the FEC- and VEC-containing electrolytes. In the appendix, **Figure A44** and **Figure A45** show the elemental distribution for the other investigated electrolyte formulations, as well as a separation of the different monitored Li-species.

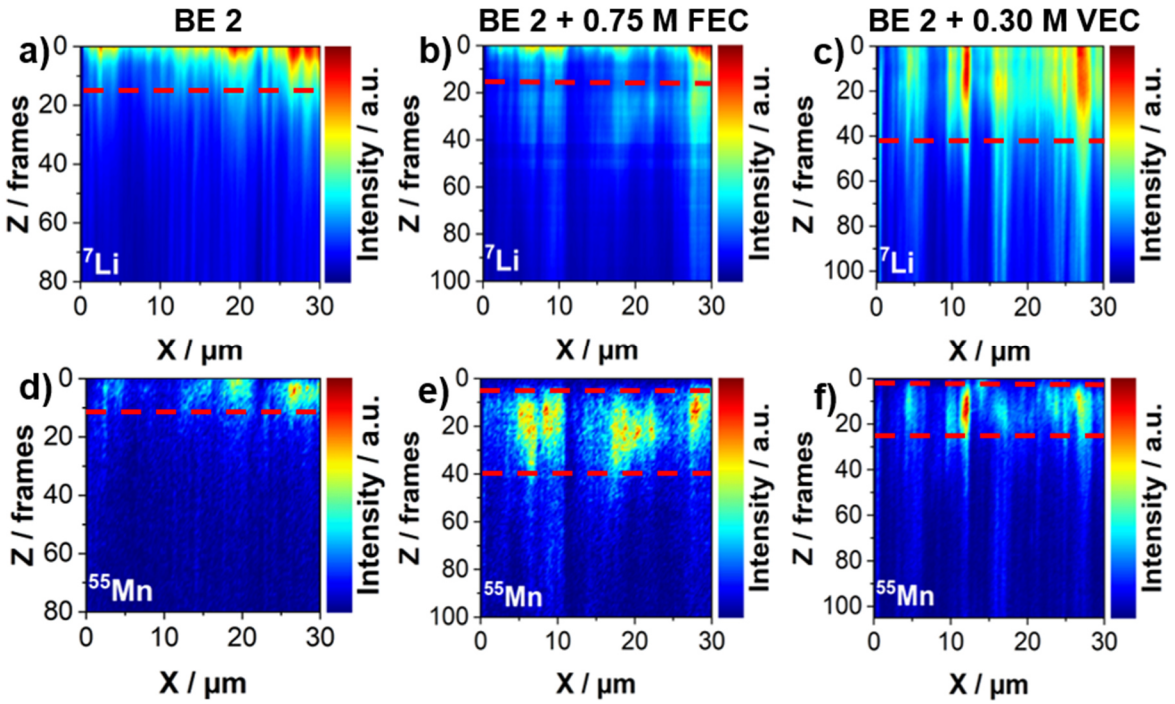

Figure 34: Depth profiles obtained for the surface layers from graphite electrodes extracted from NMC622||graphite pouch cells after galvanostatic charge/discharge cycling. Investigation was performed *via* focused ion beam secondary mass spectrometry equipped with a time of flight analyzer. The figure shows the elemental distribution of the combined Li-species (**a** – **c**) and of Mn (**d** – **f**), for graphite electrodes cycled in the presence of the BE 2 (1 $_{M}$ $LiPF_6$ in EC:EMC 3:7 by weight; left), the FEC-containing electrolyte (center), and the VEC-containing electrolyte (right). Segments of the depth profiles with high concentration of the respective element are highlighted by red lines in the figure. Note that due to the similar sample compositions it can be assumed that the thickness of each ablated layer (frame) is similar, enabling the comparison of the investigated samples. For the depth profiles of the separated LI-species and the depth profiles obtained for the other considered electrolyte formulations, the reader is referred to **Figure A44** and **Figure A45**. Figure redrawn with permission from [159].

As shown in **Figure 34**, **Figure A44**, and **Figure A45**, the obtained depth profiles exhibit distinct difference for the probed elements. Concerning the distribution of Li-species, a notable concentration of Li-species was found in the very top layers of the graphite electrodes taken from the BE 2-, FEC-, and VC-cells. In contrast, the electrodes extracted from cells cycled in the presence of ClEC and VEC demonstrate the presence of Li-species in deeper layers of the electrode surface. The concentration of Li-species in the electrode top layers indicates the formation of a more effective SEI, effectively keeping the electrolyte away from the electrode, limiting its decomposition. On the contrary, the presence of Li-species in deeper electrode layers suggests the formation of an ineffective SEI, allowing the penetration of the electrolyte through the interphase closer to the electrodes surface, which results in ongoing electrolyte degradation. This finding corresponds well with the SEM images discussed, showing a brittle and patchy SEI formed in the presence of ClEC and VEC, ineffective in expelling the electrolyte. Interestingly, a contrary trend can be observed for the elemental distribution of Mn. Here, a notable concentration of Mn was found only in the top layers of the graphite electrode for the BE 2-, VC-, and VEC-samples. In contrast, the graphite electrodes taken from cells cycled in the presence of FEC and ClEC exhibit the

presence of Mn also in deeper electrode layers. The penetration of Mn into deeper electrode layers is the result of TM etching from the cathode active material, aggravated by the presence of hydrofluoric and hydrochloric from FEC and ClEC degradation.[197,198] While the BE 2- and VC-samples show similar Mn distributions as the electrode taken from the VEC cell, the individual cycle numbers have to be considered. While BE 2 and VC cells only performed about 400 – 500 charge/discharge cycles, the cycle life in the presence of VEC was almost quadrupled. The similarity of the Mn distribution despite the difference in cycle numbers clearly indicates a reduced dissolution of TM ions in the presence of VEC. Therefore, it can be suggested that the VEC-derived CEI accounts for the observed improvement during galvanostatic cycling, greatly reducing TM dissolution from the cathode active material and effectively suppressing the roll-over failure.

7.6. Characterization of the VEC-derived CEI by Raman Spectroscopy

Following the additionally performed measurements, which highlighted the formation of an effective CEI in the presence of VEC, SHINERS investigations were performed to characterize the additive-derived interphase. To ensure that the addition of VEC to the electrolyte formulation is the main reason behind the observed CEI formation, SHINER spectra were recorded from the surface of NMC622 electrodes in the presence of the BE 2 and the BE 2 + 0.30 $_{M}$ VEC. The obtained spectra are depicted in **Figure 35**. Again, only relevant bands will be discussed in the following segment. For a complete assignment of all identified bands and the full range spectra, the reader is kindly referred to **Table A13** – **Table A15** and **Figure A46** – **Figure A49** in the Appendix. As expected, the SHINER spectra recorded from the surface of the NMC622 electrode in the presence of the BE 2 did not exhibit prominent bands, assignable to or indicating the formation of a CEI (**Figure 35a** and **Figure A46**). This finding is also in good agreement with the results of the SHINERS experiments performed in the previous chapters, showing little to no CEI formation in the presence of a carbonate-based electrolyte without additive (**Figure 13** and **Figure 23**; **Chapters 5** and **6**). In contrast, the SHINER spectra recorded in the presence of the BE 2 + 0.30 $_{M}$ VEC exhibit several new bands arising at the cut-off potential of 4.50 V *vs*. Li|Li^{+}, confirming CEI formation.

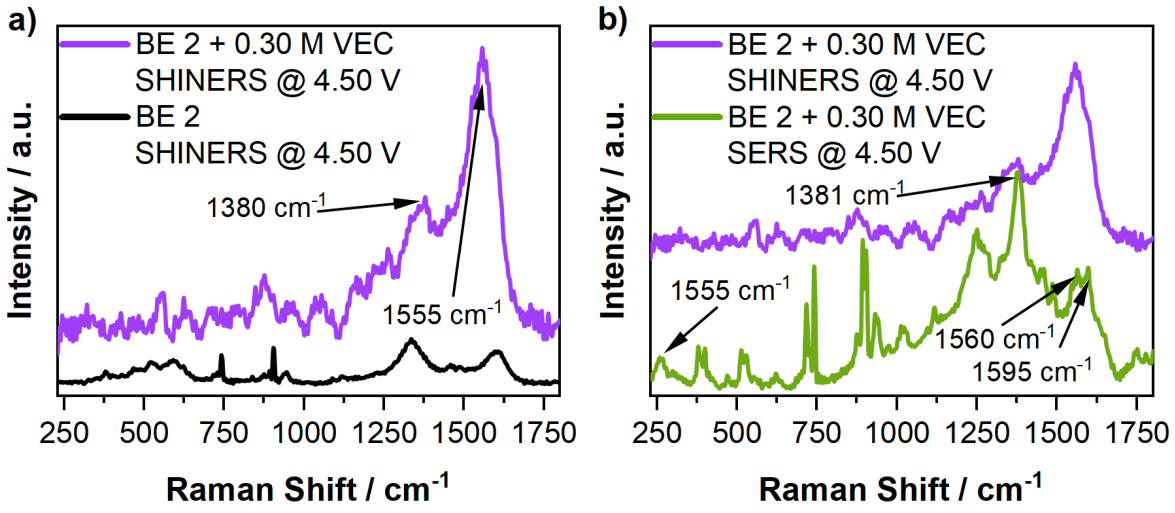

Figure 35: **a)** *Operando* SHINER spectra recorded from the surface of an NMC622 electrode in the presence of the BE 2 (1 M $LiPF_6$ in EC:EMC 3:7 by weight; **black**) and the BE 2 + 0.30 M VEC (**purple**), recorded at the cut-off potential of 4.50 V *vs.* Li|Li^+. For the SHINERS measurement, the NMC622 electrode was connected as working electrode paired against a graphite counter electrode. In addition, a Li-metal electrode was introduced as reference electrode to monitor the electrodes potential. Galvanostatic charge was performed at a C-rate of C/3. Au SHINs with a diameter of 55 nm were introduced to the electrode surface before cell assembly. **b)** Comparison of the SHINER and SER spectra (**green**) recorded in the presence of the VEC-containing electrolyte of the surface of a NMC622 or roughened Au electrode, respectively, at the cut-off potential of 4.50 V *vs.* Li|Li^+. For the SERS measurement, the Au electrode was charged with a sweep rate of 150 μV s^{-1}. For spectrum acquisition, the samples were excited using a 633 nm laser, adjusted to a power output of 1.05 mW. Spectra were acquired over three accumulations of 35 s. Important bands are highlighted by arrows and band positions are noted in the spectra. Figure redrawn with permission from [159].

At the OCP, the SHINER spectrum exhibits the typical bands assigned to the NMC active material, the graphitic conductive agent, and the electrolyte species. Moreover, one distinct band was observed around 870 cm^{-1}, corresponding to VEC molecule. Upon galvanostatic charging of the cathode new bands were identified, starting already at relatively low electrode potentials of 3.30 V *vs.* Li|Li^+. With increasing electrode potential, additional bands were observed and became more distinct. Most of the newly arising bands can be ascribed to the presence of semi-carbonate species, originating from VEC decomposition. However, the most prominent bands observed around 1380 cm^{-1} and 1555 cm^{-1} are typically ascribed to alkyl-carboxylates. Based on the band intensities it can be further suggested that the alkyl-carboxylates make up the majority of the VEC-derived CEI. Albeit showing the clear formation of a CEI in the presence of VEC, the obtained SHINERS results have to interpreted with care, due to interferences with bands ascribed to the electrode material. Especially the prominent bands around 1380 cm^{-1} and 1555 cm^{-1}, highly characteristic for the VEC-derived CEI, are overlapping with broad D- and G-bands of the graphitic conductive agent observed around 1335 cm^{-1} and 1600 cm^{-1}, jeopardizing a clear assignment. To overcome this challenge, additional *in situ* SERS measurements were performed in the presence of the BE 2 and the VEC-containing electrolyte. A roughened Au electrode was employed for the SERS investigations, limiting the bands originating from the electrode. The recorded SER spectra are depicted in **Figure A48** and **Figure A49** and a detailed band assignment can be found in **Table A15** and **Table A16**. The SER spectra

recorded in the presence of the BE 2 did not demonstrate the formation of a CEI, similar to the performed SHINERS investigations. This further strengthens the previous results of the CV, d*Q*/d*V* *vs*. voltage, SEM, and SHINERS experiments. In good agreement with the SHINER spectra recorded in the presence of the VEC-containing electrolyte, the SERS counterparts clearly exhibited the formation of an interphase. In addition, the characteristic bands around 1380 cm^{-1} and 1560 cm^{-1} were clearly identified in the SER spectra at high electrode potentials, as shown in **Figure 35b**. At 4.50 V *vs*. Li|Li^+ the SER spectrum revealed the presence of another band around 1595 cm^{-1}, covered by the G-band in the original SHINER spectra. In accordance with the other prominent bands, the band around 1595 cm^{-1} can also be attributed to alky-carboxylates. In addition, the SERS spectra recorded at 4.50 V *vs*. Li|Li^+ exhibited an arising of a band around 267 cm^{-1}, characteristic for the C–C deformation vibrations of aliphatic chains, according to the literature.[195]

7.7. Unraveling the Cross-Talk Mechanism of VEC

Up to this point, all performed investigations undoubtably highlight the formation of an interphase on the cathode surface in the presence of VEC. SHINERS and supporting SERS measurements identified alkyl-carboxylates as main components of the VEC-derived CEI. Nevertheless, the underlying formation mechanism still remains unsolved. This is especially interesting, as alkyl-carboxylates, typical products of reductive decomposition reactions, are mostly found on the anode side.[199,200] Subsequently, the presence of alkyl-carboxylates on the cathode side could be explained by two different mechanisms. The first one being the oxidation of VEC on the cathode surface, the second one resembles a cross-talk phenomenon. In this cross-talk VEC is initially reductively degrading on the anode, followed by a transport to the cathode side. The first mechanism is contradicted by the previously performed experiments in this chapter. SHINER spectra recorded in the presence of VEC indicate CEI formation already at a potential of 3.30 V *vs*. Li|Li^+ (**Figure A47**). In contrast, the CV measurement performed of the VEC-containing electrolyte on an NMC622 WE did not exhibit a notable oxidation peak below said potential. Therefore, the cross-talk is strongly suggested by the experimental data.

To clarify the origin of VEC-derived alkyl carboxylates the reductive degradation product of VEC was synthesized, following an approach presented by Lucht *et al*.[25,181] In this approach, Li-naphthalenide is used for modelling of the reactivity of graphite electrodes, which enables a straightforward synthesis of a considerable amount of realistic additive degradation products for further characterization investigations. Initial characterization of the obtained VEC reduction product was conducted *via* cross-polarization magic-angle spinning $^{13}C\{^1H\}$ NMR (**Figure A50**). The NMR analysis presented alkene-, carbonate-, carboxylate-, and alcoholate-species as main products of the reductive VEC decomposition.

Additionally, SERS investigations were performed for the comparison of the synthesized VEC-degradation product with the SHINERS and SERS investigations of the cathode surface in the presence of the VEC-containing electrolyte. As shown in **Figure A51**, the SER spectrum of the artificial VEC-degradation product exhibits the characteristic bands around 1380 cm^{-1}, 1550 cm^{-1}, and 1600 cm^{-1}. As discussed above, these bands can be attributed to the presence of alkyl-carboxylates as already observed in the initial Raman investigations. This finding conclusively demonstrates that the alkyl-carboxylates, which make up the majority of the VEC-derived CEI, originate from initial reductive degradation on the anode and are subsequently transferred to the cathode side.

After confirming the origin of the carboxylate ions detected on the cathode surface, and thus the suggested cross-talk phenomenon, the final mechanism behind the formation of a VEC-derived CEI has yet to be elucidated. Therefore, an in-depth analysis of all obtained SHINER and SER spectra was conducted. By combining information obtained from the anode and the cathode side, a comprehensive mechanism was postulated (**Figure 36**). In the suggested mechanism, three main steps were considered. The first step (**1**) is ascribed to the notable shift of the band observed around 1651 cm^{-1} to 1639 cm^{-1}, observed in the presence of the VEC-containing electrolyte between a cell voltage of 2.40 V and 3.00 V. As discussed above, this band corresponds to the C=C bond of the VEC vinyl group, rendering this band highly characteristic for the additive molecule. As indicated by the DFT-calculated Raman spectrum shown in **Figure A37**, the discussed band shift can be ascribed to the ring-opening reaction following the reduction of VEC. With increasing cell voltage, a severe decrease of the band around 1639 cm^{-1} was observed (**2**), indicating the dissolution of the ring-opened VEC degradation product from the anode surface and its subsequent transfer to the cathode side driven by electro-migration. Contrary to initial expectations, the presence of a C=C double bond, originating from the VEC-degradation product, was not confirmed by the SERS measurements. However, in the SER spectrum recorded at a potential of 4.50 V *vs.* $Li|Li^+$, an additional distinct band around 267 cm^{-1} was identified. In addition, less prominent bands were observed around 1027 cm^{-1} and 1151 cm^{-1}. All of the mentioned bands correspond to different C–C stretching vibrations, while the band around 267 cm^{-1} is especially characteristic for the presence of aliphatic chains. Following the absence of C=C double bonds and the creation of additional aliphatic C–C bonds indicated by the SER spectrum, it can be assumed that the ring-opened VEC degradation product undergoes oxidative polymerization on the cathode surface, resulting in the formation of polymeric CEI (**3**).

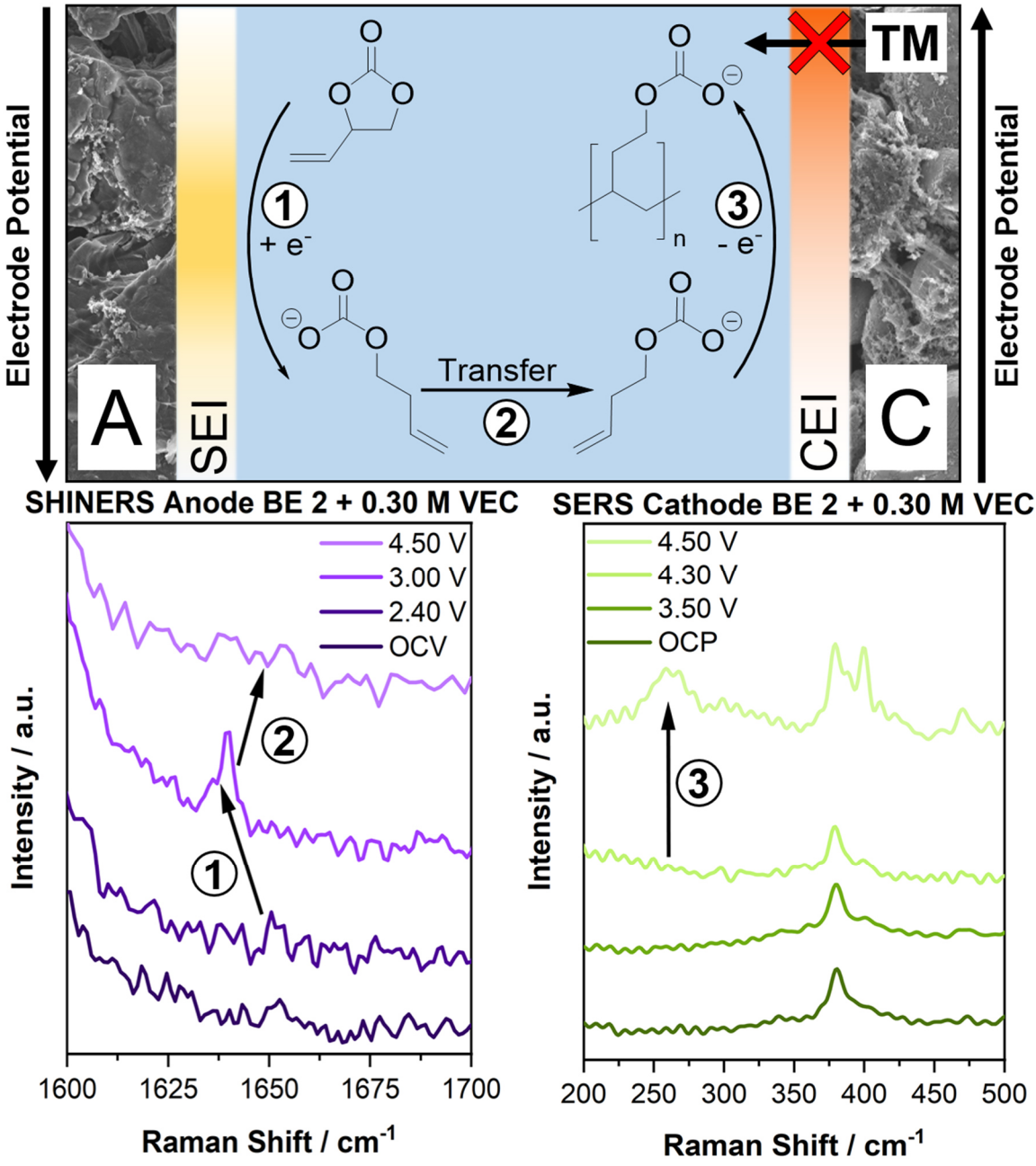

Figure 36: Schematic depiction of the cross-talk mechanism suggested for the electrolyte with VEC, based on the results of the SHINERS (**purple**) and SERS (**green**) investigations of the electrode surfaces in the presence of the BE 2 (1 M $LiPF_6$ in EC:EMC 3:7 by weight) + 0.30 M VEC shown in the lower segment of the figure. The upper segment of the presented overview displays a schematic lithium-ion battery (LIB), comprising of an anode (graphite, **A**) and a cathode (NMC622, **C**) and the SEI (**yellow**) and CEI (**red**) formed on the respective surfaces. Here, changes in the color intensity resemble formation or dissolution of the particular interphase depending on the electrode potential. The proposed reaction mechanism, resulting in the formation of the interphases is displayed in the center of the schematic LIB and important steps are highlighted by numbers, ascribed to the following processes: **1**: Reduction of VEC leading to a ring-opening of the molecule. **2**: Dissolution of the VEC reduction product and subsequent transfer to the cathode side *via* electro-migration. **3**: Oxidative Electro-polymerization of the VEC reductive degradation product on the surface of the cathode, leading to the formation of a polymeric CEI. Finally, the formed VEC-derived CEI is effective in suppressing transition metal (**TM**) dissolution into the electrolyte accounting for the enhanced performed during galvanostatic cycling. Note that the numbers displayed in the Raman spectra can be ascribed directly to the numbers in the reaction mechanism, resembling the respective reaction step. Figure redrawn with permission from [159].

The oxidative polymerization of molecules featuring vinyl groups is known in the literature, supporting this assumption.[201] It can be further concluded that the formed polymeric VEC-

derived CEI effectively suppresses the dissolution of TM ions from the cathode active material into the electrolyte, thus accounting for the enhanced galvanostatic cycling performance. The presented conclusion and the proposed mechanism for the VEC cross-talk mechanism are in good agreement with the results of all investigations discussed in this chapter. Nevertheless, it has to be emphasized that the formation of the polymeric VEC-derived CEI was only observed for high electrode potentials / high cell voltages. This is in good agreement with literature findings, suggesting CEI formation in the presence of VEC under harsh conditions.[10,202,203] Therefore, it is most likely that the beneficial influence of VEC can only be observed at these harsh, high-voltage conditions. At lower cell voltages, *e.g.* 4.20 V, it can be suggested that the performance of VEC-containing cells decreases, due to the formation of an ineffective SEI. Another important aspect to consider is the instability of NMC at high voltages, determining the cycle life of the employed cells. At lower cell voltages, cathode stability is notably higher. In such a scenario, the FEC-, and maybe ClEC-containing cells are expected to show the highest performance, as they form a more effective SEI. Indeed, this hypothesis was validated by GC-MS and galvanostatic cycling experiments.

7.8. Conclusion

The objective of the presented study was to investigate the cross-talk mechanism of film-forming electrolyte additives in high-voltage NMC622||graphite pouch cells. The introduction of the EC-derived electrolyte additives FEC, ClEC, VC, and VEC notably influenced the electrochemical performance of the respective cells during galvanostatic charge/discharge cycling. Especially the VEC-containing cells exhibited a drastic improvement, notably outperforming the cells containing the other investigated electrolyte formulations. The conducted GC-MS measurements of the aged electrolyte indicated the formation of an ineffective SEI in the presence of VEC, identifying a distinct concentration of typical reductive electrolyte decomposition products. A following SHINERS characterization of the SEI composition did not reveal a reasonable explanation of the observed phenomenon. Instead, additional CV, d*Q*/d*V* *vs.* voltage, SEM and FIB-SIMS investigations indicated the formation of an interphase on the cathode side in the presence of VEC. SHINERS investigations of the cathode surface, supported by complementary SERS measurements, finally confirmed the formation of a VEC-derived CEI. Raman experiments identified alkyl-carboxylates as main composition product of the additive-derived interphase. Typically, these species are formed on the anode side following carbonate reduction, and raised the assumption of a cross-talk phenomenon occurring in the presence of VEC. The synthesis of a reductive decomposition product from VEC and a comparison with the CEI Raman spectra confirmed this hypothesis. Based on the combined Raman spectra obtained from the anode and cathode surface in the presence of VEC, a comprehensive cross-talk

mechanism was assembled, underlining the formation of a polymeric VEC-derived CEI. Ultimately, the proposed mechanism unites the collected data and provides reasonable explanations for all phenomena encountered within this study. Additionally, these findings nicely support the previously outlined potential of the SHINERS technique for the collection of molecular information of both the anode and cathode side under real working conditions. Thereby, the combination of the received data allows the understanding of complex processes and the postulation of comprehensive mechanisms explaining interphase formation.

8. General Conclusion and Future Perspectives

In the presented thesis, two major objectives were pursued, as depicted in **Figure 37**. First, the optimization of the electrode-electrolyte interphase in high-voltage LIBs to enhance galvanostatic cycling performance employing electrolyte additives. The second objective of this thesis was the successful implementation and optimization of the SHINERS technique into the LIB context were demonstrated, and the formation and composition of interphases formed on the surface of various electrode materials were investigated under real working (*operando*) conditions. These objectives also included the characterization of the additive-derived interphases by the established *operando* SHINERS measurements. Thus, enabling the investigation of the underlying interphase formation mechanisms and the relation between additive structure, interphase properties and composition through the combination of both objectives of this thesis.

Starting with the optimization of the SHINERS technique (**Chapter 4.2.5)**, the NP synthesis, coating and characterization, preparation of the SHINERS samples, and the development of specific cell and electrode configurations are discussed in detail. This section also contains a comprehensive overview of common challenges encountered during SHINERS experiments and possible causes elucidated by supporting experiments. In the first main part of the thesis (**Chapter 5**) the focus was set on the implementation of SHINERS into the LIB context. As a proof-of-concept, SHINERS was employed for the investigation of the formation of an additive-derived CEI in an established LIB system. Initially, performed galvanostatic cycling experiments in high-voltage NMC111|graphite cells demonstrated a distinct influence of the THP additive on the electrochemical performance, reducing capacity fading and prolonging the cycle life of the respective cells. Supported by SEM and EDX, *operando* SHINERS measurements finally captured the formation of a THP-induced CEI on the surface of the NMC cathodes at high electrode potentials. In addition, poly(THP) was identified as the main interphase component, accompanied by the formation of an EC-THP copolymer in low margins. Based on the obtained SHINERS results a reaction mechanism was proposed for the electro-polymerization of THP, employing QC calculations and in good agreement with the results of the electrochemical investigations. Indeed, the performed proof-of-concept study successfully demonstrated the implementation of SHINERS in LIBs, allowing the monitoring of interphase formation under real working conditions. The obtained Raman spectroscopy results were in good agreement with the QC calculations and electrochemical investigations, further outlining the potential of the SHINERS technique for providing reliable information on the complex formations of interphases.

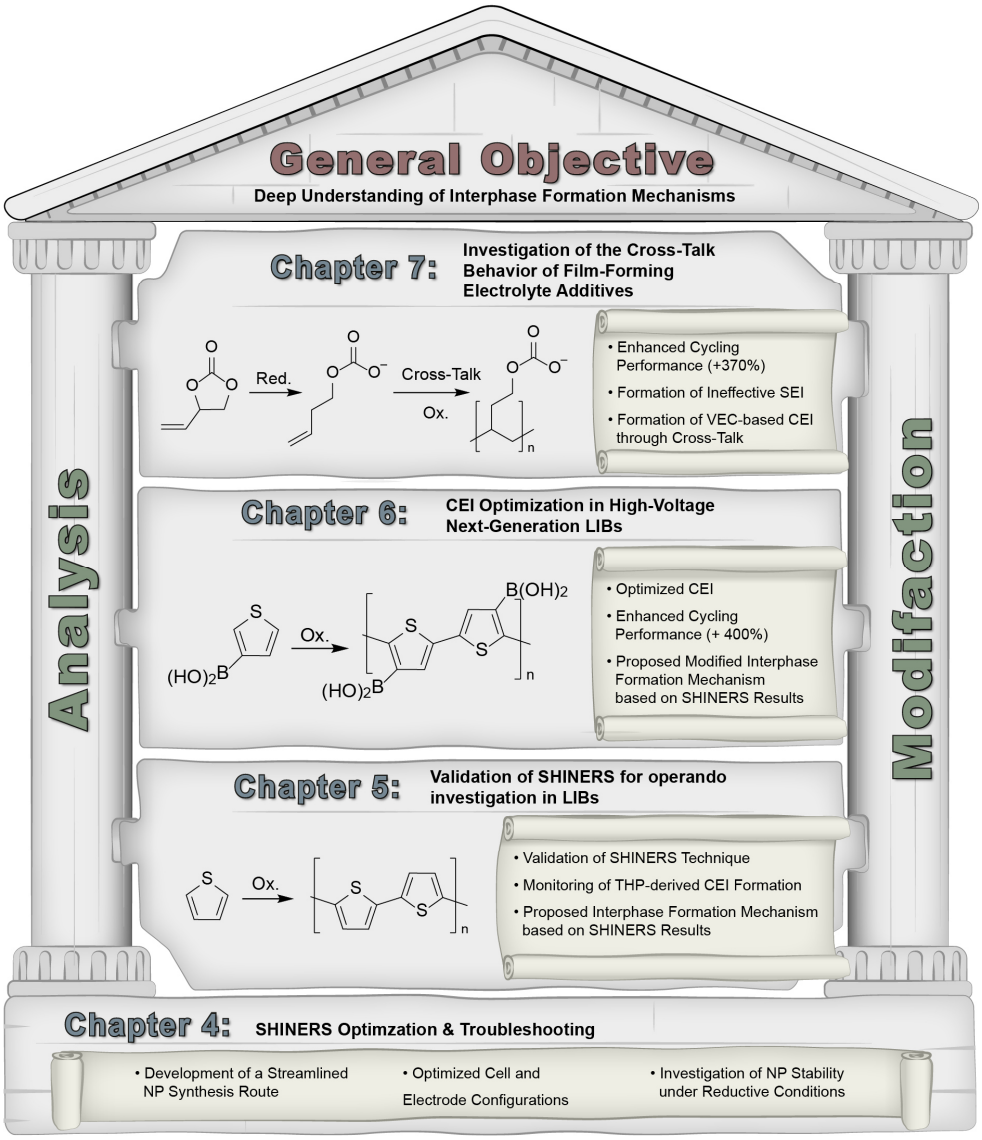

Figure 37: Comprehensive overview of the main objectives accomplished within this thesis. Based upon the proposed structure depicted in **Figure 7**, the most important achievements are presented for the respective chapters. In addition, interphase formation mechanisms unraveled using *operando* SHINERS are depicted for the regarding chapters.

The optimization of the cathode-electrolyte interphase was the primary objective of the second main chapter (**Chapter 6**). Therefore, a variety of THP-based electrolyte additives featuring diverse functional groups were investigated on their impact on the cycling behavior of high-voltage NMC811||graphite pouch cells. The performed galvanostatic charge/discharge cycling experiments revealed a beneficial influence of electron withdrawing functional groups on the electrochemical performance and identified 3-THP-BOH as the most promising candidate. Further galvanostatic cycling experiments with an optimized concentration of 3-THP-BOH revealed a dramatically enhanced electrochemical performance of the additive-containing cells, resulting in reduced capacity fading and a suppressed roll-over failure, and hence a quadrupled cycle life of the respective cells. Supported by SEM and EDX, *operando* SHINERS investigations of the NMC811 electrodes in the presence of 3-THP-BOH showed the formation of a polymeric additive-derived CEI

comprising mostly of poly(3-THP-BOH), and a minor share of an EC-3-THP-BOH copolymer. Interphase formation was observed at notably lower electrode potentials compared to pure THP. This can be attributed to the presence of the boronic acid group, which enables a modified reaction mechanism for the additives' electro-polymerization as shown by the proposed mechanism calculated *via* QC (**Figure 26**). The successful optimization of the NMC811-electrolyte interphase resulted in greatly enhanced galvanostatic cycling performance and the stabilization of the NMC811 material through the implementation of 3-THP-BOH. In addition, the conducted study also further outlines the power of the SHINERS technique. Here, SHINERS provided detailed information on the potential-depended interphase formation, elucidating the influence of the boronic acid group on the formation mechanism.

In the third part of the thesis (**Chapter 7**), the cross-talk behavior of film-forming electrolyte additives was investigated. In galvanostatic charge/discharge cycling experiments in high-voltage NMC622||graphite pouch cells, several EC-based electrolyte additives exhibited a distinct influence on the electrochemical performance. The well-established electrolyte additives FEC and VC demonstrated only a minor improvement, compared to the BE 2 cells. In contrast, cells containing an optimized concentration of VEC showed a notably improved electrochemical performance, reduced capacity fading and a suppressed roll-over failure. This resulted in a cycle life three times higher, compared to the other considered electrolyte formulations. Despite the drastically improved performance and the initial ambition to optimize the SEI, GC-MS investigations showed notable concentrations of reductive electrolyte decomposition products, indicating the formation of an ineffective interphase on the graphite electrode in the presence of VEC. In addition, *operando* SHINERS measurements of the different additive-derived SEIs did not yield sophisticated explanations to elucidate the observed phenomena. Following these conclusions, a cathode-activity of the VEC additive was suggested to account for the enhanced electrochemical performance and the suppressed roll-over failure. This assumption was strengthened by CV and SEM investigations, indicating the formation of a VEC-derived CEI. *Operando* SHINERS and SERS measurements captured the presence of an interphase for the VEC-containing electrolyte at high electrode potentials, identifying carboxylate-species as main interphase product. The presence of carboxylates on the cathode side, which are typically formed on the anode through reductive carbonate decomposition, suggests the existence of a cross-talk mechanism. After synthesis of the reductive decomposition product of VEC, CEI SHINER and SER measurements were conducted, in which identical characteristic bands were able to validate the proposed mechanism. The combination of *operando* Raman spectra recorded from anode and cathode surface in the presence VEC allowed the postulation of a comprehensive cross-talk mechanism, shown in **Figure 36**. The

presented mechanism includes reductive VEC decomposition on the anode surface, dissolution and subsequent transfer to the cathode, and electro-polymerization of VEC decomposition products on the cathode surface. In this part of the thesis, o*perando* SHINERS was employed for the elucidation of the complex cross-talk mechanism in the presence of VEC in high-voltage applications, and for the explanation of the prolonged cycle life. Moreover, a greatly enhanced galvanostatic cycling performance of the NMC622||graphite pouch cells, was achieved in this part of the thesis, compared to the cells cycled in the presence of the BE 2, FEC, and VC.

In conclusion, this thesis demonstrated the impact of suitable electrolyte additives on the galvanostatic cycling performance of high-voltage pouch cells with Ni-rich NMC materials, achieving dramatically enhanced cycle lives by interphase optimization. It was possible to suppress the effect of roll-over failure through the implementation of suitable additives, which remained a severe challenge for NMC cathodes in high-voltage applications. In addition, 3-THP-BOH was presented as a new and promising CEI-forming additive for high-voltage LIBs. Besides interphase optimization, the main focus of this work was the optimization and implementation of SHINERS in LIBs for the systematic characterization of interphases under real working conditions. The successful implementation and the utilization of SHINERS in the characterization of additive-derived interphases was achieved within this thesis, elucidating different complex interphase formation mechanisms.

Nevertheless, limitations of the SHINERS technique were encountered. For investigations on the cathode side, SHINERS proved to be a reliable tool, working without major interferences and challenges. This suggests a straightforward transfer of SHINERS from NMC cathodes to other promising positive electrode materials such as LNMO, for the characterization of interphases at even higher electrode potentials. On the anode side however, major challenges were faced, as discussed in **Chapter 4.3**. Here, SHINERS measurements were greatly hindered by the NPs instability towards lithiation at lower potentials and by burying of the NPs under the growing SEI with a subsequent quenching of the SHINERS effect. Albeit, the investigation of interphases on the anode side is of great importance, as next-generation anode materials, *e.g.* Si, Li-metal or Na-metal, have to be stabilized by effective SEIs for their implementation. To enable the utilization of SHINERS in these challenging conditions, further development of the technique is necessary. One factor that can easily be modified is the protective coating around the NPs. During this thesis solely, NPs with a SiO_x shell were utilized, where SiO_x is prone to lithiation. The use of other suitable coating materials could overcome this limitation and enhance the reductive stability of the NPs. The second adjustable factor is the size of the NPs. NPs with a greater diameter exhibit a higher signal enhancement and are less vulnerable to interphase burying, resulting in a greater accessibility for laser excitement. The variation of the NP shape, *e.g.* star,

pyramidal or raspberry, can also lead to higher signal enhancements, coping with the encountered quenching effects on the anode side. [204,205]

Besides technical limitations, challenges regarding the identification of additive-derived interphase species were encountered. Especially in **Chapter 7**, the separation of species originating from the carbonate-based electrolyte and from the carbonate-based electrolyte additives was challenging. For future studies, a cautious selection of the electrolyte system or the investigated electrolyte additives is to be advised. One possible brief example is presented in **Figure A5**, where *γ*-butyrolactone was employed as electrolyte solvent for carbonate-based film-forming additives. The performed SHINERS investigations yielded very promising results, exhibiting several characteristic bands, which could be directly attributed to additive degradation products.

In this thesis, SHINERS was presented as a very powerful and versatile tool for interphase characterization. Addressing the challenges discussed above would greatly improve the technique, making it more flexible and adaptable for the complex investigations in varying cell systems, further enhancing the potential and efficiency of SHINERS.

9. Appendix

9.1. Appendix for Chapter 4

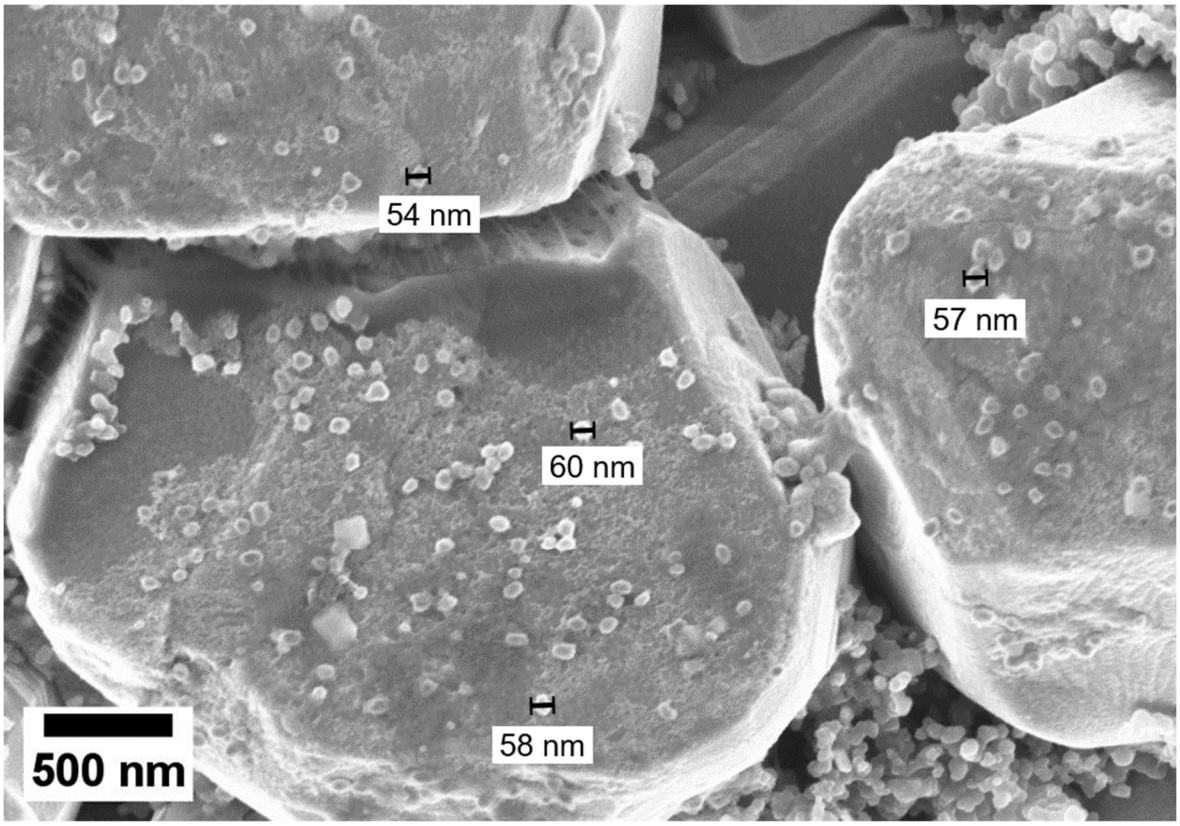

Figure A1: SEM image of silica coated Au nanoparticles with a targeted size of 55 nm drop cast on an NMC811 electrode.

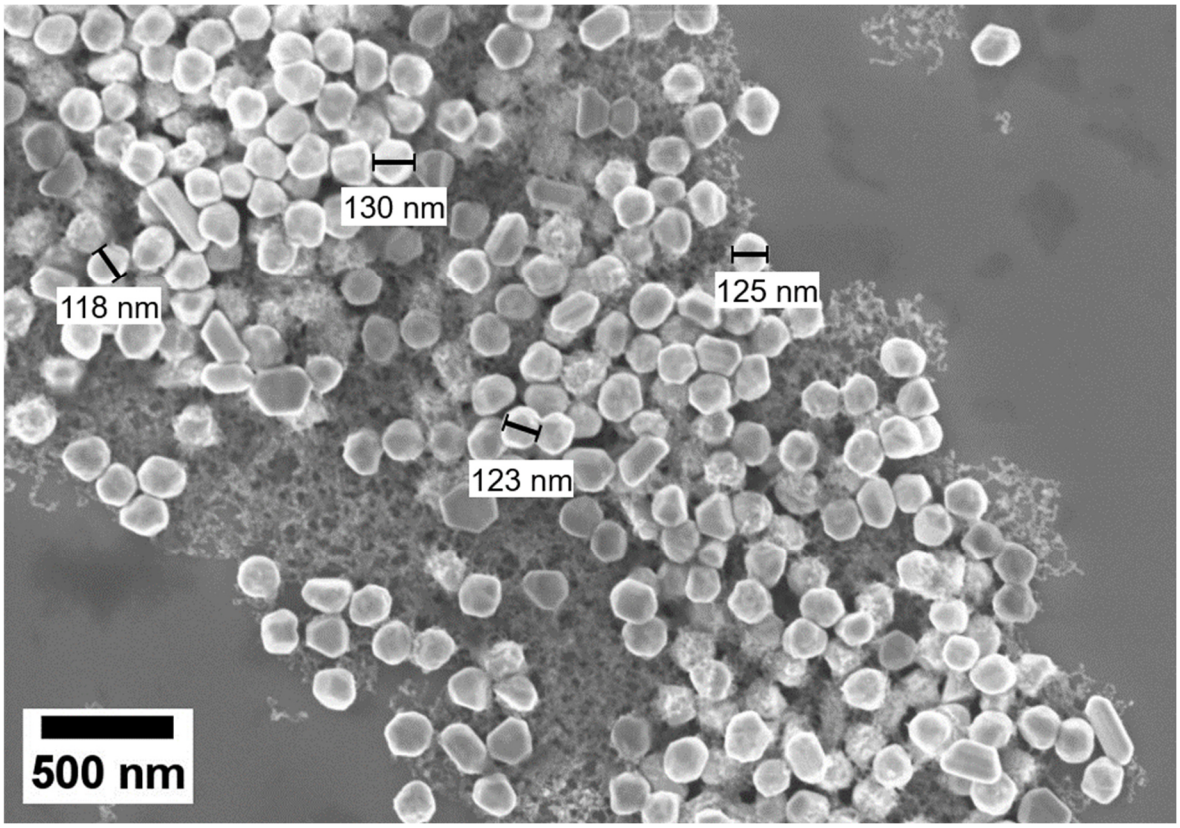

Figure A2: SEM image of silica coated Au nanoparticles with a targeted size of 120 nm drop cast on a Si-wafer.

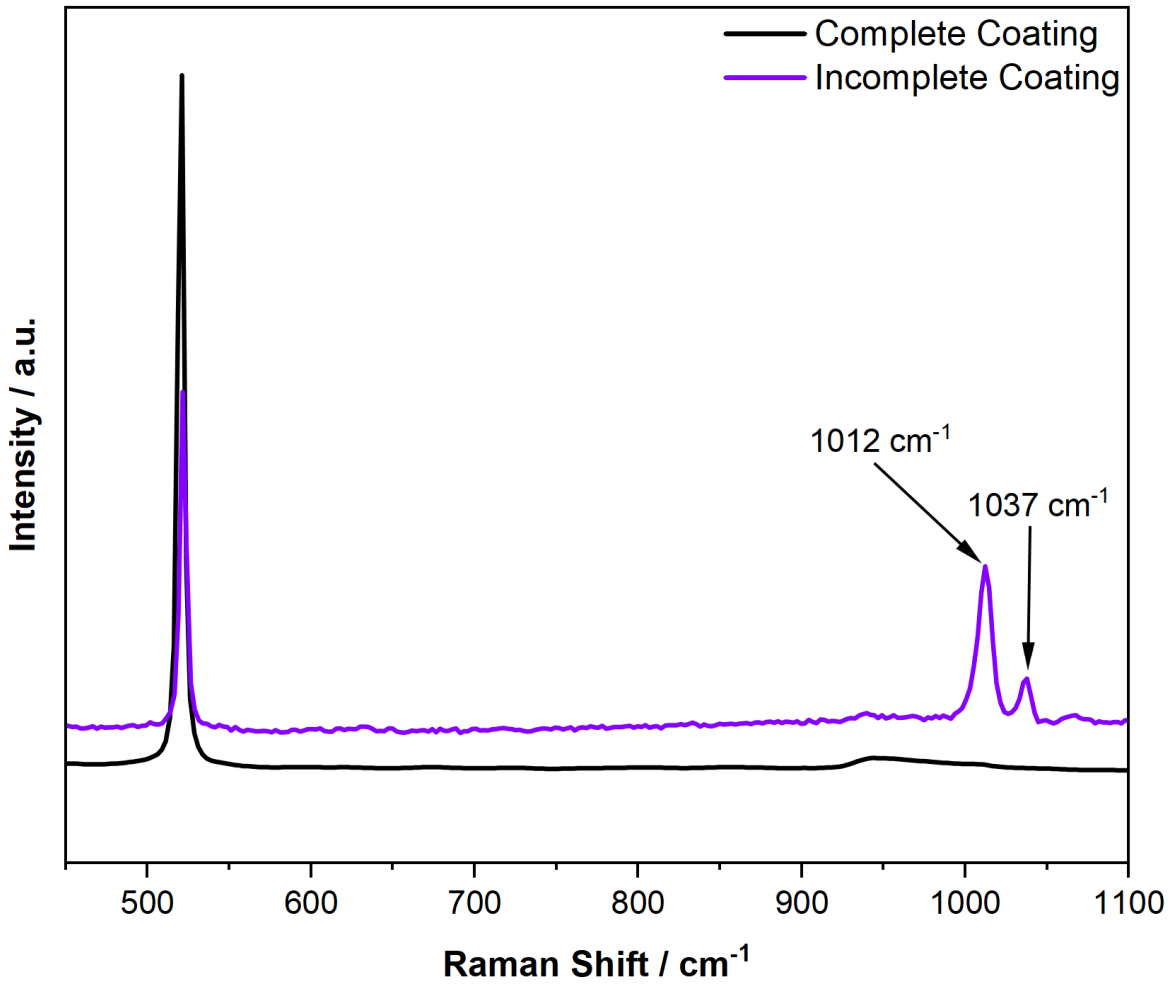

Figure A3: Raman spectra of a Si-wafer in the presence of 55 nm Au NPs with a complete silica coating (**black**) and an incomplete silica coating (**purple**). The wafer was infused with a 10 mM pyridine solution before acquisition of the spectra. The sample was excited using a red laser (633 nm). Spectra were acquired for 20 s with 3 accumulations. Laser power was adjusted using a 10% filter.

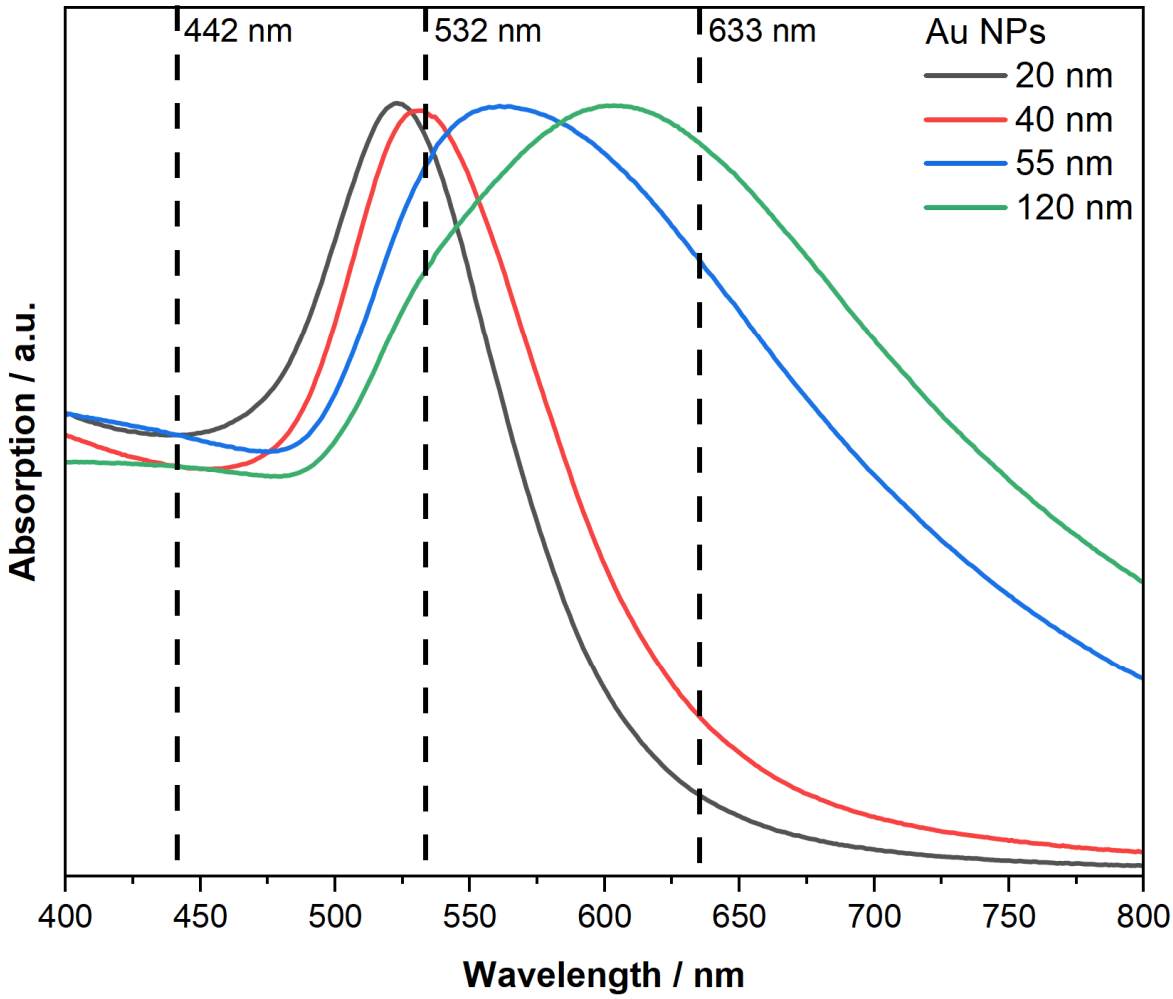

Figure A4: UV/Vis absorption spectra of Au NPs with 20 nm, 40 nm, 55 nm, and 120 nm diameters, dispersed in Milli-Q water. The spectrum additionally highlights the wavelengths emitted by the lasers available for the Raman system utilized in this thesis by dashed lines.

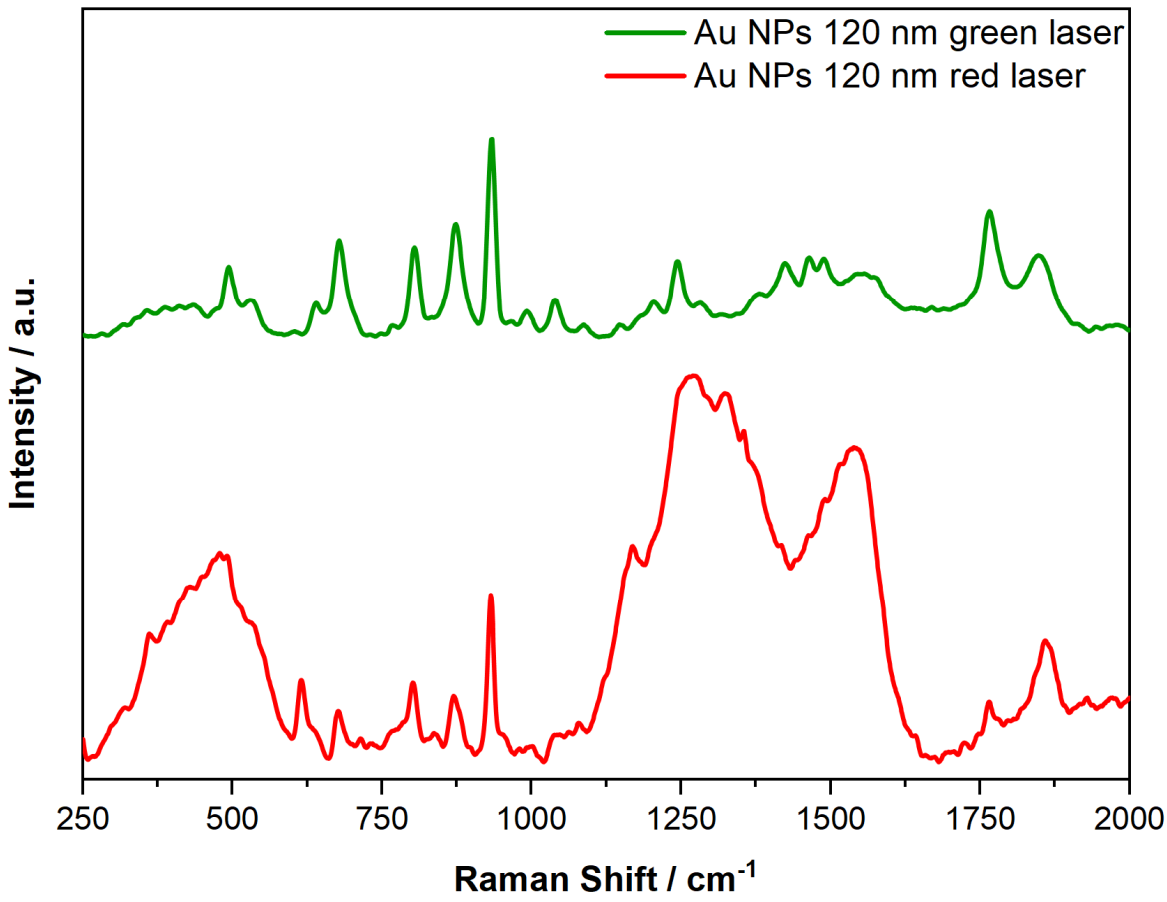

Figure A5: SHINER spectra taken from the surface of a Si-wafer in the presence of a GBL-based electrolyte (1 M $LiBF_4$, E-Lyte Innovations, battery grade) in GBL (Sigma Aldrich, 99%) at an electrode potential of 50 mV *vs.* $Li|Li^+$. Spectra were taken using a red and a green laser. Spectra were acquired for 25 s with 4 accumulations. Laser power was regulated to 1.05 mW and 1.22 mW, respectively. 120 nm Au NPs used for SHINERS enhancement were introduced to the Si-wafer *via* drop casting prior to the measurement.

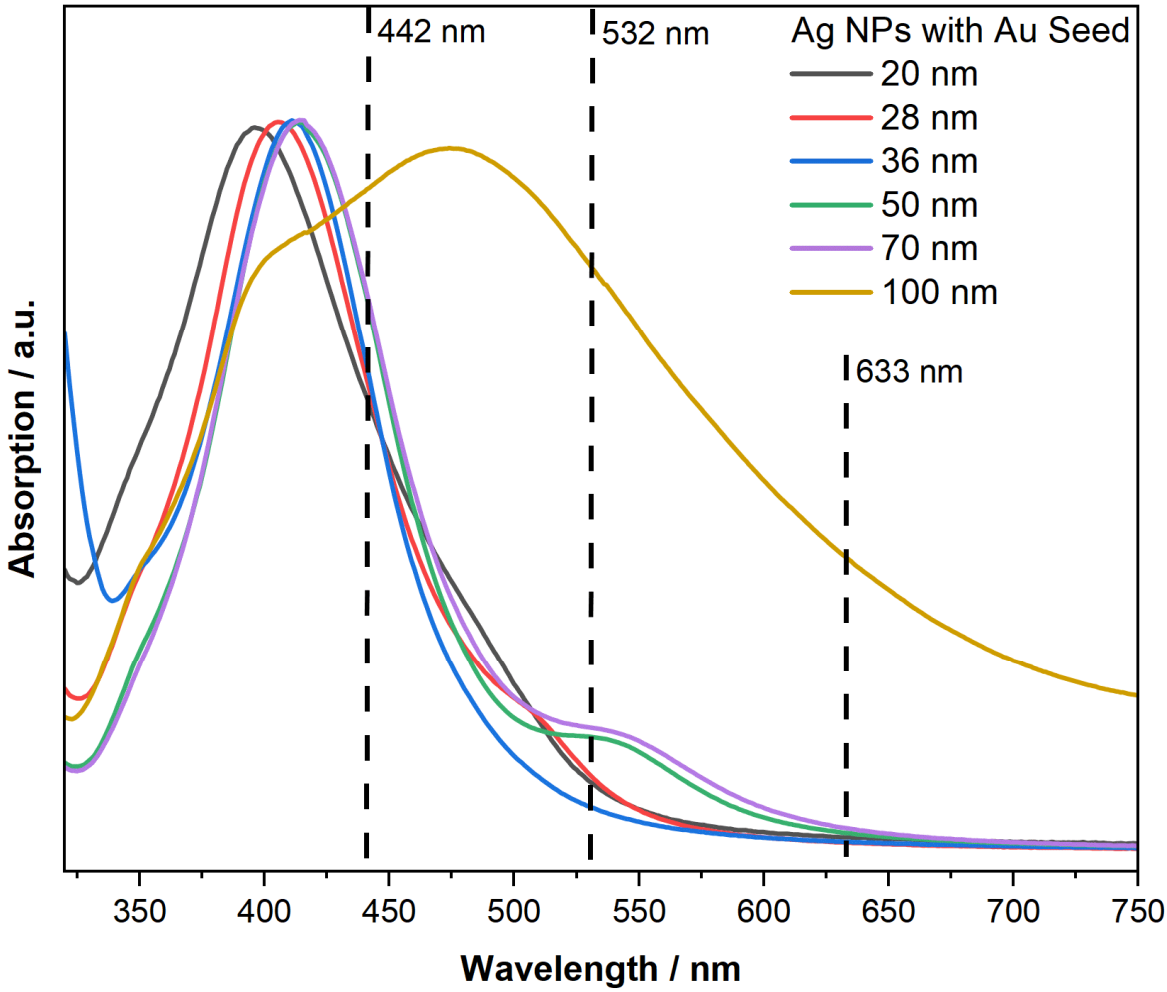

Figure A6: UV/Vis absorption spectra of Ag NPs with 20 nm, 28 nm, 36 nm, 50 nm, 70 nm, and 100 nm diameters synthesized with the use of 12 nm Au seeds, dispersed in Milli-Q water. The spectrum additionally highlights the wavelengths emitted by the lasers available for the Raman system utilized in this thesis by dashed lines.

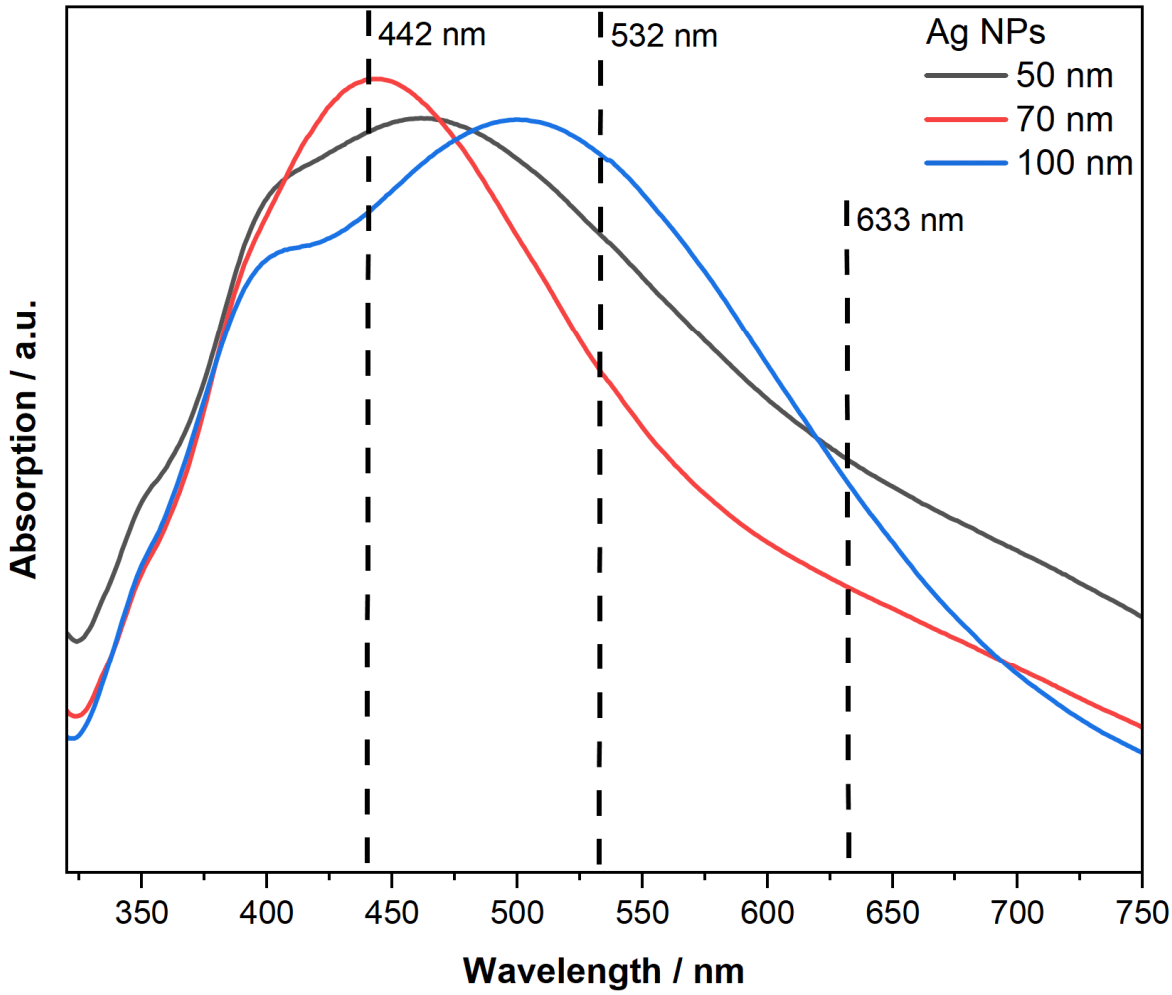

Figure A7: UV/Vis absorption spectra of Ag NPs with 50 nm, 70 nm, and 100 nm diameters synthesized without the use of Au seeds, dispersed in Milli-Q water. The spectrum additionally highlights the wavelengths emitted by the lasers available for the Raman system utilized in this thesis by dashed lines.

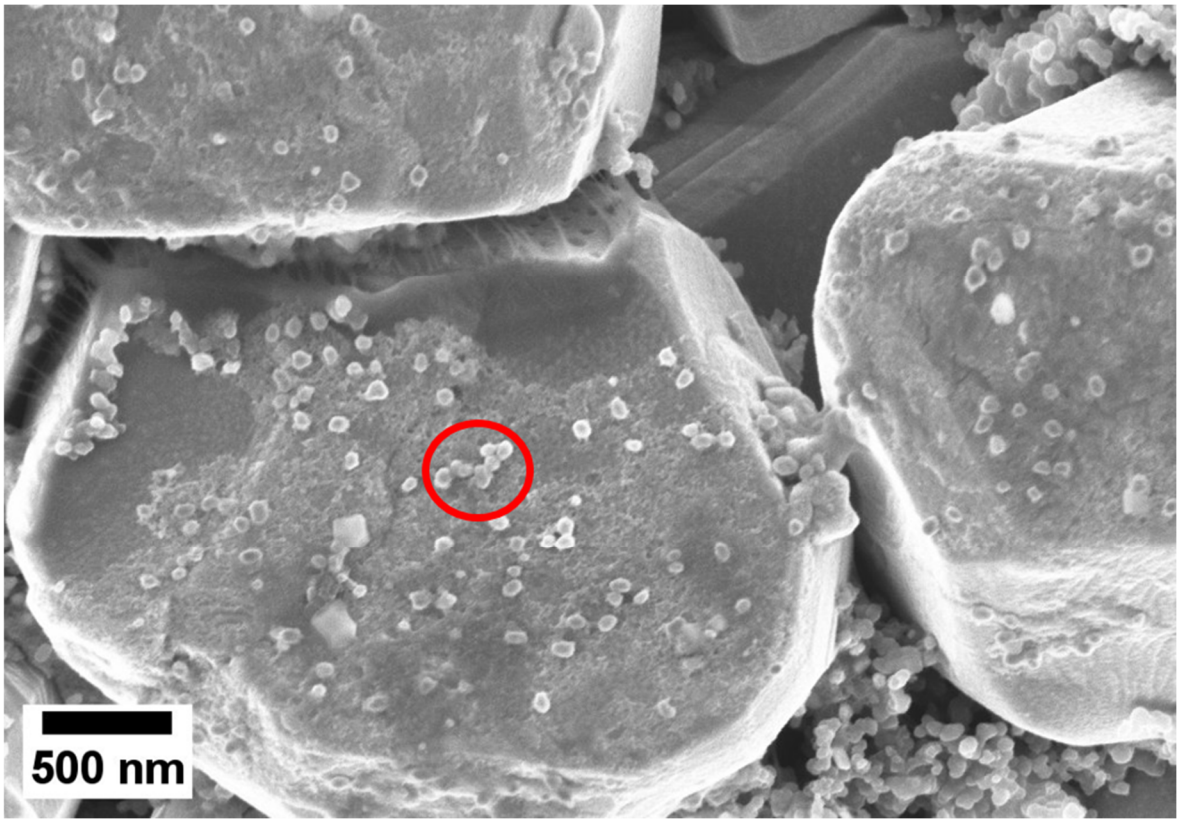

Figure A8: SEM image of silica coated Au nanoparticles with a diameter of 55 nm drop cast on a single crystal NMC811 electrode. In total 500 µL (5 x 100 µL) of concentrated NP solution were added to the electrode. Area of high NP concentration is highlighted by a red circle.

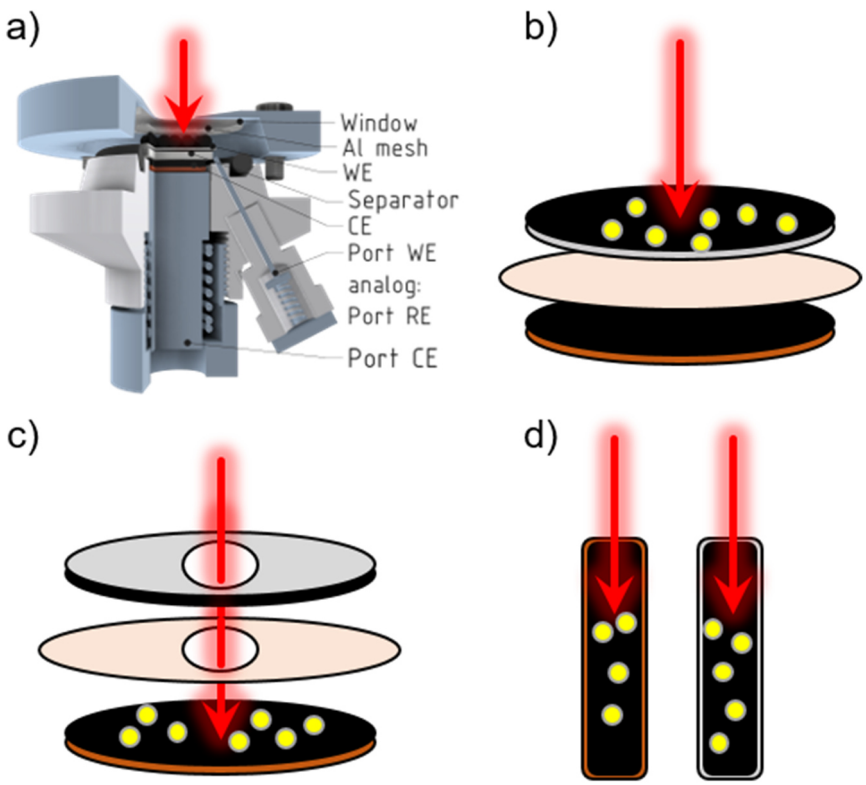

Figure A9: Schematic depiction of **a)** the optical cell and **b)** – **c)** the electrode configurations, employed in this thesis. The red arrows symbolize the Raman laser, while the yellow balls represent silica coated Au NPs. Active material of the negative and positive electrode are represented by black color. Current collectors are colored in grey and brown to depict aluminum and copper current collectors for positive and negative electrode, respectively. In general, the electrode with NPs is connected as WE, serving as main focus for Raman investigation, with **d)** being the exception, as both electrode surfaces are to be investigated. Here the positive electrode is connected as WE. **b)** represents the "sandwich" configuration, **c)** the "donut" configuration, and **c)** the "side-by-side" configuration. RE is not depicted, as in practical use it is always placed on the outer side, next to WE and CE.

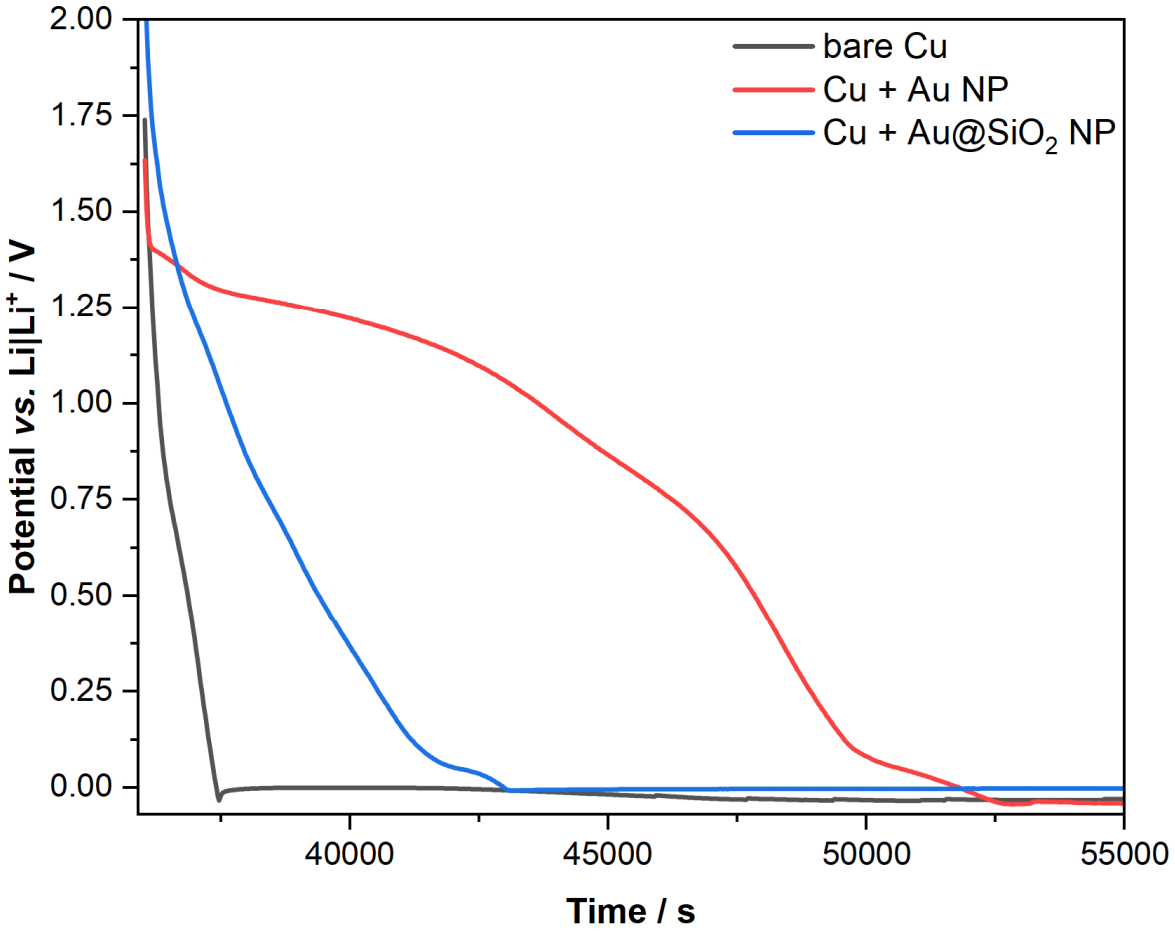

Figure A10: Potential response of a Li-plating experiment to investigate Au NP alloying behavior. In a Swagelok cell a Cu electrode (WE) was paired against a Li-metal CE. A constant current of 50 µA cm^{-2} was applied to induce Li plating. The experiment was performed with a bare Cu electrode as reference (**grey**), a Cu electrode with 55 nm Au NPs (**red**) and a Cu electrode with 55 nm SiO_2 coated Au NPs (**blue**). Roughly double the amount of SiO_2 coated NPs is expected to be on the Cu electrode, in comparison to uncoated NPs. However, the ratio of NPs can only be estimated.

9.2. Appendix for Chapter 5

9.2.1. Electrochemical Investigation

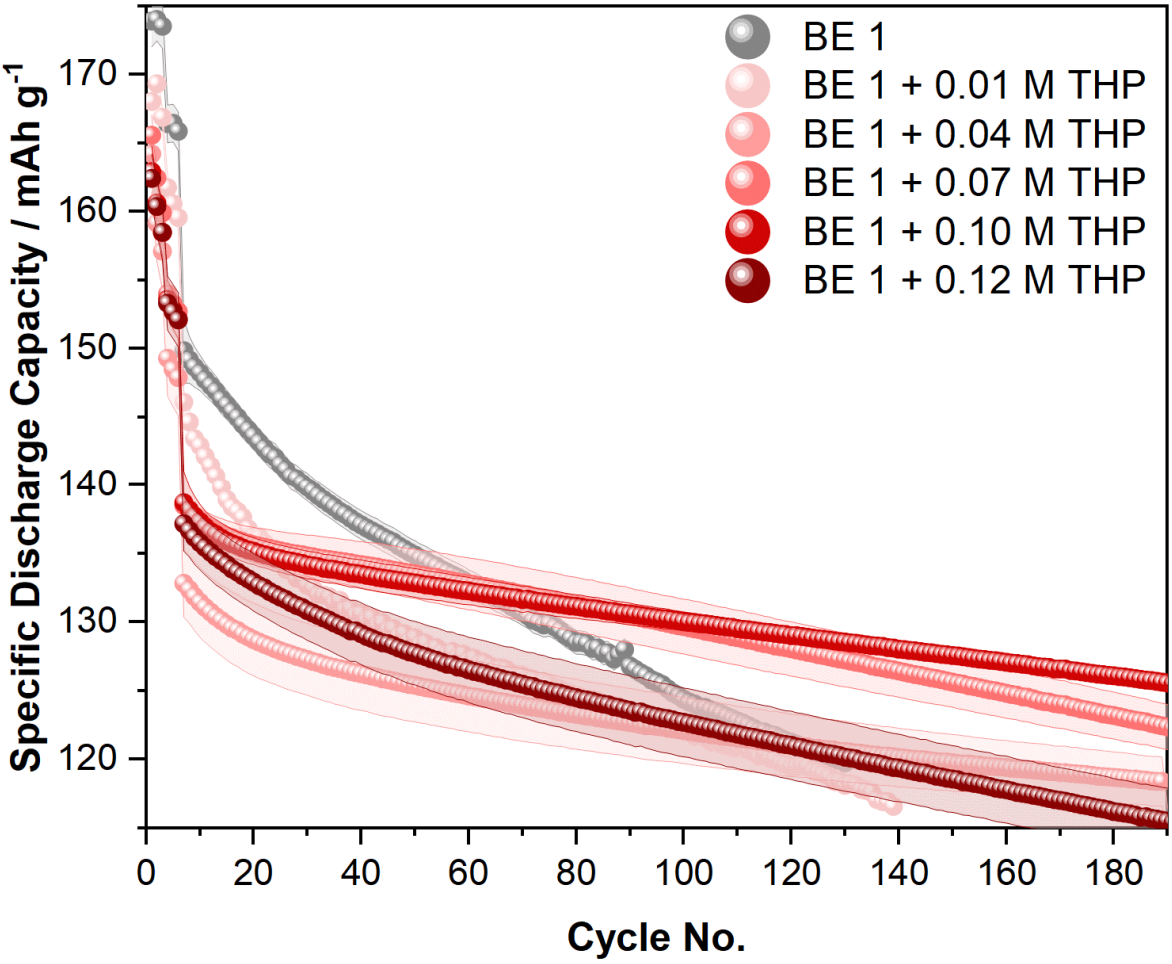

Figure A11: Specific discharge capacities obtained from galvanostatic charge/discharge cycling at a C-rate of 1 C in a voltage range of 2.80 V – 4.50 V of NMC111||graphite coin cells, cycled in the presence of the BE 1 (1 $_{M}$ $LiPF_6$ in EC:DEC 1:1 by weight; **grey**) and the BE 1 + different concentrations of thiophene (THP, **red** color gradation). Cell formation was performed by 3 charge/discharge cycles at a C-rate of C/10, followed by 3 charge/discharge cycles at a C-rate of C/3. Graph redrawn from [28].

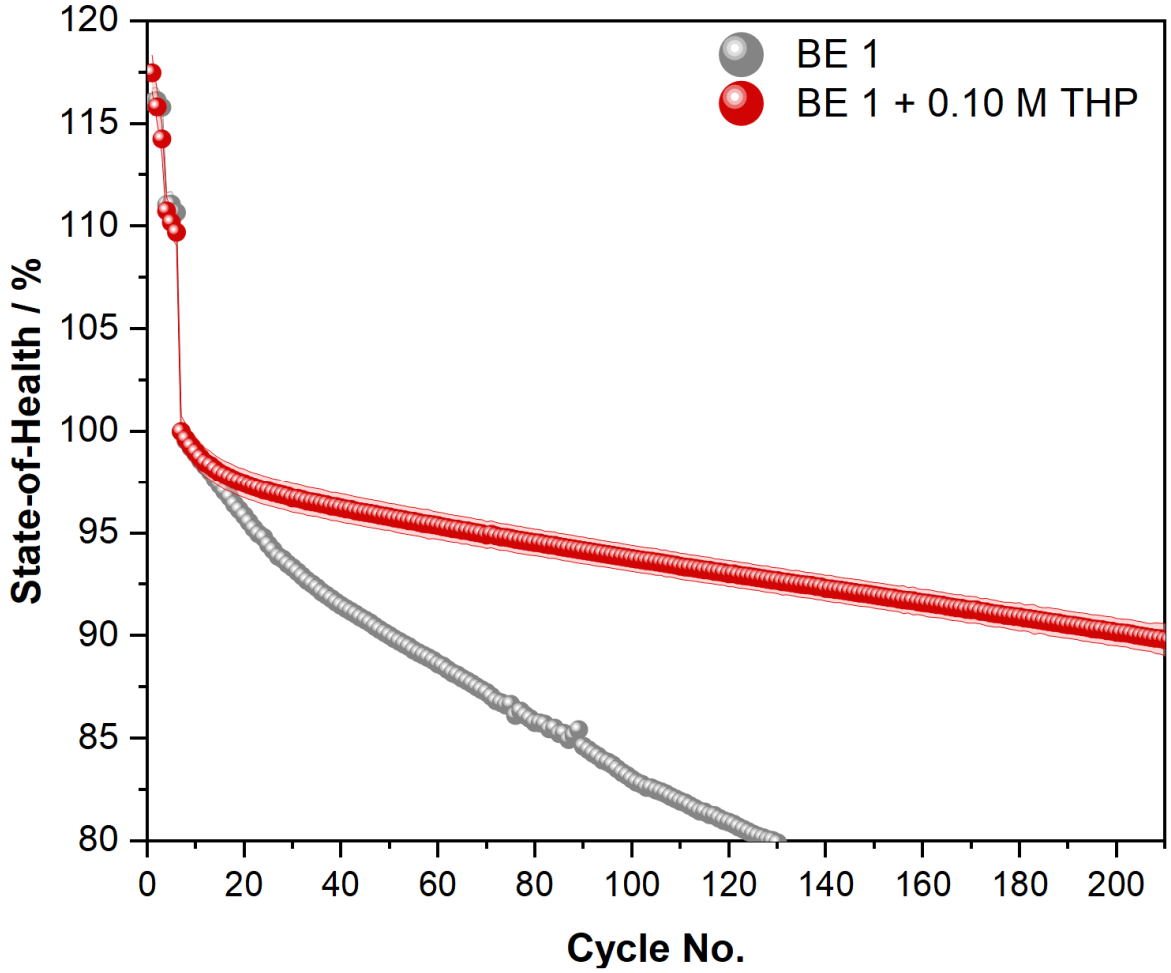

Figure A12: State-of-health obtained from galvanostatic charge/discharge cycling at a C-rate of 1 C in a voltage range of 2.80 V – 4.50 V of NMC111||graphite coin cells, cycled in the presence of the BE 1 (1 M $LiPF_6$ in EC:DEC 1:1 by weight; **grey**) and the BE 1 + 0.10 M thiophene (THP, **red**). Cell formation was performed by 3 charge/discharge cycles at a C-rate of C/10, followed by 3 charge/discharge cycles at a C-rate of C/3. Note that the state-of-health is calculated based on the 7th cycle, being the first one performed at a C-rate of 1 C. Graph redrawn from [28].

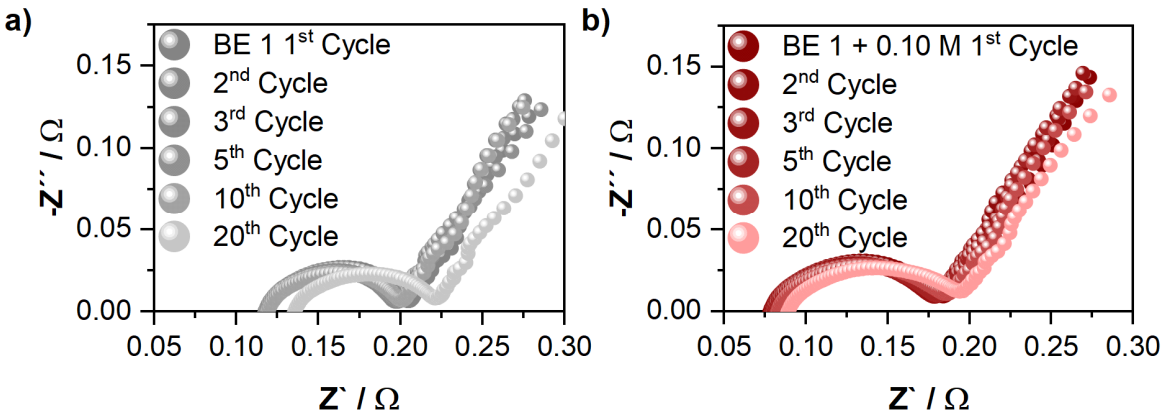

Figure A13: Electrochemical impedance spectra obtained from NMC111||graphite pouch cells galvanostatically cycled in the presence of **a)** BE 1 (1 M $LiPF_6$ in EC:DEC 1:1 by weight; **grey**) and **b)** BE 1 + 0.10 M THP (**red**) in a voltage range of 2.80 V – 4.50 V at a C-rate of C/2. Impedance spectra were recorded during every charge cycle at 50% state-of-charge. Graph redrawn from [28].

Electrochemical impedance spectroscopy (EIS) was performed to monitor the internal resistance of the prepared electrolyte formulations. As depicted in **Figure A13**, notably

lower impedance was recorded for the NMC111||graphite pouch cell cycled in the presence of BE 1, compared to the additive-containing cells. However, BE 1 cells also exhibit a distinct increase in internal resistance, especially from the 10th to the 20th cycle, while impedance growth for the THP-containing cells remains limited. These findings are in good agreement with electrochemical investigations, accounting for initially lower discharge capacities in the presence of THP, due to higher resistance and thus higher overvoltages. In addition, the observed trend of impedance growth corresponds with the results of the ΔV analysis, demonstrating reduced impedance growth in the presence of THP, due to formation of an effective interphase.

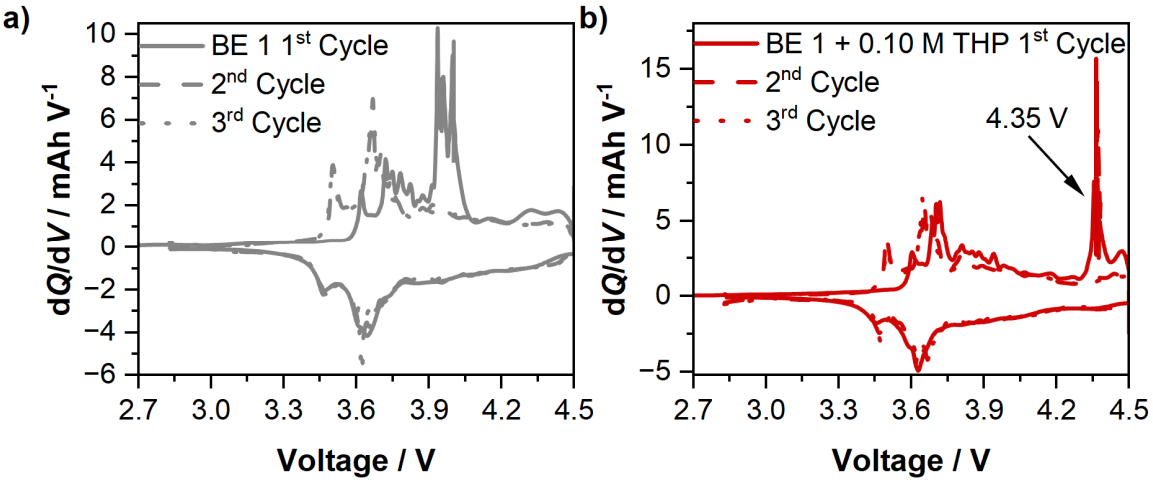

Figure A14: dQ/dV *vs.* voltage plots drawn for the first three galvanostatic charge/discharge cycles of NMC111||graphite coin cells in the presence of **a)** BE 1 (1 $_M$ $LiPF_6$ in EC:DEC 1:1 by weight; **grey**) and **b)** BE 1 + 0.10 $_M$ THP (**red**). Galvanostatic charge/discharge cycling was performed in a voltage range between 2.80 V and 4.50 V with a C-rate of C/10 at the depicted cycles. Note that the first cycle is marked by a solid line, while the second and third cycle are marked by dashed and dotted lines, respectively. Important peaks discussed in the main text are highlighted by arrows and the peak voltage is noted. Graph redrawn from [28].

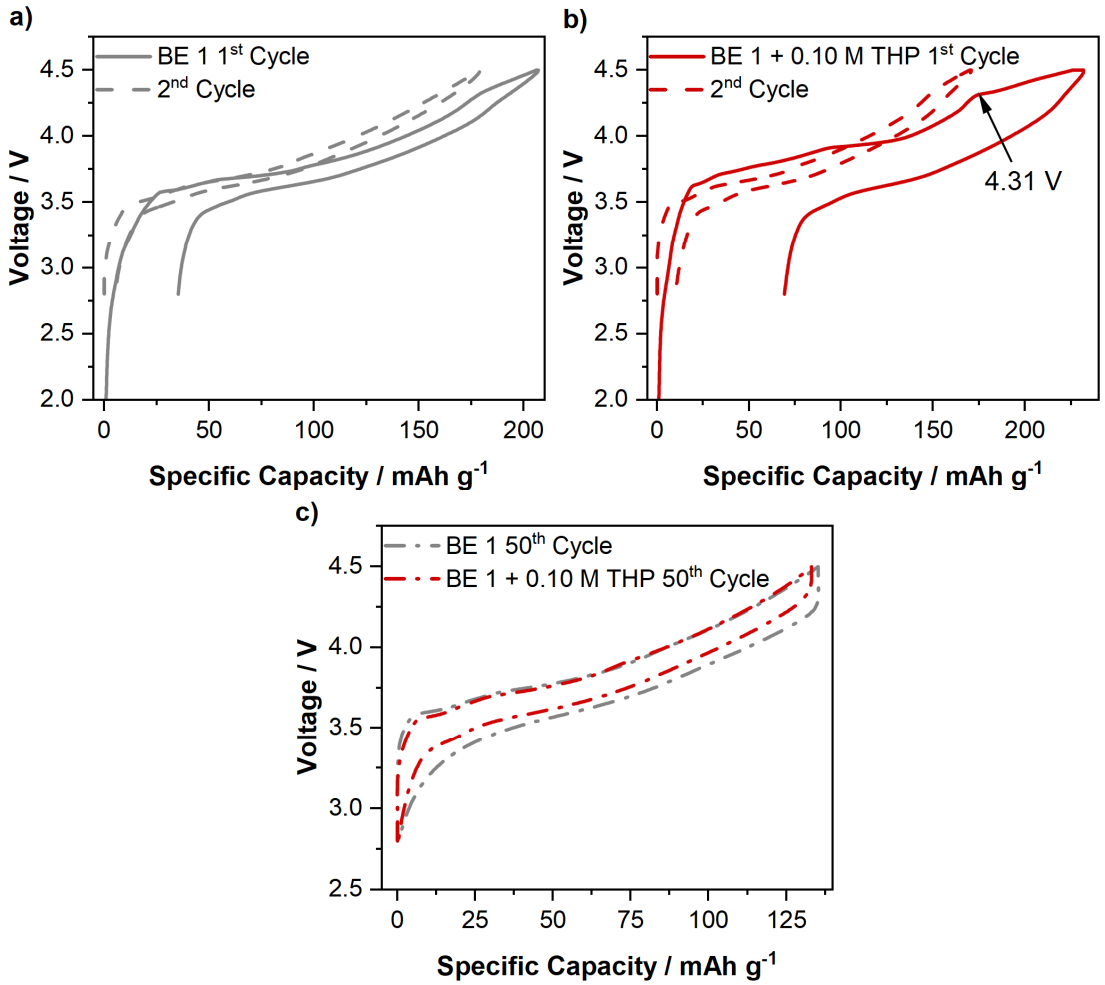

Figure A15: Voltage *vs.* capacity histograms of NMC111||Graphite coin-cells cycled in the presence of the BE 1 (1 $_M$ $LiPF_6$ in EC:DEC 1:1 by weight; **grey**) and **b)** BE 1 + 0.10 $_M$ THP (**red**). **a)** and **b)** show the first and second of the BE 1 and the BE 1 + 0.10 $_M$ THP, indicated by full and dashed lines, respectively. **c)** shows the comparison of the 50th cycle obtained from coin cells, cycled in the presence of the considered electrolyte formulations. Important features discussed in the main text are highlighted by arrows and the respective voltage is noted.

9.2.2. Surface Characterization by SEM, EDX and Raman Spectroscopy

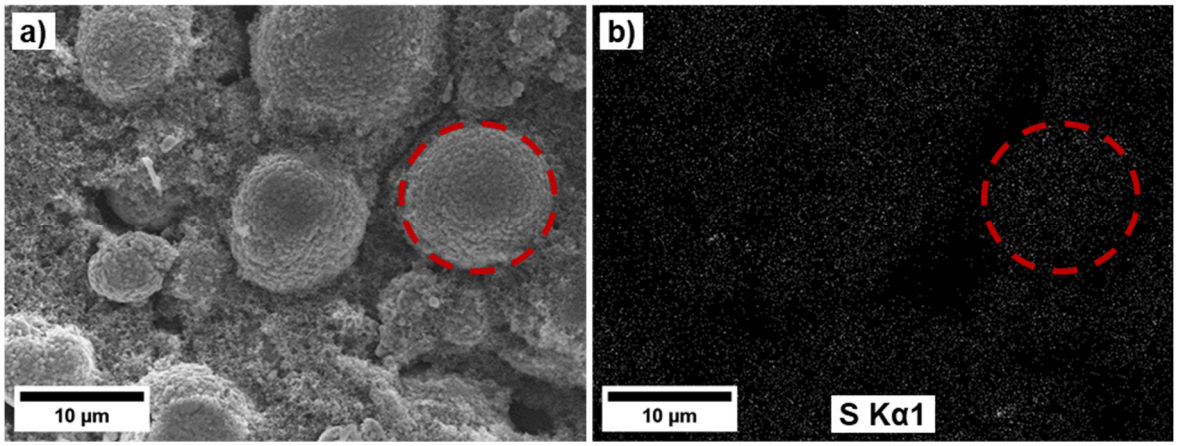

Figure A16: Results of the EDX investigation performed on the surface of a NMC111 electrode electrochemically aged in the presence of BE 1 (1 $_M$ $LiPF_6$ in EC:DEC 1:1 by weight) + 0.10 $_M$ THP. **a)** shows the SEM image of the electrode spot selected for EDX investigation. **b)** shows the distribution of sulfur (S) on the surface of the probed electrode. While sulfur was identified on the whole electrode, a distinct concentration was observed on NMC particles, highlighted by a red dashed circle. Figure adapted from [28].

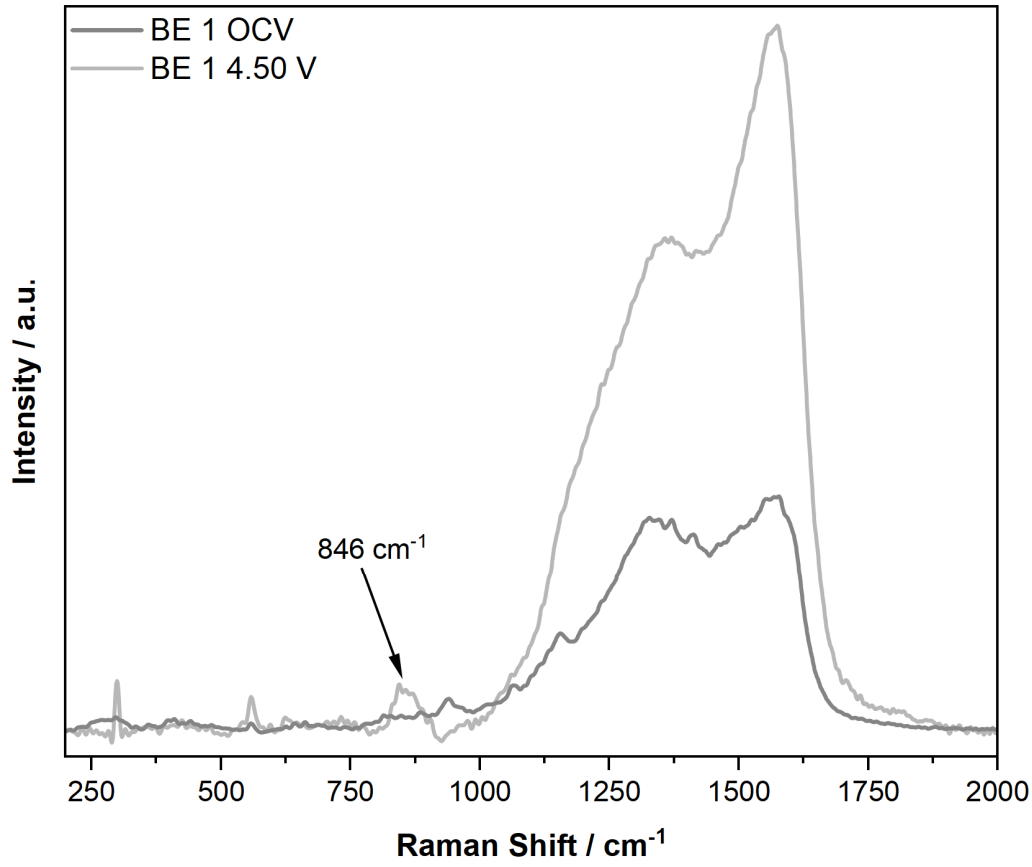

Figure A17: *Operando* SHINER spectra taken from the surface of an NMC111 electrode in the presence of BE 1 (1 $_M$ $LiPF_6$ in EC:DEC 1:1 by weight). For the SHINERS measurement the NMC electrode was connected as working electrode, paired against a graphite counter electrode. Galvanostatic charge was performed at a C-rate of C/3 and Au SHINs with a diameter of 55 nm were introduced to the electrode surface before the cell assembly. Spectra were recorded at the open circuit voltage (OCV, **grey**) and the cut-off voltage of 4.50 V (**light grey**). For spectrum acquisition the samples were excited using a 633 nm laser, adjusted to a power output of 1.05 mW. Spectra were acquired over two accumulations of 50 s. Important newly arising bands observed in the spectra are highlighted by arrows. In addition, band positions are noted. Figure adapted from [28].

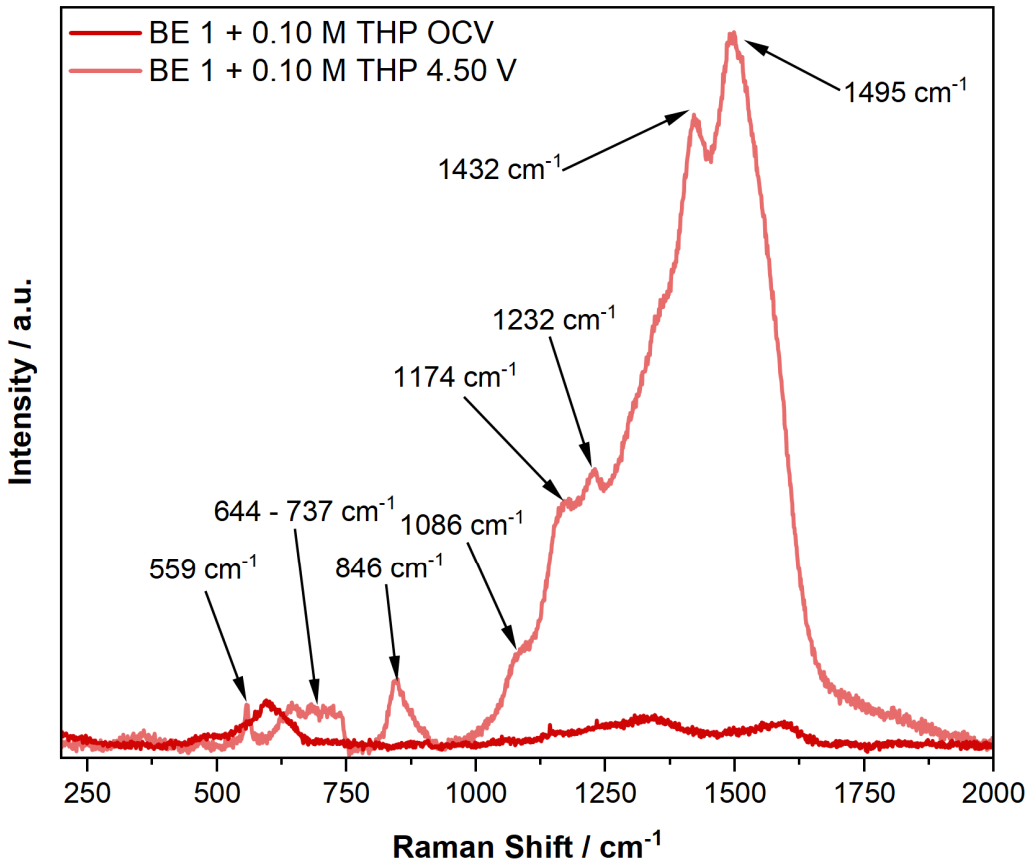

Figure A18: *Operando* SHINER spectra taken from the surface of an NMC111 electrode in the presence of BE 1 (1 $_M$ $LiPF_6$ in EC:DEC 1:1 by weight) + 0.10 $_M$ THP. For the SHINERS measurement the NMC electrode was connected as working electrode, paired against a graphite counter electrode. Galvanostatic charge was performed at a C-rate of C/3 and Au SHINs with a diameter of 55 nm were introduced to the electrode surface before the cell assembly. Spectra were recorded at the open circuit voltage (OCV, **red**) and the cut-off voltage of 4.50 V (**light red**). For spectrum acquisition, the samples were excited using a 633 nm laser, adjusted to a power output of 1.05 mW. Spectra were acquired over two accumulations of 50 s. Important newly arising bands observed in the spectra are highlighted by arrows. In addition, band positions are noted. Figure adapted from [28].

9.2.3.QC Calculations

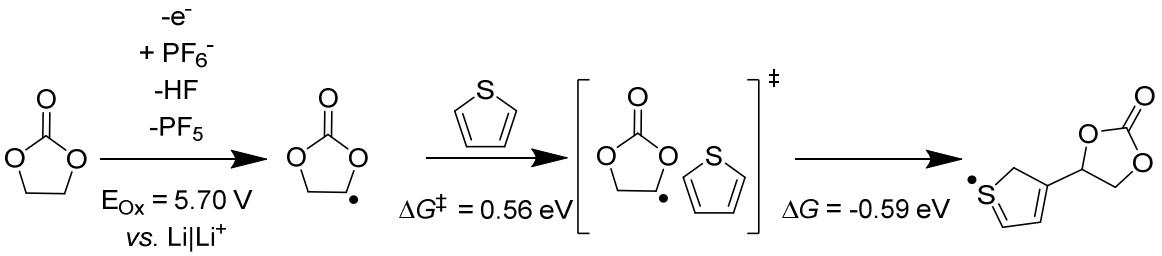

Figure A19: Proposed reaction mechanism for the co-polymerization of EC and thiophene. Calculated differences in free energy (ΔG, computed at 298 K) are given for every reaction step in electron volts (eV), initial oxidation potential of EC is given on the $Li|Li^+$ scale. Figure adapted from [28].

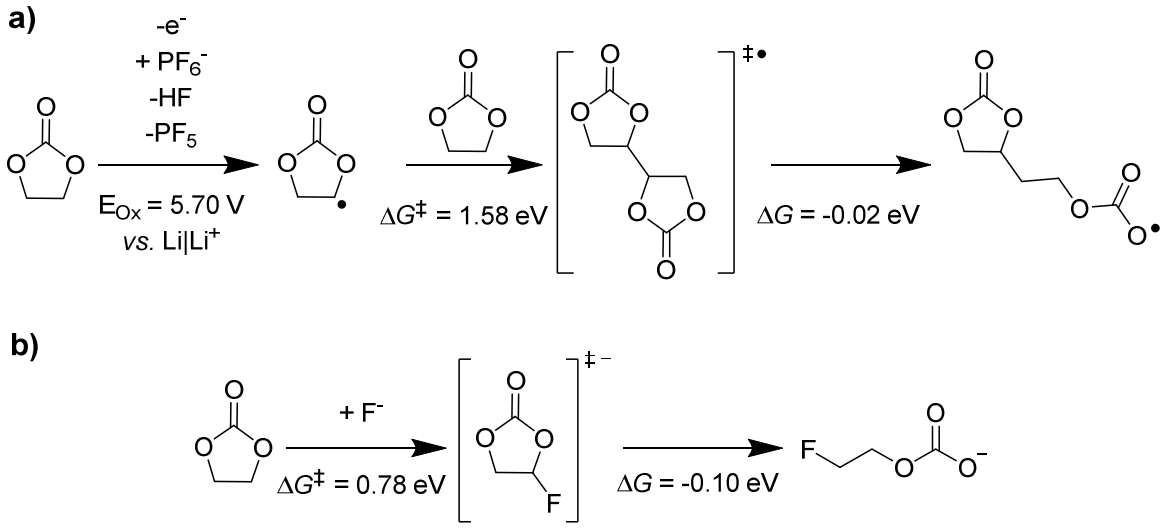

Figure A20: Proposed reaction mechanisms for the polymerization of EC. **a)** shows the suggested mechanism for a radical polymerization, while **b)** depicts the mechanism for an anionic mechanism, initiated by a nucleophilic F^- attack. Calculated differences in free energy (ΔG, computed at 298 K) are given for every reaction step in electron volts (eV), initial oxidation potential of EC is given on the $Li|Li^+$ scale. Figure adapted from [28].

9.3. Appendix for Chapter 6

9.3.1.Electrochemical Investigation

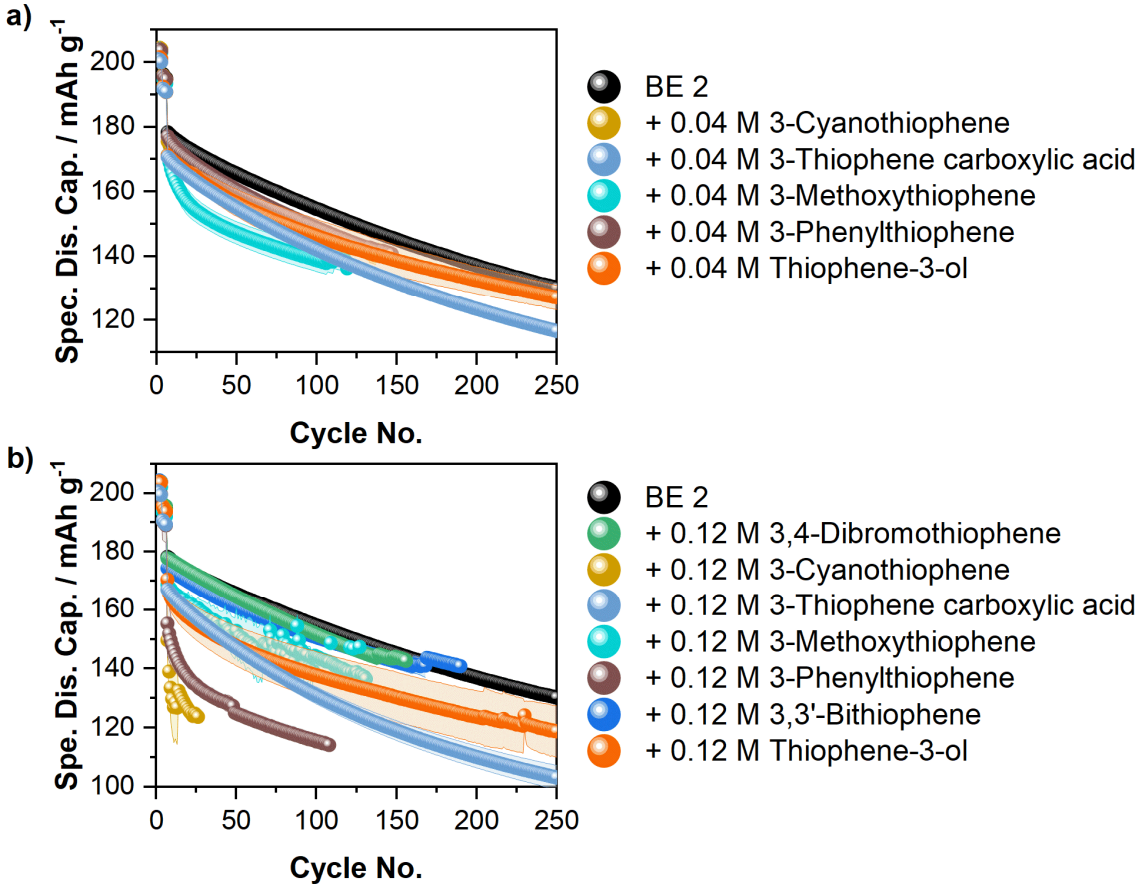

Figure A21: Specific discharge capacities (Spec. Dis. Cap.) obtained from NMC811||graphite pouch cells galvanostatically charge/discharge cycled at a C-rate of 1 C in a voltage range between 2.80 V – 4.50 V. Depicted are the discharge capacities of cells containing different thiophene-based electrolyte additives in the concentration of **a)** 0.04 $_{M}$ and **b)** 0.12 $_{M}$, in comparison to the discharge capacities obtained from the cells cycled in the presence of the BE 2 (1 $_{M}$ $LiPF_6$ in EC:EMC 3:7 by weight; **black**). Note that this figure only depicts the additive-containing cells exhibiting a decreased electrochemical performance compared to the BE 2 cells. For the results of the other investigated electrolyte formulation the reader is kindly referred to **Figure 17**.

Table A1: Key data of the galvanostatic charge/discharge investigation of NMC811||graphite pouch cells, cycled in the presence of the BE 2 (1 M $LiPF_6$ in EC:EMC 3:7 by weight) and BE 2 + 0.04 M additive. Shown are the discharge capacity at the 7th cycle, the discharge capacity at the 200th cycle, and the cycle number at which the respective cells reached a state of health (SoH) of 80%. Note that the 7th cycle equals the first cycle after formation. Percental changes in the obtained values are calculated in comparison to the BE 2 cells. The values shown were obtained from **Figure 17** and **Figure A21**.

Electrolyte	Capacity @ 7th Cycle / mAh g^{-1}	Capacity @ 200th Cycle / mAh g^{-1}	Cycle No. @ 80% SoH
BE 2	**178**	**137**	**167**
BE 2 + 0.04 M THP	**177 – 1%**	**143 + 4%**	**210 + 25%**
BE 2 + 0.04 M 3-Bromothiophene	**179 + 1%**	**144 + 5%**	**211 + 26%**
BE 2 + 0.04 M 3,4-Dibromothiophene	**179 + 1%**	**NA**	**186 + 11%**
BE 2 + 0.04 M 3-Cyanothiophene	**175 – 2%**	**NA**	**146 – 13%**
BE 2 + 0.04 M 3-Thiophene boronic acid	**178**	**146 + 7%**	**232 + 38%**
BE 2 + 0.04 M 3-Thiophene carboxylic acid	**171 – 4%**	**124 – 10%**	**126 – 25%**
BE 2 + 0.04 M 3-Methoxythiophene	**171 – 4%**	**NA**	**119 – 29%**
BE 2 + 0.04 M 3-Phenylthiophene	**177 – 1%**	**NA**	**140 – 16%**
BE 2 + 0.04 M 3,3'-Bithiophene	**176 – 2%**	**143 + 4%**	**219 + 31%**
BE 2 + 0.04 M Thiophene-3-ol	**171 – 4%**	**132 – 4%**	**163 – 3%**

Table A2: Key data of the galvanostatic charge/discharge investigation of NMC811||graphite pouch cells, cycled in the presence of the BE 2 (1 M $LiPF_6$ in EC:EMC 3:7 by weight) and BE 2 + 0.12 M additive. Shown are the discharge capacity at the 7th cycle, the discharge capacity at the 200th cycle, and the cycle number at which the respective cells reached a state of health (SoH) of 80%. Note that the 7th cycle equals the first cycle after formation. Percental changes in the obtained values are calculated in comparison to the BE 2 cells. The values shown were obtained from **Figure 17** and **Figure A21**.

Electrolyte	Capacity @ 7th Cycle / mAh g^{-1}	Capacity @ 200th Cycle / mAh g^{-1}	Cycle No. @ 80% SoH
BE 2	**178**	**137**	**167**
BE 2 + 0.12 M THP	**175 – 2%**	**144 + 5%**	**234 + 40%**
BE 2 + 0.12 M 3-Bromothiophene	**179 + 1%**	**144 + 5%**	**211 + 26%**
BE 2 + 0.12 M 3,4-Dibromothiophene	**178**	**NA**	**156 – 7%**
BE 2 + 0.12 M 3-Cyanothiophene	**150 – 16%**	**NA**	**26 – 84%**
BE 2 + 0.12 M 3-Thiophene boronic acid	**177 – 1%**	**156 + 13%**	**424 + 154%**
BE 2 + 0.12 M 3-Thiophene carboxylic acid	**167 – 6%**	**66 – 52%**	**91 – 46%**
BE 2 + 0.12 M 3-Methoxythiophene	**169 – 5%**	**NA**	**132 – 21%**
BE 2 + 0.12 M 3-Phenylthiophene	**155 – 13%**	**NA**	**109 – 35%**
BE 2 + 0.12 M 3,3'-Bithiophene	**174 – 2%**	**NA**	**168 + 1%**
BE 2 + 0.12 M Thiophene-3-ol	**170 – 4%**	**124 – 9%**	**109 – 35%**

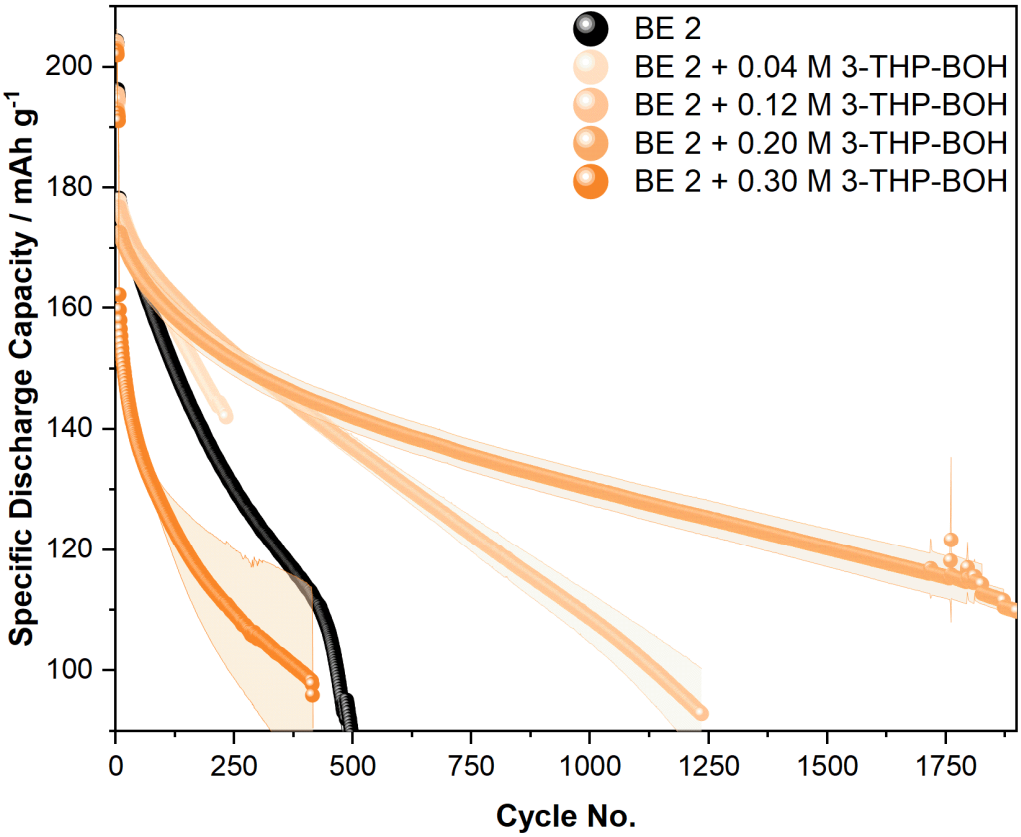

Figure A22: Specific discharge capacities obtained from NMC811||graphite pouch cells galvanostatically charge/discharge cycled at a C-rate of 1 C in a voltage range between 2.80 V – 4.50 V. Depicted are the discharge capacities of cells containing the BE 2 (1 M $LiPF_6$ in EC:EMC 3:7 by weight; **black**) and the BE 2 + varying concentrations of 3-THP-BOH (0.04 M, 0.12 M, 0.20 M and 0.30 M, **orange**). Figure redrawn with permission from [29].

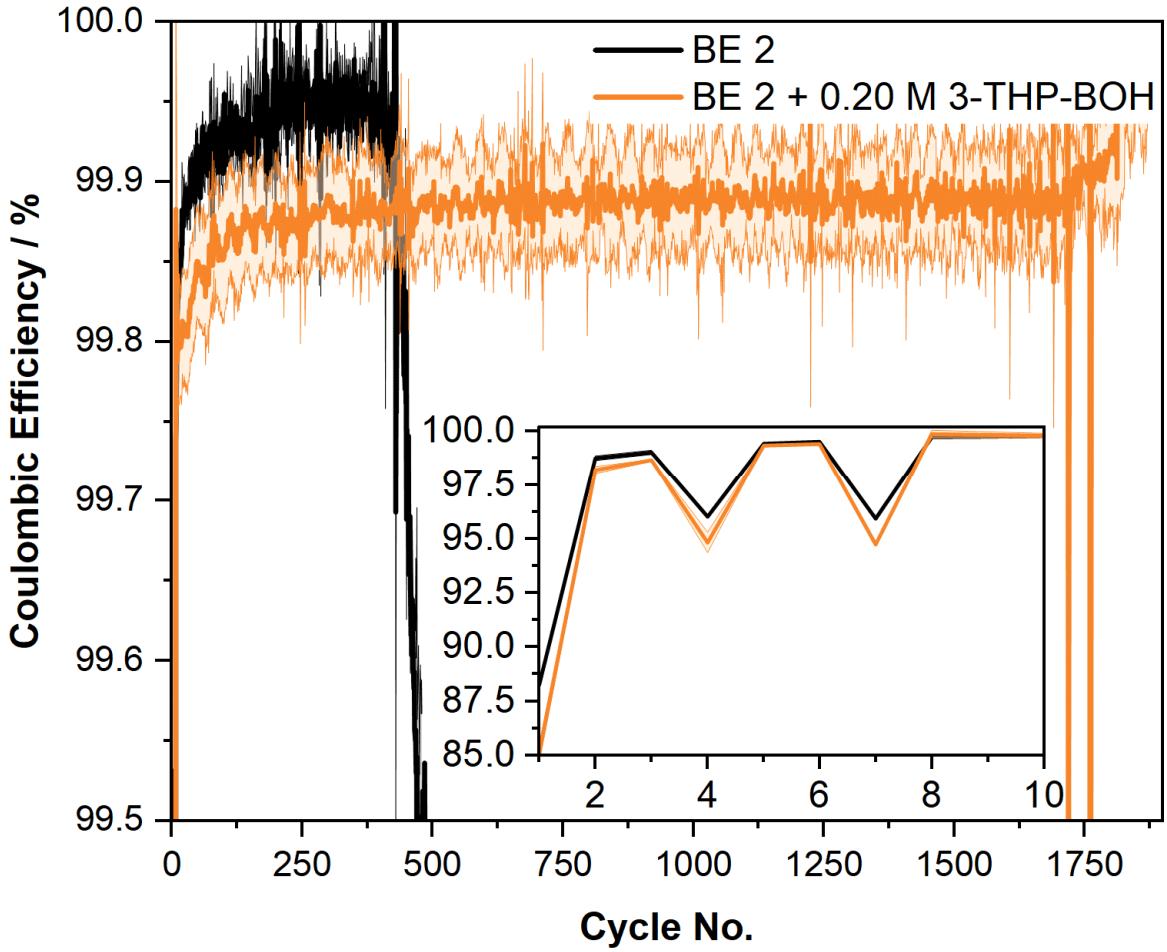

Figure A23: Coulombic efficiencies (CEs) obtained from NMC811||graphite pouch cells galvanostatically charge/discharge cycled at a C-rate of 1 C in a voltage range between 2.80 V – 4.50 V. Depicted are the CEs of cells containing the BE 2 (1 $_{M}$ $LiPF_6$ in EC:EMC 3:7 by weight; **black**) and the BE 2 + 0.20 $_{M}$ 3-THP-BOH (**orange**). The inset in the figure puts the focus on the initial 10 charge/discharge cycles, including the formation cycles. Figure redrawn with permission from [29].

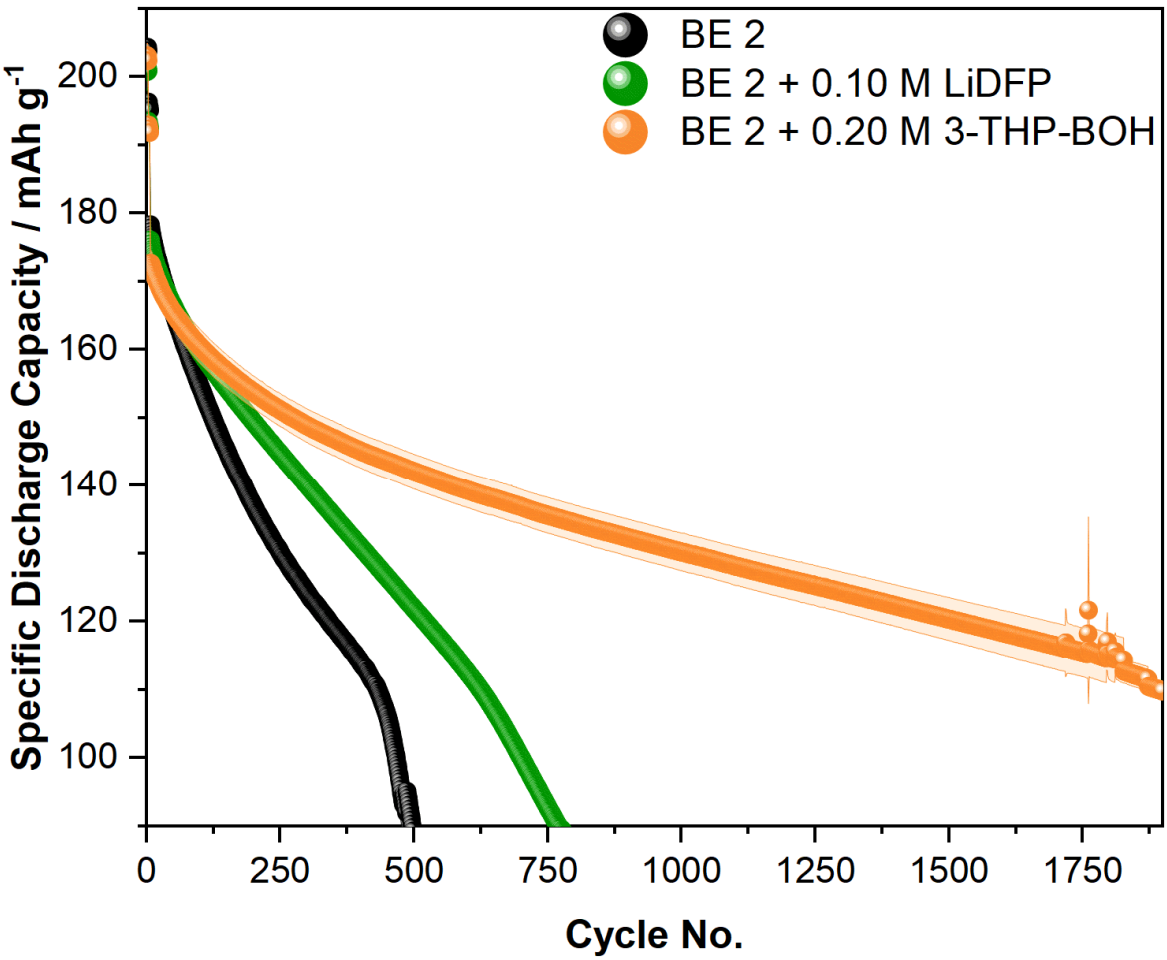

Figure A24: Specific discharge capacities obtained from NMC811||graphite pouch cells galvanostatically charge/discharge cycled at a C-rate of 1 C in a voltage range between 2.80 V – 4.50 V. Depicted are the discharge capacities of cells containing the BE 2 (1 M $LiPF_6$ in EC:EMC 3:7 by weight; **black**), the BE 2 + 0.20 M 3-THP-BOH (**orange**), and the BE 2 + 0.10 M $LiPO_2F_2$ (LiDFP, **green**). Figure redrawn with permission from [29].

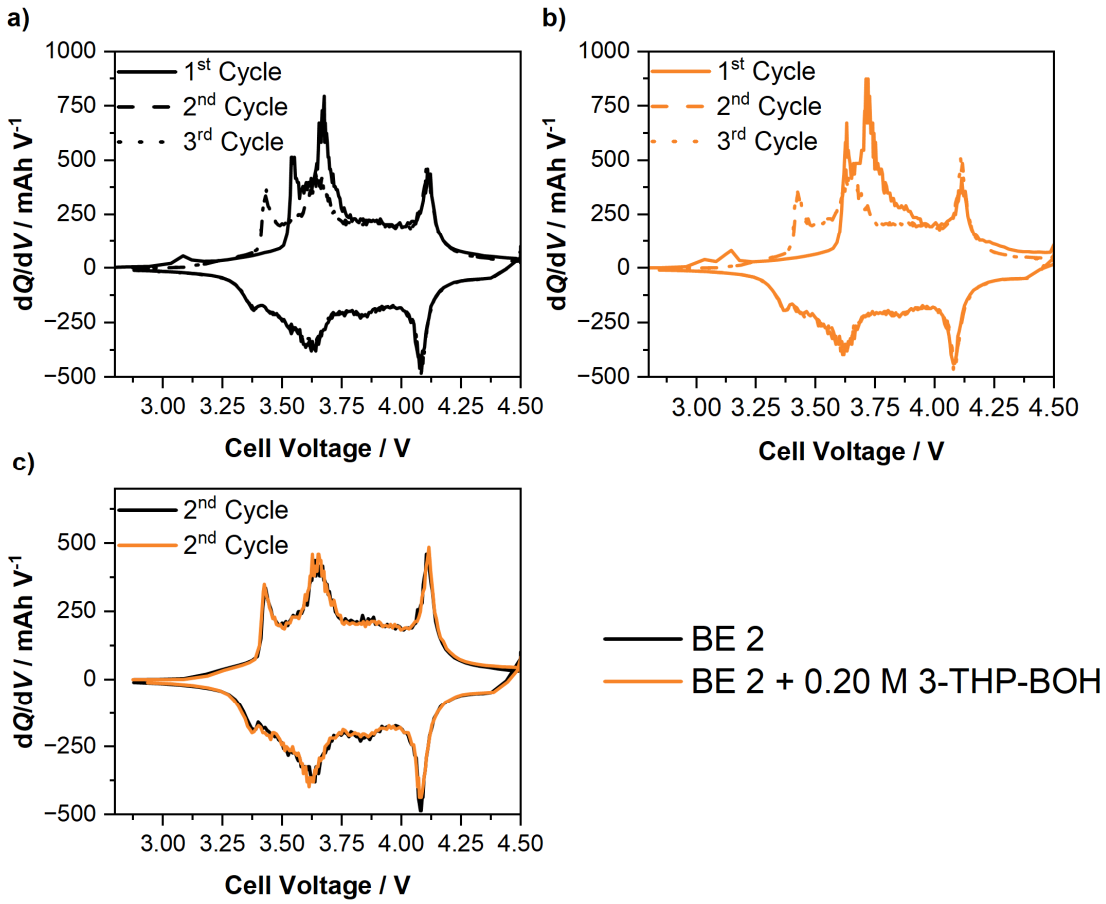

Figure A25: d*Q*/d*V* *vs.* voltage plots drawn for the first three charge/discharge cycles of NMC811||graphite pouch cells in the presence of **a)** the BE 2 (1 M $LiPF_6$ in EC:EMC 3:7 by weight; **black**) and **b)** the BE 2 + 0.20 M 3-THP-BOH (**orange**). **c)** shows the comparison of the second cycle of both investigated electrolyte formulations. Galvanostatic charge/discharge cycling was performed in a voltage range between 2.80 V and 4.50 V with a C-rate of C/10 at the depicted cycles. Note that in **a)** and **b)** the first cycle is marked by a solid line, while the second and third cycles are marked by dashed and dotted lines, respectively. Figure redrawn with permission from [29].

9.3.2.Surface Characterization via SEM, EDX and Raman Spectroscopy

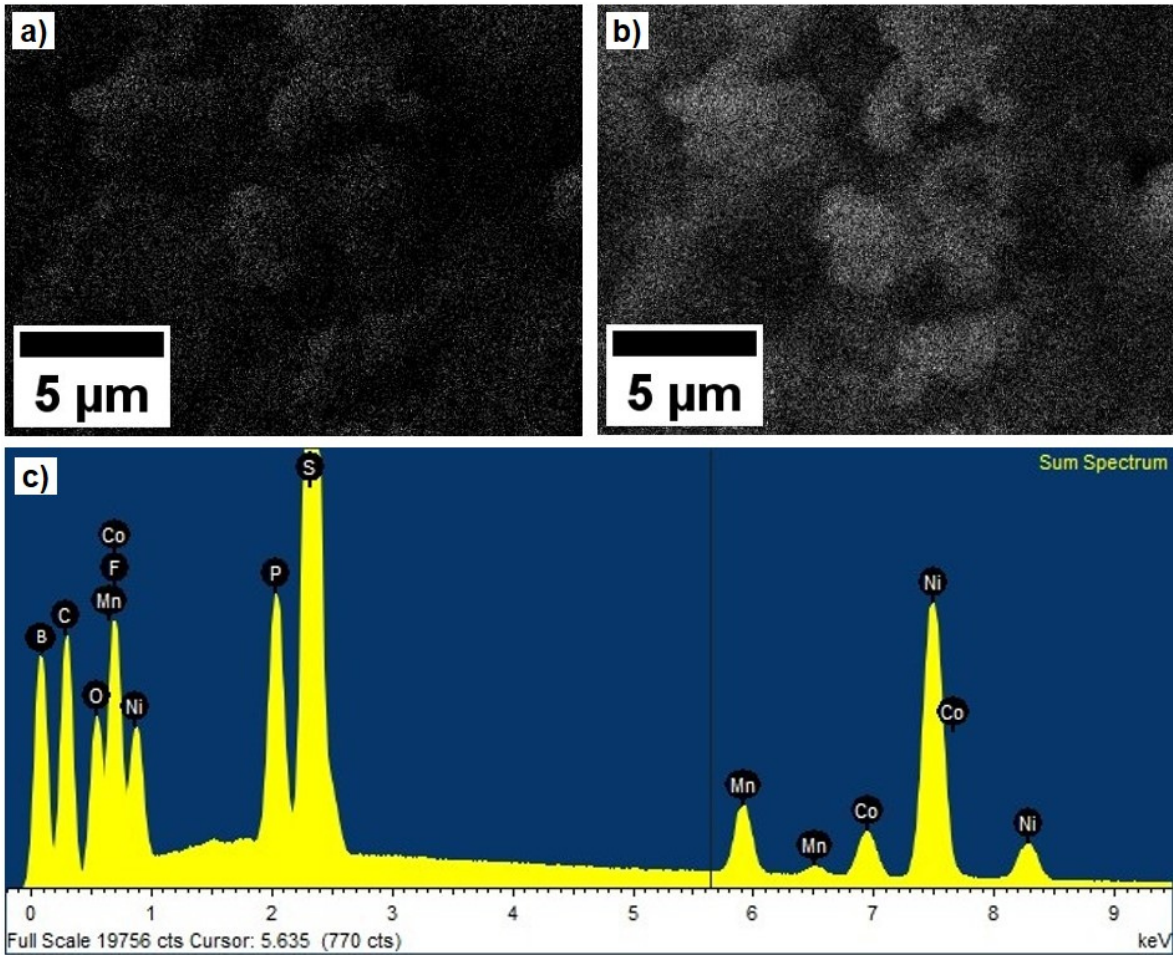

Figure A26: Elemental distribution of **a)** boron and **b)** sulfur on the surface of an NMC811 electrode taken from a NMC811||graphite cell, cycled in the presence of the BE 2 (1 $_M$ $LiPF_6$ in EC:EMC 3:7 by weight) + 0.20 $_M$ 3-THP-BOH. **c)** shows the sum spectrum of the performed EDX analysis and corresponding elements are marked within the spectrum. Figure redrawn with permission from [29].

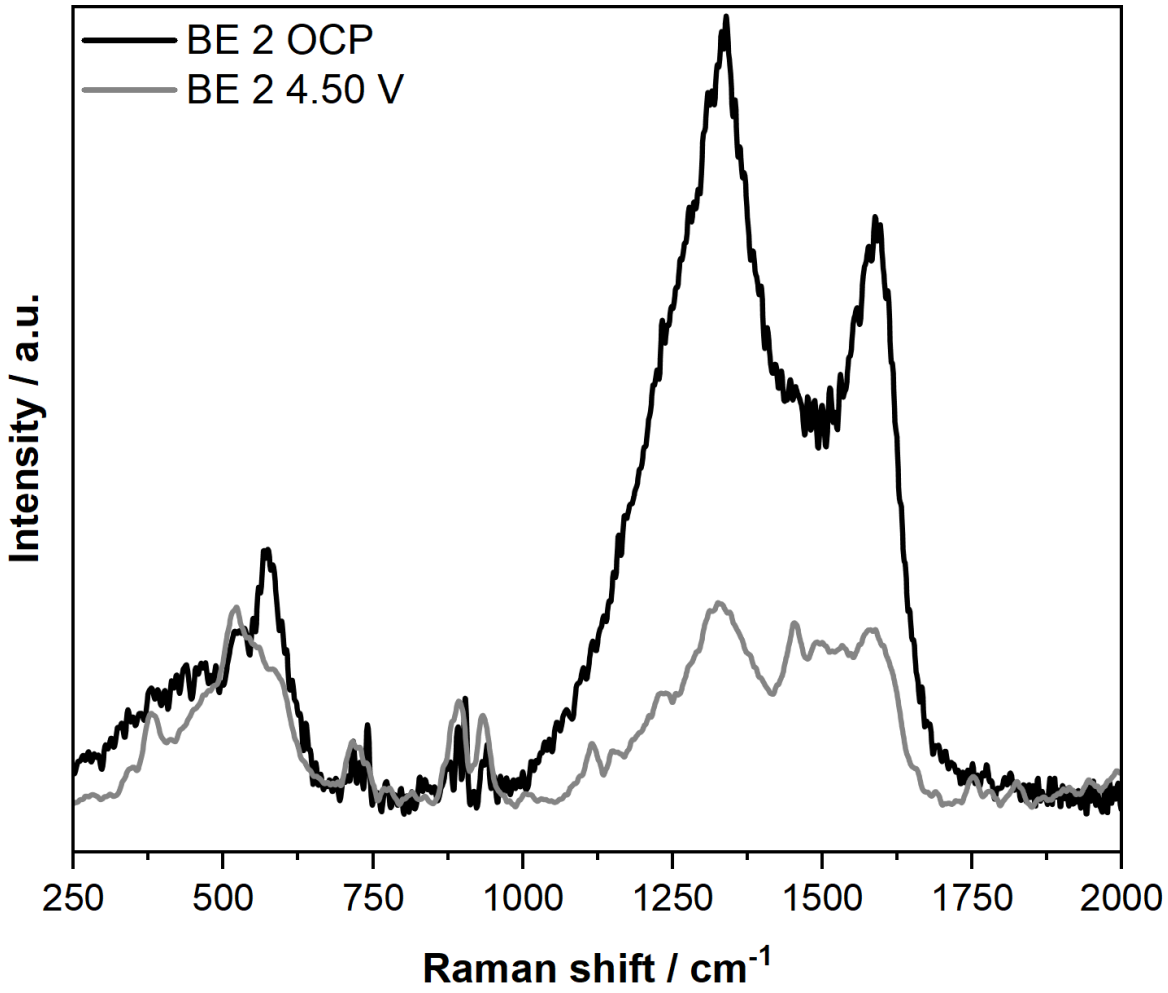

Figure A27: *Operando* SHINER spectra taken from the surface of an NMC811 electrode in the presence of the BE 2 (1 M $LiPF_6$ in EC:EMC 3:7 by weight) at the open circuit potential (OCP, **black**) and the cut-off voltage of 4.50 V *vs*. $Li|Li^+$ (**grey**). For the SHINERS measurement the NMC electrode was connected as working electrode, paired against a graphite counter electrode. Galvanostatic charge was performed at a C-rate of C/3. Au SHINs with a diameter of 55 nm were introduced to the electrode surface before cell assembly. For spectrum acquisition the samples were excited using a 633 nm laser, adjusted to a power output of 1.05 mW. Spectra were acquired over three accumulations of 35 s. Figure redrawn with permission from [29].

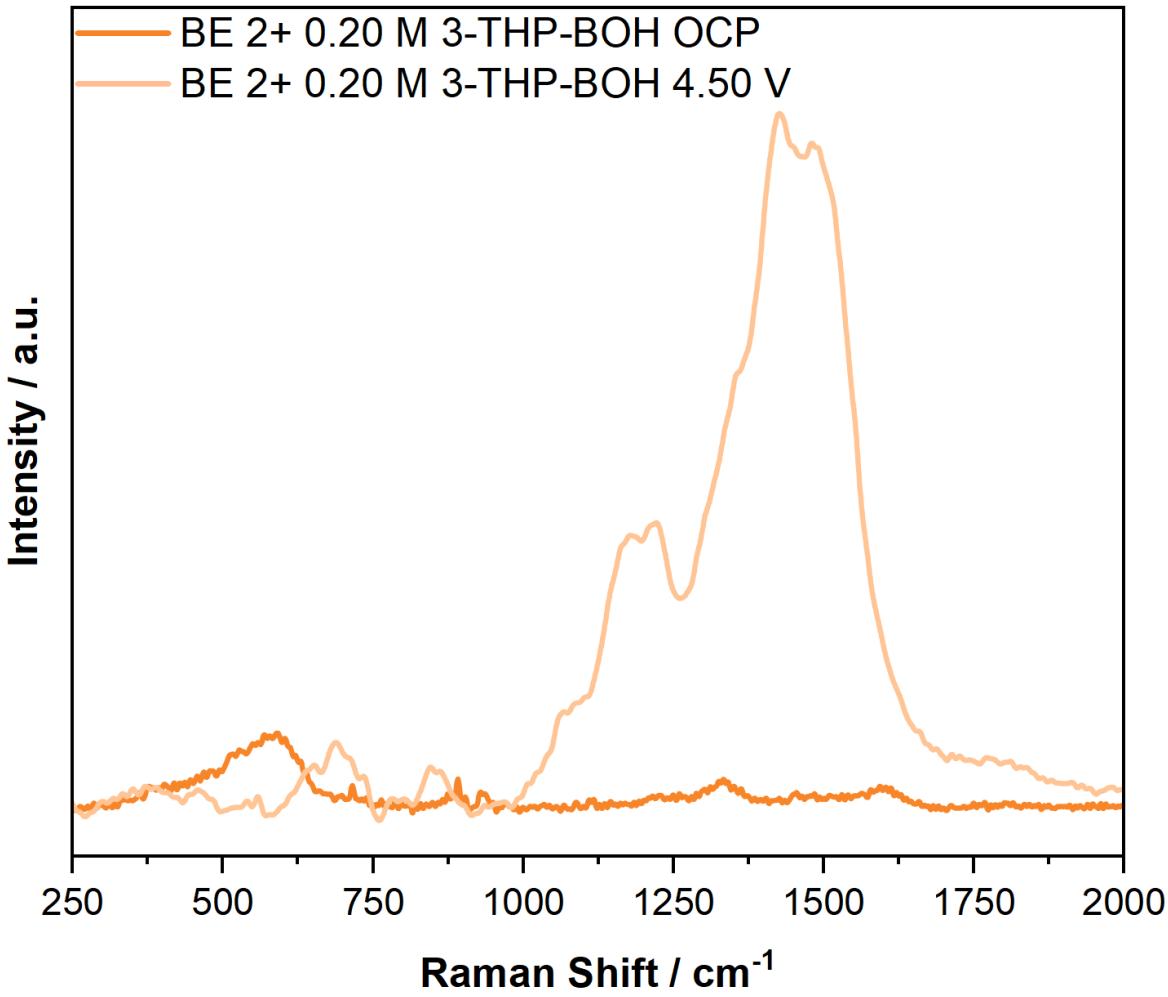

Figure A28: *Operando* SHINER spectra taken from the surface of an NMC811 electrode in the presence of the BE 2 (1 $_M$ $LiPF_6$ in EC:EMC 3:7 by weight) + 0.20 $_M$ 3-THP-BOH at the open circuit potential (OCP, **orange**) and the cut-off voltage of 4.50 V *vs.* $Li|Li^+$ (**light orange**). For the SHINERS measurement the NMC electrode was connected as working electrode, paired against a graphite counter electrode. Galvanostatic charge was performed at a C-rate of C/3. Au SHINs with a diameter of 55 nm were introduced to the electrode surface before cell assembly. For spectrum acquisition the samples were excited using a 633 nm laser, adjusted to a power output of 1.05 mW. Spectra were acquired over three accumulations of 35 s. Figure redrawn with permission from [29].

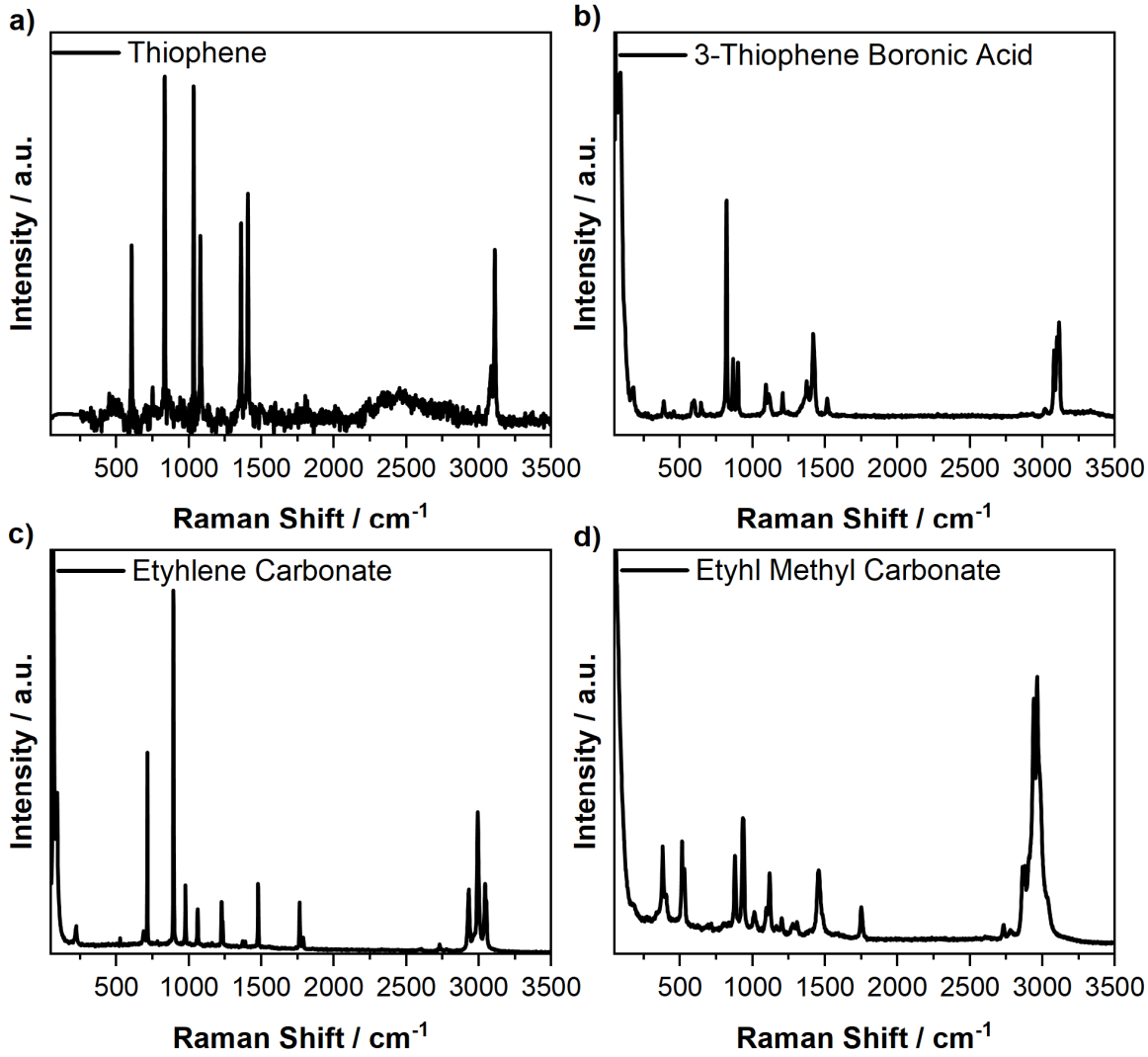

Figure A29: Raman spectra of pure a) thiophene, b) 3-thiophene boronic acid, c) ethylene carbonate, and d) ethyl methyl carbonate. These spectra were utilized to assign bands in the obtained SHINERS spectra. For spectrum acquisition the samples were excited using a 532 nm laser, adjusted to a power output of 6.10 mW. Spectra were acquired over three accumulations of 25 s. Figure redrawn with permission from [29].

Table A3: Assignment of bands observed in the SHINER spectra recorded from the surface of a NMC811 electrode in a NMC811||graphite optical cell with a Li-metal reference electrode containing the BE 2 (1 M $LiPF_6$ in EC:EMC 3:7 by weight) + 0.20 M 3-THP-BOH at the open circuit potential. Table reproduced with permission from [29].

Peak Position [cm^{-1}]	Peak Assignment	Reference
475	NMC Ni E_g	[206]
485	NMC lattice vibrations	[135]
525	EMC O-C-O bending vibrations	[207]
555	NMC Ni A_{1g}	[206]
595	NMC Mn E_g	[206]
715	EC O-C-O bending vibrations	[206]
735	EC*Li^+ O-C-O bending vibrations	[206]
875	EMC CO_3^{2-} bending vibrations	Own reference spectrum
890	EC ring breathing vibrations	[206]
935	EMC	Own reference spectrum
970	Electrolyte	[32]
1115	Thiophene boronic acid	Own reference spectrum
1345	Graphite D-band	[208]
1455	EMC	Own reference spectrum
1600	Graphite G-band	[208]

Table A4: Assignment of bands observed in the SHINER spectra recorded from the surface of a NMC811 electrode in a NMC811||graphite optical cell with a Li-metal reference electrode containing the BE 2 (1 M $LiPF_6$ in EC:EMC 3:7 by weight) + 0.20 M 3-THP-BOH at the cut-off potential of 4.50 V *vs.* Li|Li^+. Table reproduced with permission from [29].

Peak Position [cm^{-1}]	Peak Assignment	Reference
460	NMC Ni E_g	[206]
475	NMC Ni E_g	[206]
525	EMC O-C-O bending vibrations	[207]
535	NMC811 Co A_{1g}	[206]
560	NMC Ni A_{1g}	[206]
650	Polythiophene C-C ring in plane deformation vibrations	[182]
690	Polythiophene C-S-C ring deformation vibrations	[183]
710	EC O-C-O bending or Polythiophene C-S-C in plane deformation vibrations	[182,206]
735	EC*Li^+ O-C-O bending or C-S-C ring deformation vibrations	[183,206]
780	Polythiophene C-S-C in plane deformation vibrations	[182]
845	Polythiophene C-H out of plane deformation vibrations	[182]
860	Li_2CO_3	[209]
865	Thiophene boronic acid	Own reference spectrum
890	EC ring breathing vibrations	[206]
935	EMC	Own reference spectrum

1055	Polythiophene C-H in plane deformation vibrations	[182]
1085	Li_2CO_3	[156]
1180	Semi-carbonate	[32]
1225	Polythiophene C-C ring stretching vibrations	[182]
1345	Graphite D-band	[208]
1425	Polythiophene C=C ring stretching vibrations	[183]
1455	EMC	Own reference spectrum
1490	Polythiophene C=C anti ring stretching vibrations	[183]
1505	Polythiophene	[210]

Table A5: Assignment of bands observed in the SHINER spectra recorded from the surface of a NMC811 electrode in a NMC811||graphite optical cell with a Li-metal reference electrode containing the BE 2 (1 $_M$ $LiPF_6$ in EC:EMC 3:7 by weight) at the open circuit potential. Table reproduced with permission from [29].

Peak Position [cm^{-1}]	**Peak Assignment**	**Reference**
465	NMC Ni E_g	[206]
525	EMC O-C-O bending vibrations	[207]
570	NMC Ni A_{1g}	[206]
680	NMC Co_3O_4 A_{1g}	[206]
720	EC O-C-O bending vibrations	[206]
740	EC*Li^+ O-C-O bending vibrations	[206]
875	EMC CO_3^{2-} bending vibrations	Own reference spectrum
885	EC ring breathing vibrations	[206]
900	EC*Li^+ ring breathing vibrations	[206]
940	EMC	Own reference spectrum
1095	EMC O-C-O sym. stretching vibrations	[211]
1340	Graphite D-band	[208]
1455	EMC	Own reference spectrum
1595	Graphite G-band	[208]

Table A6: Assignment of bands observed in the SHINER spectra recorded from the surface of a NMC811 electrode in a NMC811||graphite optical cell with a Li-metal reference electrode containing the BE 2 (1 $_M$ $LiPF_6$ in EC:EMC 3:7 by weight) at the cut-off potential of 4.50 V *vs*. Li|Li^+. Table reproduced with permission from [29].

Peak Position [cm^{-1}]	**Peak Assignment**	**Reference**
525	EMC O-C-O bending vibrations	[207]
560	NMC Ni A_{1g}	[206]
590	NMC Mn E_g	[206]
715	EC O-C-O bending vibrations	[206]
740	EC*Li^+ O-C-O bending vibrations	[206]
895	EC ring breathing vibrations	[206]
935	EMC	Own reference spectrum
1010	Semi-carbonate	[32]
1120	EMC CH_3 CH_3 rocking vibrations	[211]
1150	Semi-carbonate	[151]
1235	Semi-carbonate	[32]
1340	Graphite D-band	[208]
1455	EMC	Own reference spectrum
1505	Li_2CO_3 C-O stretching vibrations	[212]
1535	Semi-carbonate	[151]
1595	Graphite G-band	[208]

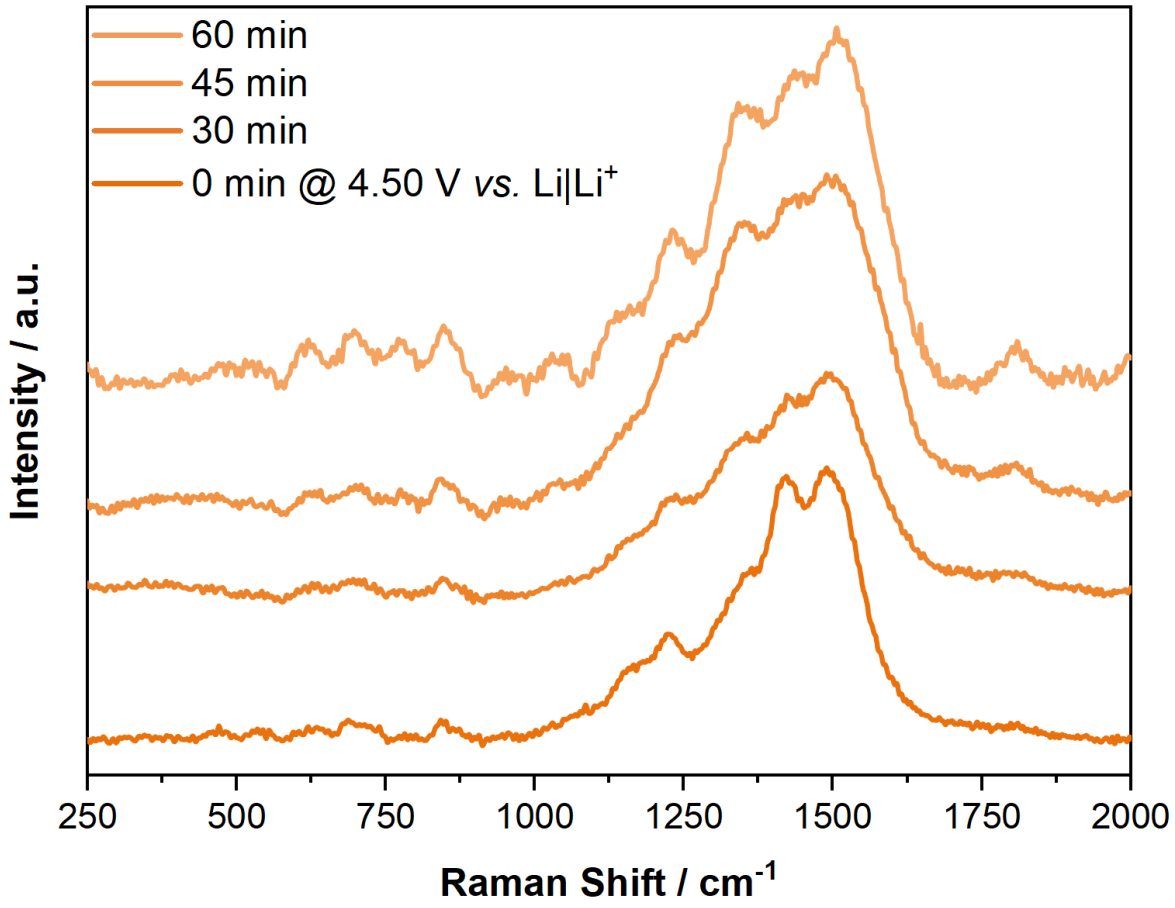

Figure A30: Time-dependent SHINER spectra taken from the surface of an NMC811 electrode in the presence of the BE 2 (1 M $LiPF_6$ in EC:EMC 3:7 by weight) + 0.20 M 3-THP-BOH. First, the electrode was charged to the cut-off voltage of 4.50 V *vs.* Li|Li$^+$. Afterwards, a constant potential was applied to the cell to hold the electrode potential. SHINER spectra were recorded at 0 min, 30 min, 45 min, and 60 min after reaching 4.50 V *vs.* Li|Li$^+$. For the SHINERS measurement the NMC electrode was connected as working electrode, paired against a graphite counter electrode. Galvanostatic charge was performed at a C-rate of C/3. Au SHINs with a diameter of 55 nm were introduced to the electrode surface before cell assembly. For spectrum acquisition the samples were excited using a 633 nm laser, adjusted to a power output of 1.05 mW. Spectra were acquired over three accumulations of 35 s. Figure redrawn with permission from [29].

9.3.3. QC Calculations

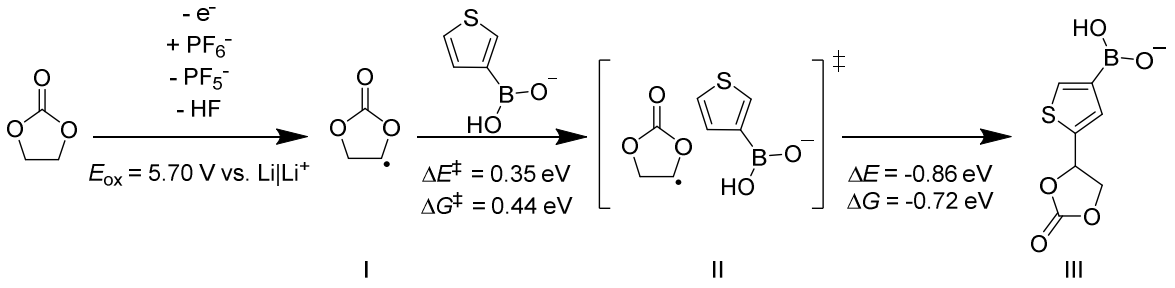

Figure A31: Suggested reaction mechanisms for the electro-co-polymerization of EC and 3-THP-BOH. Given are the energy differences (Δ*E*, computed at 0 K) and the free energy difference (Δ*G*, computed at 298 K) calculated for each step. The determined energy values are given in electron volts (eV). Figure redrawn with permission from [29].

9.4. Appendix for Chapter 7

9.4.1.Electrochemical Investigation

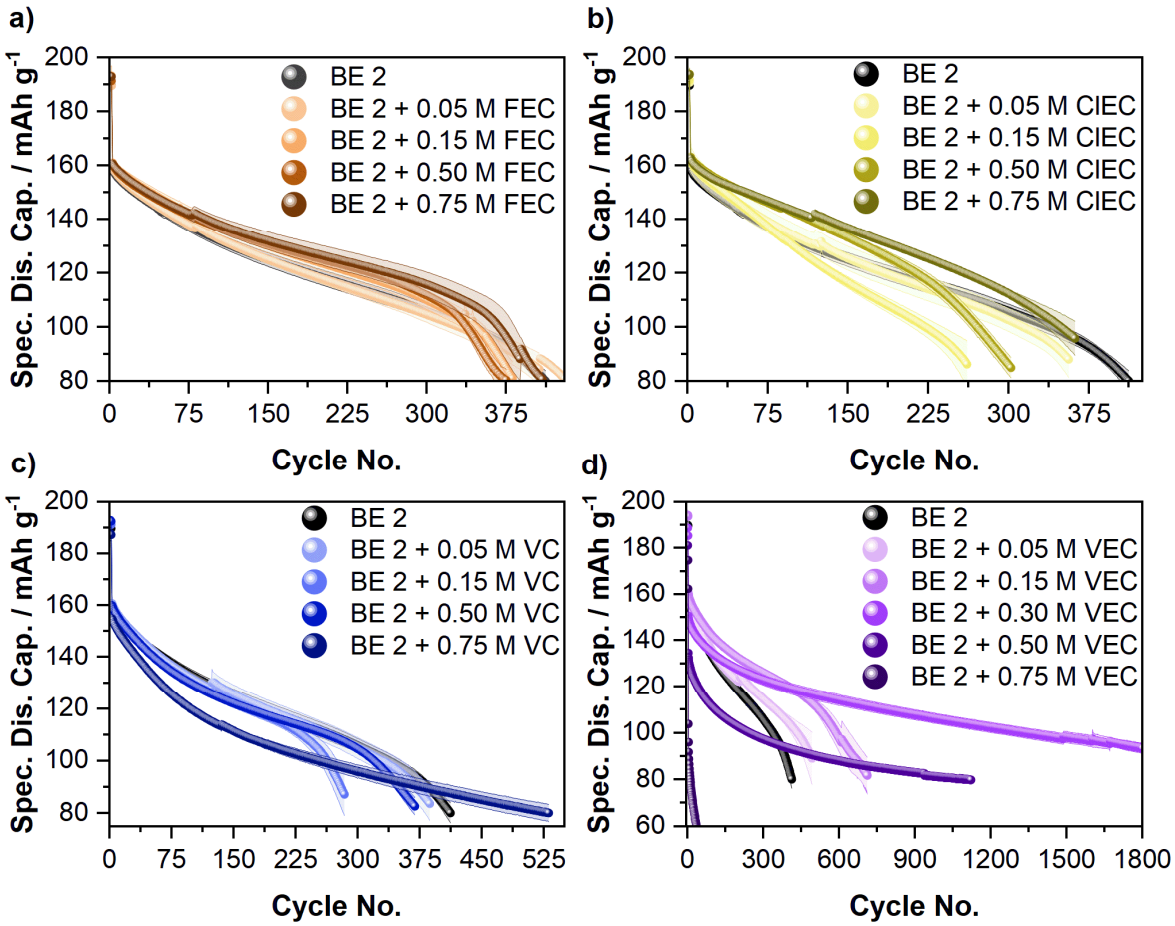

Figure A32: Specific discharge capacities (Spec. Dis. Cap.) obtained during the galvanostatic charge/discharge cycling experiments performed with NMC622||graphite pouch cells at a C-rate of 1 C in a voltage range between 2.80 V – 4.50 V to determine the optimum electrolyte additive concentration for **a)** FEC (**brown**), **b)** ClEC (**dark yellow**), **c)** VC (**blue**), and **d)** VEC (**purple**). Note that all investigated electrolyte formulations are compared to the BE 2 electrolyte (1 M $LiPF_6$ in EC:EMC, 3:7 by weight). A comparison of the electrolyte formulations containing the optimized additive concentration is depicted in **Figure 27**. Figure redrawn with permission from [159].

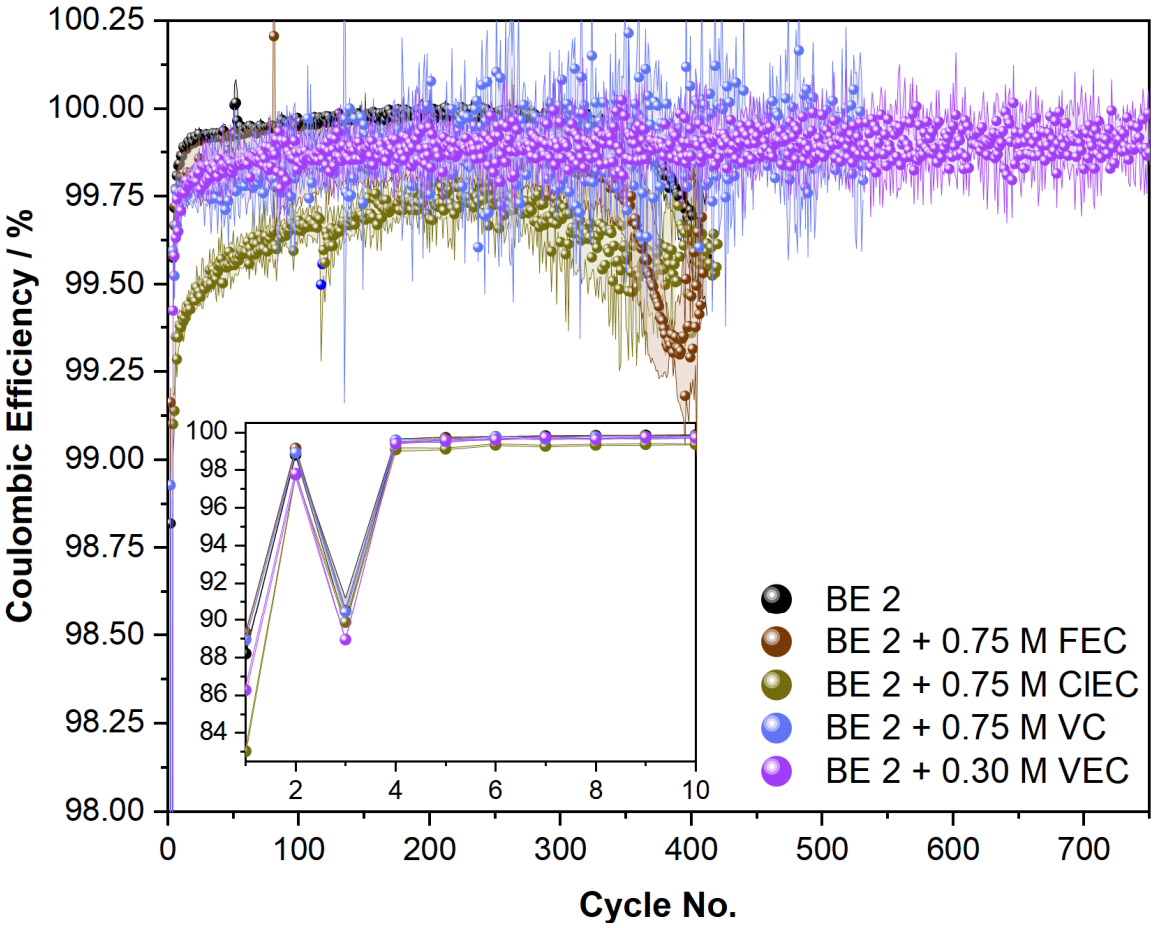

Figure A33: Coulombic efficiencies (CEs) obtained from NMC622||graphite pouch cells galvanostatically charge/discharge cycled at a C-rate of 1 C in a voltage range between 2.80 V – 4.50 V. Depicted are the CEs of cells containing the BE 2 (1 $_{M}$ $LiPF_6$ in EC:EMC 3:7 by weight; **black**) and the cells containing the optimum electrolyte additive concentration for FEC (**brown**), ClEC (**dark yellow**), VC (**blue**), and VEC (**purple**). The inset in the figure puts the focus on the initial 10 charge/discharge cycles, including the formation cycles. Figure redrawn with permission from [159].

9.4.2.GC-MS Investigation of the Aged Electrolyte

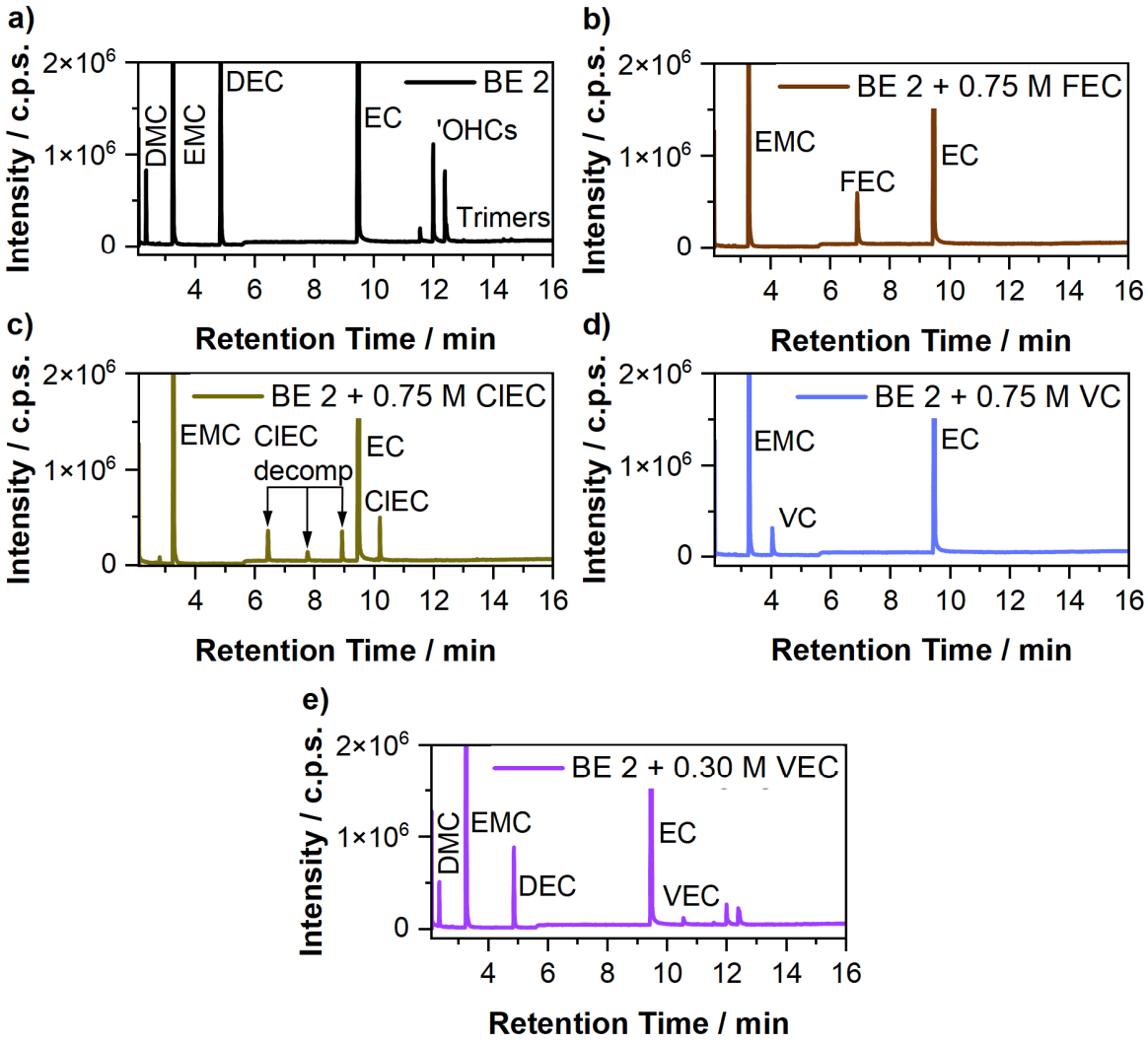

Figure A34: Individual gas chromatograms recorded from the investigated electrolyte formulations electrochemically aged in NMC622||graphite pouch cells. The respective electrolytes were extracted after 100 galvanostatic charge/discharge cycles. Peak identification was performed *via* mass spectrometry and peaks are assigned in the respective chromatograms. Depicted are the chromatograms of the electrochemically aged **a)** BE 2 (1 M $LiPF_6$ in EC:EMC 3:7 by weight ; **black**) and the additive-containing electrolyte formulations at the optimum electrolyte additive concentration for **b)** FEC (**brown**), **c)** CIEC (**dark yellow**), **d)** VC (**blue**), and **e)** VEC (**purple**). Figure redrawn with permission from [159].

As discussed in the main text, the CIEC-containing electrolyte formulation was the only aged electrolyte, exhibiting distinct additive decomposition products. These were further analyzed *via* GC-HRAM-MS. Based on the fragment pattern, three different decomposition product structures were identified, depicted in **Figure A35** below

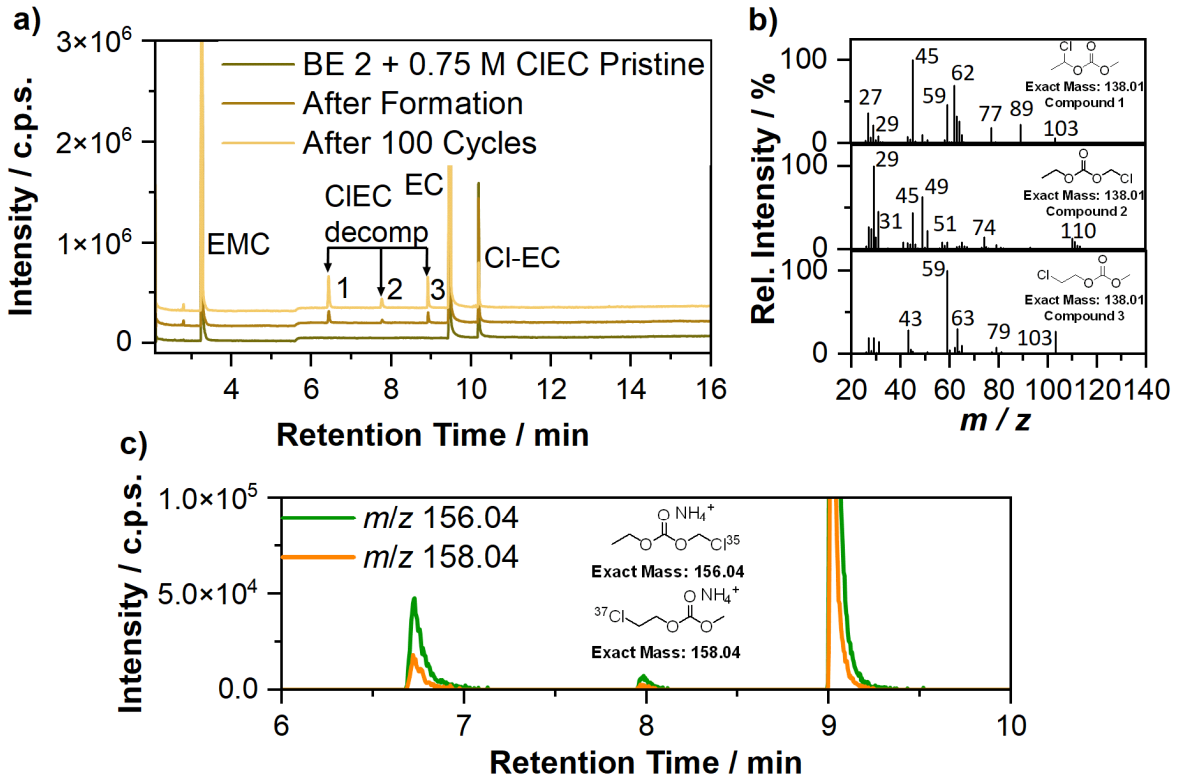

Figure A35: Results of the additionally performed gas chromatography high resolution accurate mass spectrometry analysis of the decomposition products identified for the ClEC-containing electrolyte formulation. **a)** shows the regular gas chromatograms of the investigated electrolyte formulation at a pristine state, after formation, and after 100 consecutive galvanostatic charge/discharge cycles. Peak assignments were obtained by mass spectrometry and are noted in the chromatogram. **b)** Mass spectra of the fragment pattern obtained through electron ionization of the compounds 1 – 3, identified as ClEC decomposition products in the gas chromatogram. In addition, molecular structures proposed based on the fragment pattern of the identified compounds are depicted. **c)** Extracted ion chromatogram of the $[M+NH_4]^+$ adducts obtained by chemical ionization, characteristic for chlorine containing compounds, with a *m/z* of 156.04 and 158.04. Figure redrawn with permission from [159].

9.4.3. SHINERS SEI Investigation

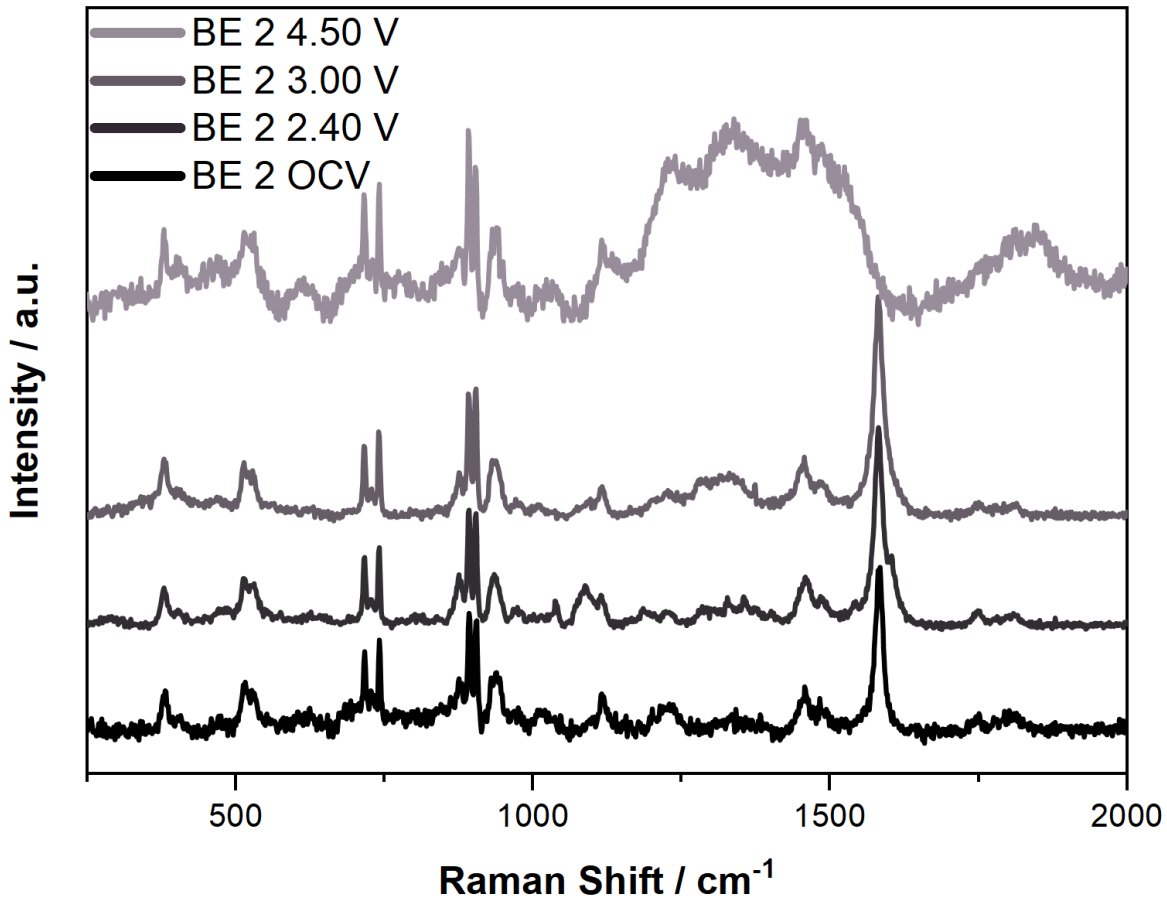

Figure A36: *Operando* SHINER spectra taken from the surface of a graphite electrode in the presence of the BE 2 (1 M $LiPF_6$ in EC:EMC 3:7 by weight). For the SHINERS measurement the graphite electrode was connected as working electrode, paired against a NMC622 counter electrode. Galvanostatic charge was performed at a C-rate of C/3. Au SHINs with a diameter of 55 nm were introduced to the electrode surface before cell assembly. Spectra were recorded at different cell voltages, denoted in the spectra and indicated by the intensity of the color. For spectrum acquisition the samples were excited using a 633 nm laser, adjusted to a power output of 1.05 mW. Spectra were acquired over three accumulations of 35 s. Figure redrawn with permission from [159].

Table A7: Detailed assignment for the bands observed during the *operando* SHINERS measurement of the surface of the graphite electrode galvanostatically charged in the presence of the BE 2 (1 $_M$ $LiPF_6$ in EC:EMC 3:7 by weight). The absence of specific bands at selected cell voltages is indicated by empty cells. In these cases, the band was observed at higher or lower cell voltages, respectively. The reference "own spectrum" refers to reference spectra reported in the Appendix chapter. Table redrawn with permission from [159].

Observed band [cm^{-1}]				Assignment	Reference
OCV	2.40 V	3.00 V	4.50 V		
380	380	380	380	EMC	Own reference spectrum
405	404	403	405	EMC	Own reference spectrum
514	514	514	512	EMC O=C=O bending vibrations	Own reference spectrum, [206]
529	529	529	529	EMC	Own reference spectrum
715	717	717	715	EC C=O bending vibrations	[206]
730	727	727	728	EC coordinated to Li^+	[211]
742	742	742	742	PF_6^- sym. vibrations	[206,211]
875	876	876	876	EMC	Own reference spectrum
893	891	893	891	EC ring breathing vibrations	[206,211]
903	903	903	903	EC coordinated to Li^+	[206,211]
		913	913	DEDOHC	Own reference spectrum
938	935	934	935	EMC	Own reference spectrum
970	970	970	973	Electrolyte (EC)	[32]
1015		1012		EMC	Own reference spectrum
	1040		1037	DEDOHC	Own reference spectrum
	1089	1094		Electrolyte (EMC; O-C-O bending), Li_2CO_3, semi-carbonates	[32,162,211]
1116	1114	1116	1116	EMC	Own reference spectrum
	1186			Semi-carbonates (LMC)	[32]
1225	1225	1225	1228	Electrolyte (EC)	[32]
	1292	1285		DMDHOC	Own reference spectrum
1340	1327	1327	1332	Graphite D-band	
	1357			Semi-carbonate (LMC)	Own reference spectrum
1456	1458	1456	1453	EMC	Own reference spectrum
1488	1485	1488	1485	EC CH bending vibrations	[211]
1582	1582	1582		Graphite G-band	
1751	1748	1748		EMC	Own reference spectrum
	1780	1778		EC C=O stretching vibrations	[211]

1813	1810	1810	1810	EC C=O stretching vibrations	[207]
2690	2687	2685		Electrolyte	
2878	2878	2878		EMC	Own reference spectrum
2940	2940	2940	2940	EMC	Own reference spectrum
2967	2967	2967	2967	EMC	Own reference spectrum

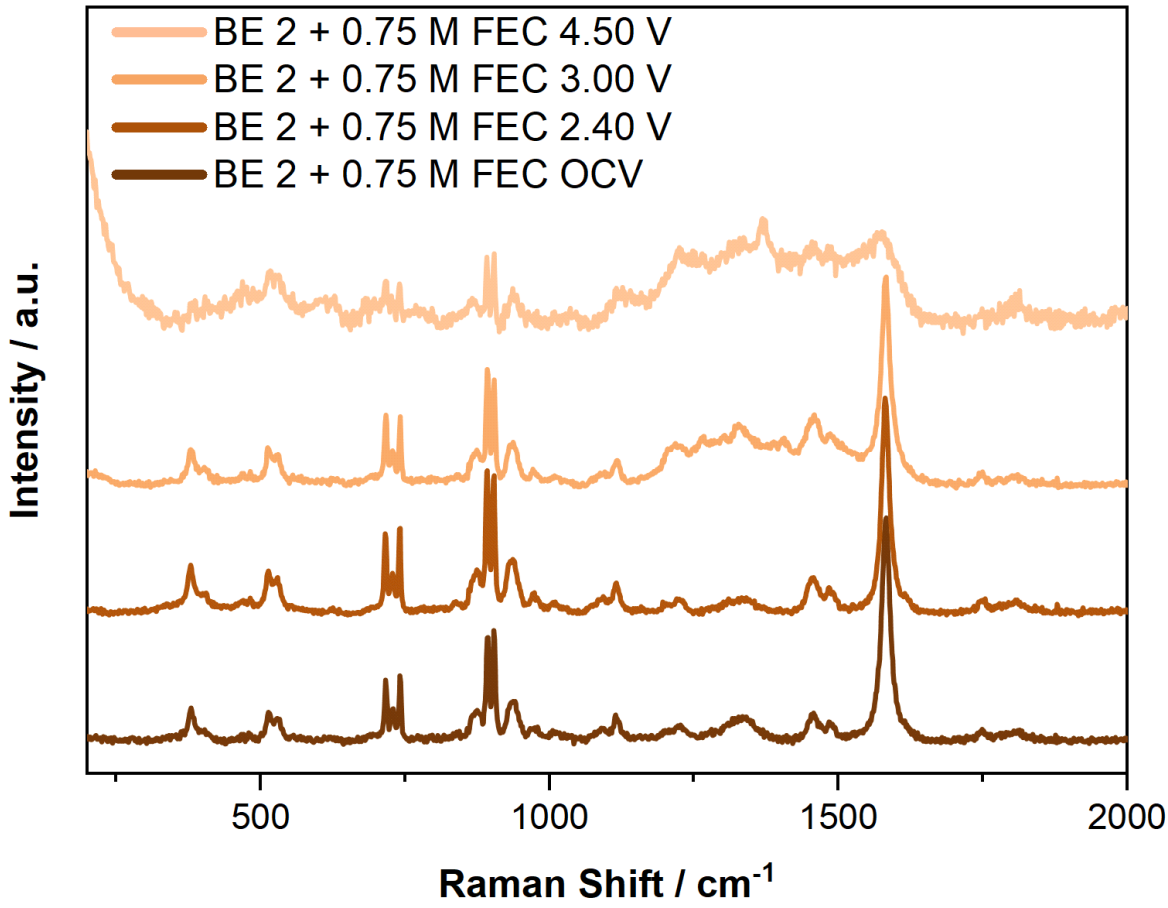

Figure A37: *Operando* SHINER spectra taken from the surface of a graphite electrode in the presence of the BE 2 (1 $_M$ $LiPF_6$ in EC:EMC 3:7 by weight) + 0.75 $_M$ FEC. For the SHINERS measurement the graphite electrode was connected as working electrode, paired against a NMC622 counter electrode. Galvanostatic charge was performed at a C-rate of C/3. Au SHINs with a diameter of 55 nm were introduced to the electrode surface before cell assembly. Spectra were recorded at different cell voltages, denoted in the spectra and indicated by the intensity of the color. For spectrum acquisition the samples were excited using a 633 nm laser, adjusted to a power output of 1.05 mW. Spectra were acquired over three accumulations of 35 s. Figure redrawn with permission from [159].

Table A8: Detailed assignment for the bands observed during the *operando* SHINERS measurement of the surface of the graphite electrode galvanostatically charged in the presence of the BE 2 (1 $_M$ $LiPF_6$ in EC:EMC 3:7 by weight) + 0.75 $_M$ FEC. The absence of specific bands at selected cell voltages is indicated by empty cells. In these cases, the band was observed at higher or lower cell voltages, respectively. The reference "own spectrum" refers to reference spectra reported in the Appendix chapter. Table redrawn with permission from [159].

Observed band [cm^{-1}]				Assignment	Reference
OCV	**2.40 V**	**3.00 V**	**4.50 V**		
380	378	380	380	EMC	Own reference spectrum
404	405	403		EMC	Own reference spectrum
482	479	482		FEC	Own reference spectrum
514	514	514	515	EMC O=C=O bending vibrations	Own reference spectrum, [206]
528	529	529	529	EMC	Own reference spectrum
	626	626	626	LiF, LiOH; organic C-F stretching vibrations	[148,195]
718	717	717	717	EC C=O bending vibrations	[206]
729	727	727	728	EC coordinated to Li^+	[211]
741	740	740	741	PF_6^- sym. vibrations	[206,211]
	841	839		Semi-carbonates (DMDOHC)	Own reference spectrum
873	876	873	876	EMC	Own reference spectrum
893	891	893	892	EC ring breathing vibrations	[206,211]
904	903	903	904	EC coordinated to Li^+	[206,211]
938	935	935	937	EMC	Own reference spectrum
974	973	973		Electrolyte (EC)	[32]
1009	1007	1010		EMC	Own reference spectrum
1090	1091	1090		Electrolyte (EMC; O-C-O bending vibrations), Li_2CO_3, semi-carbonates	[32,162,211]
1115	1114	1116	1120	EMC	Own reference spectrum
	1159			Semi-carbonates (LMC, DMDOHC)	Own reference spectrum, [32]
	1201			EMC	Own reference spectrum
1225	1225	1225	1225	Electrolyte (EC)	[32]
		1265		Semi-carbonates (LEMC)	[32]
		1301		Semi-carbonates (DEDOHC)	Own reference spectrum, [32]
1337	1337	1327	1328	Graphite D-band	
			1370	Semi-carbonates (LMC), C-F, poly-furan	Own reference spectrum, [182,195]

				(C-C stretching vibrations)	
		1406		Semi-carbonates (DEDOHC)	Own reference spectrum
1457	1456	1456	1452	EMC	Own reference spectrum
1485	1483	1485	1485	EC CH bending vibrations	[211]
1581	1582	1582	1572	Graphite G-band	
1749	1748	1748		EMC	Own reference spectrum
	1783	1780		EC C=O stretching vibrations	[211]
1811	1808	1810	1810	EC C=O stretching vibrations	[207]
	2685	2687		Electrolyte	
	2878	2878		EMC	Own reference spectrum
	2940	2940	2938	EMC	Own reference spectrum
	2967	2967	2967	EMC	Own reference spectrum

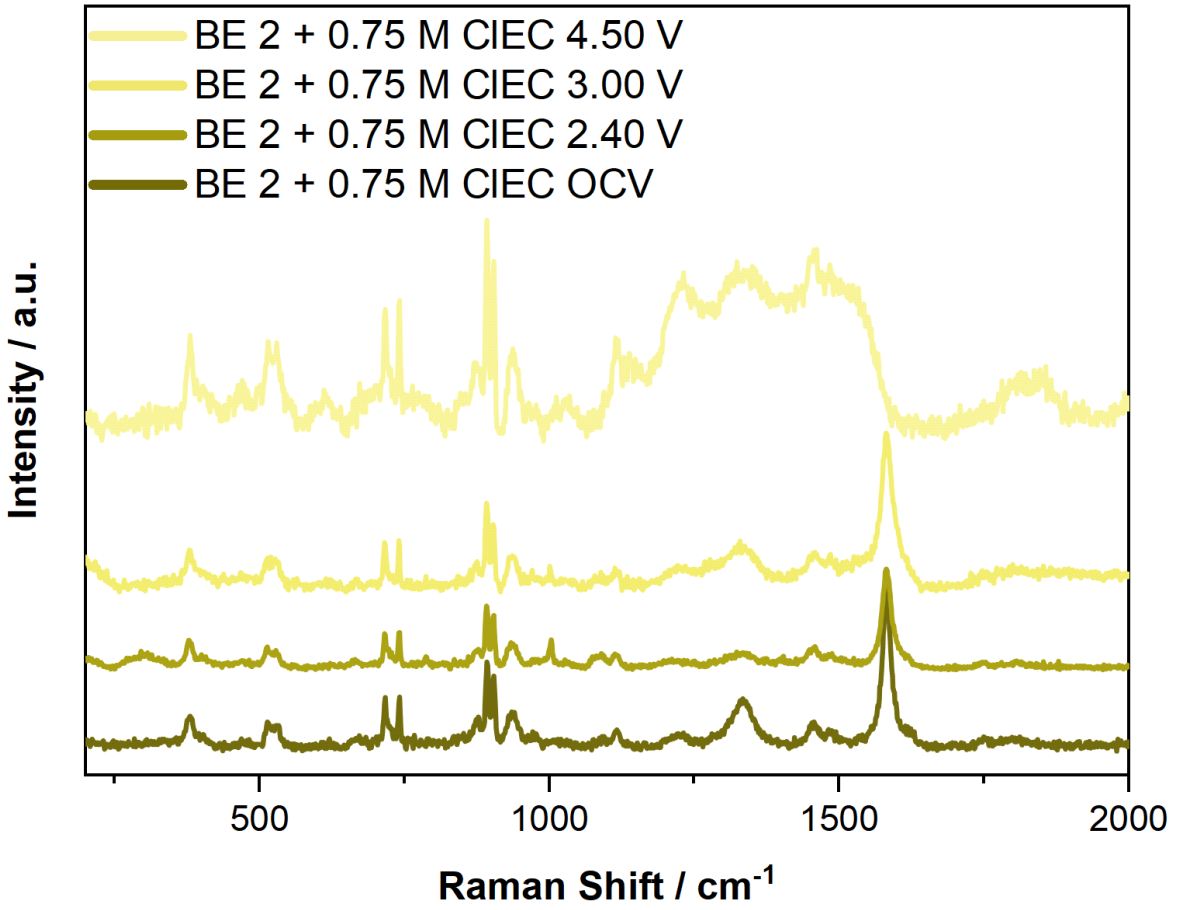

Figure A38: *Operando* SHINER spectra taken from the surface of a graphite electrode in the presence of the BE 2 (1 $_M$ $LiPF_6$ in EC:EMC 3:7 by weight) + 0.75 $_M$ ClEC. For the SHINERS measurement the graphite electrode was connected as working electrode, paired against a NMC622 counter electrode. Galvanostatic charge was performed at a C-rate of C/3. Au SHINs with a diameter of 55 nm were introduced to the electrode surface before cell assembly. Spectra were recorded at different cell voltages, denoted in the spectra and indicated by the intensity of the color. For spectrum acquisition the samples were excited using a 633 nm laser, adjusted to a power output of 1.05 mW. Spectra were acquired over three accumulations of 35 s. Figure redrawn with permission from [159].

Table A9: Detailed assignment for the bands observed during the *operando* SHINERS measurement of the surface of the graphite electrode galvanostatically charged in the presence of the BE 2 (1 $_M$ $LiPF_6$ in EC:EMC 3:7 by weight) + 0.75 $_M$ ClEC. The absence of specific bands at selected cell voltages is indicated by empty cells. In these cases, the band was observed at higher or lower cell voltages, respectively. The reference "own spectrum" refers to reference spectra reported in the Appendix chapter. Table redrawn with permission from [159].

Observed band [cm^{-1}]				Assignment	Reference
OCV	**2.40 V**	**3.00 V**	**4.50 V**		
380	378	380	380	EMC	Own reference spectrum
403	403	405		EMC	Own reference spectrum
	470		470	DEDOHC; C-Cl	Own reference spectrum, [32], [195]
514	514	514	515	EMC O=C=O bending vibrations	Own reference spectrum, [206]
531	529	529	529	EMC	Own reference spectrum
670	665	665	667	ClEC	Own reference spectrum

717	717	717	718	EC C=O bending vibrations	[206]
727	727	727	729	EC coordinated to Li^+	[211]
742	742	741	739	PF_6^- sym. vibrations	[206,211]
876	876	876	875	EMC	Own reference spectrum
893	893	893	892	EC ring breathing vibrations	[206,211]
903	903	903	904	EC coordinated to Li^+	[206,211]
937	935	935	937	EMC	Own reference spectrum
	1003	1003	1003	Semi-carbonates	[32]
	1030			Semi-carbonates	Own reference spectrum, [32]
	1080			Li_2CO_3	[162]
	1090	1090	1090	Electrolyte (EMC; O-C-O bending vibrations), Li_2CO_3, semi-carbonates	[32,162,211]
1116	1114	1116	1114	EMC	Own reference spectrum
1223	1220	1221	1221	Electrolyte (EC)	[32]
1334	1334	1331	1330	Graphite D-band	
1456	1456	1456	1458	EMC	Own reference spectrum
1485	1483	1484	1484	EC CH bending vibrations	[211]
1582	1582	1582	1582	Graphite G-band	
1748	1751			EMC	Own reference spectrum
	1778			EC C=O stretching vibrations	[211]
	1805			EC C=O stretching vibrations	[207]
2687	2687	2688	2686	Electrolyte	
2881	2881	2874	2874	EMC	Own reference spectrum
2940	2940	2941	2939	EMC	Own reference spectrum
2970	2967	2967	2967	EMC	Own reference spectrum

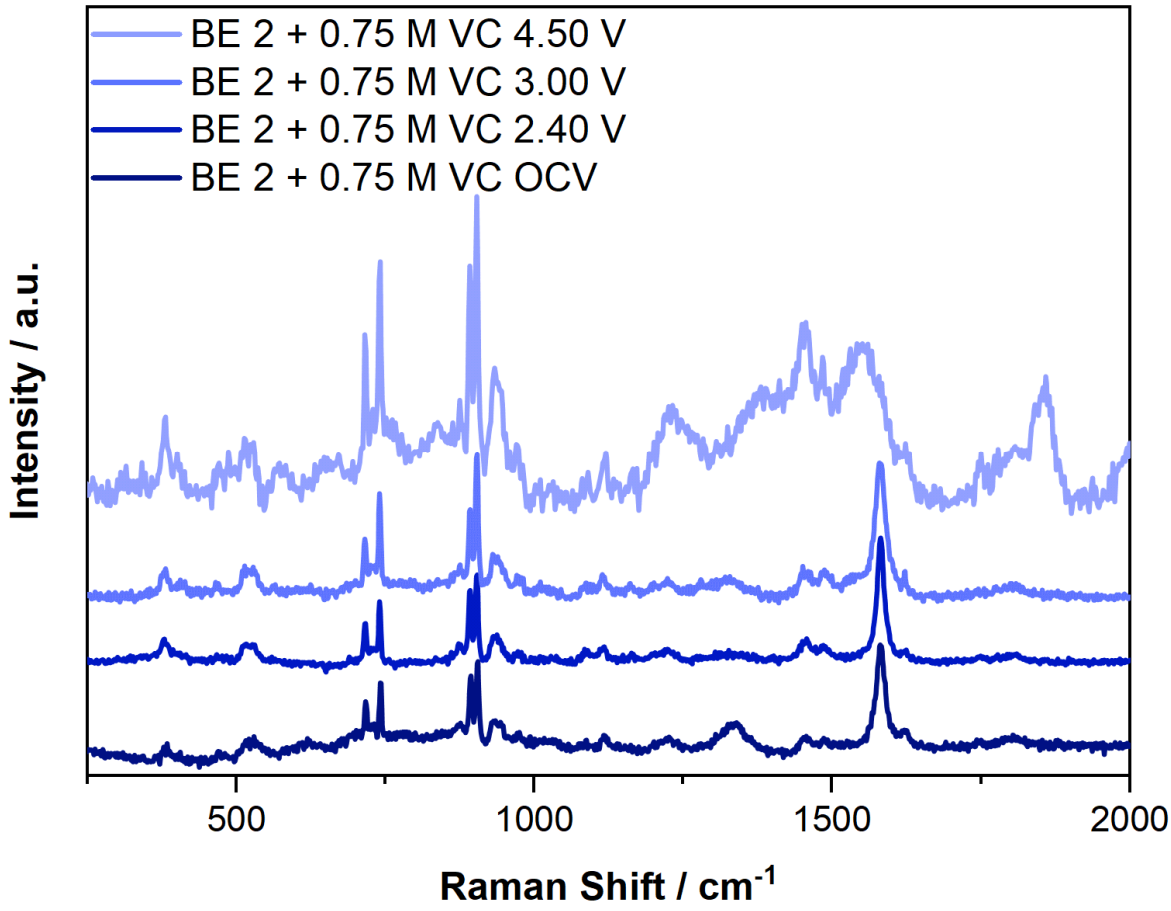

Figure A39: *Operando* SHINER spectra taken from the surface of a graphite electrode in the presence of the BE 2 (1 M $LiPF_6$ in EC:EMC 3:7 by weight) + 0.75 M VC. For the SHINERS measurement the graphite electrode was connected as working electrode, paired against a NMC622 counter electrode. Galvanostatic charge was performed at a C-rate of C/3. Au SHINs with a diameter of 55 nm were introduced to the electrode surface before cell assembly. Spectra were recorded at different cell voltages, denoted in the spectra and indicated by the intensity of the color. For spectrum acquisition the samples were excited using a 633 nm laser, adjusted to a power output of 1.05 mW. Spectra were acquired over three accumulations of 35 s. Figure redrawn with permission from [159].

Table A10: Detailed assignment for the bands observed during the *operando* SHINERS measurement of the surface of the graphite electrode galvanostatically charged in the presence of the BE 2 (1 M $LiPF_6$ in EC:EMC 3:7 by weight) + 0.75 M VC. The absence of specific bands at selected cell voltages is indicated by empty cells. In these cases, the band was observed at higher or lower cell voltages, respectively. The reference "own spectrum" refers to reference spectra reported in the Appendix chapter. Table redrawn with permission from [159].

Observed band [cm^{-1}]				Assignment	Reference
OCV	**2.40 V**	**3.00 V**	**4.50 V**		
381	378	380	381	EMC	Own reference spectrum
		405	402	EMC	Own reference spectrum
	517	517	513	EMC O=C=O bending vibrations	Own reference spectrum, [206]
529	529	529	525	EMC	Own reference spectrum
		564		VC	Own reference spectrum
	690	688		Semi-carbonates (DMDOHC)	Own reference spectrum
717	717	717	717	EC C=O bending vibrations	[206]
730	730	727	729	EC coordinated to Li^+	[211]
742	742	740	741	PF_6^- sym. vibrations	[206,211]
873	873	873	876	EMC	Own reference spectrum
893	893	893	892	EC ring breathing vibrations	[206,211]
906	906	903	904	EC coordinated to Li^+	[206,211]
935	935	938	937	EMC	Own reference spectrum
973	973	978	973	Electrolyte (EC)	[32]
	1090	1090		Electrolyte (EMC; O-C-O bending vibrations), Li_2CO_3, semi-carbonates	[32,162,211]
1116	1116	1116	1120	EMC	Own reference spectrum
	1161	1161	1160	Semi-carbonates (LMC), VC	Own reference spectrum, [32]
	1203	1201		EMC	Own reference spectrum
1225	1223	1223		Electrolyte (EC)	[32]
		1280		Semi-carbonates (DEDOHC)	Own reference spectrum
	1307			EMC	Own reference spectrum
1334	1330	1329		Graphite D-band	
1456	1456	1456	1454	EMC	Own reference spectrum
1485	1488	1485	1484	EC CH bending	[211]
		1533		Carboxylates COO^- stretching vibrations	[195]
			1560	VC	Own reference spectrum

1580	1582	1580		Graphite G-band	
1622	1622	1622		VC C=C	Own reference spectrum
	1748			EMC	Own reference spectrum
1803	1808	1803		EC C=O stretching vibrations	[207]
			1854	Li_2C_2	[162]
2685	2687	2685		Electrolyte	
2878	2878	2878	2879	EMC	Own reference spectrum
2940	2940	2940	2941	EMC	Own reference spectrum
2972	2970	2970	2969	EMC	Own reference spectrum

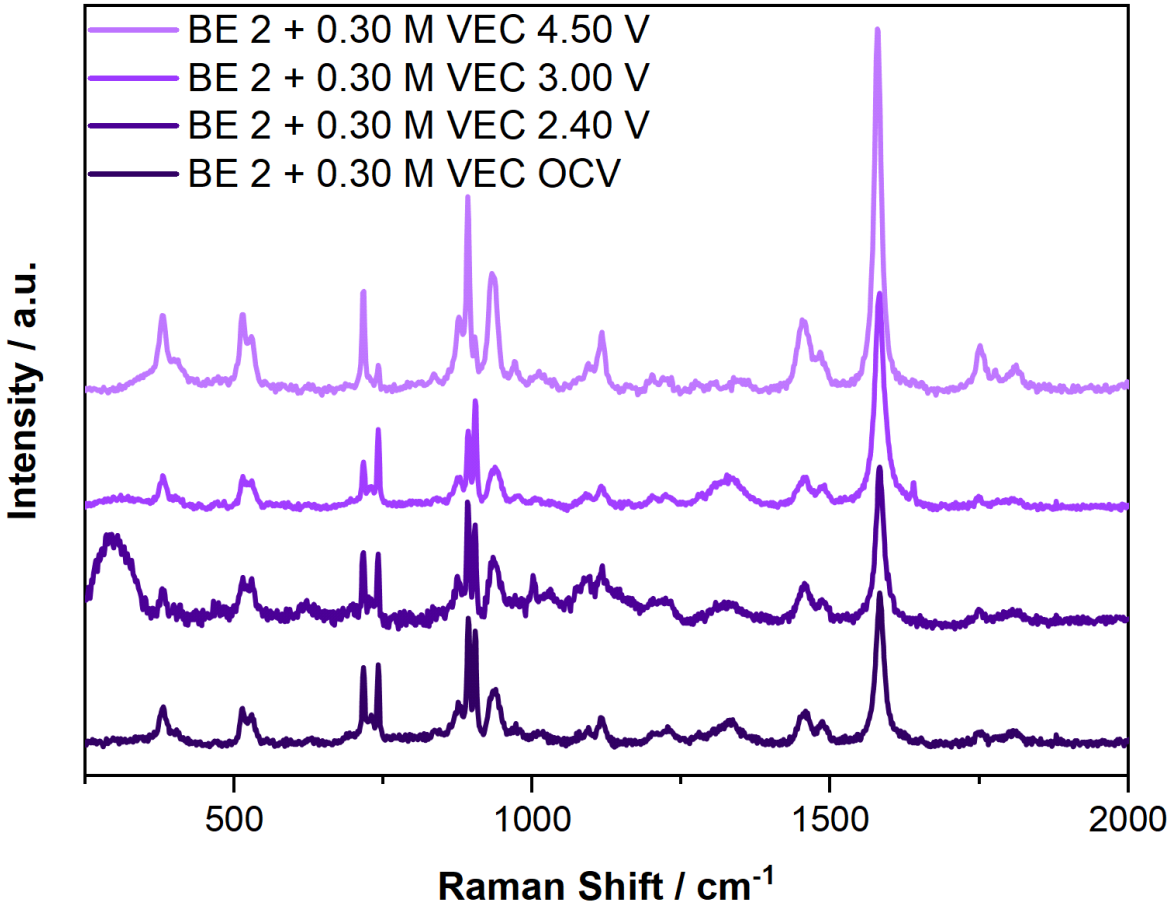

Figure A40: *Operando* SHINER spectra taken from the surface of a graphite electrode in the presence of the BE 2 (1 M $LiPF_6$ in EC:EMC 3:7 by weight) + 0.30 M VEC. For the SHINERS measurement the graphite electrode was connected as working electrode, paired against a NMC622 counter electrode. Galvanostatic charge was performed at a C-rate of C/3. Au SHINs with a diameter of 55 nm were introduced to the electrode surface before cell assembly. Spectra were recorded at different cell voltages, denoted in the spectra and indicated by the intensity of the color. For spectrum acquisition the samples were excited using a 633 nm laser, adjusted to a power output of 1.05 mW. Spectra were acquired over three accumulations of 35 s. Figure redrawn with permission from [159].

Table A11: Detailed assignment for the bands observed during the *operando* SHINERS measurement of the surface of the graphite electrode galvanostatically charged in the presence of the BE 2 (1 M $LiPF_6$ in EC:EMC 3:7 by weight) + 0.30 M VEC. The absence of specific bands at selected cell voltages is indicated by empty cells. In these cases, the band was observed at higher or lower cell voltages, respectively. The reference "own spectrum" refers to reference spectra reported in the Appendix chapter. Table redrawn with permission from [159].

Observed band [cm^{-1}]				Assignment	Reference
OCV	**2.40 V**	**3.00 V**	**4.50 V**		
380	380	380	380	EMC	Own reference spectrum
405		405	403	EMC	Own reference spectrum
514	513	514	514	EMC O=C=O bending vibrations	Own reference spectrum, [206]
529	530	529	529	EMC	Own Spectrum
	619			Semi-carbonate (LEMC)	[32]
717	717	717	717	EC C=O bending vibrations	[206]
730	729	730	729	EC coordinated to Li^+	[211]
742	741	742	742	PF_6^- sym. vibrations	[206,211]
840		839	836	Semi-carbonates (DMDOHC)	Own reference spectrum
875	876	876	878	EMC	Own reference spectrum
893	893	893	895	EC ring breathing vibrations	[206,211]
903	905	903	904	EC coordinated to Li^+	[206,211]
938	936	938	935	EMC	Own reference spectrum
973		975	970	Electrolyte (EC)	[32]
	1003	1009	1009	Semi-carbonates (LEMC)	[32]
1015				EMC	Own reference spectrum
1094	1092	1091	1092	Electrolyte (EMC; O-C-O bending), Li_2CO_3, semi-carbonates	[32,162,211]
1116	1116	1116	1116	EMC	Own reference spectrum
		1162	1162	Semi-carbonates (LMC)	[32]
1205		1203	1203	EMC	Own reference spectrum
1225	1222	1225	1223	Electrolyte (EC)	[32]
			1272	Semi-carbonates (LEMC, LEC)	[32]
			1302	Semi-carbonates (DEDOHC)	Own reference spectrum, [32]
1334	1330	1334	1352	Graphite D-band	
1458	1457	1456	1455	EMC	Own reference spectrum
1485	1486	1485	1483	EC CH bending	[211]
1582	1582	1582	1579	Graphite G-band	
		1639	1638	VEC C=C double bond (ring-opened)*, semi-	Own reference spectrum, [212]

				carbonates (C=O stretching vibrations)	
1651	1651		1654	VEC, semi-carbonates (C=O stretching vibrations)	Own reference spectrum, [212]
1751	1750	1748	1751	EMC	Own reference spectrum
			1778	EC C=O stretching vibrations	[211]
1805	1810	1805	1810	EC C=O stretching vibrations	[207]
2687	2690	2687	2684	Electrolyte	
			2717	DEDOHC	Own reference spectrum
			2863	DMDOHC	Own reference spectrum
2876	2877	2878	2881	EMC	Own reference spectrum
2940	2940	2940	2940	EMC	Own reference spectrum
2970	2969	2970	2965	EMC	Own reference spectrum

Table A12: Denotation of the calculated Raman shifts for the ring-opened VEC molecule after reduction and the assigned vibrations of the molecule. Note that the calculated Raman shifts were scaled by a factor of 1.08. Table redrawn with permission from [159].

Raman Mode	Calculated Raman Shift / cm^{-1}	Raman Activity
C-C wagging	27.81	9.44
Wagging vibrations (skeletal)	68.93	3.77
Wagging vibrations (skeletal)	74.98	0.98
C-C wagging vibrations	214.98	9.53
C-C deformation vibrations	306.31	3.84
CH_2 twisting vibrations	353.46	0.95
C-C-O rocking vibrations	414.83	5.28
C-C=C rocking vibrations	573.64	1.72
C-C=C twisting vibrations	579.01	1.44
CH_2 twisting vibrations	680.75	1.04
Deformation vibrations (skeletal)	699.03	3.60
O-C-O breathing vibrations	748.25	6.98
CH_2 rocking vibrations	867.42	38.17
CO_3^- stretching vibrations	889.24	0.12

C-O stretching vibrations	901.57	11.67
CH_2 twisting vibrations	1063.74	14.00
CH_2 twisting vibrations	1072.64	3.90
CH_2 twisting vibrations	1078.83	0.29
C-C-C stretching vibrations	1113.10	45.15
C-O stretching vibrations	1160.66	19.91
C-H scissoring vibrations	1261.00	36.02
C-C-C stretching vibrations	1330.84	25.99
CH_2 twisting vibrations	1379.26	14.49
O-C-O stretching vibrations	1394.64	18.709
CH_2-CH_2 rocking vibrations	1474.47	19.25
CH_2-CH_2 rocking vibrations	1546.67	13.39
CH_2 scissoring vibrations	1555.23	25.93
CH_2 wagging vibrations	1587.80	10.53
C=C stretching vibrations	1640.56	42.29
O-C-O deformation vibrations	1831.51	6.44
C-H stretching vibrations	3231.82	385.72
CH_2 deformation vibrations	3261.49	164.73
C-H stretching vibrations	3373.06	170.84
CH_2 stretching vibrations	3386.15	272.83
C-H stretching vibrations	3418.96	336.40
CH_2 deformation vibrations	3481.59	146.35

9.4.4. Electrochemical Cathode Characterization

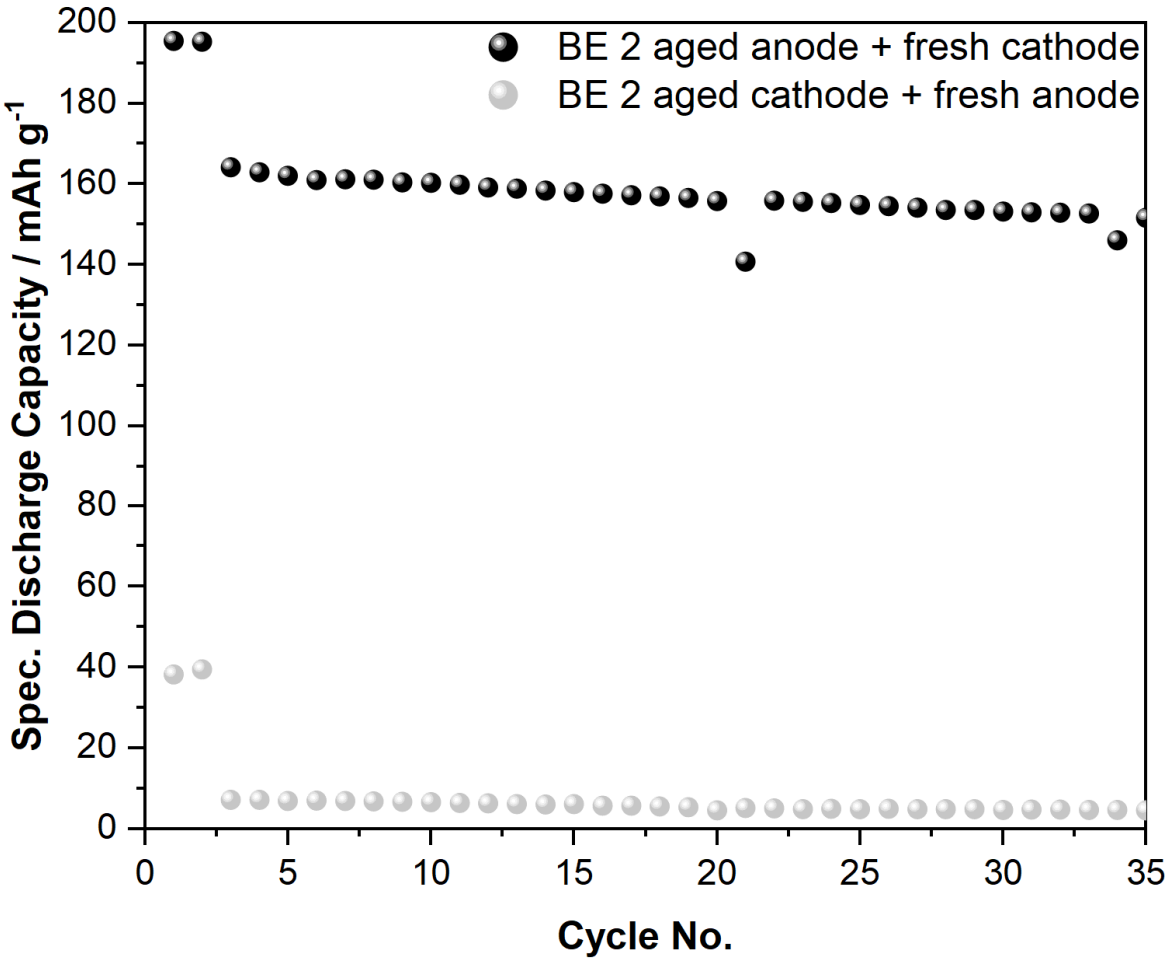

Figure A41: Specific discharge capacities obtained from NMC622||graphite coin cell cycled in the presence of the BE 2 (1 M $LiPF_6$ in EC:EMC 3:7 by weight). The coin cells consist of an electrochemically aged electrode paired with a pristine counterpart. The aged electrodes were extracted from NMC622||graphite pouch cells cycled in the presence of the BE 2 until reaching a SoH of 50%. Depicted are coin cell containing the aged graphite electrode (**black**) and the aged cathode (**grey**). Figure redrawn with permission from [159].

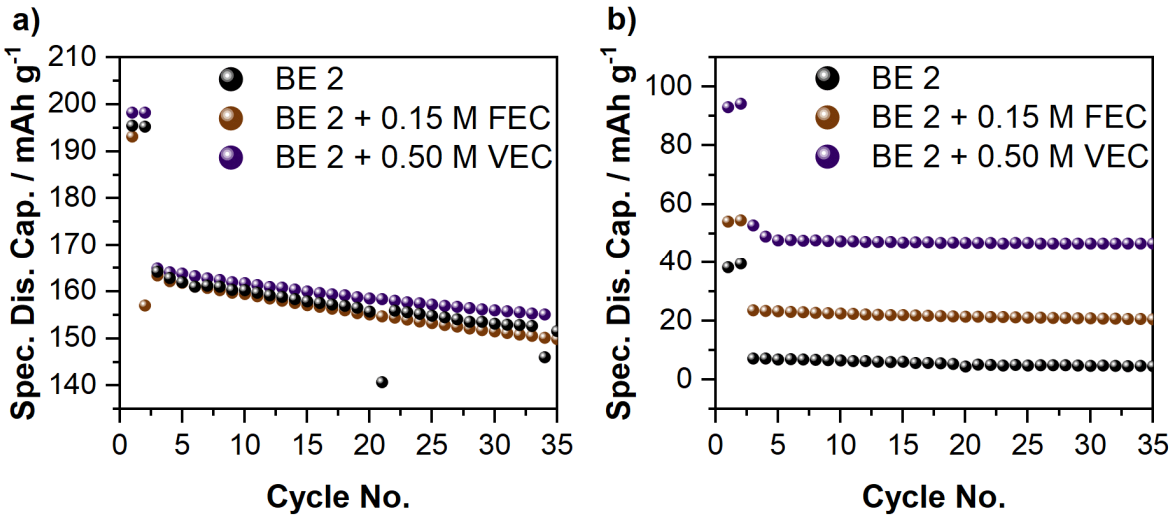

Figure A42: Specific discharge capacities (Spec. Dis. Cap.) obtained from NMC622||graphite coin cell cycled in the presence of the BE 2 (1 $_{M}$ $LiPF_6$ in EC:EMC 3:7 by weight). The coin cells consist of an electrochemically aged anode (**a**) or cathode (**b**) paired with a pristine counterpart. The depicted electrodes were taken from NMC622||graphite pouch cells galvanostatically cycled in the presence of the BE 2, the BE 2 + 0.15 $_{M}$ FEC (**brown**), and the BE 2 + 0.50 $_{M}$ VEC (**purple**) after reaching a SoH of 50%. Figure redrawn with permission from [159].

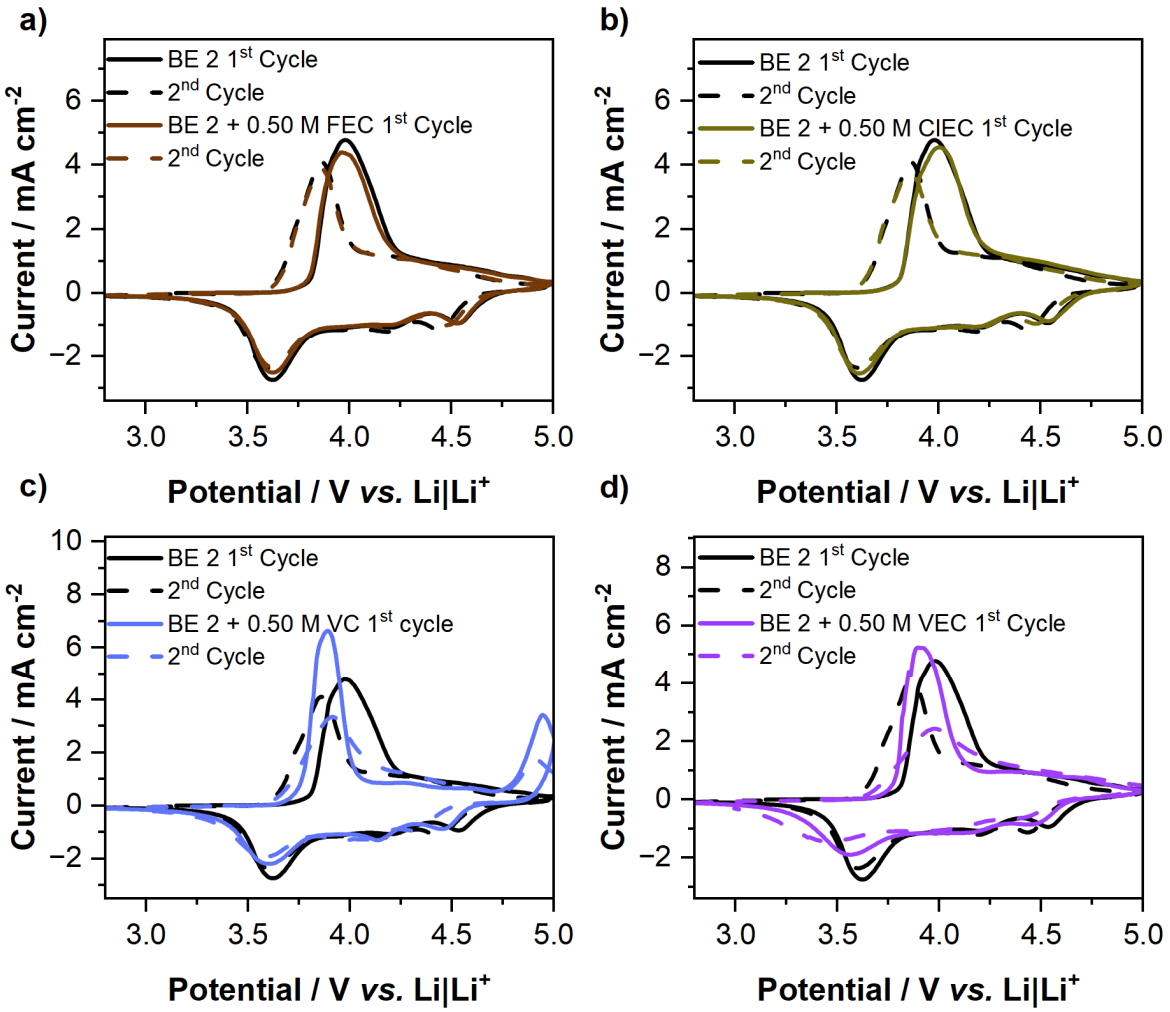

Figure A43: Cyclic voltammograms (CVs) of NMC622||graphite T-type Swagelok® cells with Li-metal reference electrodes obtained in the presence of the BE 2 (1 M $LiPF_6$ in EC:EMC 3:7 by weight, **black**) and the different electrolyte additive-containing electrolyte formulations. Shown are the CVs recorded for **a)** FEC (**brown**), **b)** ClEC (**dark yellow**), **c)** VC (**blue**), and **d)** VEC (**purple**) in comparison to the BE 2 CVs. Cyclic voltammetry was performed in a potential range of 2.80 V – 4.50 V *vs.* $Li|Li^+$ with a scan rate of 150 µV s^{-1}. In total 2 charge/discharge cycles were performed marked by full and dashed lines in the depicted voltammograms. Figure redrawn with permission from [159].

9.4.5. Surface Characterization *via* ToF FIB-SIMS

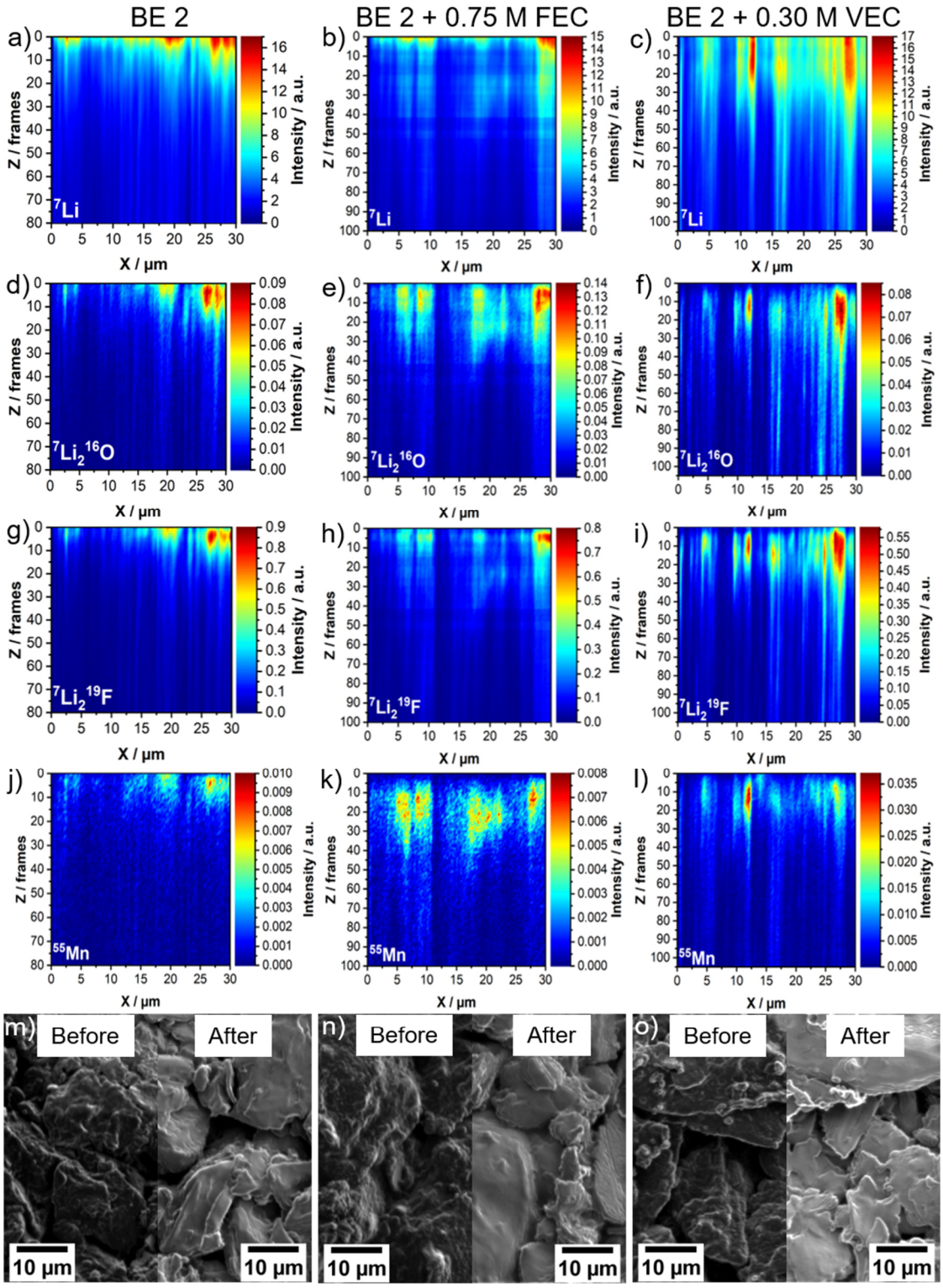

Figure A44: Depth profiles obtained for the surface layers from graphite electrodes extracted from NMC622||graphite pouch cells after galvanostatic charge/discharge cycling. Investigation was performed *via* focused ion beam secondary mass spectrometry equipped with a time of flight analyzer. The figure shows the elemental distribution of the combined Li-species (**a** – **c**), Li_2O (**d** – **f**), Li_2F (**g** – **i**), and of Mn (**j** – **l**), for graphite electrodes cycled in the presence of the BE 2 (1 M $LiPF_6$ in EC:EMC 3:7 by weight; left), the FEC-containing electrolyte (center), and the VEC-containing electrolyte (right). In addition, images of the surface before and after the performed investigation are depicted (**m** – **o**). Note that due to the similar sample compositions it can be assumed that the thickness of each ablated layer (frame) is similar, enabling the comparison of the investigated samples. Figure redrawn with permission from [159].

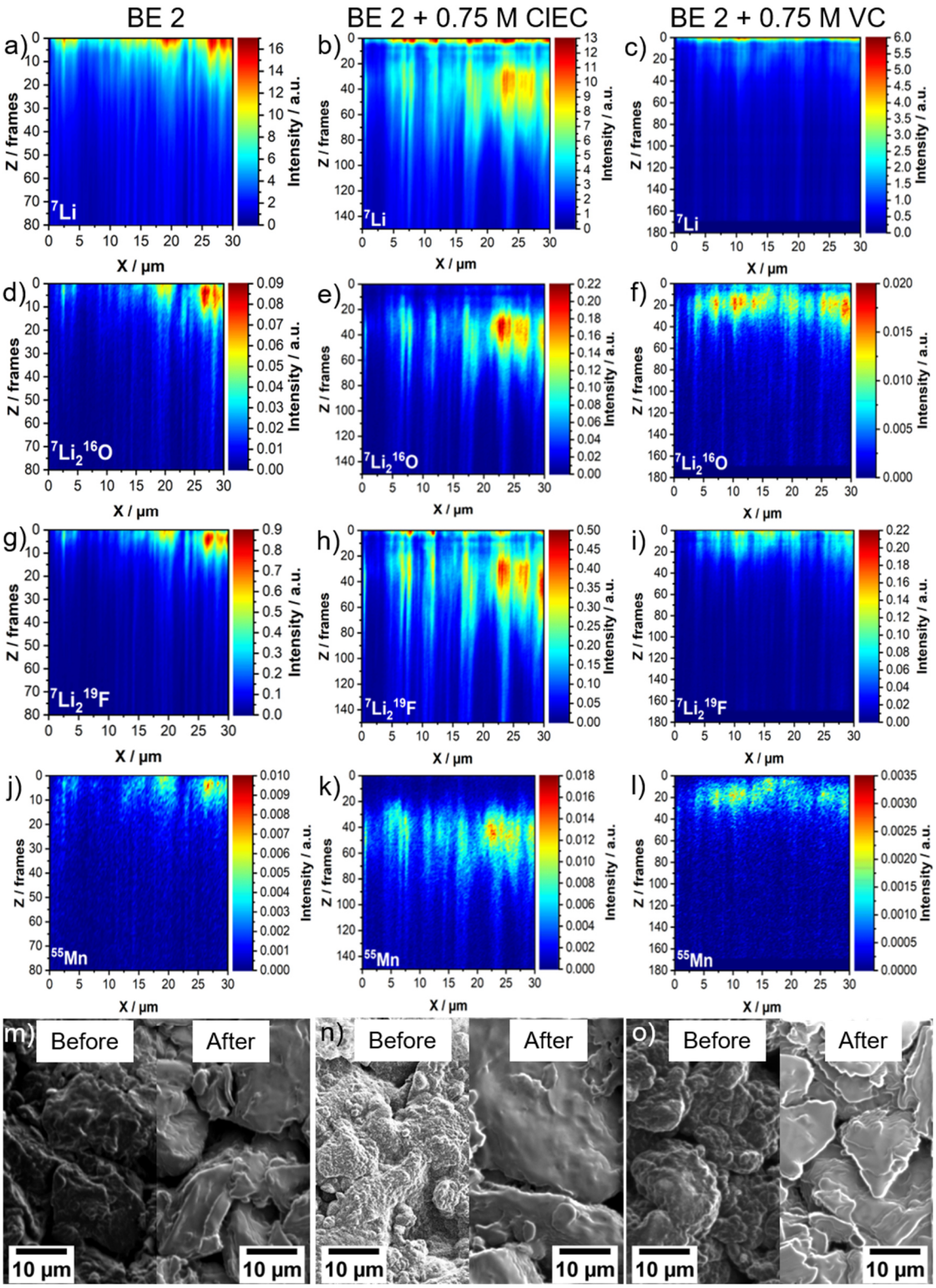

Figure A45: Depth profiles obtained for the surface layers from graphite electrodes extracted from NMC622||graphite pouch cells after galvanostatic charge/discharge cycling. Investigation was performed *via* focused ion beam secondary mass spectrometry equipped with a time of flight analyzer. The figure shows the elemental distribution of the combined Li-species (**a** – **c**), Li_2O (**d** – **f**), Li_2F (**g** – **i**), and of Mn (**j** – **l**), for graphite electrodes cycled in the presence of the BE 2 (1 M $LiPF_6$ in EC:EMC 3:7 by weight; left), the ClEC-containing electrolyte (center), and the VC-containing electrolyte (right). In addition, images of the surface before and after the performed investigation are depicted (**m** – **o**). Note that due to the similar sample compositions it can be assumed that the thickness of each ablated layer (frame) is similar, enabling the comparison of the investigated samples. Figure redrawn with permission from [159].

9.4.6. CEI Characterization by Raman Spectroscopy

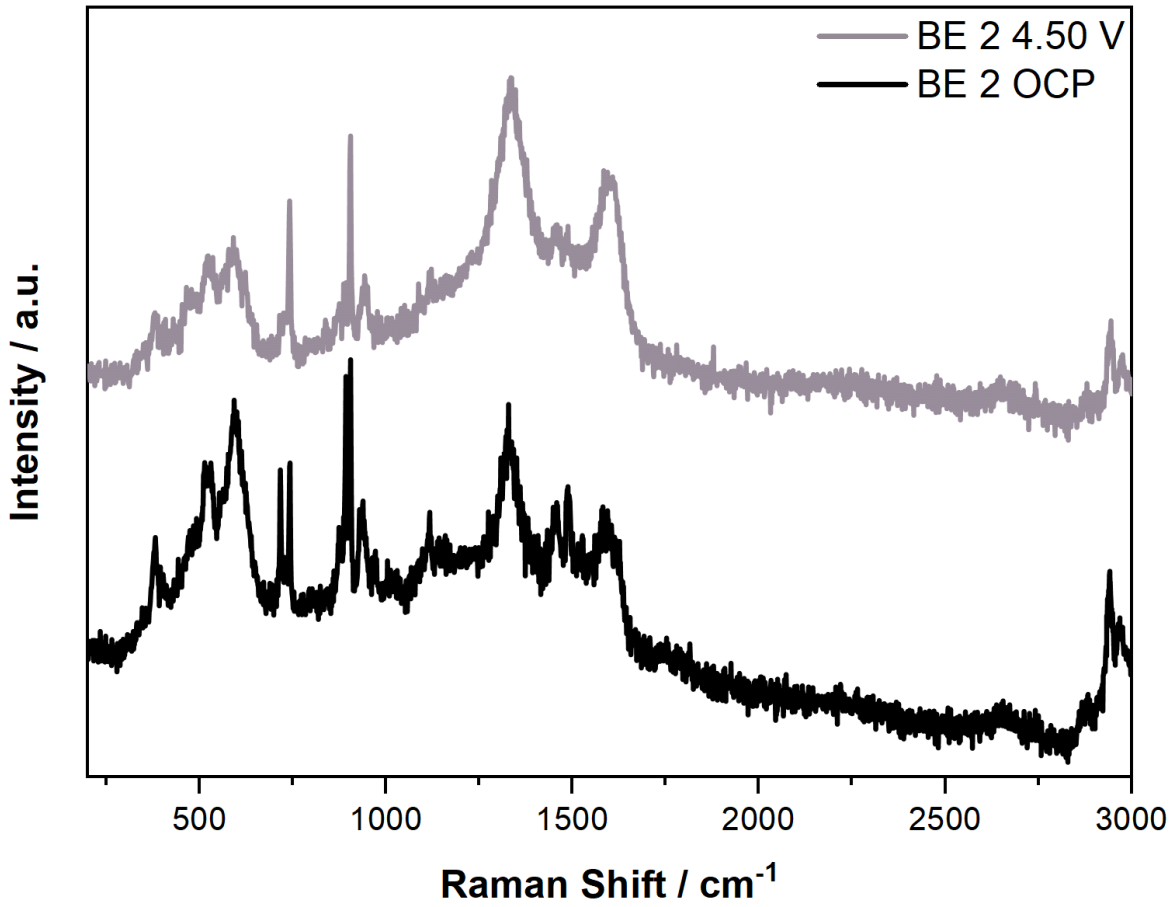

Figure A46: *Operando* SHINER spectra taken from the surface of a NMC622 electrode in the presence of the BE 2 (1 M $LiPF_6$ in EC:EMC 3:7 by weight). For the SHINERS measurement the NMC622 electrode was connected as working electrode, paired against a graphite counter electrode. In addition, a Li-metal electrode was introduced as reference electrode to monitor the electrodes potential. Galvanostatic charge was performed at a C-rate of C/3. Au SHINs with a diameter of 55 nm were introduced to the electrode surface before cell assembly. Spectra were recorded at different electrode potentials, denoted in the spectra and indicated by the intensity of the color. For spectrum acquisition the samples were excited using a 633 nm laser, adjusted to a power output of 1.05 mW. Spectra were acquired over three accumulations of 35 s. Figure redrawn with permission from [159].

Table A13: Detailed assignment for the bands observed during the *operando* SHINERS measurement of the surface of the NMC622 electrode galvanostatically charged in the presence of the BE 2 (1 $_M$ $LiPF_6$ in EC:EMC 3:7 by weight). The absence of specific bands at selected cell voltages is indicated by empty cells. In these cases, the band was observed at higher or lower cell voltages, respectively. The reference "own spectrum" refers to reference spectra reported in the Appendix chapter. Table redrawn with permission from [159].

Observed band [cm^{-1}]		Assignment	Reference
OCP	**4.50 V**		
380	380	EMC	Own reference spectrum
401		EMC	Own reference spectrum
	473	NMC lattice vibrations (delithiated)*	[135]
520		EMC O=C=O bending, NMC (Co E_g)	Own reference spectrum, [206]
	545	NMC (Co A_{1g}) (delithiated)*	[206]
594		NMC (Mn E_g)	[206]
	696	Semi-carbonates (DMDOHC)	Own reference spectrum
716	717	EC C=O bending vibrations	[206]
727	731	EC coordinated to Li^+	[211]
740	740	PF_6^- sym. vibrations	[206,211]
876	876	EMC	Own reference spectrum
892	890	EC ring breathing vibrations	[206,211]
903	905	EC coordinated to Li^+	[206,211]
934	937	EMC	Own reference spectrum
972	977	Electrolyte (EC)	[32]
1096	1090	Electrolyte (EMC; O-C-O bending vibrations), Li_2CO_3, semi-carbonates	[32,162,211]
1116	1117	EMC	Own reference spectrum
1337	1331	Graphite D-band	
1458	1459	EMC	Own reference spectrum
1486	1485	EMC	Own reference spectrum
1593	1598	Graphite G-band	
1751		EMC	Own reference spectrum
2879		EMC	Own reference spectrum
2940	2940	EMC	Own reference spectrum
2965	2977	EMC	Own reference spectrum

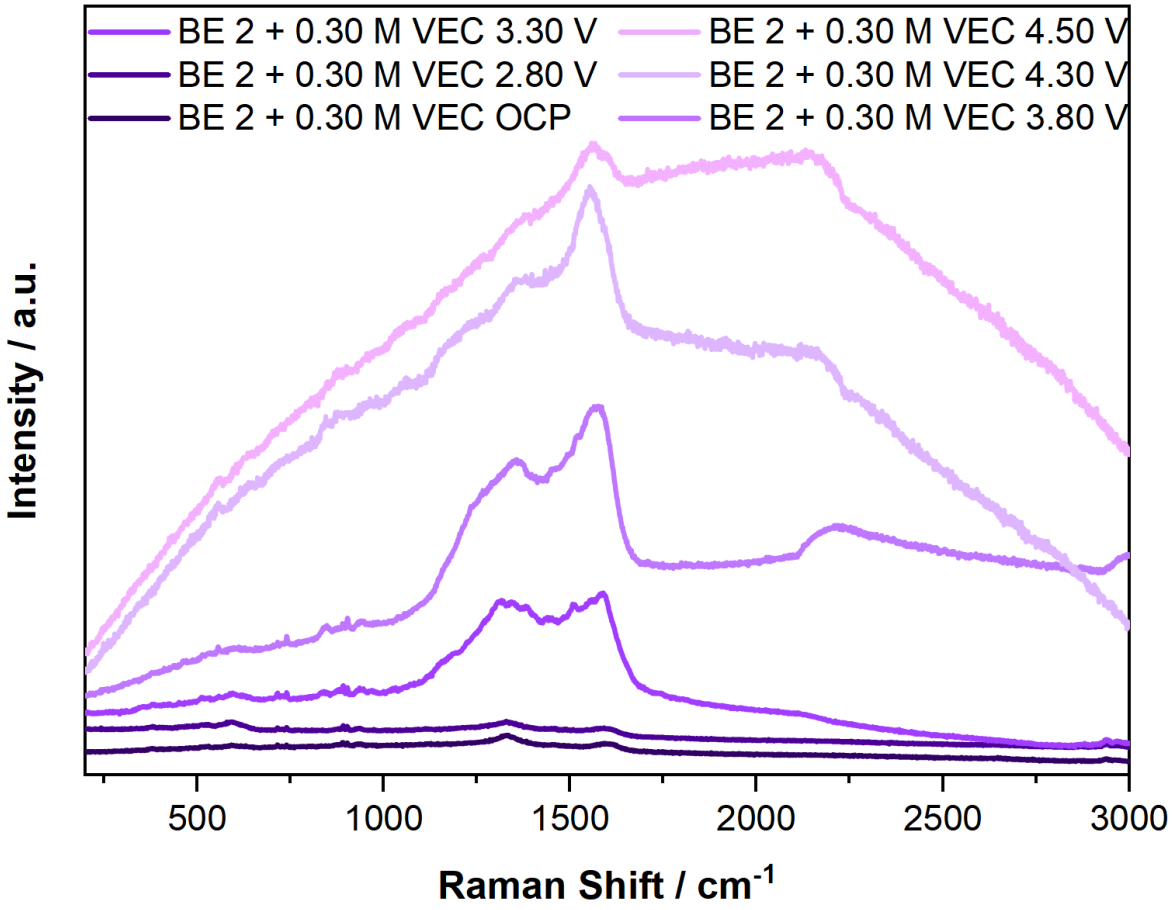

Figure A47: *Operando* SHINER spectra taken from the surface of a NMC622 electrode in the presence of the BE 2 (1 M $LiPF_6$ in EC:EMC 3:7 by weight) + 0.30 M VEC. For the SHINERS measurement the NMC622 electrode was connected as working electrode, paired against a graphite counter electrode. In addition, a Li-metal electrode was introduced as reference electrode to monitor the electrodes potential. Galvanostatic charge was performed at a C-rate of C/3. Au SHINs with a diameter of 55 nm were introduced to the electrode surface before cell assembly. Spectra were recorded at different electrode potentials, denoted in the spectra and indicated by the intensity of the color. For spectrum acquisition the samples were excited using a 633 nm laser, adjusted to a power output of 1.05 mW. Spectra were acquired over three accumulations of 35 s. Figure redrawn with permission from [159].

Table A14: Detailed assignment for the bands observed during the *operando* SHINERS measurement of the surface of the NMC622 electrode galvanostatically charged in the presence of the BE 2 (1 M $LiPF_6$ in EC:EMC 3:7 by weight) + 0.30 M VEC. The absence of specific bands at selected cell voltages is indicated by empty cells. In these cases, the band was observed at higher or lower cell voltages, respectively. The reference "own spectrum" refers to reference spectra reported in the Appendix chapter. Table redrawn with permission from [159].

Observed band [cm^{-1}]						Assignment	Reference
OCP	**2.8 V**	**3.3 V**	**3.8 V**	**4.3 V**	**4.5 V**		
		357				LiOH	[162]
380	380	381	378			EMC	Own reference spectrum
	404					EMC	Own reference spectrum
			462			NMC (Ni E_g)	[206]
481						NMC	[135]
515	512	513	516			EMC O=C=O bending vibrations	Own reference spectrum, [206]

530	531	531		535		EMC, NMC (Co E_g)	Own reference spectrum, [206]
		555	556	555	558	NMC delithiated	[135]
595	594	595				NMC (Mn E_g)	[206]
		695				Semi-carbonates (DMDOHC)	Own reference spectrum
714	716	716	716			EC C=O bending vibrations	[206]
730	729	728	729			EC coordinated to Li^+	[211]
741	740	741	741			PF_6^- sym. vibrations	[206,211]
		850	846	843	850	Semi-carbonates (LPDC)	[32]
870						Semi-carbonates (LEMC, DMDOHC)	Own reference spectrum, [32]
874	878	877		875	875	EMC	Own reference spectrum
894	891	892	891			EC ring breathing vibrations	[206,211]
904	904	902	903			EC coordinated to Li^+	[206,211]
936	933	941	939			EMC	Own reference spectrum
	976	969				Electrolyte (EC)	[32]
1119	1116					EMC	Own reference spectrum
				1158		Semi-carbonates (LMC)	[32]
		1190				Semi-carbonates (LMC)	[32]
			1235			Semi-carbonates (LEMC)	[32]
		1250				Semi-carbonates (DEDOHC, DMDHOC)	Own reference spectrum
		1309				Semi-carbonates (DEDOHC)	Own reference spectrum, [32]
1335	1330	1346	1356	1352	1350	Graphite D-band	
		1380	1374	1380	1380	COO- sym. stretching vibrations	[195,213]
1455	1457	1450	1458			EMC	Own reference spectrum
	1487					EC CH bending vibrations	[211]
			1498			Li_2CO_3 C-O stretching vibrations	[212]
		1513	1522			Semi-carbonates	[151]
		1555	1558	1556	1561	Carboxylates COO^- stretching vibrations	[195]
1600	1587	1587	1580	1595	1595	Graphite G-band	

	2869	2867				EMC	Own reference spectrum
2937	2940	2937				EMC	Own reference spectrum
2967	2967	2967				EMC	Own reference spectrum

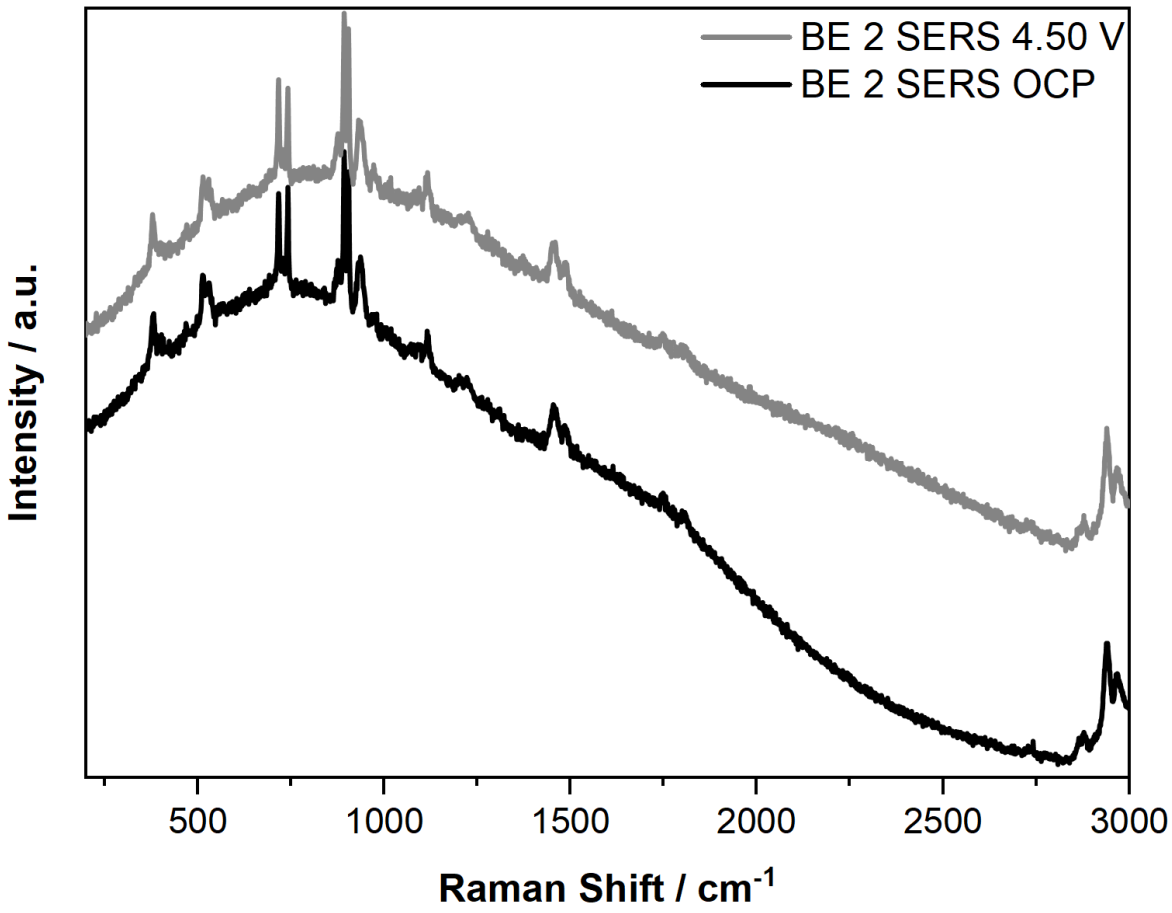

Figure A48: *Operando* SER spectra taken from the surface of a roughened Au electrode in the presence of the BE 2 (1 $_{M}$ $LiPF_6$ in EC:EMC 3:7 by weight). For the SERS measurement the Au electrode was connected as working electrode, paired against a Li-metal electrode. The electrode was charged with a sweep rate of 150 µV s^{-1}. Au SHINs with a diameter of 55 nm were introduced to the electrode surface before cell assembly. Spectra were recorded at the open circuit potential (OCP) and the cut-off potential of 4.50 V vs. $Li|Li^+$. For spectrum acquisition the samples were excited using a 633 nm laser, adjusted to a power output of 1.05 mW. Spectra were acquired over three accumulations of 35 s. Figure redrawn with permission from [159].

Table A15: Detailed assignment for the bands observed during the *operando* SERS measurement of the surface of the Au electrode galvanostatically charged in the presence of the BE 2 (1 M $LiPF_6$ in EC:EMC 3:7 by weight). The absence of specific bands at selected cell voltages is indicated by empty cells. In these cases, the band was observed at higher or lower cell voltages, respectively. The reference "own spectrum" refers to reference spectra reported in the Appendix chapter. Table redrawn with permission from [159].

Observed band [cm^{-1}]		Assignment	Reference
OCP	**4.50 V**		
381	381	EMC	Own reference spectrum
401	401	EMC	Own reference spectrum
513	513	EMC O=C=O bending vibrations	Own reference spectrum, [206]
530	530	EMC	Own reference spectrum
717	717	EC C=O bending vibrations	[206]
727	729	EC coordinated to Li^+	[211]
741	742	PF_6^- sym. vibrations	[206,211]
876	876	EMC	Own reference spectrum
893	893	EC ring breathing vibrations	[206,211]
903	903	EC coordinated to Li^+	[206,211]
938	936	EMC	Own reference spectrum
973	973	Electrolyte (EC)	[32]
1092	1092	Electrolyte (EMC; O-C-O bending vibrations), Li_2CO_3, semi-carbonates	[32,162,211]
1117	1115	EMC	Own reference spectrum
1202	1202	EMC	Own reference spectrum
1222	1227	Electrolyte (EC)	[32]
1456	1456	EMC	Own reference spectrum
1485	1485	EC CH bending vibrations	[211]
1749	1747	EMC	Own reference spectrum
1806	1809	EC C=O stretching vibrations	[207]
2878	2878	EMC	Own reference spectrum
2941	2941	EMC	Own reference spectrum
2968	2968	EMC	Own reference spectrum

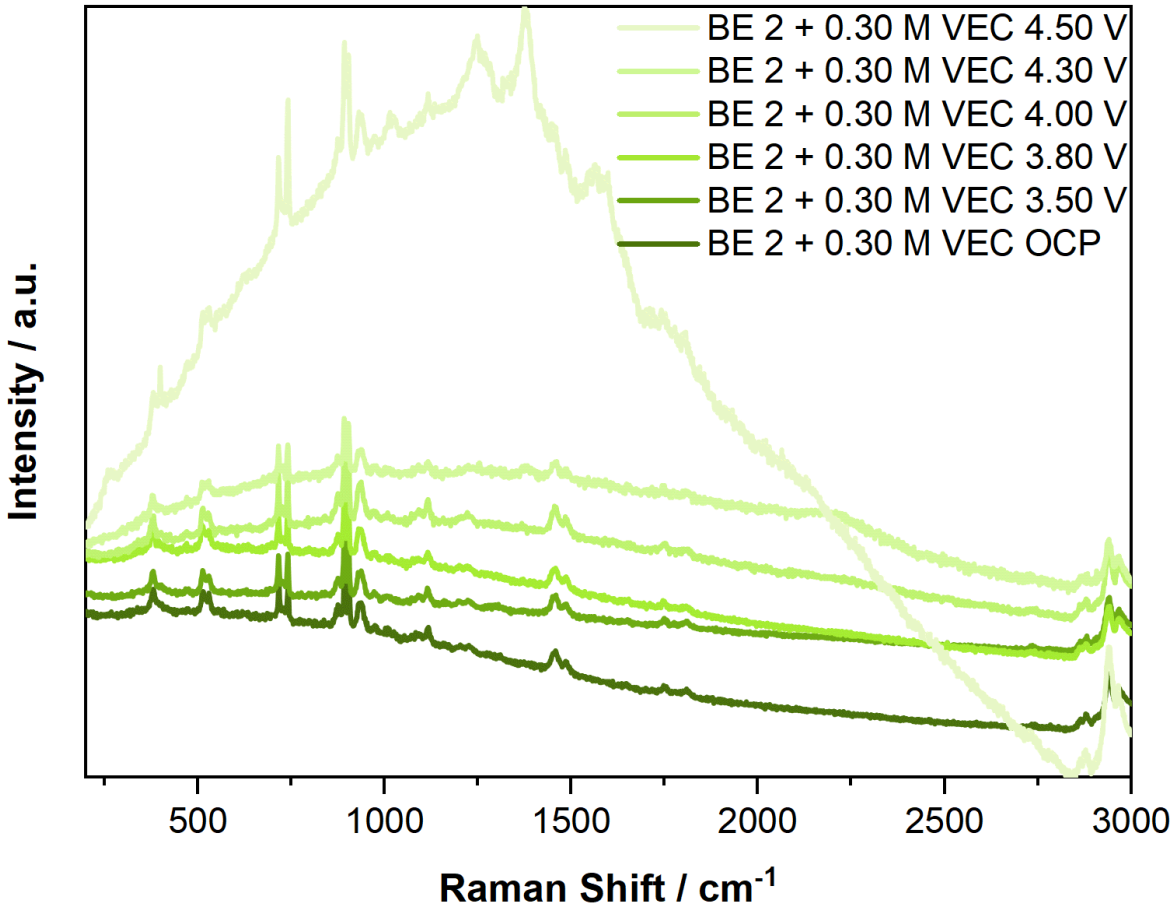

Figure A49: *Operando* SER spectra taken from the surface of a roughened Au electrode in the presence of the BE 2 (1 M $LiPF_6$ in EC:EMC 3:7 by weight) + 0.30 M VEC. For the SERS measurement the Au electrode was connected as working electrode, paired against a Li-metal electrode. The electrode was charged with a sweep rate of 150 µV s^{-1}. Au SHINs with a diameter of 55 nm were introduced to the electrode surface before cell assembly. Spectra were recorded at different electrode potentials, denoted in the spectra and indicated by the intensity of the color. For spectrum acquisition the samples were excited using a 633 nm laser, adjusted to a power output of 1.05 mW. Spectra were acquired over three accumulations of 35 s. Figure redrawn with permission from [159].

Table A16: Detailed assignment for the bands observed during the *operando* SERS measurement of the surface of the Au electrode galvanostatically charged in the presence of the BE 2 (1 M $LiPF_6$ in EC:EMC 3:7 by weight) + 0.30 M VEC. The absence of specific bands at selected cell voltages is indicated by empty cells. In these cases, the band was observed at higher or lower cell voltages, respectively. The reference "own spectrum" refers to reference spectra reported in the Appendix chapter. Table redrawn with permission from [159].

Observed band [cm^{-1}]						Assignment	Reference
OCP	**3.5 V**	**3.8 V**	**4.0 V**	**4.3 V**	**4.5 V**		
					267	Li_2CO_3, C-C deformation of aliphatic chains	[151], [195]
379	379	379	379	380	380	EMC	Own reference spectrum
400	400	400	400	401	401	EMC	Own reference spectrum
	475				476	Semi-carbonates (DEDOHC); Li_2CO_3	Own reference spectrum, [32],[162]

514	514	514	514	514	514	EMC O=C=O bending vibrations	Own reference spectrum, [206]
529	529	529	529	527	528	EMC	Own reference spectrum
717	716	715	717	716	717	EC C=O bending vibrations	[206]
730	729	728	727	728	728	EC coordinated to Li^+	[211]
741	741	741	743	740	740	PF_6^- sym. vibrations	[206,211]
877	877	877	876	876	876	EMC	Own reference spectrum
893	892	893	892	891	893	EC ring breathing vibrations	[206,211]
903	903	903	903	902	903	EC coordinated to Li^+	[206,211]
939	937	934	935	937	937	EMC	Own reference spectrum
975	973	973	973	972	972	Electrolyte (EC)	[32]
	1009	1009	1008	1009	1015	Semi-carbonates (LEMC)	[32]
					1027	C-C stretching vibrations	[195]
1090	1090	1090	1092	1091		Electrolyte (EMC; O-C-O bending vibrations), Li_2CO_3, semi-carbonates	[32,162,211]
1117	1115	1115	1115	1117	1116	EMC	Own reference spectrum
					1151	C-C stretching vibrations	[195]
	1161					Semi-carbonates (LMC)	[32]
1202	1200	1200	1203			EMC	Own reference spectrum
1226	1226	1223	1223	1230		Electrolyte (EC)	[32]
				1253	1247	Semi-carbonates (DEDOHC, DMDHOC)	Own reference spectrum
				1381	1378	COO- sym. stretching vibrations	[195,213]
1455	1455	1455	1457	1456	1453	EMC	Own reference spectrum
1486	1486	1486	1485	1485	1485	EC CH bending vibrations	[211]
					1560	Carboxylates COO^- stretching vibrations	[195]
					1595	Carboxylates COO^- stretching vibrations	[195]

1649	1654	1651	1655	1650		VEC	Own reference spectrum
1749	1749	1749	1750	1746	1746	EMC	Own reference spectrum
	1775					EC C=O stretching	[211]
1810	1809	1811	1809	1807	1804	EC C=O stretching vibrations	[207]
2732	2735	2735	2735			EMC	Own reference spectrum
2864						EMC	Own reference spectrum
2879	2877	2877	2879	2871	2879	EMC	Own reference spectrum
2941	2939	2939	2940	2940	2940	EMC	Own reference spectrum
2967	2967	2967	2966	2966	2966	EMC	Own reference spectrum

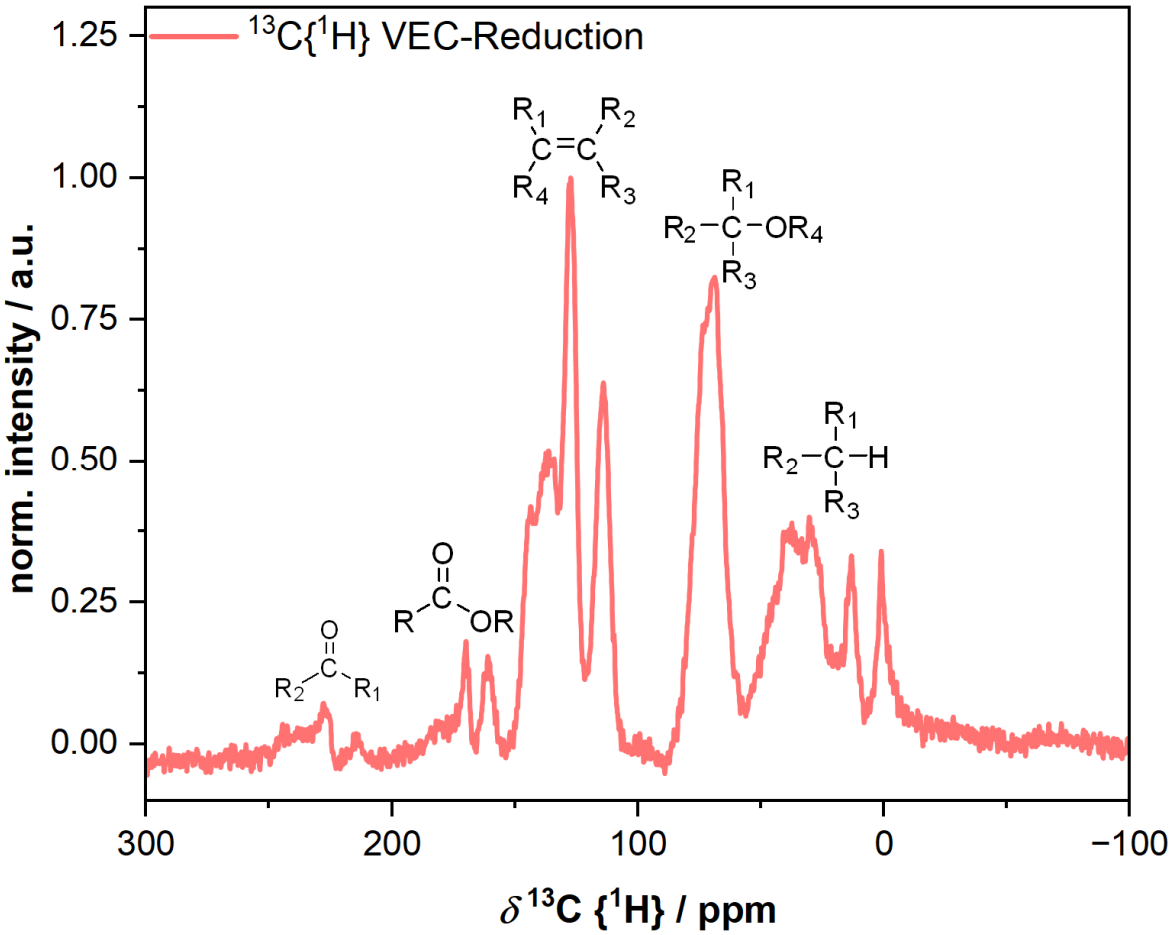

Figure A50: NMR spectrum recorded obtained from the $^{13}C\{^1H\}$ cross polarization magic angle spinning NMR investigation of the synthesized product of the VEC reduction. In the spectrum, prominent peaks are ascribed to characteristic C-species. Figure redrawn with permission from [159].

$^{13}C\{^1H\}$ CP-MAS NMR: δ (ppm) = 227, 213 (C=O); 170, 160 (R-COO or R-OCOO); 136, 127, 114 (C=C); 68 (R-CO^-); 38, 30, 13 (R-CH).

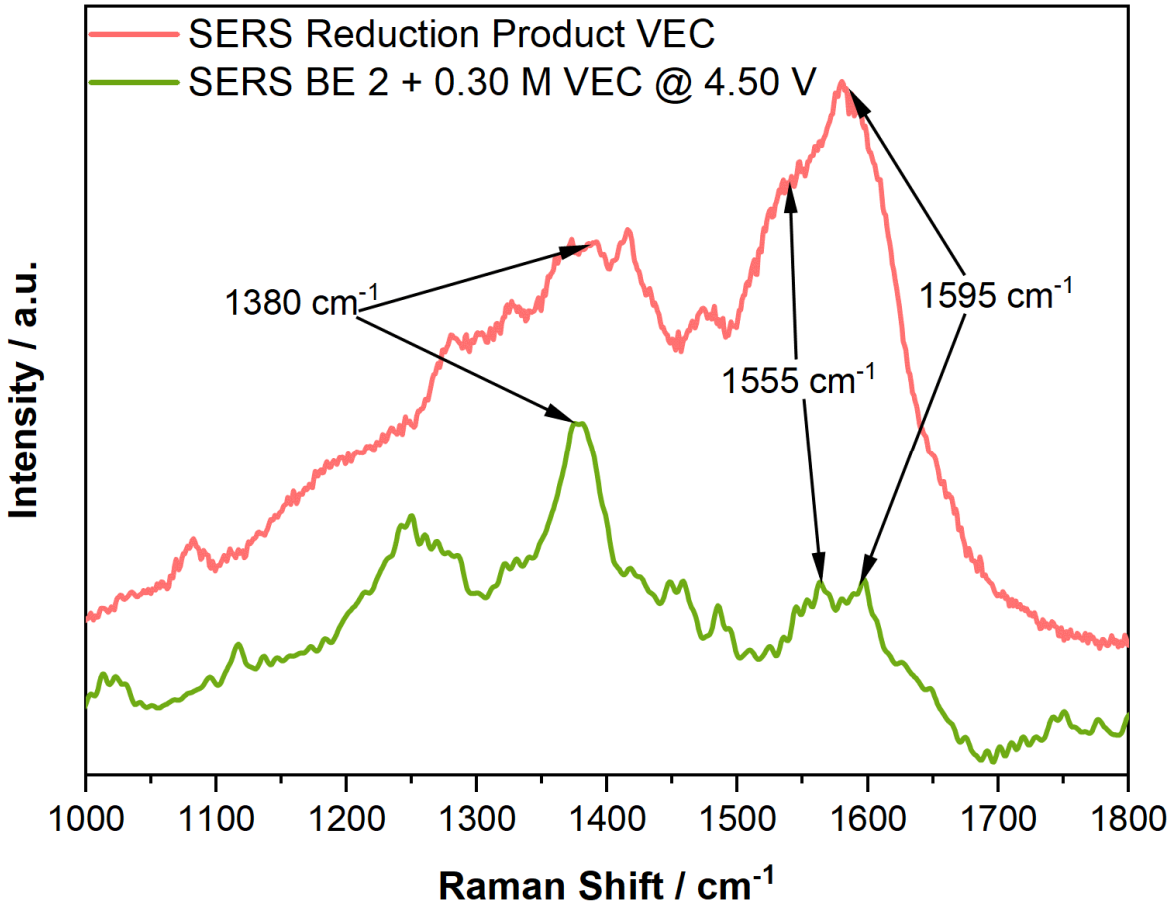

Figure A51: Comparison of the SER spectra recorded of the surface of a roughened Au electrode in the presence of the BE 2 (1 $_M$ $LiPF_6$ in EC:EMC 3:7 by weight) + 0.30 $_M$ VEC at the cut-off potential of 4.50 V *vs.* $Li|Li^+$ (**green**) and the SER spectrum recorded from the synthesized VEC reduction product (**red**). To obtain the SER spectrum of the reduction product, the synthesized product was suspended in THF and drop cast on an AgAu SERS substrate. Characteristic bands are highlighted by arrows and band positions are noted in the spectrum. For spectrum acquisition the samples were excited using a 633 nm laser, adjusted to a power output of 1.05 mW. Spectra were acquired over three accumulations of 35 s. Figure redrawn with permission from [159].

9.4.7. Raman Reference Spectra

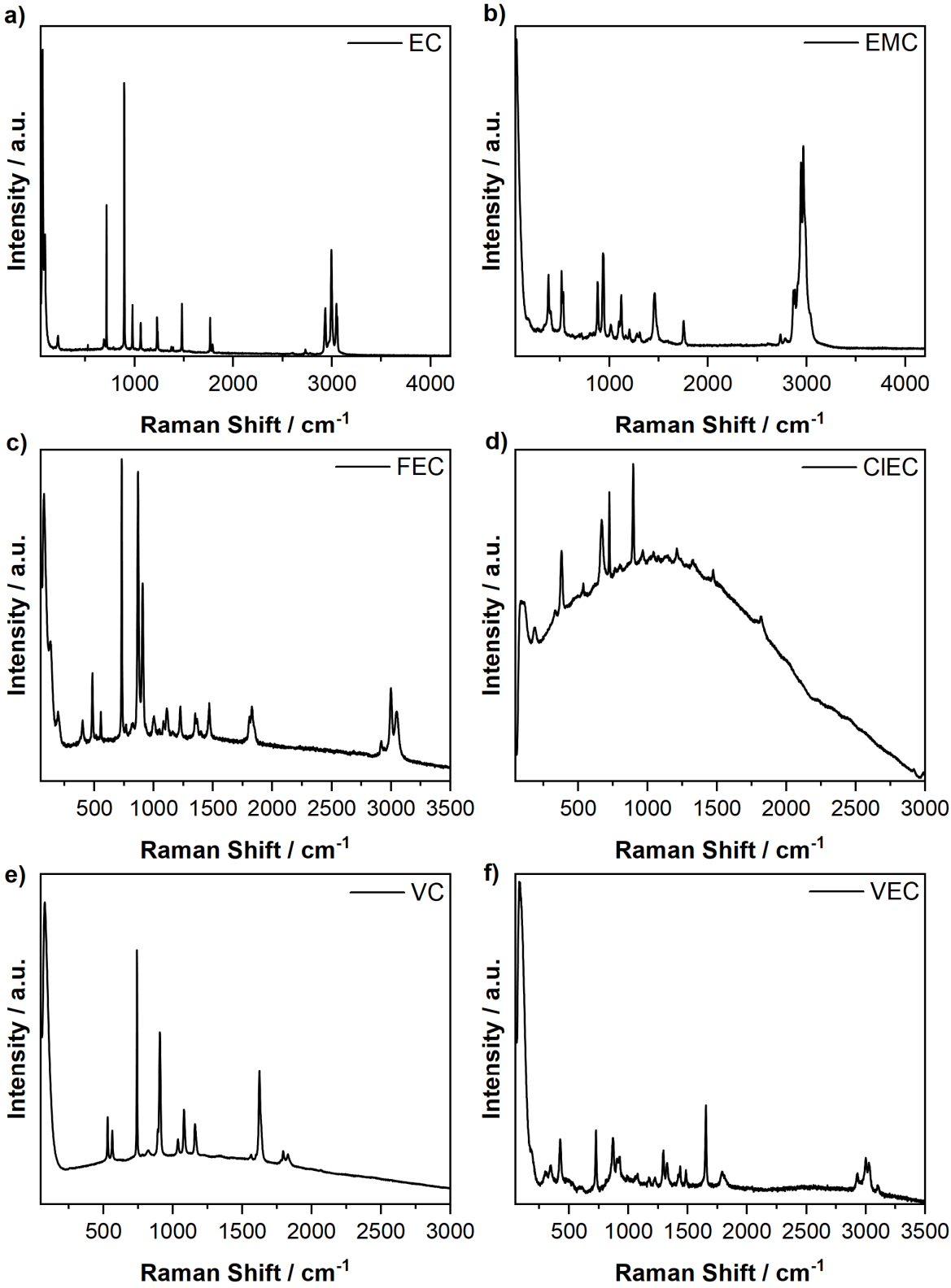

Figure A52: Reference Raman spectra of pure **a)** EC, **b)** EMC, **c)** FEC, **d)** ClEC, **e)** VC, and **f)** VEC. These reference spectra were used for the assignment of bands during the performed SHINERS and SERS investigations, indicated by "Own Spectrum". For spectrum acquisition the samples were excited using a 532 nm laser, adjusted to a power output of 6.10 mW. Spectra were acquired over three accumulations of 25 s. Figure redrawn with permission from [159].

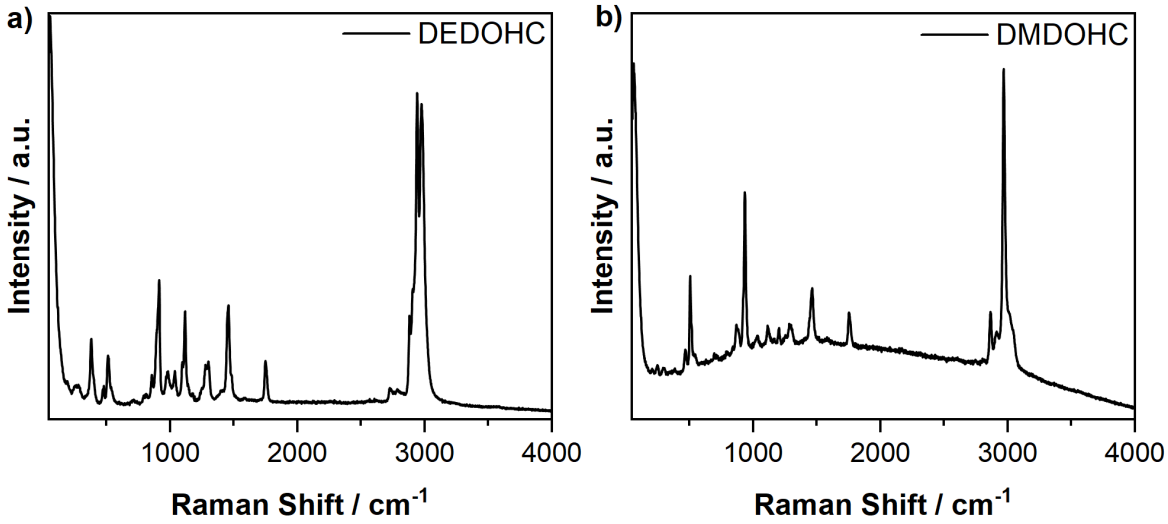

Figure A53: Reference Raman spectra of pure **a)** DEDOHC, **b)** DMDOHC. These reference spectra were used for the assignment of bands during the performed SHINERS and SERS investigations, indicated by "Own Spectrum". For spectrum acquisition the samples were excited using a 532 nm laser, adjusted to a power output of 6.10 mW. Spectra were acquired over three accumulations of 25 s. Figure redrawn with permission from [159].

10. Glossary

10.1. List of Figures

Figure 1: Schematic illustration of a LIB, consisting of a graphite anode and a layered lithium transition metal oxide ($LiTMO_x$) cathode. The electrodes are separated using a separator, soaked with a Li ion-containing electrolyte. Upon charging, electrons and Li-ions migrate to the anode. During discharge, this process is reverted. Li-ions deintercalate from the anode active material and migrate to the cathode side, re-inserting into the vacancies of the $LiTMO_x$ host cathode. During charge and discharge interphases form on the surfaces of the anode and cathode, the so called SEI and CEI, respectively. 4
Figure 2: Schematic representation of the SEI on the surface of a graphite anode consisting of an inner layer dominated by inorganic species like LiF, Li_2O, and Li_2CO_3, and an outer layer comprising mostly organic semi-carbonates and polyolefins. Li-ions can still migrate through the interphase, facilitating functionality of the LIB. 5
Figure 3: Schematic overview of the different strategies of artificial interphase formation strategies, divided into in vitro and in vivo techniques. Note that the in vitro techniques are further divided into top-down and bottom-up techniques. For every subgroup specific advantages are noted and exemplary techniques visualized. Note that in the depicted images the artificially formed interphase is represented by the green layer on the electrode (dark grey). 8
Figure 4: Schematic representation of the working principle of IR and Raman spectroscopy. The figure includes the process of IR absorption, Raman scattering, and fluorescence. Arrows symbolize the excitation of molecules from the vibrational ground state (g_x) to a state of higher energy, including virtual states (v_o) or excited states (e_x). The thickness of the arrows corresponds to the energy of the irradiated or emitted / scattered photon, while curved arrows depict relaxation of the molecule. 15
Figure 5: Schematic illustration of the surface plasmon effect, highlighting the difference between **a)** the surface plasmon resonance, occurring on smooth metal surfaces, and **b)** the localized surface plasmon resonance on a nanostructured metal substrate. Arrows on the side represent the estimated size of the surface plasmon above the respective substrate. 18

Figure 6: Schematic representation of the different near-field Raman spectroscopy techniques, developed from the initial surface enhanced Raman spectroscopy configuration. **a)** Tip enhanced Raman spectroscopy (TERS), **b)** nanoparticle enhanced Raman spectroscopy (NERS), and **c)** depiction of an Au-nanoparticle coated with a SiO_x shell, as commonly used for shell isolated nanoparticle enhanced Raman spectroscopy (SHINERS). SHINERS experimental configuration resembles the configuration presented for NERS. This figure is adapted with permission from [133]. 20
Figure 7: Overview of the proposed structure of this thesis. Two areas of focus, interphase modification and analysis, make up the main work performed during this thesis. The three main chapters of this thesis, **Chapters 5 – 7** bridge the areas of focus.....24
Figure 8: Synthesis route for the VEC decomposition product using Li-naphthalenide to resemble the reactivity of a lithiated graphite electrode. In addition, the structures of the proposed reaction products are depicted, based on the results of the $^{13}C\{^1H\}$ CP MAS NMR analysis.....42
Figure 9: **a)** Specific discharge capacities (Spec. Dis. Cap.) obtained from galvanostatic charge/discharge cycling at a C-rate of 1 C in a voltage range of 2.80 V – 4.50 V of NMC111||graphite coin cells, cycled in the presence of the BE 1 (1 $_M$ $LiPF_6$ in EC:DEC 1:1 by weight; **grey**) and the BE 1 + 0.10 $_M$ thiophene (THP, **red**). Cell formation was performed by 3 charge/discharge cycles at a C-rate of C/10, followed by 3 charge/discharge cycles at a C-rate of C/3. Graph redrawn from [28]. **b)** State-of-health of the NMC111||graphite coin cells. Note that the state-of-health is calculated based on the 7th cycle, being the first one performed at a C-rate of 1 C. 45
Figure 10: **a)** Coulombic efficiencies calculated for NMC111||graphite coin cells galvanostatically charge/discharge cycled at a C-rate of 1 C in a voltage range of 2.80 V – 4.50 V of, cycled in the presence of the BE 1 (1 $_M$ $LiPF_6$ in EC:DEC 1:1 by weight; **grey**) and the BE 1 + 0.10 $_M$ thiophene (THP, **red**). **b)** Differential voltage (□V) analysis of the NMC111||graphite coin cells, cycled in the presence of BE 1 and BE 1 + 0.10 $_M$ THP. Note that the displayed □V value corresponds to the difference between the mean charge and the mean discharge voltage. Figure adapted from [28].....45
Figure 11: Cyclic voltammograms of NMC111||graphite T-type Swagelok® cells with Li-metal reference electrodes obtained in the presence of **a)** BE 1 (1 $_M$ $LiPF_6$ in EC:DEC 1:1 by weight; **grey**) and **b)** BE 1 + 0.10 $_M$ THP (**red**). Cyclic voltammetry was performed in a potential range of 2.80 V – 4.50 V vs. $Li|Li^+$ with a scan rate of 150 μV s^{-1}. In total 3 charge/discharge cycles were performed marked by full, dashed, and dotted lines in the depicted voltammograms. Important peaks, discussed in the main text, are highlighted by arrows and the peak potential is noted. Distinct peak shifts are highlighted by bold arrows. Figure adapted from [28].....47
Figure 12: SEM images obtained from the surface of different NMC111 cathodes. **a)** and **d)** display SEM images of a pristine electrode. **b)** and **e)** show the SEM images of an electrode electrochemically aged in the presence of BE 1 (1 $_M$ $LiPF_6$ in EC:DEC 1:1 by weight), while **c)** and **f)** depict the surface of an electrode electrochemically aged in the presence of BE 1 + 0.10 M THP. Figure adapted from [28].....49
Figure 13: Operando SHINER spectra taken from the surface of an NMC111 electrode in the presence of BE 1 (1 $_M$ $LiPF_6$ in EC:DEC 1:1 by weight; **grey**) and BE 1 + 0.10 $_M$ THP (**red**). For the SHINERS measurement the NMC electrode was connected as working electrode, paired against a graphite counter electrode. Galvanostatic charging was performed at a C-rate of C/3. Au SHINs with a diameter of 55 nm were introduced to the electrode surface before the cell assembly. Spectra were recorded at the cut-off voltage of 4.50 V. For spectrum acquisition the samples were excited using a 633 nm laser, adjusted to a power output of 1.05 mW. Spectra were acquired over two accumulations of 50 s. Important, newly arising bands observed in the spectra are highlighted by arrows. In addition, band positions are noted. Figure adapted from [28].....51

Figure 14: Operando SHINER spectra taken from the surface of an NMC111 electrode in the presence of BE 1 (1 $_M$ $LiPF_6$ in EC:DEC 1:1 by weight) + 0.10 $_M$ THP. For the SHINERS measurement the NMC electrode was connected as working electrode, paired against a Li-metal counter electrode. Potentiostatic polarization of the cathode was performed at a scan rate of 150 μV s^{-1}. Au SHINs with a diameter of 55 nm were introduced to the electrode surface before the cell assembly. For spectrum acquisition the samples were excited using a 633 nm laser, adjusted to a power output of 1.05 mW. Spectra were acquired over two accumulations of 50 s. Spectra were recorded at different potentials, marked in the depicted spectra referenced against $Li|Li^+$. In addition, dashed lines represent the respective spectra background to highlight changes in the background intensity. Figure adapted from [28]. ... 52
Figure 15: Proposed reaction mechanism for the oxidative electro-polymerization of thiophene. Calculated differences in free energy (□G, computed at 298 K) are given for every reaction step in electron volts (eV). Figure adapted from [28]. ... 53
Figure 16: Overview of the thiophene derivatives investigated within this study as CEI-forming electrolyte additives. Given are the molecular structure, as well as the name of the respective molecules. Supplier and purity of the employed additives are noted in **Chapter 4.1**. ... 58
Figure 17: Specific discharge capacities (Spec. Dis. Cap.) obtained from NMC811||graphite pouch cells galvanostatically charge/discharge cycled at a C-rate of 1 C in a voltage range between 2.80 V – 4.50 V. Depicted are the discharge capacities of cells containing different thiophene-based electrolyte additives in the concentration of **a)** 0.04 $_M$ and **b)** 0.12 $_M$, in comparison to the discharge capacities obtained from the cells cycled in the presence of the BE 2 (1 $_M$ $LiPF_6$ in EC:EMC 3:7 by weight; **black**). Note that this figure only depicts the additive-containing cells exhibiting an improved electrochemical performance compared to the BE 2 cells. For the results of the other investigated electrolyte formulation the reader is kindly referred to **Figure A21**. ... 59
Figure 18: **a)** Specific discharge capacities (Spec. Dis. Cap.) obtained from NMC811||graphite pouch cells galvanostatically charge/discharge cycled at a C-rate of 1 C in a voltage range between 2.80 V – 4.50 V in the presence of the BE 2 (1 $_M$ $LiPF_6$ in EC:EMC 3:7 by weight; **black**) and the BE 2 + 0.20 $_M$ 3-THP-BOH (**orange**). Note that cycling was performed until reaching a state-of-health of 50%. However, cycling of the additive-containing cells was stopped at a state-of-health of 65%. **b)** Accumulated specific discharge energies (Acc. Spec. Dis. En.) obtained from NMC811||graphite pouch-cells containing the BE 2 and the BE 2 + 0.20 $_M$ 3-THP-BOH. Figure redrawn with permission from [29]. ... 61
Figure 19: **a)** Differential voltage (□V) analysis of the NMC811||graphite pouch cells, cycled in the presence of the BE 2 (1 $_M$ $LiPF_6$ in EC:EMC 3:7 by weight; **black**) and the BE 2 + 0.20 $_M$ 3-THP-BOH (**orange**) at a C-rate of 1 C in voltage range of 2.80 V – 4.50 V. Note that the displayed □V value corresponds to the difference between the mean charge and the mean discharge voltage. **b)** Electrochemical impedance spectra obtained from NMC811||graphite pouch cells galvanostatically cycled in the presence of the BE 2 and the BE 2 + 0.20 $_M$ 3-THP-BOH in a voltage range of 2.80 V – 4.50 V at a C-rate of C/2. Impedance spectra were recorded during every charge cycle at 50% state-of-charge for the 1st, the 50th and the 100th cycle. Figure redrawn with permission from [29]. ... 63
Figure 20: dQ/dV vs. voltage plots drawn for **a)** the 1st and **b)** the 450th galvanostatic charge/discharge cycle of NMC811||graphite pouch cells in the presence of the BE 2 (1 $_M$ $LiPF_6$ in EC:EMC 3:7 by weight; **black**) and the BE 2 + 0.20 $_M$ 3-THP-BOH (**orange**). Cycling was performed in a voltage range between 2.80 V and 4.50 V with a C-rate of C/10 and 1 C at the depicted cycles, respectively. Note that the first cycle is marked by a solid line, while the 450th cycle is marked with a dashed line. Important peaks, discussed in the main text, are highlighted by arrows and the peak voltage is noted. Figure redrawn with permission from [29]. ... 64

Figure 21: **a)** Voltage vs. time profiles of the first three galvanostatic charge/discharge cycles obtained from NMC811||graphite pouch cells cycled in the presence of the BE 2 (1 $_M$ $LiPF_6$ in EC:EMC 3:7 by weight; **black**) and the BE 2 + 0.20 $_M$ 3-THP-BOH (**orange**). Note that the depicted voltage profile is the average of four individual cells. **b)** Magnification of the initial charge cycle. The chosen inset is representative for the blue box in **a)**. Figure redrawn with permission from [29]. 65
Figure 22: SEM images obtained from the surface of different NMC811 cathodes. **a)** and **d)** display SEM images of a pristine electrode. **b)** and **e)** show the SEM images of an electrode electrochemically aged in the presence of BE 2 (1 $_M$ $LiPF_6$ in EC:EMC 3:7 by weight), while **c)** and **f)** depict the surface of an electrode electrochemically aged in the presence of BE 2 + 0.20 $_M$ 3-THP-BOH. Figure redrawn with permission from [29]. 67
Figure 23: **a)** Operando SHINER spectra taken from the surface of an NMC811 electrode in the presence of the BE 2 (1 $_M$ $LiPF_6$ in EC:EMC 3:7 by weight; **black**) and the BE 2 + 0.20 $_M$ 3-THP-BOH (**orange**). For the SHINERS measurement the NMC electrode was connected as working electrode, paired against a graphite counter electrode. Galvanostatic charge was performed at a C-rate of C/3. Au SHINs with a diameter of 55 nm were introduced to the electrode surface before cell assembly. Spectra were recorded at the cut-off potential of 4.50 V vs. $Li|Li^+$. **b)** Enlargement of the spectra shown in **a)** in the Raman shift range of 400 cm^{-1} to 1000 cm^{-1}. The respective inset is represented by a blue box in **a)**. For spectrum acquisition the samples were excited using a 633 nm laser, adjusted to a power output of 1.05 mW. Spectra were acquired over three accumulations of 35 s. Important, newly arising bands observed in the spectra are highlighted by arrows and band positions are noted. Figure redrawn with permission from [29]. 68
Figure 24: Operando SHINER spectra taken from the surface of an NMC811 electrode in the presence of the BE 2 (1 $_M$ $LiPF_6$ in EC:EMC 3:7 by weight) + 0.20 $_M$ 3-THP-BOH. For the SHINERS measurement, the NMC electrode was connected as working electrode, paired against a Li-metal counter electrode. Galvanostatic charge was performed at a C-rate of C/3. Au SHINs with a diameter of 55 nm were introduced to the electrode surface before the cell assembly. Spectra were recorded at different potentials against $Li|Li^+$, marked in the depicted spectra. For spectrum acquisition, the samples were excited using a 633 nm laser, adjusted to a power output of 1.05 mW. Spectra were acquired over three accumulations of 35 s. Important, newly arising bands observed in the spectra are highlighted by colored boxes and band positions or regions are noted. In addition, molecular structures of the attributed molecules are depicted. Figure redrawn with permission from [29]. 70
Figure 25: Schematic overview of the proposed potential-dependent CEI formation on the surface of an NMC811 electrode in the presence of the BE 2 (1 $_M$ $LiPF_6$ in EC:EMC 3:7 by weight) + 0.20 $_M$ 3-THP-BOH, based on the obtained operando SHINERS results. Note that the depicted electrode potential increases from left to right. Denoted potentials are referenced against $Li|Li^+$ and correspond to the recorded SHINER spectra. The presence of poly(3-THP-BOH) is indicated by **green** blocks, while the EC-3-THP-BOH copolymer is indicated by **orange** blocks and other interphase components by **grey** blocks. Figure redrawn with permission from [29]. 72
Figure 26: Suggested reaction mechanisms for the electro-polymerization of 3-THP-BOH. Shown are two alternative reaction routes **A** and **B**, characterized by alternative deprotonation options. The figure also provides the energy differences (ΔE, computed at 0 K) and the free energy difference (ΔG, computed at 298 K) calculated for each step. The determined energy values are given in electron volts (eV). Note that a value of 1.40 V has to be subtracted from the calculated energies to determine the potential on the experimental relevant $Li|Li^+$ scale. Figure redrawn with permission from [29]. 73
Figure 27: Overview of the results of the galvanostatic cycling experiments obtained from NMC622||graphite pouch cells charge/discharge cycled at a C-rate of 1 C in a voltage range

between 2.80 V – 4.50 V in the presence of the BE 2 (1 $_M$ $LiPF_6$ in EC:EMC 3:7 by weight, **black**) and the BE 2 + the optimized concentrations of FEC (**brown**), ClEC (**dark yellow**), VC (**blue**), and VEC (**purple**). Shown are **a)** the specific discharge capacities (Spec. Dis. Cap.) obtained from NMC622||graphite pouch cells, **b)** the differential voltage (□V) analysis, **c)** the accumulated specific discharge energies (Acc. Spec. Dis. En.), and **d)** the molecular structure of the employed electrolyte additives. Figure redrawn with permission from [159]. 78
Figure 28: Cyclic voltammograms (CVs) of graphite||Li-metal T-type Swagelok® cells with Li-metal reference electrodes obtained in the presence of the BE 2 (1 $_M$ $LiPF_6$ in EC:EMC 3:7 by weight, **black**) and the different electrolyte additive-containing electrolyte formulations. Shown are the CVs recorded for **a)** FEC (**brown**), **b)** ClEC (**dark yellow**), **c)** VC (**blue**), and **d)** VEC (**purple**) in comparison to the BE 2 CVs. Cyclic voltammetry was performed in a potential range of 2.80 V – 4.50 V vs. Li|Li^+ with a scan rate of 150 µV s^{-1}. In total 2 charge/discharge cycles were performed, marked by full and dashed lines in the depicted voltammograms. Figure redrawn with permission from [159]. 82
Figure 29: Comparison of the gas chromatograms recorded from the investigated electrolyte formulations electrochemically aged in NMC622||graphite pouch cells. The respective electrolytes were extracted after 100 galvanostatic charge/discharge cycles. Peak identification was performed via mass spectrometry and peaks are assigned in the respective chromatograms. Depicted are the chromatograms of the electrochemically aged BE 2 (1 $_M$ $LiPF_6$ in EC:EMC 3:7 by weight; **black**) and the additive-containing electrolyte formulations at the optimum electrolyte additive concentration for FEC (**brown**), ClEC (**dark yellow**), VC (**blue**), and VEC (**purple**). The individual chromatograms are depicted in **Figure A34**. Figure redrawn with permission from [159]. 84
Figure 30: Operando SHINER spectra taken from the surface of a graphite electrode in the presence of the BE 2 (1 $_M$ $LiPF_6$ in EC:EMC 3:7 by weight) and the additive-containing electrolytes. For the SHINERS measurement, the graphite electrode was connected as working electrode, paired against a NMC622 counter electrode. Galvanostatic charge was performed at a C-rate of C/3. Au SHINs with a diameter of 55 nm were introduced to the electrode surface before cell assembly. Spectra were recorded at different cell voltages, denoted in the spectra and indicated by the intensity of the color. Spectra were recorded in the presence of **a)** the BE 2 (**black**) **b)** FEC (**brown**), **c)** ClEC (**dark yellow**), **d)** VC (**blue**), and **e)** VEC (**purple**). For spectrum acquisition, the samples were excited using a 633 nm laser, adjusted to a power output of 1.05 mW. Spectra were acquired over three accumulations of 35 s. Important newly arising bands observed in the spectra are highlighted by grey boxes. Figure redrawn with permission from [159]. 85
Figure 31: Cyclic voltammograms (CVs) of NMC622||graphite T-type Swagelok® cells with Li-metal reference electrodes obtained in the presence of the BE 2 (1 $_M$ $LiPF_6$ in EC:EMC 3:7 by weight, **black**) and the BE 2 + 0.30 $_M$ VEC (**colored**). Depicted are the **a)** 1st and **b)** 2nd scan. In addition, for the VEC-containing electrolyte the scans are separated into the anodic (an.; **purple**) and cathodic (cat.; **red**) scan. Cyclic voltammetry was performed in a potential range of 2.80 V – 5.00 V vs. Li|Li^+ with a scan rate of 150 µV s^{-1}. Important peaks and the characteristic potential shift of bands observed for the CVs of the VEC-containing electrolyte formulation are highlighted by arrows and the recorded potential. Figure redrawn with permission from [159]. 89
Figure 32: SEM images of the surface of a graphite electrode extracted from NMC622||graphite pouch cells after formation. The respective cells were cycled in the presence of **b)** the BE 2 (1 $_M$ $LiPF_6$ in EC:EMC 3:7 by weight) and the BE 2 + the optimized additive concentrations: **c)** FEC, **d)** ClEC, **e)** VC, and **f)** VEC. **a)** shows the pristine graphite electrode as reference. Figure redrawn with permission from [159]. 90
Figure 33: SEM images of the surface of an NMC622 electrode extracted from NMC622||graphite pouch cells after formation. The respective cells were cycled in the

presence of **b)** the BE 2 (1 $_M$ $LiPF_6$ in EC:EMC 3:7 by weight) and BE 2 + the optimized additive concentrations: **c)** FEC, **d)** ClEC, **e)** VC, and **f)** VEC. **a)** shows the pristine NMC622 electrode as reference. Figure redrawn with permission from [159]. 90
Figure 34: Depth profiles obtained for the surface layers from graphite electrodes extracted from NMC622||graphite pouch cells after galvanostatic charge/discharge cycling. Investigation was performed via focused ion beam secondary mass spectrometry equipped with a time of flight analyzer. The figure shows the elemental distribution of the combined Li-species (**a** – **c**) and of Mn (**d** – **f**), for graphite electrodes cycled in the presence of the BE 2 (1 $_M$ $LiPF_6$ in EC:EMC 3:7 by weight; left), the FEC-containing electrolyte (center), and the VEC-containing electrolyte (right). Segments of the depth profiles with high concentration of the respective element are highlighted by red lines in the figure. Note that due to the similar sample compositions it can be assumed that the thickness of each ablated layer (frame) is similar, enabling the comparison of the investigated samples. For the depth profiles of the separated LI-species and the depth profiles obtained for the other considered electrolyte formulations, the reader is referred to **Figure A44** and **Figure A45**. Figure redrawn with permission from [159]. 92
Figure 35: **a)** Operando SHINER spectra recorded from the surface of an NMC622 electrode in the presence of the BE 2 (1 $_M$ $LiPF_6$ in EC:EMC 3:7 by weight; **black**) and the BE 2 + 0.30 $_M$ VEC (**purple**), recorded at the cut-off potential of 4.50 V vs. $Li|Li^+$. For the SHINERS measurement, the NMC622 electrode was connected as working electrode paired against a graphite counter electrode. In addition, a Li-metal electrode was introduced as reference electrode to monitor the electrodes potential. Galvanostatic charge was performed at a C-rate of C/3. Au SHINs with a diameter of 55 nm were introduced to the electrode surface before cell assembly. **b)** Comparison of the SHINER and SER spectra (**green**) recorded in the presence of the VEC-containing electrolyte of the surface of a NMC622 or roughened Au electrode, respectively, at the cut-off potential of 4.50 V vs. $Li|Li^+$. For the SERS measurement, the Au electrode was charged with a sweep rate of 150 µV s^{-1}. For spectrum acquisition, the samples were excited using a 633 nm laser, adjusted to a power output of 1.05 mW. Spectra were acquired over three accumulations of 35 s. Important bands are highlighted by arrows and band positions are noted in the spectra. Figure redrawn with permission from [159]. 94
Figure 36: Schematic depiction of the cross-talk mechanism suggested for the electrolyte with VEC, based on the results of the SHINERS (**purple**) and SERS (**green**) investigations of the electrode surfaces in the presence of the BE 2 (1 $_M$ $LiPF_6$ in EC:EMC 3:7 by weight) + 0.30 $_M$ VEC shown in the lower segment of the figure. The upper segment of the presented overview displays a schematic lithium-ion battery (LIB), comprising of an anode (graphite, **A**) and a cathode (NMC622, **C**) and the SEI (**yellow**) and CEI (**red**) formed on the respective surfaces. Here, changes in the color intensity resemble formation or dissolution of the particular interphase depending on the electrode potential. The proposed reaction mechanism, resulting in the formation of the interphases is displayed in the center of the schematic LIB and important steps are highlighted by numbers, ascribed to the following processes: **1**: Reduction of VEC leading to a ring-opening of the molecule. **2**: Dissolution of the VEC reduction product and subsequent transfer to the cathode side via electro-migration. **3**: Oxidative Electro-polymerization of the VEC reductive degradation product on the surface of the cathode, leading to the formation of a polymeric CEI. Finally, the formed VEC-derived CEI is effective in suppressing transition metal (**TM**) dissolution into the electrolyte accounting for the enhanced performed during galvanostatic cycling. Note that the numbers displayed in the Raman spectra can be ascribed directly to the numbers in the reaction mechanism, resembling the respective reaction step. Figure redrawn with permission from [159]. 97
Figure 37: Comprehensive overview of the main objectives accomplished within this thesis. Based upon the proposed structure depicted in **Figure 7**, the most important achievements

are presented for the respective chapters. In addition, interphase formation mechanisms unraveled using operando SHINERS are depicted for the regarding chapters..... 101

10.2. List of Appendix Figures

Figure A1: SEM image of silica coated Au nanoparticles with a targeted size of 55 nm drop cast on an NMC811 electrode. 105
Figure A2: SEM image of silica coated Au nanoparticles with a targeted size of 120 nm drop cast on a Si-wafer..... 106
Figure A3: Raman spectra of a Si-wafer in the presence of 55 nm Au NPs with a complete silica coating (**black**) and an incomplete silica coating (**purple**). The wafer was infused with a 10 $_{mM}$ pyridine solution before acquisition of the spectra. The sample was excited using a red laser (633 nm). Spectra were acquired for 20 s with 3 accumulations. Laser power was adjusted using a 10% filter. 107
Figure A4: UV/Vis absorption spectra of Au NPs with 20 nm, 40 nm, 55 nm, and 120 nm diameters, dispersed in Milli-Q water. The spectrum additionally highlights the wavelengths emitted by the lasers available for the Raman system utilized in this thesis by dashed lines. 108
Figure A5: SHINER spectra taken from the surface of a Si-wafer in the presence of a GBL-based electrolyte (1 $_{M}$ $LiBF_4$, E-Lyte Innovations, battery grade) in GBL (Sigma Aldrich, 99%) at an electrode potential of 50 mV vs. Li|Li^+. Spectra were taken using a red and a green laser. Spectra were acquired for 25 s with 4 accumulations. Laser power was regulated to 1.05 mW and 1.22 mW, respectively. 120 nm Au NPs used for SHINERS enhancement were introduced to the Si-wafer via drop casting prior to the measurement. 109
Figure A6: UV/Vis absorption spectra of Ag NPs with 20 nm, 28 nm, 36 nm, 50 nm, 70 nm, and 100 nm diameters synthesized with the use of 12 nm Au seeds, dispersed in Milli-Q water. The spectrum additionally highlights the wavelengths emitted by the lasers available for the Raman system utilized in this thesis by dashed lines..... 110
Figure A7: UV/Vis absorption spectra of Ag NPs with 50 nm, 70 nm, and 100 nm diameters synthesized without the use of Au seeds, dispersed in Milli-Q water. The spectrum additionally highlights the wavelengths emitted by the lasers available for the Raman system utilized in this thesis by dashed lines..... 111
Figure A8: SEM image of silica coated Au nanoparticles with a diameter of 55 nm drop cast on a single crystal NMC811 electrode. In total 500 µL (5 x 100 µL) of concentrated NP solution were added to the electrode. Area of high NP concentration is highlighted by a red circle..... 112
Figure A9: Schematic depiction of **a)** the optical cell and **b)** – **c)** the electrode configurations, employed in this thesis. The red arrows symbolize the Raman laser, while the yellow balls represent silica coated Au NPs. Active material of the negative and positive electrode are represented by black color. Current collectors are colored in grey and brown to depict aluminum and copper current collectors for positive and negative electrode, respectively. In general, the electrode with NPs is connected as WE, serving as main focus for Raman investigation, with **d)** being the exception, as both electrode surfaces are to be investigated. Here the positive electrode is connected as WE. **b)** represents the “sandwich” configuration, **c)** the “donut” configuration, and **c)** the “side-by-side” configuration. RE is not depicted, as in practical use it is always placed on the outer side, next to WE and CE.. 113
Figure A10: Potential response of a Li-plating experiment to investigate Au NP alloying behavior. In a Swagelok cell a Cu electrode (WE) was paired against a Li-metal CE. A constant current of 50 µA cm^{-2} was applied to induce Li plating. The experiment was

performed with a bare Cu electrode as reference (**grey**), a Cu electrode with 55 nm Au NPs (**red**) and a Cu electrode with 55 nm SiO_2 coated Au NPs (**blue**). Roughly double the amount of SiO_2 coated NPs is expected to be on the Cu electrode, in comparison to uncoated NPs. However, the ratio of NPs can only be estimated. 114
Figure A11: Specific discharge capacities obtained from galvanostatic charge/discharge cycling at a C-rate of 1 C in a voltage range of 2.80 V – 4.50 V of NMC111||graphite coin cells, cycled in the presence of the BE 1 (1 $_M$ $LiPF_6$ in EC:DEC 1:1 by weight; **grey**) and the BE 1 + different concentrations of thiophene (THP, **red** color gradation). Cell formation was performed by 3 charge/discharge cycles at a C-rate of C/10, followed by 3 charge/discharge cycles at a C-rate of C/3. Graph redrawn from [28]. 115
Figure A12: State-of-health obtained from galvanostatic charge/discharge cycling at a C-rate of 1 C in a voltage range of 2.80 V – 4.50 V of NMC111||graphite coin cells, cycled in the presence of the BE 1 (1 $_M$ $LiPF_6$ in EC:DEC 1:1 by weight; **grey**) and the BE 1 + 0.10 $_M$ thiophene (THP, **red**). Cell formation was performed by 3 charge/discharge cycles at a C-rate of C/10, followed by 3 charge/discharge cycles at a C-rate of C/3. Note that the state-of-health is calculated based on the 7th cycle, being the first one performed at a C-rate of 1 C. Graph redrawn from [28]. 116
Figure A13: Electrochemical impedance spectra obtained from NMC111||graphite pouch cells galvanostatically cycled in the presence of **a)** BE 1 (1 $_M$ $LiPF_6$ in EC:DEC 1:1 by weight; **grey**) and **b)** BE 1 + 0.10 $_M$ THP (**red**) in a voltage range of 2.80 V – 4.50 V at a C-rate of C/2. Impedance spectra were recorded during every charge cycle at 50% state-of-charge. Graph redrawn from [28]. 116
Figure A14: dQ/dV vs. voltage plots drawn for the first three galvanostatic charge/discharge cycles of NMC111||graphite coin cells in the presence of **a)** BE 1 (1 $_M$ $LiPF_6$ in EC:DEC 1:1 by weight; **grey**) and **b)** BE 1 + 0.10 $_M$ THP (**red**). Galvanostatic charge/discharge cycling was performed in a voltage range between 2.80 V and 4.50 V with a C-rate of C/10 at the depicted cycles. Note that the first cycle is marked by a solid line, while the second and third cycle are marked by dashed and dotted lines, respectively. Important peaks discussed in the main text are highlighted by arrows and the peak voltage is noted. Graph redrawn from [28] 117
Figure A15: Voltage vs. capacity histograms of NMC111||Graphite coin-cells cycled in the presence of the BE 1 (1 $_M$ $LiPF_6$ in EC:DEC 1:1 by weight; **grey**) and **b)** BE 1 + 0.10 $_M$ THP (**red**). **a)** and **b)** show the first and second of the BE 1 and the BE 1 + 0.10 $_M$ THP, indicated by full and dashed lines, respectively. **c)** shows the comparison of the 50th cycle obtained from coin cells, cycled in the presence of the considered electrolyte formulations. Important features discussed in the main text are highlighted by arrows and the respective voltage is noted. 118
Figure A16: Results of the EDX investigation performed on the surface of a NMC111 electrode electrochemically aged in the presence of BE 1 (1 $_M$ $LiPF_6$ in EC:DEC 1:1 by weight) + 0.10 $_M$ THP. **a)** shows the SEM image of the electrode spot selected for EDX investigation. **b)** shows the distribution of sulfur (S) on the surface of the probed electrode. While sulfur was identified on the whole electrode, a distinct concentration was observed on NMC particles, highlighted by a red dashed circle. Figure adapted from [28]. 119
Figure A17: Operando SHINER spectra taken from the surface of an NMC111 electrode in the presence of BE 1 (1 $_M$ $LiPF_6$ in EC:DEC 1:1 by weight). For the SHINERS measurement the NMC electrode was connected as working electrode, paired against a graphite counter electrode. Galvanostatic charge was performed at a C-rate of C/3 and Au SHINs with a diameter of 55 nm were introduced to the electrode surface before the cell assembly. Spectra were recorded at the open circuit voltage (OCV, **grey**) and the cut-off voltage of 4.50 V (**light grey**). For spectrum acquisition the samples were excited using a 633 nm laser, adjusted to a power output of 1.05 mW. Spectra were acquired over two

accumulations of 50 s. Important newly arising bands observed in the spectra are highlighted by arrows. In addition, band positions are noted. Figure adapted from [28]. .. 119
Figure A18: Operando SHINER spectra taken from the surface of an NMC111 electrode in the presence of BE 1 (1 $_M$ $LiPF_6$ in EC:DEC 1:1 by weight) + 0.10 $_M$ THP. For the SHINERS measurement the NMC electrode was connected as working electrode, paired against a graphite counter electrode. Galvanostatic charge was performed at a C-rate of C/3 and Au SHINs with a diameter of 55 nm were introduced to the electrode surface before the cell assembly. Spectra were recorded at the open circuit voltage (OCV, **red**) and the cut-off voltage of 4.50 V (**light red**). For spectrum acquisition, the samples were excited using a 633 nm laser, adjusted to a power output of 1.05 mW. Spectra were acquired over two accumulations of 50 s. Important newly arising bands observed in the spectra are highlighted by arrows. In addition, band positions are noted. Figure adapted from [28]. .. 120
Figure A19: Proposed reaction mechanism for the co-polymerization of EC and thiophene. Calculated differences in free energy (□G, computed at 298 K) are given for every reaction step in electron volts (eV), initial oxidation potential of EC is given on the $Li|Li^+$ scale. Figure adapted from [28]. 120
Figure A20: Proposed reaction mechanisms for the polymerization of EC. **a)** shows the suggested mechanism for a radical polymerization, while **b)** depicts the mechanism for an anionic mechanism, initiated by a nucleophilic F^- attack. Calculated differences in free energy (□G, computed at 298 K) are given for every reaction step in electron volts (eV), initial oxidation potential of EC is given on the $Li|Li^+$ scale. Figure adapted from [28]..... 121
Figure A21: Specific discharge capacities (Spec. Dis. Cap.) obtained from NMC811||graphite pouch cells galvanostatically charge/discharge cycled at a C-rate of 1 C in a voltage range between 2.80 V – 4.50 V. Depicted are the discharge capacities of cells containing different thiophene-based electrolyte additives in the concentration of **a)** 0.04 $_M$ and **b)** 0.12 $_M$, in comparison to the discharge capacities obtained from the cells cycled in the presence of the BE 2 (1 $_M$ $LiPF_6$ in EC:EMC 3:7 by weight; **black**). Note that this figure only depicts the additive-containing cells exhibiting a decreased electrochemical performance compared to the BE 2 cells. For the results of the other investigated electrolyte formulation the reader is kindly referred to **Figure 17**. 122
Figure A22: Specific discharge capacities obtained from NMC811||graphite pouch cells galvanostatically charge/discharge cycled at a C-rate of 1 C in a voltage range between 2.80 V – 4.50 V. Depicted are the discharge capacities of cells containing the BE 2 (1 $_M$ $LiPF_6$ in EC:EMC 3:7 by weight; **black**) and the BE 2 + varying concentrations of 3-THP-BOH (0.04 $_M$, 0.12 $_M$, 0.20 $_M$ and 0.30 $_M$, **orange**). Figure redrawn with permission from [29]. 125
Figure A23: Coulombic efficiencies (CEs) obtained from NMC811||graphite pouch cells galvanostatically charge/discharge cycled at a C-rate of 1 C in a voltage range between 2.80 V – 4.50 V. Depicted are the CEs of cells containing the BE 2 (1 $_M$ $LiPF_6$ in EC:EMC 3:7 by weight; **black**) and the BE 2 + 0.20 $_M$ 3-THP-BOH (**orange**). The inset in the figure puts the focus on the initial 10 charge/discharge cycles, including the formation cycles. Figure redrawn with permission from [29]. 126
Figure A24: Specific discharge capacities obtained from NMC811||graphite pouch cells galvanostatically charge/discharge cycled at a C-rate of 1 C in a voltage range between 2.80 V – 4.50 V. Depicted are the discharge capacities of cells containing the BE 2 (1 $_M$ $LiPF_6$ in EC:EMC 3:7 by weight; **black**), the BE 2 + 0.20 $_M$ 3-THP-BOH (**orange**), and the BE 2 + 0.10 $_M$ $LiPO_2F_2$ (LiDFP, **green**). Figure redrawn with permission from [29]..... 127
Figure A25: dQ/dV vs. voltage plots drawn for the first three charge/discharge cycles of NMC811||graphite pouch cells in the presence of **a)** the BE 2 (1 $_M$ $LiPF_6$ in EC:EMC 3:7 by weight; **black**) and **b)** the BE 2 + 0.20 $_M$ 3-THP-BOH (**orange**). **c)** shows the comparison of the second cycle of both investigated electrolyte formulations. Galvanostatic charge/discharge cycling was performed in a voltage range between 2.80 V and 4.50 V with

a C-rate of C/10 at the depicted cycles. Note that in **a)** and **b)** the first cycle is marked by a solid line, while the second and third cycles are marked by dashed and dotted lines, respectively. Figure redrawn with permission from [29]. 128
Figure A26: Elemental distribution of **a)** boron and **b)** sulfur on the surface of an NMC811 electrode taken from a NMC811||graphite cell, cycled in the presence of the BE 2 (1 $_M$ $LiPF_6$ in EC:EMC 3:7 by weight) + 0.20 $_M$ 3-THP-BOH. **c)** shows the sum spectrum of the performed EDX analysis and corresponding elements are marked within the spectrum. Figure redrawn with permission from [29]. 129
Figure A27: Operando SHINER spectra taken from the surface of an NMC811 electrode in the presence of the BE 2 (1 $_M$ $LiPF_6$ in EC:EMC 3:7 by weight) at the open circuit potential (OCP, **black**) and the cut-off voltage of 4.50 V vs. Li|Li^+ (**grey**). For the SHINERS measurement the NMC electrode was connected as working electrode, paired against a graphite counter electrode. Galvanostatic charge was performed at a C-rate of C/3. Au SHINs with a diameter of 55 nm were introduced to the electrode surface before cell assembly. For spectrum acquisition the samples were excited using a 633 nm laser, adjusted to a power output of 1.05 mW. Spectra were acquired over three accumulations of 35 s. Figure redrawn with permission from [29]. 130
Figure A28: Operando SHINER spectra taken from the surface of an NMC811 electrode in the presence of the BE 2 (1 $_M$ $LiPF_6$ in EC:EMC 3:7 by weight) + 0.20 $_M$ 3-THP-BOH at the open circuit potential (OCP, **orange**) and the cut-off voltage of 4.50 V vs. Li|Li^+ (**light orange**). For the SHINERS measurement the NMC electrode was connected as working electrode, paired against a graphite counter electrode. Galvanostatic charge was performed at a C-rate of C/3. Au SHINs with a diameter of 55 nm were introduced to the electrode surface before cell assembly. For spectrum acquisition the samples were excited using a 633 nm laser, adjusted to a power output of 1.05 mW. Spectra were acquired over three accumulations of 35 s. Figure redrawn with permission from [29]. 131
Figure A29: Raman spectra of pure a) thiophene, b) 3-thiophene boronic acid, c) ethylene carbonate, and d) ethyl methyl carbonate. These spectra were utilized to assign bands in the obtained SHINERS spectra. For spectrum acquisition the samples were excited using a 532 nm laser, adjusted to a power output of 6.10 mW. Spectra were acquired over three accumulations of 25 s. Figure redrawn with permission from [29]. 132
Figure A30: Time-dependent SHINER spectra taken from the surface of an NMC811 electrode in the presence of the BE 2 (1 $_M$ $LiPF_6$ in EC:EMC 3:7 by weight) + 0.20 $_M$ 3-THP-BOH. First, the electrode was charged to the cut-off voltage of 4.50 V vs. Li|Li^+. Afterwards, a constant potential was applied to the cell to hold the electrode potential. SHINER spectra were recorded at 0 min, 30 min, 45 min, and 60 min after reaching 4.50 V vs. Li|Li^+. For the SHINERS measurement the NMC electrode was connected as working electrode, paired against a graphite counter electrode. Galvanostatic charge was performed at a C-rate of C/3. Au SHINs with a diameter of 55 nm were introduced to the electrode surface before cell assembly. For spectrum acquisition the samples were excited using a 633 nm laser, adjusted to a power output of 1.05 mW. Spectra were acquired over three accumulations of 35 s. Figure redrawn with permission from [29]. 136
Figure A31: Suggested reaction mechanisms for the electro-co-polymerization of EC and 3-THP-BOH. Given are the energy differences (ΔE, computed at 0 K) and the free energy difference (ΔG, computed at 298 K) calculated for each step. The determined energy values are given in electron volts (eV). Figure redrawn with permission from [29]. 136
Figure A32: Specific discharge capacities (Spec. Dis. Cap.) obtained during the galvanostatic charge/discharge cycling experiments performed with NMC622||graphite pouch cells at a C-rate of 1 C in a voltage range between 2.80 V – 4.50 V to determine the optimum electrolyte additive concentration for **a)** FEC (**brown**), **b)** ClEC (**dark yellow**), **c)** VC (**blue**), and **d)** VEC (**purple**). Note that all investigated electrolyte formulations are compared to the BE 2 electrolyte (1 $_M$ $LiPF_6$ in EC:EMC, 3:7 by weight). A comparison of

the electrolyte formulations containing the optimized additive concentration is depicted in **Figure 27**. Figure redrawn with permission from [159]. 137
Figure A33: Coulombic efficiencies (CEs) obtained from NMC622||graphite pouch cells galvanostatically charge/discharge cycled at a C-rate of 1 C in a voltage range between 2.80 V – 4.50 V. Depicted are the CEs of cells containing the BE 2 (1 $_M$ $LiPF_6$ in EC:EMC 3:7 by weight; **black**) and the cells containing the optimum electrolyte additive concentration for FEC (**brown**), ClEC (**dark yellow**), VC (**blue**), and VEC (**purple**). The inset in the figure puts the focus on the initial 10 charge/discharge cycles, including the formation cycles. Figure redrawn with permission from [159]. 138
Figure A34: Individual gas chromatograms recorded from the investigated electrolyte formulations electrochemically aged in NMC622||graphite pouch cells. The respective electrolytes were extracted after 100 galvanostatic charge/discharge cycles. Peak identification was performed via mass spectrometry and peaks are assigned in the respective chromatograms. Depicted are the chromatograms of the electrochemically aged **a)** BE 2 (1 $_M$ $LiPF_6$ in EC:EMC 3:7 by weight ; **black**) and the additive-containing electrolyte formulations at the optimum electrolyte additive concentration for **b)** FEC (**brown**), **c)** ClEC (**dark yellow**), **d)** VC (**blue**), and **e)** VEC (**purple**). Figure redrawn with permission from [159]. 139
Figure A35: Results of the additionally performed gas chromatography high resolution accurate mass spectrometry analysis of the decomposition products identified for the ClEC-containing electrolyte formulation. **a)** shows the regular gas chromatograms of the investigated electrolyte formulation at a pristine state, after formation, and after 100 consecutive galvanostatic charge/discharge cycles. Peak assignments were obtained by mass spectrometry and are noted in the chromatogram. **b)** Mass spectra of the fragment pattern obtained through electron ionization of the compounds 1 – 3, identified as ClEC decomposition products in the gas chromatogram. In addition, molecular structures proposed based on the fragment pattern of the identified compounds are depicted. **c)** Extracted ion chromatogram of the $[M+NH_4]^+$ adducts obtained by chemical ionization, characteristic for chlorine containing compounds, with a m/z of 156.04 and 158.04. Figure redrawn with permission from [159]. 140
Figure A36: Operando SHINER spectra taken from the surface of a graphite electrode in the presence of the BE 2 (1 $_M$ $LiPF_6$ in EC:EMC 3:7 by weight). For the SHINERS measurement the graphite electrode was connected as working electrode, paired against a NMC622 counter electrode. Galvanostatic charge was performed at a C-rate of C/3. Au SHINs with a diameter of 55 nm were introduced to the electrode surface before cell assembly. Spectra were recorded at different cell voltages, denoted in the spectra and indicated by the intensity of the color. For spectrum acquisition the samples were excited using a 633 nm laser, adjusted to a power output of 1.05 mW. Spectra were acquired over three accumulations of 35 s. Figure redrawn with permission from [159]. 141
Figure A37: Operando SHINER spectra taken from the surface of a graphite electrode in the presence of the BE 2 (1 $_M$ $LiPF_6$ in EC:EMC 3:7 by weight) + 0.75 $_M$ FEC. For the SHINERS measurement the graphite electrode was connected as working electrode, paired against a NMC622 counter electrode. Galvanostatic charge was performed at a C-rate of C/3. Au SHINs with a diameter of 55 nm were introduced to the electrode surface before cell assembly. Spectra were recorded at different cell voltages, denoted in the spectra and indicated by the intensity of the color. For spectrum acquisition the samples were excited using a 633 nm laser, adjusted to a power output of 1.05 mW. Spectra were acquired over three accumulations of 35 s. Figure redrawn with permission from [159]. 143
Figure A38: Operando SHINER spectra taken from the surface of a graphite electrode in the presence of the BE 2 (1 $_M$ $LiPF_6$ in EC:EMC 3:7 by weight) + 0.75 $_M$ ClEC. For the SHINERS measurement the graphite electrode was connected as working electrode, paired against a NMC622 counter electrode. Galvanostatic charge was performed at a C-rate of

C/3. Au SHINs with a diameter of 55 nm were introduced to the electrode surface before cell assembly. Spectra were recorded at different cell voltages, denoted in the spectra and indicated by the intensity of the color. For spectrum acquisition the samples were excited using a 633 nm laser, adjusted to a power output of 1.05 mW. Spectra were acquired over three accumulations of 35 s. Figure redrawn with permission from [159]. 146
Figure A39: Operando SHINER spectra taken from the surface of a graphite electrode in the presence of the BE 2 (1 $_M$ $LiPF_6$ in EC:EMC 3:7 by weight) + 0.75 $_M$ VC. For the SHINERS measurement the graphite electrode was connected as working electrode, paired against a NMC622 counter electrode. Galvanostatic charge was performed at a C-rate of C/3. Au SHINs with a diameter of 55 nm were introduced to the electrode surface before cell assembly. Spectra were recorded at different cell voltages, denoted in the spectra and indicated by the intensity of the color. For spectrum acquisition the samples were excited using a 633 nm laser, adjusted to a power output of 1.05 mW. Spectra were acquired over three accumulations of 35 s. Figure redrawn with permission from [159]. 148
Figure A40: Operando SHINER spectra taken from the surface of a graphite electrode in the presence of the BE 2 (1 $_M$ $LiPF_6$ in EC:EMC 3:7 by weight) + 0.30 $_M$ VEC. For the SHINERS measurement the graphite electrode was connected as working electrode, paired against a NMC622 counter electrode. Galvanostatic charge was performed at a C-rate of C/3. Au SHINs with a diameter of 55 nm were introduced to the electrode surface before cell assembly. Spectra were recorded at different cell voltages, denoted in the spectra and indicated by the intensity of the color. For spectrum acquisition the samples were excited using a 633 nm laser, adjusted to a power output of 1.05 mW. Spectra were acquired over three accumulations of 35 s. Figure redrawn with permission from [159]. 150
Figure A41: Specific discharge capacities obtained from NMC622||graphite coin cell cycled in the presence of the BE 2 (1 $_M$ $LiPF_6$ in EC:EMC 3:7 by weight). The coin cells consist of an electrochemically aged electrode paired with a pristine counterpart. The aged electrodes were extracted from NMC622||graphite pouch cells cycled in the presence of the BE 2 until reaching a SoH of 50%. Depicted are coin cell containing the aged graphite electrode (**black**) and the aged cathode (**grey**). Figure redrawn with permission from [159]. 154
Figure A42: Specific discharge capacities (Spec. Dis. Cap.) obtained from NMC622||graphite coin cell cycled in the presence of the BE 2 (1 $_M$ $LiPF_6$ in EC:EMC 3:7 by weight). The coin cells consist of an electrochemically aged anode (**a**) or cathode (**b**) paired with a pristine counterpart. The depicted electrodes were taken from NMC622||graphite pouch cells galvanostatically cycled in the presence of the BE 2, the BE 2 + 0.15 $_M$ FEC (**brown**), and the BE 2 + 0.50 $_M$ VEC (**purple**) after reaching a SoH of 50%. Figure redrawn with permission from [159]. 155
Figure A43: Cyclic voltammograms (CVs) of NMC622||graphite T-type Swagelok® cells with Li-metal reference electrodes obtained in the presence of the BE 2 (1 $_M$ $LiPF_6$ in EC:EMC 3:7 by weight, **black**) and the different electrolyte additive-containing electrolyte formulations. Shown are the CVs recorded for **a)** FEC (**brown**), **b)** ClEC (**dark yellow**), **c)** VC (**blue**), and **d)** VEC (**purple**) in comparison to the BE 2 CVs. Cyclic voltammetry was performed in a potential range of 2.80 V – 4.50 V vs. Li|Li^+ with a scan rate of 150 µV s^{-1}. In total 2 charge/discharge cycles were performed marked by full and dashed lines in the depicted voltammograms. Figure redrawn with permission from [159]. 156
Figure A44: Depth profiles obtained for the surface layers from graphite electrodes extracted from NMC622||graphite pouch cells after galvanostatic charge/discharge cycling. Investigation was performed via focused ion beam secondary mass spectrometry equipped with a time of flight analyzer. The figure shows the elemental distribution of the combined Li-species (**a** – **c**), Li_2O (**d** – **f**), Li_2F (**g** – **i**), and of Mn (**j** – **l**), for graphite electrodes cycled in the presence of the BE 2 (1 $_M$ $LiPF_6$ in EC:EMC 3:7 by weight; left), the FEC-containing electrolyte (center), and the VEC-containing electrolyte (right). In addition, images of the surface before and after the performed investigation are depicted (**m** – **o**). Note that due to

the similar sample compositions it can be assumed that the thickness of each ablated layer (frame) is similar, enabling the comparison of the investigated samples. Figure redrawn with permission from [159]. 157
Figure A45: Depth profiles obtained for the surface layers from graphite electrodes extracted from NMC622||graphite pouch cells after galvanostatic charge/discharge cycling. Investigation was performed via focused ion beam secondary mass spectrometry equipped with a time of flight analyzer. The figure shows the elemental distribution of the combined Li-species (**a** – **c**), Li_2O (**d** – **f**), Li_2F (**g** – **i**), and of Mn (**j** – **l**), for graphite electrodes cycled in the presence of the BE 2 (1 $_M$ $LiPF_6$ in EC:EMC 3:7 by weight; left), the ClEC-containing electrolyte (center), and the VC-containing electrolyte (right). In addition, images of the surface before and after the performed investigation are depicted (**m** – **o**). Note that due to the similar sample compositions it can be assumed that the thickness of each ablated layer (frame) is similar, enabling the comparison of the investigated samples. Figure redrawn with permission from [159]. 158
Figure A46: Operando SHINER spectra taken from the surface of a NMC622 electrode in the presence of the BE 2 (1 $_M$ $LiPF_6$ in EC:EMC 3:7 by weight). For the SHINERS measurement the NMC622 electrode was connected as working electrode, paired against a graphite counter electrode. In addition, a Li-metal electrode was introduced as reference electrode to monitor the electrodes potential. Galvanostatic charge was performed at a C-rate of C/3. Au SHINs with a diameter of 55 nm were introduced to the electrode surface before cell assembly. Spectra were recorded at different electrode potentials, denoted in the spectra and indicated by the intensity of the color. For spectrum acquisition the samples were excited using a 633 nm laser, adjusted to a power output of 1.05 mW. Spectra were acquired over three accumulations of 35 s. Figure redrawn with permission from [159]. .. 159
Figure A47: Operando SHINER spectra taken from the surface of a NMC622 electrode in the presence of the BE 2 (1 $_M$ $LiPF_6$ in EC:EMC 3:7 by weight) + 0.30 $_M$ VEC. For the SHINERS measurement the NMC622 electrode was connected as working electrode, paired against a graphite counter electrode. In addition, a Li-metal electrode was introduced as reference electrode to monitor the electrodes potential. Galvanostatic charge was performed at a C-rate of C/3. Au SHINs with a diameter of 55 nm were introduced to the electrode surface before cell assembly. Spectra were recorded at different electrode potentials, denoted in the spectra and indicated by the intensity of the color. For spectrum acquisition the samples were excited using a 633 nm laser, adjusted to a power output of 1.05 mW. Spectra were acquired over three accumulations of 35 s. Figure redrawn with permission from [159]. 161
Figure A48: Operando SER spectra taken from the surface of a roughened Au electrode in the presence of the BE 2 (1 $_M$ $LiPF_6$ in EC:EMC 3:7 by weight). For the SERS measurement the Au electrode was connected as working electrode, paired against a Li-metal electrode. The electrode was charged with a sweep rate of 150 µV s^{-1}. Au SHINs with a diameter of 55 nm were introduced to the electrode surface before cell assembly. Spectra were recorded at the open circuit potential (OCP) and the cut-off potential of 4.50 V vs. $Li|Li^+$. For spectrum acquisition the samples were excited using a 633 nm laser, adjusted to a power output of 1.05 mW. Spectra were acquired over three accumulations of 35 s. Figure redrawn with permission from [159]. 163
Figure A49: Operando SER spectra taken from the surface of a roughened Au electrode in the presence of the BE 2 (1 $_M$ $LiPF_6$ in EC:EMC 3:7 by weight) + 0.30 $_M$ VEC. For the SERS measurement the Au electrode was connected as working electrode, paired against a Li-metal electrode. The electrode was charged with a sweep rate of 150 µV s^{-1}. Au SHINs with a diameter of 55 nm were introduced to the electrode surface before cell assembly. Spectra were recorded at different electrode potentials, denoted in the spectra and indicated by the intensity of the color. For spectrum acquisition the samples were excited using a 633 nm

laser, adjusted to a power output of 1.05 mW. Spectra were acquired over three accumulations of 35 s. Figure redrawn with permission from [159]. 165
Figure A50: NMR spectrum recorded obtained from the $^{13}C\{^{1}H\}$ cross polarization magic angle spinning NMR investigation of the synthesized product of the VEC reduction. In the spectrum, prominent peaks are ascribed to characteristic C-species. Figure redrawn with permission from [159]. 167
Figure A51: Comparison of the SER spectra recorded of the surface of a roughened Au electrode in the presence of the BE 2 (1 $_M$ $LiPF_6$ in EC:EMC 3:7 by weight) + 0.30 $_M$ VEC at the cut-off potential of 4.50 V vs. $Li|Li^+$ (**green**) and the SER spectrum recorded from the synthesized VEC reduction product (**red**). To obtain the SER spectrum of the reduction product, the synthesized product was suspended in THF and drop cast on an AgAu SERS substrate. Characteristic bands are highlighted by arrows and band positions are noted in the spectrum. For spectrum acquisition the samples were excited using a 633 nm laser, adjusted to a power output of 1.05 mW. Spectra were acquired over three accumulations of 35 s. Figure redrawn with permission from [159].....168
Figure A52: Reference Raman spectra of pure **a)** EC, **b)** EMC, **c)** FEC, **d)** ClEC, **e)** VC, and **f)** VEC. These reference spectra were used for the assignment of bands during the performed SHINERS and SERS investigations, indicated by "Own Spectrum". For spectrum acquisition the samples were excited using a 532 nm laser, adjusted to a power output of 6.10 mW. Spectra were acquired over three accumulations of 25 s. Figure redrawn with permission from [159]. 169
Figure A53: Reference Raman spectra of pure **a)** DEDOHC, **b)** DMDOHC. These reference spectra were used for the assignment of bands during the performed SHINERS and SERS investigations, indicated by "Own Spectrum". For spectrum acquisition the samples were excited using a 532 nm laser, adjusted to a power output of 6.10 mW. Spectra were acquired over three accumulations of 25 s. Figure redrawn with permission from [159]. ...170

10.3. List of Tables

Table 1: Summary of chemicals and materials used in this thesis, including supplier and purity.....26
Table 2: Necessary volume of $AgNO_3$ solution added to the reaction mixture to achieve formation of Ag NPs with targeted diameters. 34
Table 3: Key data of the galvanostatic charge/discharge investigation of NMC111||graphite coin-cells, cycled in the presence of BE 1 (1 $_M$ $LiPF_6$ in EC:DEC 1:1 by weight) and BE 1 + 0.10 $_M$ THP. Shown are the discharge capacity, the state-of-health (SoH), Coulombic efficiency (CE), and ΔV at selected cycles numbers. Note that the 7th cycle equals the first cycle after formation.....46
Table 4: Key data of the galvanostatic charge/discharge investigation of NMC622||graphite pouch cells, cycled in the presence of the BE 2 (1 $_M$ $LiPF_6$ in EC:EMC 3:7 by weight) and BE 2 + the optimized additive concentrations. Listed are the number of performed cycles until a 50% SoH, the average Coulombic efficiency (CE), the ΔV value at a 50% SoH, and the accumulated specific discharge energies (ADE) recorded at 80% and 50% SoH. Percental changes in the obtained values are calculated in comparison to the BE 2 cells. The shown values were obtained from **Figure 27** and **Figure A33.** Table redrawn with permission from [159]. 77

10.4. List of Appendix Tables

Table A1: Key data of the galvanostatic charge/discharge investigation of NMC811||graphite pouch cells, cycled in the presence of the BE 2 (1 $_M$ $LiPF_6$ in EC:EMC

3:7 by weight) and BE 2 + 0.04 $_M$ additive. Shown are the discharge capacity at the 7th cycle, the discharge capacity at the 200th cycle, and the cycle number at which the respective cells reached a state of health (SoH) of 80%. Note that the 7th cycle equals the first cycle after formation. Percental changes in the obtained values are calculated in comparison to the BE 2 cells. The values shown were obtained from **Figure 17** and **Figure A21**..... 123
Table A2: Key data of the galvanostatic charge/discharge investigation of NMC811||graphite pouch cells, cycled in the presence of the BE 2 (1 $_M$ $LiPF_6$ in EC:EMC 3:7 by weight) and BE 2 + 0.12 $_M$ additive. Shown are the discharge capacity at the 7th cycle, the discharge capacity at the 200th cycle, and the cycle number at which the respective cells reached a state of health (SoH) of 80%. Note that the 7th cycle equals the first cycle after formation. Percental changes in the obtained values are calculated in comparison to the BE 2 cells. The values shown were obtained from **Figure 17** and **Figure A21**..... 124
Table A3: Assignment of bands observed in the SHINER spectra recorded from the surface of a NMC811 electrode in a NMC811||graphite optical cell with a Li-metal reference electrode containing the BE 2 (1 $_M$ $LiPF_6$ in EC:EMC 3:7 by weight) + 0.20 $_M$ 3-THP-BOH at the open circuit potential. Table reproduced with permission from [29]. 133
Table A4: Assignment of bands observed in the SHINER spectra recorded from the surface of a NMC811 electrode in a NMC811||graphite optical cell with a Li-metal reference electrode containing the BE 2 (1 $_M$ $LiPF_6$ in EC:EMC 3:7 by weight) + 0.20 $_M$ 3-THP-BOH at the cut-off potential of 4.50 V vs. Li|Li^+. Table reproduced with permission from [29]. 133
Table A5: Assignment of bands observed in the SHINER spectra recorded from the surface of a NMC811 electrode in a NMC811||graphite optical cell with a Li-metal reference electrode containing the BE 2 (1 $_M$ $LiPF_6$ in EC:EMC 3:7 by weight) at the open circuit potential. Table reproduced with permission from [29]. 134
Table A6: Assignment of bands observed in the SHINER spectra recorded from the surface of a NMC811 electrode in a NMC811||graphite optical cell with a Li-metal reference electrode containing the BE 2 (1 $_M$ $LiPF_6$ in EC:EMC 3:7 by weight) at the cut-off potential of 4.50 V vs. Li|Li^+. Table reproduced with permission from [29]. 135
Table A7: Detailed assignment for the bands observed during the operando SHINERS measurement of the surface of the graphite electrode galvanostatically charged in the presence of the BE 2 (1 $_M$ $LiPF_6$ in EC:EMC 3:7 by weight). The absence of specific bands at selected cell voltages is indicated by empty cells. In these cases, the band was observed at higher or lower cell voltages, respectively. The reference “own spectrum” refers to reference spectra reported in the Appendix chapter. Table redrawn with permission from [159]. 142
Table A8: Detailed assignment for the bands observed during the operando SHINERS measurement of the surface of the graphite electrode galvanostatically charged in the presence of the BE 2 (1 $_M$ $LiPF_6$ in EC:EMC 3:7 by weight) + 0.75 $_M$ FEC. The absence of specific bands at selected cell voltages is indicated by empty cells. In these cases, the band was observed at higher or lower cell voltages, respectively. The reference “own spectrum” refers to reference spectra reported in the Appendix chapter. Table redrawn with permission from [159]. 144
Table A9: Detailed assignment for the bands observed during the operando SHINERS measurement of the surface of the graphite electrode galvanostatically charged in the presence of the BE 2 (1 $_M$ $LiPF_6$ in EC:EMC 3:7 by weight) + 0.75 $_M$ ClEC. The absence of specific bands at selected cell voltages is indicated by empty cells. In these cases, the band was observed at higher or lower cell voltages, respectively. The reference “own spectrum” refers to reference spectra reported in the Appendix chapter. Table redrawn with permission from [159]. 146
Table A10: Detailed assignment for the bands observed during the operando SHINERS measurement of the surface of the graphite electrode galvanostatically charged in the presence of the BE 2 (1 $_M$ $LiPF_6$ in EC:EMC 3:7 by weight) + 0.75 $_M$ VC. The absence of

specific bands at selected cell voltages is indicated by empty cells. In these cases, the band was observed at higher or lower cell voltages, respectively. The reference “own spectrum” refers to reference spectra reported in the Appendix chapter. Table redrawn with permission from [159]. 149
Table A11: Detailed assignment for the bands observed during the operando SHINERS measurement of the surface of the graphite electrode galvanostatically charged in the presence of the BE 2 (1 $_M$ $LiPF_6$ in EC:EMC 3:7 by weight) + 0.30 $_M$ VEC. The absence of specific bands at selected cell voltages is indicated by empty cells. In these cases, the band was observed at higher or lower cell voltages, respectively. The reference “own spectrum” refers to reference spectra reported in the Appendix chapter. Table redrawn with permission from [159]. 151
Table A12: Denotation of the calculated Raman shifts for the ring-opened VEC molecule after reduction and the assigned vibrations of the molecule. Note that the calculated Raman shifts were scaled by a factor of 1.08. Table redrawn with permission from [159]. 152
Table A13: Detailed assignment for the bands observed during the operando SHINERS measurement of the surface of the NMC622 electrode galvanostatically charged in the presence of the BE 2 (1 $_M$ $LiPF_6$ in EC:EMC 3:7 by weight). The absence of specific bands at selected cell voltages is indicated by empty cells. In these cases, the band was observed at higher or lower cell voltages, respectively. The reference “own spectrum” refers to reference spectra reported in the Appendix chapter. Table redrawn with permission from [159]. 160
Table A14: Detailed assignment for the bands observed during the operando SHINERS measurement of the surface of the NMC622 electrode galvanostatically charged in the presence of the BE 2 (1 $_M$ $LiPF_6$ in EC:EMC 3:7 by weight) + 0.30 $_M$ VEC. The absence of specific bands at selected cell voltages is indicated by empty cells. In these cases, the band was observed at higher or lower cell voltages, respectively. The reference “own spectrum” refers to reference spectra reported in the Appendix chapter. Table redrawn with permission from [159]. 161
Table A15: Detailed assignment for the bands observed during the operando SERS measurement of the surface of the Au electrode galvanostatically charged in the presence of the BE 2 (1 $_M$ $LiPF_6$ in EC:EMC 3:7 by weight). The absence of specific bands at selected cell voltages is indicated by empty cells. In these cases, the band was observed at higher or lower cell voltages, respectively. The reference “own spectrum” refers to reference spectra reported in the Appendix chapter. Table redrawn with permission from [159]. 164
Table A16: Detailed assignment for the bands observed during the operando SERS measurement of the surface of the Au electrode galvanostatically charged in the presence of the BE 2 (1 $_M$ $LiPF_6$ in EC:EMC 3:7 by weight) + 0.30 $_M$ VEC. The absence of specific bands at selected cell voltages is indicated by empty cells. In these cases, the band was observed at higher or lower cell voltages, respectively. The reference “own spectrum” refers to reference spectra reported in the Appendix chapter. Table redrawn with permission from [159]. 165

10.5. List of Abbreviations

3-THP-BOH ..... 3-thiophene boronic acid
ADE ..... Accumulated specific discharge energy
AFM ..... Atomic force microscopy
BE ..... Baseline electrolyte
CC ..... Constant current
CCCV ..... Constant current/constant voltage

CE ..... Coulombic efficiency, Counter Electrode
CEI ..... Cathode-electrolyte interphase
CP-MAS ..... Cross polarization magic angle spinning
CV ..... Cyclic voltammetry
DEC ..... Diethyl carbonate
DEDOHC ..... Diethyl-2,5-dioxahexane carboxylate
DFT ..... Density functional theory
DMC ..... Dimethyl carbonate
EC ..... Ethylene carbonate
EDX ..... Electron dispersive X-ray spectroscopy
EIS ..... Electrochemical impedance spectroscopy
EMC ..... Ethyl methyl carbonate
FEC ..... Fluoroethylene carbonate
FIB-SIMS ..... Focused ion beam – secondary ion mass spectrometry
GC ..... Gas chromatography
HRAM ..... High resolution-accurate mass
IR ..... Infrared
LBDC ..... Dilithium butylene dicarbonate
LEC ..... Lithium ethylcarbonate
LEDC ..... Dilithium ethylene dicarbonate
LEMC ..... Lithium ethylene mono-carbonate
LIB ..... Lithium-ion batteries
LiDFP ..... Lithium difluorophosphate
LMC ..... Lithium methylcarbonate
LNMO ..... $LiNi_xMn_yO_z$
LSPR ..... Localized surface plasmon resonance
MS ..... Mass spectrometry
NERS ..... Nanoparticle enhanced Raman spectroscopy
NMC ..... $LiNi_xCo_yMn_zO_2$
NMR ..... Nuclear magnetron resonance
NP ..... Nanoparticle
OCP ..... Open circuit potential
OHC ..... Oxa-hexane carboxylates
PEO ..... Polyethylene oxide
poly(3-THP-BOH) ..... Poly(3-thiophene boronic acid)
poly(THP) ..... Polythiophene
QC ..... Quantum chemistry
RE ..... Refrence Electrode
SEI ..... Solid-electrolyte interphase
SEM ..... Scanning electron microscopy
SERS ..... Surface enhanced Raman spectroscopy
SHINERS ..... Shell-isolated nanoparticle enhanced Raman spectroscopy
SoH ..... State-of-health
SOTA ..... State-of-the-art
TEM ..... Transmission electron microscopy
TERS ..... Tip-enhanced Raman spectroscopy
THP ..... Thiophene
TM ..... Transition metal
TOF ..... Time-of-flight
VC ..... Vinylene carbonate
VEC ..... Vinylethylene carbonate
WE ..... Working electrode
XPS ..... X-ray photoelectron spectroscopy

10.6. Licenses

For this thesis selected figures were readapted from other publications. Licenses were acquired beforehand.

License Number	5862410047771
License date	Sep 05, 2024
Licensed Content Publisher	Springer Nature
Licensed Content Publication	Nature Reviews, Physics
Licensed Content Title	Fundamental understanding and applications of plasmon-enhanced Raman spectroscopy
Licensed Content Author	Xiang Wang et al.[133]
Licensed Content Date	Apr 27, 2020

No licenses were acquired for figures reproduced or adapted from first author publications of the author of this thesis, as all these publications are open access articles distributed under the CC BY license, permitting unrestricted use, distribution, and reproduction in any medium.[28,29,159]

11. References

[1] Yaghmaeii, N., van Leonhout, J., Below, R., Guha-Sapir, D., McClean, D. Human Cost of Disasters: An Overview of the Last 20 Years 2000-2019. 1st ed.; *United Nations Publications* **2020**.

[2] Crippa, M., Guizzardi, D., Pagani, F., Banja, M., Muntean, M., Schaaf E., Becker, W., Monforti-Ferrario, F., Quadrelli, R., Risquez Martin, A., Taghavi-Moharamli, P., Köykkä, J., Grassi, G., Rossi, S., Brandao De Melo, J., Oom, D., Branco, A., San-Miguel, J., Vignati, E. GHG emissions of all world countries: 2023. *Publications Office of the European Union* **2023**.

[3] Fedorov, R. G.; Maletti, S.; Heubner, C.; Michaelis, A.; Ein-Eli, Y. Molecular Engineering Approaches to Fabricate Artificial Solid-Electrolyte Interphases on Anodes for Li-Ion Batteries: A Critical Review. *Advanced Energy Materials* **2021**, *11*, 2101173.

[4] Li, F.-S.; Wu, Y.-S.; Chou, J.; Winter, M.; Wu, N.-L. A mechanically robust and highly ion-conductive polymer-blend coating for high-power and long-life lithium-ion battery anodes. *Advanced Materials* **2015**, *27*, 130–137.

[5] Yu, X.; Manthiram, A. Electrode–electrolyte interfaces in lithium-based batteries. *Energy Environmental Science* **2018**, *11*, 527–543.

[6] Adenusi, H.; Chass, G. A.; Passerini, S.; Tian, K. V.; Chen, G. Lithium Batteries and the Solid Electrolyte Interphase (SEI)—Progress and Outlook. *Advanced Energy Materials* **2023**, *13*, 2203307.

[7] Zhang, H.; Zhao, H.; Khan, M. A.; Zou, W.; Xu, J.; Zhang, L.; Zhang, J. Recent progress in advanced electrode materials, separators and electrolytes for lithium batteries. *Journal of Materials Chemistry A* **2018**, *6*, 20564–20620.

[8] Hu, M.; Pang, X.; Zhou, Z. Recent progress in high-voltage lithium ion batteries. *Journal of Power Sources* **2013**, *237*, 229–242.

[9] Armand, M.; Tarascon, J.-M. Building better batteries. *Nature* **2008**, *451*, 652–657.

[10] Fan, X.; Wang, C. High-voltage liquid electrolytes for Li batteries: progress and perspectives. *Chemical Society Reviews* **2021**, *50*, 10486–10566.

[11] Shen, X.; Zhang, X.-Q.; Ding, F.; Huang, J.-Q.; Xu, R.; Chen, X.; Yan, C.; Su, F.; Chen, C.; Liu, X.*; et al.* Advanced Electrode Materials in Lithium Batteries: Retrospect and Prospect. *American Association for the Advancement of Science,* **2021**.

[12] Zhou, L.; Zhang, K.; Hu, Z.; Tao, Z.; Mai, L.; Kang, Y.-M.; Chou, S.-L.; Chen, J. Recent Developments on and Prospects for Electrode Materials with Hierarchical Structures for Lithium-Ion Batteries. *Advanced Energy Materials* **2018**, *8*, 1701415.

[13] Jin, Y.; Kneusels, N.-J. H.; Marbella, L. E.; Castillo-Martínez, E.; Magusin, P. C. M. M.; Weatherup, R. S.; Jónsson, E.; Liu, T.; Paul, S.; Grey, C. P. Understanding Fluoroethylene Carbonate and Vinylene Carbonate Based Electrolytes for Si Anodes in Lithium Ion Batteries with NMR Spectroscopy. *Journal of the American Chemical Society* **2018**, *140*, 9854–9867.

[14] Li, J.; Dudney, N. J.; Nanda, J.; Liang, C. Artificial solid electrolyte interphase to address the electrochemical degradation of silicon electrodes. *ACS Applied Materials & Interfaces* **2014**, *6*, 10083–10088.

[15] Reyes Jiménez, A.; Nölle, R.; Wagner, R.; Hüsker, J.; Kolek, M.; Schmuch, R.; Winter, M.; Placke, T. A step towards understanding the beneficial influence of a LIPON-based artificial SEI on silicon thin film anodes in lithium-ion batteries. *Nanoscale* **2018**, *10*, 2128–2137.

[16] Schmuch, R.; Wagner, R.; Hörpel, G.; Placke, T.; Winter, M. Performance and cost of materials for lithium-based rechargeable automotive batteries. *Nature Energy* **2018**, *3*, 267–278.

[17] Song, H. J.; Jang, S. H.; Ahn, J.; Oh, S. H.; Yim, T. Artificial cathode-electrolyte interphases on nickel-rich cathode materials modified by silyl functional group. *Journal of Power Sources* **2019**, *416*, 1–8.
[18] Jang, S. H.; Lee, K.-J.; Mun, J.; Han, Y.-K.; Yim, T. Chemically-induced cathode–electrolyte interphase created by lithium salt coating on Nickel-rich layered oxides cathode. *Journal of Power Sources* **2019**, *410-411*, 15–24.
[19] Fu, W.; Kim, D.; Wang, F.; Yushin, G. Stabilizing cathodes and interphases for next-generation Li-ion batteries. *Journal of Power Sources* **2023**, *561*, 232738.
[20] Klein, S.; van Wickeren, S.; Röser, S.; Bärmann, P.; Borzutzki, K.; Heidrich, B.; Börner, M.; Winter, M.; Placke, T.; Kasnatscheew, J. Understanding the Outstanding High-Voltage Performance of NCM523||Graphite Lithium Ion Cells after Elimination of Ethylene Carbonate Solvent from Conventional Electrolyte. *Advanced Energy Materials* **2021**, *11.*
[21] Klein, S.; Haneke, L.; Harte, P.; Stolz, L.; van Wickeren, S.; Borzutzki, K.; Nowak, S.; Winter, M.; Placke, T.; Kasnatscheew, J. Suppressing Electrode Crosstalk and Prolonging Cycle Life in High-Voltage Li Ion Batteries: Pivotal Role of Fluorophosphates in Electrolytes. *ChemElectroChem* **2022**, *9.*
[22] Tan, S.; Ji, Y. J.; Zhang, Z. R.; Yang, Y. Recent progress in research on high-voltage electrolytes for lithium-ion batteries. *ChemPhysChem* **2014**, *15*, 1956–1969.
[23] Kühn, S. P.; Edström, K.; Winter, M.; Cekic-Laskovic, I. Face to Face at the Cathode Electrolyte Interphase: From Interface Features to Interphase Formation and Dynamics. *Advanced Materials Interfaces* **2022**, *9*, 2102078.
[24] Xu, K. Electrolytes and interphases in Li-ion batteries and beyond. *Chemical Reviews* **2014**, *114*, 11503–11618.
[25] Michan, A. L.; Parimalam, B. S.; Leskes, M.; Kerber, R. N.; Yoon, T.; Grey, C. P.; Lucht, B. L. Fluoroethylene Carbonate and Vinylene Carbonate Reduction: Understanding Lithium-Ion Battery Electrolyte Additives and Solid Electrolyte Interphase Formation. *Chemistry of Materials* **2016**, *28*, 8149–8159.
[26] Sungjemmenla; S. K., V.; Soni, C. B.; Kumar, V.; Seh, Z. W. Understanding the Cathode–Electrolyte Interphase in Lithium-Ion Batteries. *Energy Technology* **2022**, *10*, 2200421.
[27] Maibach, J.; Rizell, J.; Matic, A.; Mozhzhukhina, N. Toward Operando Characterization of Interphases in Batteries. *ACS Materials Letters* **2023**, *5*, 2431–2444.
[28] Pfeiffer, F.; Diddens, D.; Weiling, M.; Baghernejad, M. Study of a High-Voltage NMC Interphase in the Presence of a Thiophene Additive Realized by Operando SHINERS. *ACS Applied Materials & Interfaces* **2023**, *15*, 6676–6686.
[29] Pfeiffer, F.; Diddens, D.; Weiling, M.; Frankenstein, L.; Kühn, S.; Cekic-Laskovic, I.; Baghernejad, M. Quadrupled Cycle Life of High-Voltage Nickel-Rich Cathodes: Understanding the Effective Thiophene-Boronic Acid-Based CEI via Operando SHINERS. *Advanced Energy Materials* **2023**, *13*, 2300827.
[30] Weiling, M.; Pfeiffer, F.; Baghernejad, M. Vibrational Spectroscopy Insight into the Electrode|electrolyte Interface/Interphase in Lithium Batteries. *Advanced Energy Materials* **2022**, *12.*
[31] Kühn, S. P.; Pfeiffer, F.; Bela, M.; Rodehorst, U.; Weintz, D.; Stan, M.; Baghernejad, M.; Winter, M.; Cekic-Laskovic, I. Back to the basics: Advanced understanding of the as-defined solid electrolyte interphase on lithium metal electrodes. *Journal of Power Sources* **2022**, *549*, 232118.
[32] Gajan, A.; Lecourt, C.; Torres Bautista, B. E.; Fillaud, L.; Demeaux, J.; Lucas, I. T. Solid Electrolyte Interphase Instability in Operating Lithium-Ion Batteries Unraveled by Enhanced-Raman Spectroscopy. *ACS Energy Letters* **2021**, *6*, 1757–1763.

[33] Lin, X.-D.; Uzayisenga, V.; Li, J.-F.; Fang, P.-P.; Wu, D.-Y.; Ren, B.; Tian, Z.-Q. Synthesis of ultrathin and compact Au@MnO 2 nanoparticles for shell-isolated nanoparticle-enhanced Raman spectroscopy (SHINERS). *Journal of Raman Spectroscopy* **2012**, *43*, 40–45.
[34] Tian, X.-D.; Liu, B.-J.; Li, J.-F.; Yang, Z.-L.; Ren, B.; Tian, Z.-Q. SHINERS and plasmonic properties of Au Core SiO 2 shell nanoparticles with optimal core size and shell thickness. *Journal of Raman Spectroscopy* **2013**, *44*, 994–998.
[35] Pfisterer, J. H. K.; Baghernejad, M.; Giuzio, G.; Domke, K. F. Reactivity mapping of nanoscale defect chemistry under electrochemical reaction conditions. *Nature Communications* **2019**, *10*, 5702.
[36] Winter, M.; Besenhard, J. O.; Spahr, M. E.; Novák, P. Insertion Electrode Materials for Rechargeable Lithium Batteries. *Advanced Materials* **1998**, *10*, 725–763.
[37] Guyomard, D.; Tarascon, J. M. The carbon/Li1+xMn2O4 system. *Solid State Ionics* **1994**, *69*, 222–237.
[38] Nitta, N.; Wu, F.; Lee, J. T.; Yushin, G. Li-ion battery materials: present and future. *Materials Today* **2015**, *18*, 252–264.
[39] Deimede, V.; Elmasides, C. Separators for Lithium-Ion Batteries: A Review on the Production Processes and Recent Developments. *Energy Technology* **2015**, *3*, 453–468.
[40] Irfan, M.; Atif, M.; Yang, Z.; Zhang, W. Recent advances in high performance conducting solid polymer electrolytes for lithium-ion batteries. *Journal of Power Sources* **2021**, *486*, 229378.
[41] Fan, P.; Liu, H.; Marosz, V.; Samuels, N. T.; Suib, S. L.; Sun, L.; Liao, L. High Performance Composite Polymer Electrolytes for Lithium-Ion Batteries. *Advanced Functional Materials* **2021**, *31*, 2101380.
[42] Long, L.; Wang, S.; Xiao, M.; Meng, Y. Polymer electrolytes for lithium polymer batteries. *Journal of Materials Chemistry A* **2016**, *4*, 10038–10069.
[43] Berg, C.; Morasch, R.; Graf, M.; Gasteiger, H. A. Comparison of Silicon and Graphite Anodes: Temperature-Dependence of Impedance Characteristics and Rate Performance. *Journal of the Electrochemical Society* **2023**, *170*, 30534.
[44] Zhang, S. S. Is Li/Graphite Half-Cell Suitable for Evaluating Lithiation Rate Capability of Graphite Electrode? *Journal of the Electrochemical Society* **2020**, *167*, 100510.
[45] Horstmann, B.; Single, F.; Latz, A. Review on multi-scale models of solid-electrolyte interphase formation. *Current Opinion in Electrochemistry* **2019**, *13*, 61–69.
[46] Kang, D.; Xiao, M.; Lemmon, J. P. Artificial Solid-Electrolyte Interphase for Lithium Metal Batteries. *Batteries & Supercaps* **2021**, *4*, 445–455.
[47] Xu, K. Interfaces and interphases in batteries. *Journal of Power Sources* **2023**, *559*, 232652.
[48] Li, N.-W.; Yin, Y.-X.; Yang, C.-P.; Guo, Y.-G. An Artificial Solid Electrolyte Interphase Layer for Stable Lithium Metal Anodes. *Advanced Materials* **2016**, *28*, 1853–1858.
[49] Ko, M.; Chae, S.; Cho, J. Challenges in Accommodating Volume Change of Si Anodes for Li-Ion Batteries. *ChemElectroChem* **2015**, *2*, 1645–1651.
[50] Li, J.; Baggetto, L.; Martha, S. K.; Veith, G. M.; Nanda, J.; Liang, C.; Dudney, N. J. An Artificial Solid Electrolyte Interphase Enables the Use of a LiNi 0.5 Mn 1.5 O 4 5 V Cathode with Conventional Electrolytes. *Advanced Energy Materials* **2013**, *3*, 1275–1278.
[51] Li, J.; Yang, J.; Ji, Z.; Su, M.; Li, H.; Wu, Y.; Su, X.; Zhang, Z. Prospective Application, Mechanism, and Deficiency of Lithium Bis(oxalate)Borate as the Electrolyte Additive for Lithium-Batteries. *Advanced Energy Materials* **2023**, *13*, 2301422.
[52] Kim, Y.; Dudney, N. J.; Chi, M.; Martha, S. K.; Nanda, J.; Veith, G. M.; Liang, C. A Perspective on Coatings to Stabilize High-Voltage Cathodes: LiMn 1.5 Ni 0.5 O 4 with

Sub-Nanometer Lipon Cycled with LiPF 6 Electrolyte. *Journal of the Electrochemical Society* **2013**, *160*, A3113-A3125.
[53] Kubot, M.; Frankenstein, L.; Muschiol, E.; Klein, S.; Esselen, M.; Winter, M.; Nowak, S.; Kasnatscheew, J. Lithium Difluorophosphate: A Boon for High Voltage Li Ion Batteries and a Bane for High Thermal Stability/Low Toxicity: Towards Synergistic Dual Additives to Circumvent this Dilemma. *ChemSusChem* **2023**, *16*, e202202189.
[54] Li, H.; Guo, S.; Zhou, H. In-situ/operando characterization techniques in lithium-ion batteries and beyond. *Journal of Energy Chemistry* **2021**, *59*, 191–211.
[55] Xu, R.; Zhang, X.-Q.; Cheng, X.-B.; Peng, H.-J.; Zhao, C.-Z.; Yan, C.; Huang, J.-Q. Artificial Soft–Rigid Protective Layer for Dendrite-Free Lithium Metal Anode. *Advanced Functional Materials* **2018**, *28*, 1705838.
[56] Xu, R.; Xiao, Y.; Zhang, R.; Cheng, X.-B.; Zhao, C.-Z.; Zhang, X.-Q.; Yan, C.; Zhang, Q.; Huang, J.-Q. Dual-Phase Single-Ion Pathway Interfaces for Robust Lithium Metal in Working Batteries. *Advanced Materials* **2019**, *31*, e1808392.
[57] Wang, G.; Chen, C.; Chen, Y.; Kang, X.; Yang, C.; Wang, F.; Liu, Y.; Xiong, X. Self-Stabilized and Strongly Adhesive Supramolecular Polymer Protective Layer Enables Ultrahigh-Rate and Large-Capacity Lithium-Metal Anode. *Angewandte Chemie* **2020**, *59*, 2055–2060.
[58] Adair, K. R.; Zhao, C.; Banis, M. N.; Zhao, Y.; Li, R.; Cai, M.; Sun, X. Highly Stable Lithium Metal Anode Interface via Molecular Layer Deposition Zircone Coatings for Long Life Next-Generation Battery Systems. *Angewandte Chemie* **2019**, *131*, 15944–15949.
[59] Sun, Y.; Zhao, Y.; Wang, J.; Liang, J.; Wang, C.; Sun, Q.; Lin, X.; Adair, K. R.; Luo, J.; Wang, D.*; et al.* A Novel Organic "Polyurea" Thin Film for Ultralong-Life Lithium-Metal Anodes via Molecular-Layer Deposition. *Advanced Materials* **2019**, *31*, e1806541.
[60] Zhao, Y.; Goncharova, L. V.; Sun, Q.; Li, X.; Lushington, A.; Wang, B.; Li, R.; Dai, F.; Cai, M.; Sun, X. Robust Metallic Lithium Anode Protection by the Molecular-Layer-Deposition Technique. *Small Methods* **2018**, *2.*
[61] Kazyak, E.; Wood, K. N.; Dasgupta, N. P. Improved Cycle Life and Stability of Lithium Metal Anodes through Ultrathin Atomic Layer Deposition Surface Treatments. *Chemistry of Materials* **2015**, *27*, 6457–6462.
[62] Wang, L.; Wang, Q.; Jia, W.; Chen, S.; Gao, P.; Li, J. Li metal coated with amorphous Li3PO4 via magnetron sputtering for stable and long-cycle life lithium metal batteries. *Journal of Power Sources* **2017**, *342*, 175–182.
[63] Wang, C.; Xie, Y.; Huang, Y.; Zhou, S.; Xie, H.; Jin, H.; Ji, H. Li 3 PO 4 -Enriched SEI on Graphite Anode Boosts Li + De-Solvation Enabling Fast-Charging and Low-Temperature Lithium-Ion Batteries. *Angewandte Chemie* **2024**, *136.*
[64] Li, S.; Wu, J.; Li, J.; Liu, G.; Cui, Y.; Liu, H. Facilitated Coating of Li 3 PO 4 on the Rough Surface of LiNi 0.85 Co 0.1 Mn 0.05 O 2 Cathodes by Synchronous Lithiation. *ACS Applied Energy Materials* **2021**, *4*, 2257–2265.
[65] Wang, L.; Zhang, L.; Wang, Q.; Li, W.; Wu, B.; Jia, W.; Wang, Y.; Li, J.; Li, H. Long lifespan lithium metal anodes enabled by Al2O3 sputter coating. *Energy Storage Materials* **2018**, *10*, 16–23.
[66] Girard, G. M. A.; Wang, X.; Yunis, R.; MacFarlane, D. R.; Bhattacharyya, A. J.; Forsyth, M.; Howlett, P. C. Sustainable, Dendrite Free Lithium-Metal Electrode Cycling Achieved with Polymer Composite Electrolytes Based on a Poly(Ionic Liquid) Host. *Batteries & Supercaps* **2019**, *2*, 229–239.
[67] Sun, S.; Myung, S.; Kim, G.; Lee, D.; Son, H.; Jang, M.; Park, E.; Son, B.; Jung, Y.-G.; Paik, U.*; et al.* Facile ex situ formation of a LiF–polymer composite layer as an artificial SEI layer on Li metal by simple roll-press processing for carbonate electrolyte-based Li metal batteries. *Journal of Materials Chemistry A* **2020**, *8*, 17229–17237.

[68] Wang, Y.; Ren, L.; Liu, J.; Lu, X.; Wang, Q.; Zhou, M.; Liu, W.; Sun, X. In Situ Construction of Composite Artificial Solid Electrolyte Interphase for High-Performance Lithium Metal Batteries. *ACS Applied Materials & Interfaces* **2022**, *14*, 50982–50991.
[69] Ui, K.; Kikuchi, S.; Mikami, F.; Kadoma, Y.; Kumagai, N. Improvement of electrochemical characteristics of natural graphite negative electrode coated with polyacrylic acid in pure propylene carbonate electrolyte. *Journal of Power Sources* **2007**, *173*, 518–521.
[70] Schroder, K.; Alvarado, J.; Yersak, T. A.; Li, J.; Dudney, N.; Webb, L. J.; Meng, Y. S.; Stevenson, K. J. The Effect of Fluoroethylene Carbonate as an Additive on the Solid Electrolyte Interphase on Silicon Lithium-Ion Electrodes. *Chemistry of Materials* **2015**, *27*, 5531–5542.
[71] El Ouatani, L.; Dedryvère, R.; Siret, C.; Biensan, P.; Reynaud, S.; Iratçabal, P.; Gonbeau, D. The Effect of Vinylene Carbonate Additive on Surface Film Formation on Both Electrodes in Li-Ion Batteries. *Journal of the Electrochemical Society* **2009**, *156*, A103.
[72] Ota, H.; Sakata, Y.; Inoue, A.; Yamaguchi, S. Analysis of Vinylene Carbonate Derived SEI Layers on Graphite Anode. *Journal of the Electrochemical Society* **2004**, *151*, A1659.
[73] Kamikawa, Y.; Amezawa, K.; Terada, K. First-Principles Study on the Mechanical Properties of Polymers Formed by the Electrochemical Reduction of Fluoroethylene Carbonate and Vinylene Carbonate. *The Journal of Physical Chemistry C* **2020**, *124*, 19937–19944.
[74] Olana, B. N.; Adem, L. H.; Lin, S. D.; Hwang, B.-J.; Hsieh, Y.-C.; Brunklaus, G.; Winter, M. In Situ Diffuse Reflectance Infrared Fourier-Transform Spectroscopy Investigation of Fluoroethylene Carbonate and Lithium Difluorophosphate Dual Additives in SEI Formation over Cu Anode. *ACS Applied Energy Materials* **2023**, *6*, 4800–4809.
[75] Nakai, H.; Kubota, T.; Kita, A.; Kawashima, A. Investigation of the Solid Electrolyte Interphase Formed by Fluoroethylene Carbonate on Si Electrodes. *Journal of the Electrochemical Society* **2011**, *158*, A798-A801.
[76] Jaumann, T.; Balach, J.; Langklotz, U.; Sauchuk, V.; Fritsch, M.; Michaelis, A.; Teltevskij, V.; Mikhailova, D.; Oswald, S.; Klose, M.*; et al.* Lifetime vs. rate capability: Understanding the role of FEC and VC in high-energy Li-ion batteries with nano-silicon anodes. *Energy Storage Materials* **2017**, *6*, 26–35.
[77] Lee, Y.-S.; Lee, K.-S.; Sun, Y.-K.; Lee, Y. M.; Kim, D.-W. Effect of an organic additive on the cycling performance and thermal stability of lithium-ion cells assembled with carbon anode and LiNi1/3Co1/3Mn1/3O2 cathode. *Journal of Power Sources* **2011**, *196*, 6997–7001.
[78] Lin, H. B.; Huang, W. Z.; Rong, H. B.; Mai, S. W.; Hu, J. N.; Xing, L. D.; Xu, M. Q.; Li, W. S. Improving cyclic stability and rate capability of LiNi0.5Mn1.5O4 cathode via protective film and conductive polymer formed from thiophene. *Journal of Solid State Electrochemistry* **2015**, *19*, 1123–1132.
[79] Zheng, Y.; Fang, W.; Zheng, H.; Su, Y.; Liang, X.; Chen, C.; Xiang, H. A Multifunctional Thiophene-Based Electrolyte Additive for Lithium Metal Batteries Using High-Voltage LiCoO 2 Cathode. *Journal of the Electrochemical Society* **2019**, *166*, A3222-A3227.
[80] Chae, B.-J.; Park, J. H.; Song, H. J.; Jang, S. H.; Jung, K.; Park, Y. D.; Yim, T. Thiophene-initiated polymeric artificial cathode-electrolyte interface for Ni-rich cathode material. *Electrochimica Acta* **2018**, *290*, 465–473.
[81] Zhu, Y.; Luo, X.; Zhi, H.; Liao, Y.; Xing, L.; Xu, M.; Liu, X.; Xu, K.; Li, W. Diethyl(thiophen-2-ylmethyl)phosphonate: a novel multifunctional electrolyte additive for high voltage batteries. *Journal of Materials Chemistry A* **2018**, *6*, 10990–11004.
[82] Zhou, K.; Quan, L.; Zhou, H.; Che, Y.; Li, X.; Chen, Q.; Li, W.; Xu, M. Construction of highly stable and fast kinetic interfacial films on the electrodes of

graphite//LiNi0.5Mn1.5O4 cells by introducing a novel additive of 2-thiophene boric acid (2-TPBA). *Journal of Power Sources* **2023**, *564*, 232848.
[83] Wang, A.; Wang, L.; Liang, H.; Song, Y.; He, Y.; Wu, Y.; Ren, D.; Zhang, B.; He, X. Lithium Difluorophosphate as a Widely Applicable Additive to Boost Lithium-Ion Batteries: a Perspective. *Advanced Functional Materials* **2023**, *33.*
[84] Wang, Y.; Zhang, Y.; Wang, S.; Dong, S.; Dang, C.; Hu, W.; Yu, D. Y. W. Ultrafast Charging and Stable Cycling Dual-Ion Batteries Enabled via an Artificial Cathode–Electrolyte Interface. *Advanced Functional Materials* **2021**, *31*, 2102360.
[85] Benayad, A.; Morales-Ugarte, J. E.; Santini, C. C.; Bouchet, R. Operando XPS: A Novel Approach for Probing the Lithium/Electrolyte Interphase Dynamic Evolution. *The Journal of Physical Chemistry. A* **2021**, *125*, 1069–1081.
[86] Atkins, D.; Ayerbe, E.; Benayad, A.; Capone, F. G.; Capria, E.; Castelli, I. E.; Cekic-Laskovic, I.; Ciria, R.; Dudy, L.; Edström, K.*; et al.* Understanding Battery Interfaces by Combined Characterization and Simulation Approaches: Challenges and Perspectives. *Advanced Energy Materials* **2022**, *12*, 2102687.
[87] Dietrich, P.; Gehrlein, L.; Maibach, J.; Thissen, A. Probing Lithium-Ion Battery Electrolytes with Laboratory Near-Ambient Pressure XPS. *Crystals* **2020**, *10*, 1056.
[88] Wi, S.; Shutthanandan, V.; Sivakumar, B. M.; Thevuthasan, S.; Prabhakaran, V.; Roy, S.; Karakoti, A.; Murugesan, V. In situ x-ray photoelectron spectroscopy analysis of electrochemical interfaces in battery: Recent advances and remaining challenges. *Journal of Vacuum Science & Technology A* **2022**, *40.*
[89] Lu, Y.-C.; Crumlin, E. J.; Carney, T. J.; Baggetto, L.; Veith, G. M.; Dudney, N. J.; Liu, Z.; Shao-Horn, Y. Influence of Hydrocarbon and CO 2 on the Reversibility of Li–O 2 Chemistry Using In Situ Ambient Pressure X-ray Photoelectron Spectroscopy. *The Journal of Physical Chemistry C* **2013**, *117*, 25948–25954.
[90] Etxebarria, A.; Yun, D.-J.; Blum, M.; Ye, Y.; Sun, M.; Lee, K.-J.; Su, H.; Muñoz-Márquez, M. Á.; Ross, P. N.; Crumlin, E. J. Revealing In Situ Li Metal Anode Surface Evolution upon Exposure to CO2 Using Ambient Pressure X-Ray Photoelectron Spectroscopy. *ACS Applied Materials & Interfaces* **2020**, *12*, 26607–26613.
[91] Wood, K. N.; Teeter, G. XPS on Li-Battery-Related Compounds: Analysis of Inorganic SEI Phases and a Methodology for Charge Correction. *ACS Applied Energy Materials* **2018**, *1*, 4493–4504.
[92] Niehoff, P.; Passerini, S.; Winter, M. Interface investigations of a commercial lithium ion battery graphite anode material by sputter depth profile X-ray photoelectron spectroscopy. *Langmuir : The ACS Journal of Surfaces and Colloids* **2013**, *29*, 5806–5816.
[93] Stockhausen, R.; Gehrlein, L.; Müller, M.; Bergfeldt, T.; Hofmann, A.; Müller, F. J.; Maibach, J.; Ehrenberg, H.; Smith, A. Investigating the dominant decomposition mechanisms in lithium-ion battery cells responsible for capacity loss in different stages of electrochemical aging. *Journal of Power Sources* **2022**, *543*, 231842.
[94] Sarkar, A.; Shrotriya, P.; Nlebedim, I. C. Anodic Interfacial Evolution in Extremely Fast Charged Lithium-Ion Batteries. *ACS Applied Energy Materials* **2022**, *5*, 3179–3188.
[95] Ghaur, A.; Peschel, C.; Dienwiebel, I.; Haneke, L.; Du, L.; Profanter, L.; Gomez-Martin, A.; Winter, M.; Nowak, S.; Placke, T. Effective SEI Formation via Phosphazene-Based Electrolyte Additives for Stabilizing Silicon-Based Lithium-Ion Batteries. *Advanced Energy Materials* **2023**, *13.*
[96] Wu, Z.-Y.; Deng, L.; Li, J.-T.; Zanna, S.; Seyeux, A.; Huang, L.; Sun, S.-G.; Marcus, P.; Światowska, J. Solid Electrolyte Interphase Layer Formation on the Si-Based Electrodes with and without Binder Studied by XPS and ToF-SIMS Analysis. *Batteries* **2022**, *8*, 271.

[97] Heidrich, B.; Börner, M.; Winter, M.; Niehoff, P. Quantitative determination of solid electrolyte interphase and cathode electrolyte interphase homogeneity in multi-layer lithium ion cells. *Journal of Energy Storage* **2021**, *44*, 103208.
[98] Lee, S.-H.; Jo, I.-S.; Kim, J. Surface analysis of the solid electrolyte interface formed by additives on graphite electrodes in Li-ion batteries using XPS, FE-AES, and XHR-SEM techniques. *Surface & Interface Analysis* **2014**, *46*, 570–576.
[99] Shobukawa, H.; Alvarado, J.; Yang, Y.; Meng, Y. S. Electrochemical performance and interfacial investigation on Si composite anode for lithium ion batteries in full cell. *Journal of Power Sources* **2017**, *359*, 173–181.
[100] Gunnarsdóttir, A. B.; Amanchukwu, C. V.; Menkin, S.; Grey, C. P. Noninvasive In Situ NMR Study of "Dead Lithium" Formation and Lithium Corrosion in Full-Cell Lithium Metal Batteries. *Journal of the American Chemical Society* **2020**, *142*, 20814–20827.
[101] Hsieh, Y.-C.; Leißing, M.; Nowak, S.; Hwang, B.-J.; Winter, M.; Brunklaus, G. Quantification of Dead Lithium via In Situ Nuclear Magnetic Resonance Spectroscopy. *Cell Reports Physical Science* **2020**, *1*, 100139.
[102] Lin, X.; Shen, Y.; Yu, Y.; Huang, Y. In Situ NMR Verification for Stacking Pressure-Induced Lithium Deposition and Dead Lithium in Anode-Free Lithium Metal Batteries. *Advanced Energy Materials* **2024**, *14.*
[103] Hsieh, Y.-C.; Thienenkamp, J. H.; Huang, C.-J.; Tao, H.-C.; Rodehorst, U.; Hwang, B. J.; Winter, M.; Brunklaus, G. Revealing the Impact of Film-Forming Electrolyte Additives on Lithium Metal Batteries via Solid-State NMR/MRI Analysis. *Journal of Physical Chemistry C* **2021**, *125*, 252–265.
[104] Wang, L.; Menakath, A.; Han, F.; Wang, Y.; Zavalij, P. Y.; Gaskell, K. J.; Borodin, O.; Iuga, D.; Brown, S. P.; Wang, C.*; et al.* Identifying the components of the solid-electrolyte interphase in Li-ion batteries. *Nature Chemistry* **2019**, *11*, 789–796.
[105] Leifer, N.; Smart, M. C.; Prakash, G. K. S.; Gonzalez, L.; Sanchez, L.; Smith, K. A.; Bhalla, P.; Grey, C. P.; Greenbaum, S. G. 13 C Solid State NMR Suggests Unusual Breakdown Products in SEI Formation on Lithium Ion Electrodes. *Journal of the Electrochemical Society* **2011**, *158*, A471-A480.
[106] Cuisinier, M.; Martin, J. F.; Moreau, P.; Epicier, T.; Kanno, R.; Guyomard, D.; Dupré, N. Quantitative MAS NMR characterization of the LiMn(1/2)Ni(1/2)O(2) electrode/electrolyte interphase. *Solid State Nuclear Magnetic Resonance* **2012**, *42*, 51–61.
[107] Castaing, R.; Moreau, P.; Reynier, Y.; Schleich, D.; Jouanneau Si Larbi, S.; Guyomard, D.; Dupré, N. NMR quantitative analysis of solid electrolyte interphase on aged Li-ion battery electrodes. *Electrochimica Acta* **2015**, *155*, 391–395.
[108] Michan, A. L.; Leskes, M.; Grey, C. P. Voltage Dependent Solid Electrolyte Interphase Formation in Silicon Electrodes: Monitoring the Formation of Organic Decomposition Products. *Chemistry of Materials* **2016**, *28*, 385–398.
[109] Dienwiebel, I.; Winter, M.; Börner, M. Visualization of Degradation Mechanisms of Negative Electrodes Based on Silicon Nanoparticles in Lithium-Ion Batteries via Quasi In Situ Scanning Electron Microscopy and Energy-Dispersive X-ray Spectroscopy. *Journal of Physical Chemistry C* **2022**, *126*, 11016–11025.
[110] Vorauer, T.; Schöggl, J.; Sanadhya, S. G.; Poluektov, M.; Widanage, W. D.; Figiel, L.; Schädler, S.; Tordoff, B.; Fuchsbichler, B.; Koller, S.*; et al.* Impact of solid-electrolyte interphase reformation on capacity loss in silicon-based lithium-ion batteries. *Communications Materials* **2023**, *4*, 1–12.
[111] Tripathi, R.; Yesilbas, G.; Lamprecht, X.; Gandharapu, P.; Bandarenka, A. S.; Dusane, R. O.; Mukhopadhyay, A. Understanding the Electrolyte Chemistry Induced Enhanced Stability of Si Anodes in Li-Ion Batteries based on Physico-Chemical Changes, Impedance, and Stress Evolution during SEI Formation. *Journal of the Electrochemical Society* **2023**, *170*, 90544.

[112] Dachraoui, W.; Pauer, R.; Battaglia, C.; Erni, R. Operando Electrochemical Liquid Cell Scanning Transmission Electron Microscopy Investigation of the Growth and Evolution of the Mosaic Solid Electrolyte Interphase for Lithium-Ion Batteries. *ACS Nano* **2023**, *17*, 20434–20444.
[113] Zhu, H.; Shiraz, M. H. A.; Liu, L.; Hu, Y.; Liu, J. A facile and low-cost Al2O3 coating as an artificial solid electrolyte interphase layer on graphite/silicon composites for lithium-ion batteries. *Nanotechnology* **2021**, *32*, 144001.
[114] Weiling, M.; Lechtenfeld, C.; Pfeiffer, F.; Frankenstein, L.; Diddens, D.; Wang, J.-F.; Nowak, S.; Baghernejad, M. Mechanistic Understanding of Additive Reductive Degradation and SEI Formation in High-Voltage NMC811||SiO x -Containing Cells via Operando ATR-FTIR Spectroscopy. *Advanced Energy Materials* **2024**, *14.*
[115] Jena, A.; Tong, Z.; Bazri, B.; Iputera, K.; Chang, H.; Hu, S.-F.; Liu, R.-S. In Situ / Operando Methods of Characterizing All-Solid-State Li-Ion Batteries: Understanding Li-Ion Transport during Cycle. *The Journal of Physical Chemistry C* **2021**, *125*, 16921–16937.
[116] Yang, Z.; Jiang, M.; Cui, C.; Wang, Y.; Qin, J.; Wang, J.; Wang, Y.; Mao, B.; Cao, M. In-situ cross-linking strategy for stabilizing the LEDC of the solid-electrolyte interphase in lithium-ion batteries. *Nano Energy* **2023**, *105*, 107993.
[117] Landa-Medrano, I.; Eguia-Barrio, A.; Sananes-Israel, S.; Lijó-Pando, S.; Boyano, I.; Alcaide, F.; Urdampilleta, I.; Meatza, I. de. In Situ Analysis of NMC|graphite Li-Ion Batteries by Means of Complementary Electrochemical Methods. *Journal of the Electrochemical Society* **2020**, *167*, 90528.
[118] Wang, P.; de Yan; Wang, C.; Ding, H.; Dong, H.; Wang, J.; Wu, S.; Cui, X.; Li, C.; Zhao, D.*; et al.* Study of the formation and evolution of solid electrolyte interface via in-situ electrochemical impedance spectroscopy. *Applied Surface Science* **2022**, *596*, 153572.
[119] Ma, Y.; Sun, Q.; Wang, S.; Zhou, Y.; Song, D.; Zhang, H.; Shi, X.; Zhang, L. Li salt initiated in-situ polymerized solid polymer electrolyte: new insights via in-situ electrochemical impedance spectroscopy. *Chemical Engineering Journal* **2022**, *429*, 132483.
[120] Kitz, P. G.; Lacey, M. J.; Novák, P.; Berg, E. J. Operando investigation of the solid electrolyte interphase mechanical and transport properties formed from vinylene carbonate and fluoroethylene carbonate. *Journal of Power Sources* **2020**, *477*, 228567.
[121] Zeng, Z.; Liang, W.-I.; Liao, H.-G.; Xin, H. L.; Chu, Y.-H.; Zheng, H. Visualization of electrode-electrolyte interfaces in LiPF6/EC/DEC electrolyte for lithium ion batteries via in situ TEM. *Nano Letters* **2014**, *14*, 1745–1750.
[122] Mehdi, B. L.; Qian, J.; Nasybulin, E.; Park, C.; Welch, D. A.; Faller, R.; Mehta, H.; Henderson, W. A.; Xu, W.; Wang, C. M.*; et al.* Observation and quantification of nanoscale processes in lithium batteries by operando electrochemical (S)TEM. *Nano Letters* **2015**, *15*, 2168–2173.
[123] Cheong, J. Y.; Chang, J. H.; Seo, H. K.; Yuk, J. M.; Shin, J. W.; Lee, J. Y.; Kim, I.-D. Growth dynamics of solid electrolyte interphase layer on SnO2 nanotubes realized by graphene liquid cell electron microscopy. *Nano Energy* **2016**, *25*, 154–160.
[124] Lodico, J. J.; Mecklenburg, M.; Chan, H. L.; Chen, Y.; Ling, X. Y.; Regan, B. C. Operando spectral imaging of the lithium ion battery's solid-electrolyte interphase. *Science Advances* **2023**, *9*, eadg5135.
[125] Smith, E.; Dent, G. Modern Raman spectroscopy: A practical approach. Second edition; *Wiley* **2019**.
[126] Ferraro, J. R. Introductory Raman Spectroscopy 2nd ed.; *Elsevier Science & Technology* **2003**.

[127] Dietzek, B.; Cialla, D.; Schmitt, M.; Popp, J. Introduction to the Fundamentals of Raman Spectroscopy. *Confocal Raman Microscopy* **2010**, *158*, 21–42.
[128] Albrecht, A. C. On the Theory of Raman Intensities. *The Journal of Chemical Physics* **1961**, *34*, 1476–1484.
[129] Kögler, M.; Heilala, B. Time-gated Raman spectroscopy – a review. *Measurement Science Technology* **2020**, *32*, 12002.
[130] Knorr, F.; Smith, Z. J.; Wachsmann-Hogiu, S. Development of a time-gated system for Raman spectroscopy of biological samples. *Optics Express* **2010**, *18*, 20049–20058.
[131] Matousek, P.; Towrie, M.; Ma, C.; Kwok, W. M.; Phillips, D.; Toner, W. T.; Parker, A. W. Fluorescence suppression in resonance Raman spectroscopy using a high-performance picosecond Kerr gate. *Journal of Raman Spectroscopy* **2001**, *32*, 983–988.
[132] Matousek, P.; Towrie, M.; Stanley, A.; Parker, A. W. Efficient Rejection of Fluorescence from Raman Spectra Using Picosecond Kerr Gating. *Applied Spectroscopy* **1999**, *53*, 1485–1489.
[133] Wang, X.; Huang, S.-C.; Hu, S.; Yan, S.; Ren, B. Fundamental understanding and applications of plasmon-enhanced Raman spectroscopy. *Nature Reviews Physics* **2020**, *2*, 253–271.
[134] Stancovski, V.; Badilescu, S. In situ Raman spectroscopic–electrochemical studies of lithium-ion battery materials: a historical overview. *Journal of Applied Electrochemistry* **2014**, *44*, 23–43.
[135] Flores, E.; Novák, P.; Berg, E. J. In situ and Operando Raman Spectroscopy of Layered Transition Metal Oxides for Li-ion Battery Cathodes. *Frontiers in Energy Research* **2018**, *6.*
[136] Wei, Z.; Salehi, A.; Lin, G.; Hu, J.; Jin, X.; Agar, E.; Liu, F. Probing Li-ion concentration in an operating lithium ion battery using in situ Raman spectroscopy. *Journal of Power Sources* **2020**, *449*, 227361.
[137] Hardwick, L. J.; Ruch, P. W.; Hahn, M.; Scheifele, W.; Kötz, R.; Novák, P. In situ Raman spectroscopy of insertion electrodes for lithium-ion batteries and supercapacitors: First cycle effects. *Journal of Physics and Chemistry of Solids* **2008**, *69*, 1232–1237.
[138] Krause, A.; Tkacheva, O.; Omar, A.; Langklotz, U.; Giebeler, L.; Dörfler, S.; Fauth, F.; Mikolajick, T.; Weber, W. M. In Situ Raman Spectroscopy on Silicon Nanowire Anodes Integrated in Lithium Ion Batteries. *Journal of the Electrochemical Society* **2019**, *166*, A5378-A5385.
[139] Jehnichen, P.; Korte, C. Operando Raman Spectroscopy Measurements of a High-Voltage Cathode Material for Lithium-Ion Batteries. *Analytical Chemistry* **2019**, *91*, 8054–8061.
[140] Hiraoka, K.; Seki, S. Operando Raman Spectroscopy for Evaluating Concentration Changes in Li- and Na-Based Solid Polymer Electrolytes. *Journal of Physical Chemistry C* **2023**, *127*, 11864–11874.
[141] Baazizi, M.; Karbak, M.; Aqil, M.; Sayah, S.; Dahbi, M.; Ghamouss, F. High-Valence Surface-Modified LMO Cathode Materials for Lithium-Ion Batteries: Diffusion Kinetics and Operando Thermal Stability Investigation. *ACS Applied Materials & Interfaces* **2023**, *15*, 40385–40396.
[142] Fleischmann, M.; Hendra, P. J.; McQuillan, A. J. Raman spectra of pyridine adsorbed at a silver electrode. *Chemical Physics Letters* **1974**, *26*, 163–166.
[143] Rostron, P.; Gerber, D. Raman Spectroscopy, a review. *International Journal of Engineering Research and Technology* **2016**, *6*, 50–64.
[144] Grasseschi, D.; Toma, H. E. The SERS effect in coordination chemistry. *Coordination Chemistry Reviews* **2017**, *333*, 108–131.

[145] Hong, S.; Li, X. Optimal Size of Gold Nanoparticles for Surface-Enhanced Raman Spectroscopy under Different Conditions. *Journal of Nanomaterials* **2013**, *2013.*
[146] Maibach, J.; Rizell, J.; Matic, A.; Mozhzhukhina, N. Toward Operando Characterization of Interphases in Batteries. *ACS Materials Letters* **2023**, *5*, 2431–2444.
[147] Schmitz, R.; Müller-Romek, A.; Wilhelm Schmitz, R.; Schreiner, C.; Kunze, M.; Lex-Balducci, A.; Passerini, S.; Winter, M. SEI investigations on copper electrodes after lithium plating with Raman spectroscopy and mass spectrometry. *Journal of Power Sources* **2013**, *233*, 110–114.
[148] Tang, S.; Gu, Y.; Yi, J.; Zeng, Z.; Ding, S.-Y.; Yan, J.-W.; Wu, D.-Y.; Ren, B.; Tian, Z.-Q.; Mao, B.-W. An electrochemical surface-enhanced Raman spectroscopic study on nanorod-structured lithium prepared by electrodeposition. *Journal of Raman Spectroscopy* **2016**, *47*, 1017–1023.
[149] Ha, Y.; Tremolet de Villers, B. J.; Li, Z.; Xu, Y.; Stradins, P.; Zakutayev, A.; Burrell, A.; Han, S.-D. Probing the Evolution of Surface Chemistry at the Silicon-Electrolyte Interphase via In Situ Surface-Enhanced Raman Spectroscopy. *The Journal of Physical Chemistry Letters* **2020**, *11*, 286–291.
[150] Li, H.; Mo, Y.; Pei, N.; Xu, X.; Huang, X.; Chen, L. Surface-Enhanced Raman Scattering Study on Passivating Films of Ag Electrodes in Lithium Batteries. *Journal of Physical Chemistry B* **2000**, *104*, 8477–8480.
[151] Li, G.; Li, H.; Mo, Y.; Chen, L.; Huang, X. Further identification to the SEI film on Ag electrode in lithium batteries by surface enhanced Raman scattering (SERS). *Journal of Power Sources* **2002**, *104*, 190–194.
[152] Zhang, Y.-J.; Ze, H.; Fang, P.-P.; Huang, Y.-F.; Kudelski, A.; Fernández-Vidal, J.; Hardwick, L. J.; Lipkowski, J.; Tian, Z.-Q.; Li, J.-F. Shell-isolated nanoparticle-enhanced Raman spectroscopy. *Nature Reviews Methods Primers* **2023**, *3*, 1–18.
[153] Nanda, J.; Yang, G.; Hou, T.; Voylov, D. N.; Li, X.; Ruther, R. E.; Naguib, M.; Persson, K.; Veith, G. M.; Sokolov, A. P. Unraveling the Nanoscale Heterogeneity of Solid Electrolyte Interphase Using Tip-Enhanced Raman Spectroscopy. *Joule* **2019**, *3*, 2001–2019.
[154] Li, J. F.; Huang, Y. F.; Ding, Y.; Yang, Z. L.; Li, S. B.; Zhou, X. S.; Fan, F. R.; Zhang, W.; Zhou, Z. Y.; Wu, D. Y.*; et al.* Shell-isolated nanoparticle-enhanced Raman spectroscopy. *Nature* **2010**, *464*, 392–395.
[155] Krajczewski, J.; Kudelski, A. Chapter 11 - Shell-isolated nanoparticle-enhanced Raman spectroscopy: a review. In Molecular and laser spectroscopy: Advances and applications: volume 2. Gupta, V. P., Ozaki, Y., *Elsevier* **2020**, 387–414.
[156] Piernas-Muñoz, M. J.; Tornheim, A.; Trask, S.; Zhang, Z.; Bloom, I. Surface-enhanced Raman spectroscopy (SERS): a powerful technique to study the SEI layer in batteries. *Chemical Communications* **2021**, *57*, 2253–2256.
[157] Hestenes, J. C.; Marbella, L. E. Beyond Composition: Surface Reactivity and Structural Arrangement of the Cathode–Electrolyte Interphase. *ACS Energy Letters* **2023**, *8*, 4572–4596.
[158] Khabarov, K.; Filalova, E.; Nouraldeen, M.; Kameneva, E.; Musaev, A.; Tikhonov, S.; Ivanov, V. Effect of Au Nanoparticle Agglomeration on SERS Signal Amplification. *Nanomaterials* **2023**, *13*, 812.
[159] Pfeiffer, F.; Griggio, A.; Weiling, M.; Wang, J.-F.; Reißig, F.; Peschel, C.; Pillatsch, L.; Warrington, S.; Nowak, S.; Grimaudo, V.*; et al.* Tracing the Cross-Talk Phenomenon of Vinylethylene Carbonate to Unveil its Counterintuitive Influence as an Electrolyte Additive on High-Voltage Lithium-Ion Batteries. *Advanced Energy Materials* **2024.**
[160] Cabo-Fernandez, L.; Bresser, D.; Braga, F.; Passerini, S.; Hardwick, L. J. In-Situ Electrochemical SHINERS Investigation of SEI Composition on Carbon-Coated Zn 0.9 Fe 0.1 O Anode for Lithium-Ion Batteries. *Batteries & Supercaps* **2019**, *2*, 168–177.

[161] Martín-Yerga, D.; Milan, D. C.; Xu, X.; Fernández-Vidal, J.; Whalley, L.; Cowan, A. J.; Hardwick, L. J.; Unwin, P. R. Dynamics of Solid-Electrolyte Interphase Formation on Silicon Electrodes Revealed by Combinatorial Electrochemical Screening. *Angewandte Chemie* **2022**, *61*, e202207184.
[162] Hy, S.; Felix; Chen, Y.-H.; Liu, J.; Rick, J.; Hwang, B.-J. In situ surface enhanced Raman spectroscopic studies of solid electrolyte interphase formation in lithium ion battery electrodes. *Journal of Power Sources* **2014**, *256*, 324–328.
[163] Galloway, T. A.; Cabo-Fernandez, L.; Aldous, I. M.; Braga, F.; Hardwick, L. J. Shell isolated nanoparticles for enhanced Raman spectroscopy studies in lithium-oxygen cells. *Faraday Discussions* **2017**, *205*, 469–490.
[164] Schmiegel, J.-P.; Leißing, M.; Weddeling, F.; Horsthemke, F.; Reiter, J.; Fan, Q.; Nowak, S.; Winter, M.; Placke, T. Novel In Situ Gas Formation Analysis Technique Using a Multilayer Pouch Bag Lithium Ion Cell Equipped with Gas Sampling Port. *Journal of the Electrochemical Society* **2020**, *167*, 60516.
[165] Li, J. F.; Tian, X. D.; Li, S. B.; Anema, J. R.; Yang, Z. L.; Ding, Y.; Wu, Y. F.; Zeng, Y. M.; Chen, Q. Z.; Ren, B.*; et al.* Surface analysis using shell-isolated nanoparticle-enhanced Raman spectroscopy. *Nature Protocols* **2013**, *8*, 52–65.
[166] Horsthemke, F.; Winkler, V.; Diehl, M.; Winter, M.; Nowak, S. Concept for the Analysis of the Electrolyte Composition within the Cell Manufacturing Process: From Sealing to Sample Preparation. *Energy Technology* **2020**, *8*.
[167] Peschel, C.; Horsthemke, F.; Winter, M.; Nowak, S. Implementation of orbitrap mass spectrometry for improved GC-MS target analysis in lithium ion battery electrolytes. *MethodsX* **2022**, *9*, 101621.
[168] Frisch, M. J.; Trucks, G. W.; Schlegel, H. B.; Scuseria, G. E.; Robb, M. A.; Cheeseman, J. R.; Scalmani, G.; Barone, V.; Petersson, G. A.; Nakatsuji, H.*; et al.* Gaussian 16, Revision C.01. *Wallingford CT* **2016**.
[169] Curtiss, L. A.; Redfern, P. C.; Raghavachari, K. Gaussian-4 theory using reduced order perturbation theory. *The Journal of Chemical Physics* **2007**, *127*, 124105.
[170] Hanwell, M. D.; Curtis, D. E.; Lonie, D. C.; Vandermeersch, T.; Zurek, E.; Hutchison, G. R. Avogadro: an advanced semantic chemical editor, visualization, and analysis platform. *Journal of Cheminformatics* **2012**, *4*, 17.
[171] Pracht, P.; Caldeweyher, E.; Ehlert, S.; Grimme, S. *A Robust Non-Self-Consistent Tight-Binding Quantum Chemistry Method for large Molecules*, **2019**.
[172] Pracht, P.; Bohle, F.; Grimme, S. Automated exploration of the low-energy chemical space with fast quantum chemical methods. *Physical Chemistry Chemical Physics* **2020**, *22*, 7169–7192.
[173] Grimme, S.; Bannwarth, C.; Shushkov, P. A Robust and Accurate Tight-Binding Quantum Chemical Method for Structures, Vibrational Frequencies, and Noncovalent Interactions of Large Molecular Systems Parametrized for All spd-Block Elements (Z = 1-86). *Journal of Chemical Theory and Computation* **2017**, *13*, 1989–2009.
[174] Bannwarth, C.; Ehlert, S.; Grimme, S. GFN2-xTB-An Accurate and Broadly Parametrized Self-Consistent Tight-Binding Quantum Chemical Method with Multipole Electrostatics and Density-Dependent Dispersion Contributions. *Journal of Chemical Theory and Computation* **2019**, *15*, 1652–1671.
[175] O'Boyle, N. M.; Banck, M.; James, C. A.; Morley, C.; Vandermeersch, T.; Hutchison, G. R. Open Babel: An open chemical toolbox. *Journal of Cheminformatics* **2011**, *3*, 33.
[176] Borodin, O.; Ren, X.; Vatamanu, J.; Wald Cresce, A. von; Knap, J.; Xu, K. Modeling Insight into Battery Electrolyte Electrochemical Stability and Interfacial Structure. *Accounts of Chemical Research* **2017**, *50*, 2886–2894.
[177] Borodin, O.; Olguin, M.; Spear, C. E.; Leiter, K. W.; Knap, J. Towards high throughput screening of electrochemical stability of battery electrolytes. *Nanotechnology* **2015**, *26*, 354003.

[178] Borodin, O.; Behl, W.; Jow, T. R. Oxidative Stability and Initial Decomposition Reactions of Carbonate, Sulfone, and Alkyl Phosphate-Based Electrolytes. *Journal of Physical Chemistry C* **2013**, *117*, 8661–8682.
[179] Hall, D. S.; Self, J.; Dahn, J. R. Dielectric Constants for Quantum Chemistry and Li-Ion Batteries: Solvent Blends of Ethylene Carbonate and Ethyl Methyl Carbonate. *Journal of Physical Chemistry C* **2015**, *119*, 22322–22330.
[180] Marenich, A. V.; Cramer, C. J.; Truhlar, D. G. Universal solvation model based on solute electron density and on a continuum model of the solvent defined by the bulk dielectric constant and atomic surface tensions. *Journal of Physical Chemistry B* **2009**, *113*, 6378–6396.
[181] Nie, M.; Chalasani, D.; Abraham, D. P.; Chen, Y.; Bose, A.; Lucht, B. L. Lithium Ion Battery Graphite Solid Electrolyte Interphase Revealed by Microscopy and Spectroscopy. *Journal of Physical Chemistry C* **2013**, *117*, 1257–1267.
[182] Alakhras, F.; Holze, R. Redox thermodynamics, conductivity and Raman spectroscopy of electropolymerized furan–thiophene copolymers. *Electrochimica Acta* **2007**, *52*, 5896–5906.
[183] Chen, F.; Shi, G.; Zhang, J.; Fu, M. Raman spectroscopic studies on the structural changes of electrosynthesized polythiophene films during the heating and cooling processes. *Thin Solid Films* **2003**, *424*, 283–290.
[184] Shi, G.; Xu, J.; Fu, M. Raman Spectroscopic and Electrochemical Studies on the Doping Level Changes of Polythiophene Films during Their Electrochemical Growth Processes. *Journal of Physical Chemistry B* **2002**, *106*, 288–292.
[185] Takahashi, I.; Kiuchi, H.; Ohma, A.; Fukunaga, T.; Matsubara, E. Cathode Electrolyte Interphase Formation and Electrolyte Oxidation Mechanism for Ni-Rich Cathode Materials. *Journal of Physical Chemistry C* **2020**, *124*, 9243–9248.
[186] Li, W.; Song, B.; Manthiram, A. High-voltage positive electrode materials for lithium-ion batteries. *Chemical Society Reviews* **2017**, *46*, 3006–3059.
[187] Klein, S.; Harte, P.; van Wickeren, S.; Borzutzki, K.; Röser, S.; Bärmann, P.; Nowak, S.; Winter, M.; Placke, T.; Kasnatscheew, J. Re-evaluating common electrolyte additives for high-voltage lithium ion batteries. *Cell Reports Physical Science* **2021**, *2*, 100521.
[188] Li, H.; Zhang, N.; Li, J.; Dahn, J. R. Updating the Structure and Electrochemistry of Li x NiO 2 for 0 ≤ x ≤ 1. *Journal of the Electrochemical Society* **2018**, *165*, A2985-A2993.
[189] Stolz, L.; Gaberšček, M.; Winter, M.; Kasnatscheew, J. Different Efforts but Similar Insights in Battery R&D: Electrochemical Impedance Spectroscopy vs Galvanostatic (Constant Current) Technique. *Chemistry of Materials* **2022**, *34*, 10272–10278.
[190] Li, X.; Lv, M.; Tian, Y.; Gao, L.; Liu, T.; Zhou, Q.; Xu, Y.; Shen, L.; Shi, W.; Li, X.*; et al.* Negatively charged polymeric interphase for regulated uniform lithium-ion transport in stable lithium metal batteries. *Nano Energy* **2021**, *87*, 106214.
[191] Pan, Y.; Zhou, Y.; Zhao, Q.; Dou, Y.; Chou, S.; Cheng, F.; Chen, J.; Liu, H. K.; Jiang, L.; Dou, S. X. Introducing ion-transport-regulating nanochannels to lithium-sulfur batteries. *Nano Energy* **2017**, *33*, 205–212.
[192] Zeng, J.; Liu, Q.; Jia, D.; Liu, R.; Liu, S.; Zheng, B.; Zhu, Y.; Fu, R.; Wu, D. A polymer brush-based robust and flexible single-ion conducting artificial SEI film for fast charging lithium metal batteries. *Energy Storage Materials* **2021**, *41*, 697–702.
[193] Sahore, R.; Dogan, F.; Bloom, I. D. Identification of Electrolyte-Soluble Organic Cross-Talk Species in a Lithium-Ion Battery via a Two-Compartment Cell. *Chemistry of Materials* **2019**, *31*, 2884–2891.
[194] Wölke, C.; Benayad, A.; Lai, T.-L.; Hanke, F.; Baraldi, G.; Echeverría, M.; Esen, E.; Ayerbe, E.; Neale, A. R.; Everitt, J.*; et al.* Single Versus Blended Electrolyte Additives: Impact of a Sulfur-Based Electrolyte Additive on Electrode Cross-Talk and

Electrochemical Performance of LiNiO 2 ||Graphite Cells. *Advanced Energy Materials* **2024.**
[195] Socrates, G. Infrared and Raman characteristic group frequencies: Tables and charts, 3. ed., *Wiley* **2010**.
[196] Nie, M.; Demeaux, J.; Young, B. T.; Heskett, D. R.; Chen, Y.; Bose, A.; Woicik, J. C.; Lucht, B. L. Effect of Vinylene Carbonate and Fluoroethylene Carbonate on SEI Formation on Graphitic Anodes in Li-Ion Batteries. *Journal of the Electrochemical Society* **2015**, *162*, A7008-A7014.
[197] Zhang, H.; Zeng, Z.; Ma, F.; Wang, X.; Wu, Y.; Liu, M.; He, R.; Cheng, S.; Xie, J. Juggling Formation of HF and LiF to Reduce Crossover Effects in Carbonate Electrolyte with Fluorinated Cosolvents for High-Voltage Lithium Metal Batteries. *Advanced Functional Materials* **2023**, *33.*
[198] Hekmatfar, M.; Hasa, I.; Eghbal, R.; Carvalho, D. V.; Moretti, A.; Passerini, S. Effect of Electrolyte Additives on the LiNi 0.5 Mn 0.3 Co 0.2 O 2 Surface Film Formation with Lithium and Graphite Negative Electrodes. *Advanced Materials Interfaces* **2020**, *7.*
[199] An, S. J.; Li, J.; Daniel, C.; Mohanty, D.; Nagpure, S.; Wood, D. L. The state of understanding of the lithium-ion-battery graphite solid electrolyte interphase (SEI) and its relationship to formation cycling. *Carbon* **2016**, *105*, 52–76.
[200] Zhang, S. S. A review on electrolyte additives for lithium-ion batteries. *Journal of Power Sources* **2006**, *162*, 1379–1394.
[201] Santner, H. J.; Möller, K.-C.; Ivančo, J.; Ramsey, M. G.; Netzer, F. P.; Yamaguchi, S.; Besenhard, J. O.; Winter, M. Acrylic acid nitrile, a film-forming electrolyte component for lithium-ion batteries, which belongs to the family of additives containing vinyl groups. *Journal of Power Sources* **2003**, *119-121*, 368–372.
[202] Lee, S. Y.; Park, Y. J. Effect of Vinylethylene Carbonate and Fluoroethylene Carbonate Electrolyte Additives on the Performance of Lithia-Based Cathodes. *ACS Omega* **2020**, *5*, 3579–3587.
[203] Li, B.; Wang, Y.; Lin, H.; Liu, J.; Xing, L.; Xu, M.; Li, W. Improving high voltage stability of lithium cobalt oxide/graphite battery via forming protective films simultaneously on anode and cathode by using electrolyte additive. *Electrochimica Acta* **2014**, *141*, 263–270.
[204] Lin, X.-D.; Li, J.-F.; Huang, Y.-F.; Tian, X.-D.; Uzayisenga, V.; Li, S.-B.; Ren, B.; Tian, Z.-Q. Shell-isolated nanoparticle-enhanced Raman spectroscopy: Nanoparticle synthesis, characterization and applications in electrochemistry. *Journal of Electroanalytical Chemistry* **2013**, *688*, 5–11.
[205] Yockell-Lelièvre, H.; Lussier, F.; Masson, J.-F. Influence of the Particle Shape and Density of Self-Assembled Gold Nanoparticle Sensors on LSPR and SERS. *Journal of Physical Chemistry C* **2015**, *119*, 28577–28585.
[206] Li, C.-Y.; Yu, Y.; Wang, C.; Zhang, Y.; Zheng, S.-Y.; Li, J.-F.; Maglia, F.; Jung, R.; Tian, Z.-Q.; Shao-Horn, Y. Surface Changes of LiNi x Mn y Co 1– x – y O 2 in Li-Ion Batteries Using in Situ Surface-Enhanced Raman Spectroscopy. *Journal of Physical Chemistry C* **2020**, *124*, 4024–4031.
[207] Yang, G.; Ivanov, I. N.; Ruther, R. E.; Sacci, R. L.; Subjakova, V.; Hallinan, D. T.; Nanda, J. Electrolyte Solvation Structure at Solid-Liquid Interface Probed by Nanogap Surface-Enhanced Raman Spectroscopy. *ACS Nano* **2018**, *12*, 10159–10170.
[208] Zhu, Y.; Casselman, M. D.; Li, Y.; Wei, A.; Abraham, D. P. Perfluoroalkyl-substituted ethylene carbonates: Novel electrolyte additives for high-voltage lithium-ion batteries. *Journal of Power Sources* **2014**, *246*, 184–191.
[209] Naudin, C.; Bruneel, J. L.; Chami, M.; Desbat, B.; Grondin, J.; Lassègues, J. C.; Servant, L. Characterization of the lithium surface by infrared and Raman spectroscopies. *Journal of Power Sources* **2003**, *124*, 518–525.

[210] Yong, C.; Renyuan, Q. IR and Raman studies of polythiophene prepared by electrochemical polymerization. *Solid State Communications* **1985**, *54*, 211–213.
[211] Mozhzhukhina, N.; Flores, E.; Lundström, R.; Nyström, V.; Kitz, P. G.; Edström, K.; Berg, E. J. Direct Operando Observation of Double Layer Charging and Early Solid Electrolyte Interphase Formation in Li-Ion Battery Electrolytes. *The Journal of Physical Chemistry Letters* **2020**, *11*, 4119–4123.
[212] Verma, P.; Maire, P.; Novák, P. A review of the features and analyses of the solid electrolyte interphase in Li-ion batteries. *Electrochimica Acta* **2010**, *55*, 6332–6341.
[213] Schedlbauer, T.; Krüger, S.; Schmitz, R.; Schmitz, R. W.; Schreiner, C.; Gores, H. J.; Passerini, S.; Winter, M. Lithium difluoro(oxalato)borate: A promising salt for lithium metal based secondary batteries? *Electrochimica Acta* **2013**, *92*, 102–107.

12. Acknowledgements

An dieser Stelle möchte ich mich bei Allen bedanken, die mich während meines Studiums und insbesondere während meiner Promotion unterstützt haben.

Zuerst möchte ich mich bei Prof. Dr. Martin Winter bedanken, der es mir ermöglichte, meine Promotion am HI MS durchzuführen. Ohne seine Unterstützung und die wertvollen Impulse wäre dies nicht möglich gewesen.

Ich möchte mich auch bei PD Dr. Gunther Brunklaus für interessante Gespräche und Diskussionen bedanken, sowie für seine freundliche Bereitschaft das Zweitgutachten für diese Arbeit zu erstellen.

Bei Dr. Kerstin Neuhaus möchte ich mich für ihre Unterstützung und die Korrektur meiner Arbeit bedanken.

Einen besonderen Dank schulde ich Dr. Masoud Baghernejad, der mir die Möglichkeit gegeben hat Teil seiner Forschungsgruppe zu werden. Seine Betreuung, Hilfe und Unterstützung, sowie das Vertrauen in meine Arbeit, Ideen und Ansätze hat maßgeblich zu dem Gelingen meiner Promotion beigetragen.

Auch möchte ich mich herzlich bei meinen Kollegen am HI MS und am MEET für die schöne Zeit und die Unterstützung bei meiner Arbeit bedanken. Insbesondere bei Angela Griggio, Verena Küpers, Friederike Reißig, Lars Frankenstein, Sebastian Kühn, Christoph Peschel, Diddo Diddens, Johannes Thienenkamp und den Mitgliedern des MIM-Seminars, die mich in meinen Projekten unterstützt haben. Zusätzlich möchte ich mich auch bei André Bar bedanken, der meine Projekte grafisch unterstützt hat.

Ganz besonders möchte ich mich zusätzlich bei meinen beiden Masoud-Boys 2 und 3, Matthias Weiling und Jian-Fen Wang, sowie Tobias Hinz und Patrick Mowe bedanken, die mich nicht nur wissenschaftlich unterstützt haben, sondern auch für ein entspanntes und lustiges Arbeitsumfeld gesorgt haben. Ohne euch hätten die letzten Jahre kaum so viel Spaß gemacht.

Neben denjenigen, die direkt zum wissenschaftlichen Gelingen meiner Arbeit beigetragen haben möchte ich mich auch bei Allen bedanken, die mich auf meinem Weg begleitet haben.

Angefangen bei meinen Freunden aus Wolbeck: Sebastian, Jonas, Dennis, Simon, Gerrit, Nils, Till, Alex und Tim, die mich teilweise schon seit dem Kindergarten kennen und mich immer unterstützt haben.

Ich auch möchte ich mich bei Simon, Henning, Michael, Eike und Sebastian bedanken, die mich besonders während meines Studiums unterstützt haben. Obwohl wir uns vorher nicht kannten, haben wir sehr schnell, verbunden durch unsere Passion für cineastische Meisterwerke mangelnder Qualität, zusammengefunden und gemerkt, dass ein Chemie Studium auch schöne Seiten haben kann. Erweitert durch Nadine, Norina, Melina und Lizanne, haben wir viele schöne Abende, Ausflüge und Urlaube verbracht, die mein Studium zu einer ganz besonderen Zeit gemacht haben.

Auch möchte ich mich sehr bei meinen Mitbewohner*innen bedanken, die immer eine behagliche Atmosphäre und ein zuhause für mich geschaffen haben.

Der größte Dank gebührt meiner Familie, insbesondere meinen Eltern und meiner Schwester, die mich bedingungslos unterstützt haben und es mir ermöglichten mein Leben nach meinen Wünschen zu gestalten und meinen eigenen Weg zu gehen.

Abschließend möchte ich mich besonders bei Johanna bedanken, die mich seit vielen Jahren ermutigt, begleitet und mich in schwierigen Momenten gestärkt, unterstützt und zu mir gehalten hat.

13. Curriculum Vitae

Personal Information

Name	Felix Amandus Pfeiffer
Date of Birth	18.08.1996
Place of Birth	Münster, Germany
Nationality	German

Professional Experiences

04/2020 – 12/2020	Student Assistant, MEET Battery Research Center, Münster
06/2021 – 12/2024	PhD Studies, Helmholtz Institute Münster, Supervision: Prof. Dr. Martin Winter and Dr. Masoud Baghernejad

Education

08/2006 – 07/2014:	**Gymnasium**
	Städtisches Gymnasium Wolbeck
	Abschluss: **Abitur**
10/2015 – 09/2018:	**Bachelor Studies**
	Westfälische Wilhelms-Universität Münster
	Fachbereich: Chemie
	Abschluss: **Bachelor of Science**
10/2018 – 03/2021:	**Master Studies**
	Westfälische Wilhelms-Universität Münster
	Fachbereich: Chemie
	Abschluss: **Master of Science**

Languages:

German	Mother tongue
English	Fluent

14. Contributions to Scientific Journals

1st Author Contributions

M. Weiling*, **F. Pfeiffer***, M. Baghernejad, Vibrational Spectroscopy Insight into the Electrode|electrolyte Interface/Interphase in Lithium Batteries. *Adv. Energy Mater.* **2022**, 12, 2202504.

*both authors contributed equally

F. Pfeiffer, D. Diddens, M. Weiling M. Baghernejad, Study of a High-Voltage NMC Interphase in the Presence of a Thiophene Additive Realized by Operando SHINERS. *ACS Appl. Mater. Interfaces,* **2023**, 15, 5, 6676–6686.

F. Pfeiffer, D. Diddens, M. Weiling, L. Frankenstein, S. Kühn, I. Cekic-Laskovic, M. Baghernejad, Quadrupled Cycle Life of High-Voltage Nickel-Rich Cathodes: Understanding the Effective Thiophene-Boronic Acid-Based CEI via Operando SHINERS. *Adv. Energy Mater.* **2023**, 13, 2300827.

F. Pfeiffer, A. Griggio, M. Weiling, J.-F. Wang, F. Reißig, C. Peschel, L. Pillatsch, S. Warrington, S. Nowak, V. Grimaudo, I. Wright, M. Baghernejad, Tracing the Cross-Talk Phenomenon of Vinylethylene Carbonate to Unveil its Counterintuitive Influence as an Electrolyte Additive on High-Voltage Lithium-Ion Batteries. *Adv. Energy Mater.* **2024**, 14, 2470167.

F. Pfeiffer, A. Griggio, M. Weiling, J.-F. Wang, F. Reißig, C. Peschel, L. Pillatsch, S. Warrington, S. Nowak, V. Grimaudo, I. Wright, M. Baghernejad, ***Cover Picture***, Tracing the Cross-Talk Phenomenon of Vinylethylene Carbonate to Unveil its Counterintuitive Influence as an Electrolyte Additive on High-Voltage Lithium-Ion Batteries. *Adv. Energy Mater.* **2024**, 14, 2470167.

Coauthor Contributions

S. Kühn, **F. Pfeiffer**, M. Bela, U. Rodehorst, D. Weintz, M. Stan, M. Baghernejad, I. Cekic-Laskovic, Back to the basics: Advanced understanding of the as-defined solid electrolyte interphase on lithium metal electrodes. *Journal of Power Sources*, **2022**, 549, 232118.

L. Haneke, **F. Pfeiffer**, P. Bärmann, J. Wrogemann, C. Peschel, J. Neumann, F. Kux, S. Nowak, M. Winter, T. Placke, Insights into Electrolytic Pre-Lithiation: A Thorough Analysis Using Silicon Thin Film Anodes. *Small*, **2023**, 19, 2206092.

B. A. Sadeghi, C. Wölke, F. Pfeiffer, M. Baghernejad, M. Winter, I. Cekic-Laskovic, Synergistic role of functional electrolyte additives containing phospholane-based derivative to address interphasial chemistry and phenomena in NMC811||Si-graphite cells. *Journal of Power Sources*, **2023**, 557, 232570.

A. Ghaur, **F. Pfeiffer**, D. Diddens, C. Peschel, I. Dienwiebel, L. Du, L. Profanter, M. Weiling, M. Winter, T. Placke, S. Nowak, M. Baghernejad, Molecular-Cling-Effect of Fluoroethylene Carbonate Characterized via Ethoxy(pentafluoro)cyclotriphosphazene on SiOx/C Anode Materials – A New Perspective for Formerly Sub-Sufficient SEI Forming Additive Compounds. *Small*, **2023**, 19, 2302486.

M. Weiling, C. Lechtenfeld, **F. Pfeiffer**, L. Frankenstein, D. Diddens, J.-F. Wang, S. Nowak, M. Baghernejad, Mechanistic Understanding of Additive Reductive Degradation and SEI Formation in High-Voltage NMC811||SiO_x-Containing Cells via Operando ATR-FTIR Spectroscopy. *Adv. Energy Mater.* **2024**, 14, 2303568.

M. Weiling, **F. Pfeiffer**, C. Lechtenfeld, S. Stuckenberg, N. Fehlings, L. Frankenstein, V. Küpers, J.-F. Wang, S. Nowak, M. Baghernejad, Comprehensive Study on Cell Components in High-Voltage Pouch Cells with Lithium Perchlorate: Decomposition, Transesterification, Chlorination, Deposition, and Self-Discharge. *Batteries & Supercaps*, **2024**, e202400568.

B. Ying, Z. Teng, S. Day, D. Porter, M. Winter, A. Jonas, K. Frenzel, L. Mathies, B. Beckhoff, P. Nagel, S. Schuppler, M. Merz, **F. Pfeiffer**, M. Weiling, M. Baghernejad, K. Kleiner, A review and outlook on anionic and cationic redox in Ni-, Li- and Mn-rich layered oxides LiMeO2 (Me = Li, Ni, Co, Mn). *arXiv*, **2024**, arxiv:2310.01295v2.

L. Haneke, **F. Pfeiffer**, K. Rudolf, P. Sutar, M. Baghernejad, M. Winter, T. Placke, J. Kasnatscheew, Investigating the Existence of a Cathode Electrolyte Interphase on Graphite in Dual-Ion Batteries with $LiPF_6$-Based Aprotic Electrolytes and Unraveling the Origin of Capacity Fade. *Adv. Energy Sustainability Res*. **2024**, 2400330.

P. Yan, M. Shevchuk, C. Wölke, **F. Pfeiffer**, D. Berghus, M. Baghernejad, G.-V. Röschenthaler, M. Winter, I. Cekic-Laskovic, Blended Salt Electrolyte Design for Enhanced NMC811||Graphite Cell Performance. *Small Struct.* **2024**, 5, 2300425.

J. Weidelt, J. R. Nair, D. Diddens, W. Zhang, **F. Pfeiffer**, T. O. Schneider, M. Meinert, T. Hiraoka, L. Nesterov, M. Baghernejad, D. Turchinovich, H. A. Hafez, Fundamental Picture of the Conduction Mechanism in Solid-State Polymer Electrolytes Revealed by Terahertz Spectroscopy. *J. Phys. Chem. C*, **2024**, 128, 16, 6868–6876.

J.-F. Wang, M. Weiling, **F. Pfeiffer**, K.-L. Liu, M. Baghernejad, Molecular Insights into the Interfacial Phenomena at the Li Metal | Polymer Solid-State Electrolyte in Anode-Free Configuration During Li Plating-Stripping via Advanced Operando ATR-FTIR Spectroscopy. *Adv. Energy Mater.* **2024**, 2404569.

Submitted Patents

M. Weiling, M. Baghernejad, F. Pfeiffer, J.-F. Wang, R. Guerdelli, angemeldet 10.06.2024, 102024116133.7, Deutsches Patent- und Markenamt München

Conference Contributions

F. Pfeiffer, M. Weiling, M. Winter, M. Baghernejad, Dynamic tracking of the formation of additive-tuned interphases on high voltage Ni-rich cathodes using operando SHINERS. *ABAA13*, **2022**, Marrakech, Morocco, Poster presentation.

F. Pfeiffer, M. Weiling, D. Diddens, L. Frankenstein, M. Baghernejad, Investigation of thiophene-based electrolyte additives for high voltage LIBs realized by operando SHINERS. *Advanced Battery Power*, **2023**, Aachen, Germany, Poster presentation.

F. Pfeiffer, M. Weiling, J.-F. Wang, M. Baghernejad, Interphase Characterization on High-Voltage LIB Electrodes via Advanced Operando Raman Spectroscopy. *Swiss Battery Days*, **2023**, Villingen, Switzerland, Poster Presentation.

F. Pfeiffer, M. Weiling, J.-F. Wang, M. Baghernejad, Interphase Characterization on High-Voltage LIB Electrodes via Advanced Operando Raman Spectroscopy. *Swiss Battery Days*, **2023**, Villingen, Switzerland, Oral Presentation.

F. Pfeiffer, A. Griggio, M. Weiling, J.-F. Wang, C. Peschel, M. Baghernejad, Characterization of Interphases formed by Ethylene Carbonate based Electrolyte Additives on High-Voltage Lithium-Ion Battery Electrodes via operando Advanced Raman Spectroscopy Techniques. *Advanced Battery Power*, **2024**, Münster, Germany, Poster presentation.

F. Pfeiffer, A. Griggio, M. Weiling, J.-F. Wang, C. Peschel, F. Reißig, M. Baghernejad, Investigating the Film-Forming Effect of Vinyl Ethylene Carbonate in High-Voltage Lithium-Ion Batteries by In-Situ Advanced Raman Spectroscopy. *IMLB*, **2024**, Hongkong, China, Poster presentation.

F. Pfeiffer, A. Griggio, M. Weiling, J.-F. Wang, C. Peschel, M. Baghernejad, Elucidating the Shuttle Mechanism of Vinyl Ethylene Carbonate by In-Situ Advanced Raman Spectroscopy. *ECS Prime*, **2024**, Honululu, USA, Oral presentation.